High-Pressure Diffraction Studies of Rubidium Phase IV

Lars Fahl Lundegaard

A thesis submitted in fulfilment of the requirements for the degree of Doctor of Philosophy.

School of Physics and
Centre for Science at Extreme Conditions.
University of Edinburgh.

September 2007

Foreword

This PhD project was funded by an Internationalisation Grant from the Danish Research Training Council (FUR). The funding covered fees, salary and travel expenses for attending conferences and for annual visits to the Geological Institute, University of Copenhagen which administrated the grant. With the grant followed an obligation to stay in contact with, and if possible, to initiate a collaboration with the contact person (Prof. Emil Makovicky) at the home institution.

During the first year visit to the home institution a paper was written and submitted for publication (Lundegaard et al. 2005). During the second year visit, single crystal X-ray diffraction data were collected on the in house diffractometer, which resulted in a paper (Benna et al. 2007). In the third year Prof. Emil Makovicky visited the Edinburgh High-pressure Group, where high-pressure single-crystal diffraction data were collected on a mineral.

This collaboration is not directly related to the study presented in this PhD thesis and is therefore only mentioned here in the foreword.

Declaration

This thesis has been composed by myself and it has not been submitted in any previous application for a degree. The work reported within was executed by me, unless otherwise stated. Where the work was done in collaboration with others, a significant contribution was made by the author.

Signed

Lars Fahl Lundegaard

Acknowledgment

I would like to thank Prof. Emil Makovicky for his help and support when the application for the Internationalisation Grant was written, and for his help to solve several problems related to the grant during the PhD.

I would like to thank our collaborators Prof. Sander van Smaalen and Dr Lukas Palatinus for sharing their expertise in superspace crystallography with me.

I would like to acknowledge the help and support we have received from beamline staff on experimental stations ID09, ID27, ID28 (ESRF, Grenoble, France) and 9.1, 9.5, 9.8 (SRS, Daresbury, UK) and Mr. Alfie A Neild for his valuable support at several occasions.

I would like to thank Wolfgang Morgenroth for giving me two days of test beam time on station D3 (DORISIII, Hamburg, Germany).

Finally I would like to acknowledge the help and support I have received from my present and former colleagues in the Edinburgh, School of Physics, High-Pressure Group, including Prof. Richard Nelmes, John Loveday, Eugene Gregoryanz, Ingo Loa, Clivia Hejny, Sara Falconi, Olga Degtyareva, Shaun Evans, Helen Maynard, Craig Bull, Malcolm Guthrie, Christophe Guillaume, Miriam Marques, Graham Stinton and especially my PhD supervisor Prof. Malcolm McMahon.

Abstract

Rb-IV is the stable high-pressure phase of rubidium between 16 and 21 GPa. The structure of Rb-IV has long been known to be complex, but it is only recently that it has been solved as being an incommensurate host-guest composite structure, comprising a tetragonal host framework containing chains of "guest" atoms that form structures incommensurate with the host along their common c-axis. While similar composite structures have been observed in a number of other elemental metals, Rb-IV is unique in that on pressure decrease below 16.7 GPa at 300 K, the chains of guest atoms become disordered and liquid-like. This thesis is a detailed structural study of Rb-IV.

High-pressure, combined with high-temperature powder diffraction techniques, have been used to map the P-T phase diagram of rubidium between 15 GPa and 20 GPa and between 298 K and 600 K. The results show that the guest order-disorder transition pressure is strongly temperature dependent, and that the disordered phase is observed to the highest temperatures.

Technical developments, which have made it possible to extract reliable modulation reflection intensities from a Rb-IV single crystal, are described. The resulting data are used for a full modulated structure refinement of Rb-IV, revealing a saw-tooth shaped modulation of the guest structure, from which new information on the host-guest interactions has been extracted.

Inelastic X-ray scattering techniques have been used to measure the longitudinal acoustic (LA) phonons in a Rb-IV single crystal. Two LA-like phonon branches, one for each of the two composite subsystems, are observed along the common c-axis. The sound velocities in the host and guest structures are determined and the pressure dependence is shown to differ by a factor of two.

Finally, developments that will enable future combined high-pressure high-temperature single-crystal diffraction studies, and single-crystal diffraction studies at pressures above 100 GPa, will be presented.

Contents

Chapter 1

Introduction

One of the most fundamental properties of a material is its structure in the solid state. Today 'first principal' computational techniques can reliably predict a whole range of physical properties of a material, if its structure is known, but without the structure only direct experimental measurement will reveal its physical properties.

Pressure has a dramatic effect on the structure and therefore the physical properties of materials. Until now experiments have been the only way to get reliable structural information on high-pressure phases, but recently computational high-pressure structure determination algorithms have shown some success in predicting crystal structures of high-pressure phases of silicate minerals (Oganov & Glass 2006). The same paper also predicts structures of elemental high-pressure phases, but in this case the algorithm has been shown to be less reliable (Lundegaard et al. 2006)(See Appendix B).

One of the goals of high-pressure research is the capability of reliable structure prediction of high-pressure phases, and computational techniques seem to make good progress. But there are still complications. Recent discoveries of elemental high-pressure phases displaying complex structures without the three dimensional periodicity on which the computational techniques rely, makes reliable structure prediction using current structure search algorithms impossible. This means that experimental diffraction studies of the structure of elements under high pressure is very important and probably will remain so in the near future.

Figure 1.1 A) The tetragonal host-guest structure of Rb-IV as viewed approximately along the c axis. The host framework is shown in black, and the guest structure in grey. The ratio between their periodicities along the c direction is an irrational number ($q = c_h/c_g = 1.646$ at 19 GPa), making Rb-IV an incommensurate composite structure. Only potassium has the same 16-atom per unit cell host structure. An 8-atom per unit cell host structure is observed in all other elemental host-guest structures. B) In Rb-IV the guest atoms are arranged in a tetragonal body-centered lattice. Guest chains arranged in C-centered tetragonal and monoclinic lattices are also observed in other elemental host-guest structures.

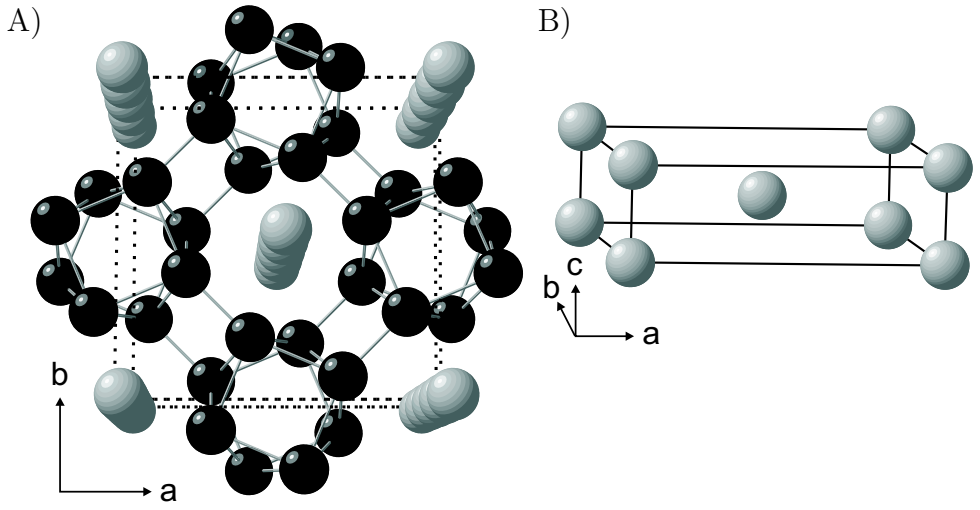

1.1 Incommensurate structures in the elements

Recent development of angle-dispersive diffraction techniques using area detectors and synchrotron radiation (Nelmes & McMahon 1994) have revealed remarkably complex crystal structures in the metallic elements at high pressure. Prior to the introduction of these techniques, only uranium was known to have an incommensurate structure amongst the elements (Smith & Lander 1984). But since their introduction, incommensurate modulated structures have been observed in the elemental high-pressure phases Iodine-V, Te-III, Se-IV, S-III, P-IV (Takemura et al. 2003, Hejny & McMahon 2003, McMahon et al. 2004, Hejny et al. 2005, Fujihisa et al. 2007)(See Appendix B) and incommensurate composite 'host-guest' structures have been observed in the alkali and alkaline-earth metals K-III, Rb-IV, Sr-V, Ba-IV (Nelmes et al. 1999, McMahon et al. 2000a, McMahon et al. 2001, McMahon et al. 2006b), the group Va elements As-III, Sb-II, Bi-III

(McMahon et al. 2000b, Degtyareva et al. 2004) and recently in the first transition metal Sc-II (Fujihisa et al. 2005, McMahon et al. 2006a)(See Appendix B). The so-called 'host-guest' structure type has a tetragonal 'host' framework with channels along the fourfold c axis. Within these channels are chains of atoms that form a 'guest' structure that is incommensurate with the host along c (Figure 1.1).

Among the elements in which the host-guest structure type has been observed, rubidium is unique in having an order-disorder transition in the guest phase (McMahon & Nelmes 2004*b*). A detailed study of this transition will be one of the main objectives of this thesis.

1.2 Rubidium phase IV

Rubidium phase IV (Rb-IV), stable in the pressure range 16.2 to 20.5 GPa, has long been known to have a complex crystal structure (Olijnyk & Holzapfel 1983). Based on X-ray powder diffraction data the host structure of Rb-IV was solved in the space group I4/mcm (Schwarz et al. 1999a), using a commensurate model for describing the guest structure resulting in 4 guest atoms and a total of 20 atoms per host unit cell. They observed one extra reflection that could not be described by their structure model, but it was assumed that it was caused by a small amount of Rb-V present in the sample.

The structure of Rb-IV was reinvestigated by McMahon et al. (2001). They observed several extra reflections that could not be indexed by the original structure model and which could not be explained as Rb-V reflections. It was realized that these extra reflections had to be explained in a structure model of Rb-IV, and this lead to the discovery of the incommensurate nature of Rb-IV. In this structure model the extra reflections are caused by guest atoms, which arrange themselves in a simple tetragonal body-centered lattice, with a periodicity along the chain direction that is incommensurate with the host structure resulting in $\sim$3.3 guest atoms and a total of $\sim$19.3 atoms per host unit cell (Figure 1.1). Further more a transition in the guest phase was observed at 16.7 GPa on pressure decrease. The transition was identified by the disappearance of all guest reflections except the (101) reflection, which was observed to broaden significantly (Figure 1.2). This phenomenen was studied in detail by McMahon & Nelmes

Figure 1.2 Integrated profiles of Rb-IV on pressure decrease from 18.5 GPa to 16.2 GPa and subsequent pressure increase to 16.7 GPa. The (101) guest reflection is the strongest reflection from the guest component; other reflections are from the host component. This figure is from (McMahon & Nelmes 2004*a*)

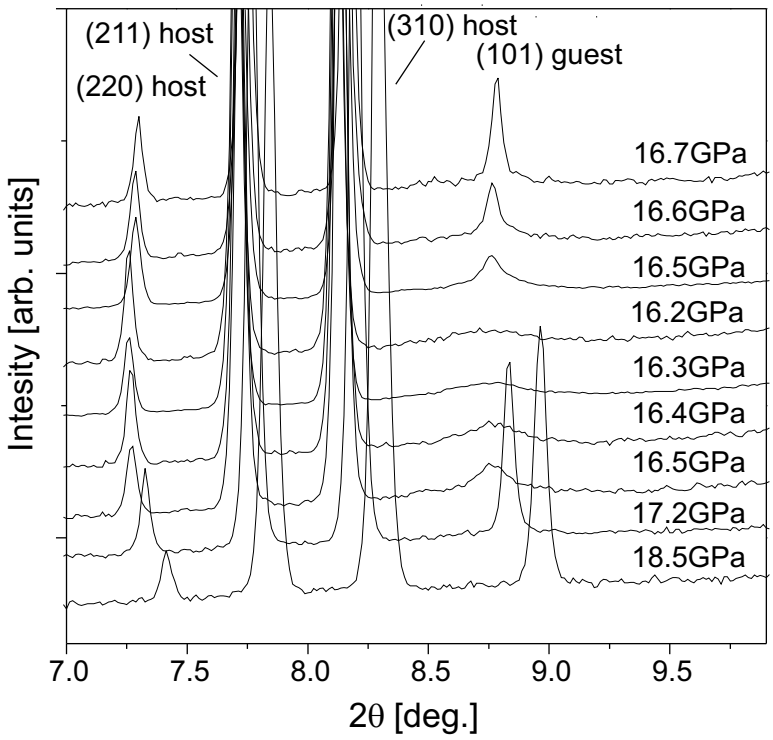

(2004*a*) who concluded that the transition corresponded to a loss in long range order between guest chains. The fact that the (101) guest reflection in the Rb-IV powder profiles is observable to the lowest pressure, even though it is getting very broad, shows that the guest structure never becomes completely disordered at room temperature. Inter-chain correlation is still ∼30 Å (∼4×inter-chain distance) at 16.2 GPa (McMahon & Nelmes 2004*a*).

1.3 Motivation for this study

As described above a considerable amount of information on the structure of Rb-IV is already known from the literature.

The basic structure of Rb-IV and the order disorder transition is known, but many questions remain unanswered. What is the pressure temperature de-

pendence of the order disorder transition observed in the guest phase? Is the disordered phase stable over a larger pressure range at high temperature? Is the disordered phase completely disordered at the highest temperature in contrast to what is observed at room temperature? Why does the guest structure disorder in the first place? And, most importantly, what is the nature of the host-guest interaction and how does it change with pressure?

This thesis will try to address all of these questions, but with one major obstacle. Incommensurate crystal structures have extra reflections in the X-ray diffraction pattern, called satellite or modulation reflections. These satellite reflections contain information on the deformation of the average structure, which in case of composite structures mean, that they contain information on how the structural components interact. In case of Sb-II and Bi-III these satellites are readily seen when using standard powder diffraction techniques (McMahon et al. 2007), but satellite reflections have never been observed in Rb-IV using this technique.

Photons scattered by a single crystal are concentrated into sharp Bragg peaks in contrast to scattering from a powder sample where scattered photons are spread out over full Debye-Sherer rings. For this reason it possible to detect much weaker Bragg peaks from single crystals. A detailed structural study of Rb-IV is therefore an interesting and very challenging problem that can only be addressed by developing new single-crystal techniques.

1.4 Thesis outline

There are six chapters in this thesis including this introduction chapter. The outline for each of the following five chapters are presented below.

- **X-ray diffraction techniques.** This chapter will describe standard X-ray diffraction crystallography and continue to introduce the superspace formalism that is needed for describing incommensurate composite structures. Finally, the diamond anvil cell will be described and the restrictions it imposes on diffraction experiments will be discussed.

- **Order-disorder transition in Rb-IV.** Using high-pressure high-temperature powder diffraction techniques, the pressure-temperature phase diagram of

solid rubidium has been studied in the pressure range 15-21 GPa. A detailed discussion on the order-disorder transition in Rb-IV at high temperature will be presented.

- **The modulated structure of Rb-IV.** The technique for preparing single crystals of Rb-IV and the developments in experimental and data reduction techniques which have made extraction of reliable satellite reflection intensities possible, are described. The resulting data are used for a full modulated structure refinement of Rb-IV, revealing a saw-tooth shaped modulation of the guest structure, from which new information on the host-guest interactions has been extracted.

- **Inelastic studies of Rb-IV.** Recent advances in X-ray inelastic scattering instrumentation have been used to make the first inelastic scattering study of an element with an incommensurate composite structure, giving new insight on the dynamic properties of the Rb-IV host and guest structure components separately.

- **Conclusion.** A summary of the main conclusions made in this thesis, and perspective for future high pressure diffraction studies.

Chapter 2

High-pressure X-ray diffraction techniques

This chapter will describe standard X-ray diffraction crystallography and introduce the superspace formalism that is needed for describing incommensurate composite structures. Finally, the diamond anvil cell (DAC) that is used for high-pressure diffraction experiments will be described and the restrictions it imposes on experiments will be discussed.

2.1 Basic X-ray diffraction theory

X-rays are photons or electromagnetic radiation with wavelengths between 1 Å - 0.001 Å. Radiation for diffraction experiments is produced either by production of element-specific characteristic X-rays (e.g. $\lambda_{MoK\alpha}$=0.71069 Å), or by a synchrotron facility where the wavelength can be tuned to fit the experiment.

X-rays interact, principally with, electrons and are therefore scattered by matter. Most of the scattered photons interact elastically with the electrons. Elastic scattering is coherent, i.e. there is a phase relation between the incident and the scattered beam, resulting in interference effects in the scattered radiation. The interference pattern contains information on the electronic structure of the scatterer, which is the reason why elastic scattering of X-rays is very important in structural science (Giacovazzo 2000).

Some photons will interact inelastically with electrons in a process where part of the photon energy is transferred to the electron (Compton scattering). This

process is incoherent and will therefore not produce any systematic interference effects, resulting in a continuous slowly varying background. Relatively few photons interacting with crystalline matter will be scattered inelastically by phonons (lattice vibrations). Inelastically scattered radiation is very weak compared to the elastically scattered radiation, and can safely be ignored in diffraction experiments where the aim is to obtain structural information.

2.2 Geometry of X-ray diffraction

Sir William Henry Bragg and his son Sir William Lawrence Bragg described scattering from a crystal as reflections from a series of parallel lattice planes. The orientation of each set of planes is described by the Miller indices (hkl) where $\boldsymbol{a}/h$, $\boldsymbol{b}/k$ and $\boldsymbol{c}/l$ are the intersections of the plane closest to the origin with the $\boldsymbol{a}$, $\boldsymbol{b}$ and $\boldsymbol{c}$ axis respectively. The condition for constructive interference is:

$$n\lambda = 2d_{hkl}\sin\theta$$

where n is an integer, θ is the angle between the primary beam and the scattering planes and d_{hkl} is the inter planar distance.

2.2.1 Laue equations

A series of point scatterers are connected by a translation vector $\boldsymbol{a}$. A primary beam, propagating in the direction of $\boldsymbol{s_0}$, is diffracted by the point scatterers in the direction of $\boldsymbol{s}$, where $\boldsymbol{s_0}$ and $\boldsymbol{s}$ are unit vectors (Figure 2.1). The difference in pathway length between the beam diffracted at O and O' is:

$$OA + OB = \boldsymbol{a}\cdot(\boldsymbol{s} - \boldsymbol{s_0})$$

which result in a phase difference of:

$$(OA + OB)\frac{2\pi}{\lambda} = 2\pi\boldsymbol{a}\cdot\boldsymbol{S}$$

Figure 2.1 Scattering from point scatterers connected by a translation vector $\boldsymbol{a}$ (left). Definition of the scattering vector $\boldsymbol{S}$ (right).

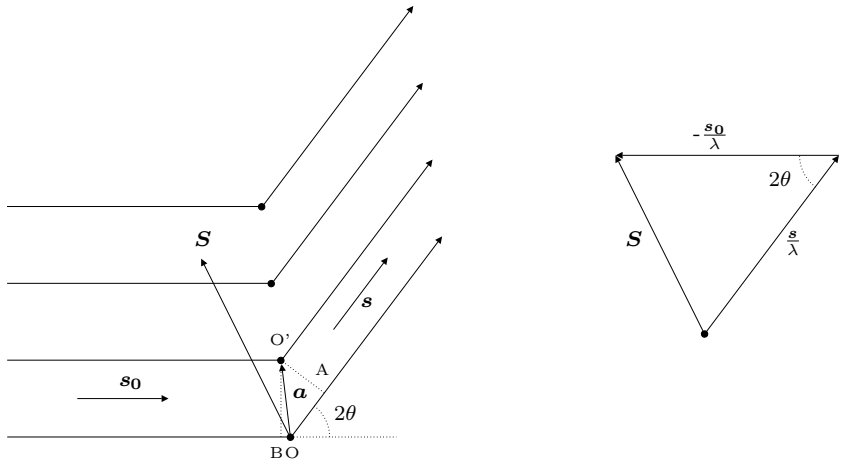

where $\boldsymbol{S} \equiv (\boldsymbol{s} - \boldsymbol{s_0})/\lambda$ is the scattering vector. For constructive interference the path length difference must be an integer multiple of the wavelength:

$$\boldsymbol{a} \cdot (\boldsymbol{s} - \boldsymbol{s_0}) = h\lambda \qquad \Leftrightarrow \qquad \boldsymbol{a} \cdot \boldsymbol{S} = h$$

If the point scatterers are arranged in a three dimensional lattice with translation vectors $\boldsymbol{a}$, $\boldsymbol{b}$ and $\boldsymbol{c}$, then the $\boldsymbol{b}$ translation will give $\boldsymbol{b} \cdot \boldsymbol{S} = k$ and the $\boldsymbol{c}$ translation will give $\boldsymbol{c} \cdot \boldsymbol{S} = l$. Only scattering vectors which satisfy these three equations simultaneously will result in constructive interference, and the three of them together form the Laue equations:

$$\begin{aligned} \boldsymbol{a} \cdot \boldsymbol{S} &= h \\ \boldsymbol{b} \cdot \boldsymbol{S} &= k \\ \boldsymbol{c} \cdot \boldsymbol{S} &= l \end{aligned}$$

The end points of the scattering vectors $\boldsymbol{S}_{hkl}$ satisfying the Laue equations, define a lattice called the reciprocal lattice. The reciprocal lattice vectors are defined as:

$$\begin{aligned} &\boldsymbol{a} \cdot \boldsymbol{a}^* = 1 \quad \boldsymbol{a} \cdot \boldsymbol{b}^* = 0 \quad \boldsymbol{a} \cdot \boldsymbol{c}^* = 0 \\ &\boldsymbol{b} \cdot \boldsymbol{a}^* = 0 \quad \boldsymbol{b} \cdot \boldsymbol{b}^* = 1 \quad \boldsymbol{b} \cdot \boldsymbol{c}^* = 0 \\ &\boldsymbol{c} \cdot \boldsymbol{a}^* = 0 \quad \boldsymbol{c} \cdot \boldsymbol{b}^* = 0 \quad \boldsymbol{c} \cdot \boldsymbol{c}^* = 1 \end{aligned} \tag{2.1}$$

Figure 2.2 The Ewald sphere. Geometry of diffraction in reciprocal space (left) and direct space (right).

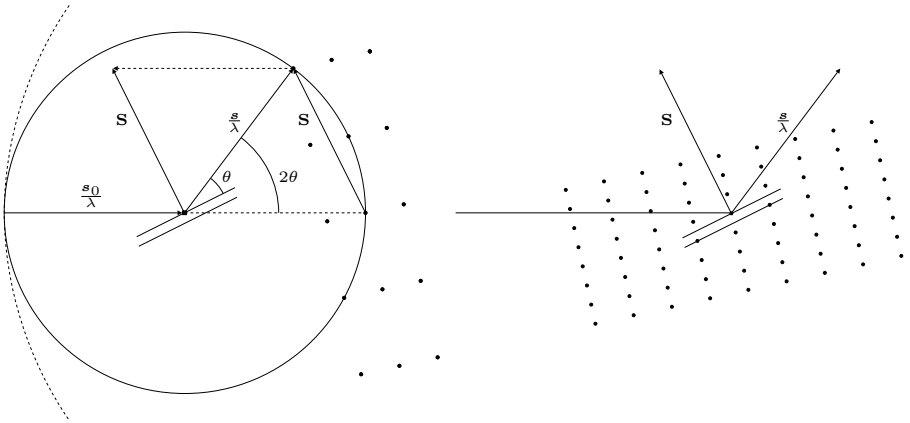

In reciprocal space the scattering vector is expressed as:

$$\boldsymbol{S} = h\boldsymbol{a}^* + k\boldsymbol{b}^* + l\boldsymbol{c}^*$$

Now consider a plane with Miller indices hkl, which by definition is spanned by the two vectors $\boldsymbol{a}/h - \boldsymbol{c}/l$ and $\boldsymbol{b}/k - \boldsymbol{c}/l$. Using the Laue equations it is easily realized that the scattering vector is perpendicular to both of these vectors, and therefore also perpendicular to the plane with the hkl Miller indices. The inter planar distance (d_{hkl}) is given by the projection of $\boldsymbol{a}/h$ onto a unit vector normal to this plane.

$$d_{hkl} = \frac{\boldsymbol{a}}{h} \cdot \frac{\boldsymbol{S}}{|\boldsymbol{S}|} = \frac{1}{|\boldsymbol{S}|} \tag{2.2}$$

This means that the scattering vector described in reciprocal space as $\boldsymbol{S} = h\boldsymbol{a}^* + k\boldsymbol{b}^* + l\boldsymbol{c}^*$, not only is perpendicular to the set of planes described by the Miller indices hkl, it also has a length that is the inverse of their inter planar distance. Because $\frac{1}{|\boldsymbol{S}|} = \frac{\lambda}{2\sin\theta}$ (see figure 2.1), it is evident from Equation 2.2 that the Bragg equation is a special case of the Laue equations.

2.2.2 The Ewald sphere

The construction where the origin of reciprocal space is shifted $1/\lambda$ in the propagation direction of the primary beam, plus a sphere of radius $1/\lambda$ with center in the origin of direct space, is called the Ewald sphere (Figure 2.2). If recip-

rocal space is rotated such that a reflection (hkl) is overlapping with the Ewald sphere, the geometry can be described by $\sin\theta = \lambda|\boldsymbol{S}|/2 = \lambda/(2d_{hkl})$. This is the Bragg equation, and the diffraction conditions are therefore always satisfied when a reciprocal lattice point intersect the Ewald sphere. The sphere with radius $2/\lambda$ centered on the reciprocal lattice origin, is called the limiting sphere, because reflections with d spacings smaller than $\lambda/2$ can not fulfill the diffraction conditions. The choice of wavelength will therefore result in a upper limit for the number of reflections that is possible to collect.

The Ewald sphere construction is a very useful tool for understanding effects like multiple diffraction, and for optimization of diffraction experiments, or visualizing how the DAC is limiting access to reciprocal space (See Section 2.5.1).

2.3 Intensity of diffracted x-rays

The scattering factor $f(\boldsymbol{S})$ of a wave scattered by the electron density $\rho(\boldsymbol{r})$ is given by the Fourier transform of the electron density, and the inverse Fourier transform of the scattering factor gives the electron density:

$$f(\boldsymbol{S}) = T[\rho(\boldsymbol{r})] = \int \rho(\boldsymbol{r}) \exp(2\pi i \boldsymbol{S}\cdot\boldsymbol{r}) d\boldsymbol{r} \tag{2.3}$$

$$\rho(\boldsymbol{r}) = T[f(\boldsymbol{S})] = \int f(\boldsymbol{S}) \exp(-2\pi i \boldsymbol{S}\cdot\boldsymbol{r}) d\boldsymbol{S} \tag{2.4}$$

where $\boldsymbol{r}$ and $\boldsymbol{S}$ are position vectors in direct and reciprocal space, respectively. In general, the electron density is a function resulting in a positive real value for any position and the scattering factor is a complex function described by its modulus and phase, which correspond to the amplitude and phase of the scattered wave respectively. In kinematic diffraction theory (which applies to almost all real crystals) the intensity of the scattered wave is proportional to the squared modulus of the scattering factor: $I(\boldsymbol{S}) \propto |f(\boldsymbol{S})|^2$ (Giacovazzo 2000).

Scattering of an atom

The electron density of a single free atom is, to a very good approximation, spherically symmetrical and can be thus expressed as a function of only the distance from the atomic center: $\rho_a = \rho(r)$, and its fourier transform will be also

spherically symmetrical. The Fourier transform of the atomic density is called the atomic scattering factor (or atomic form factor) and denoted as $f_a(S)$.

Scattering of a unit cell

If redistribution of the electron density caused by chemical bonding is neglected, the electron density of a unit cell is an assembly of free atoms: $\rho_{uc}(\boldsymbol{r}) = \sum_{i=1}^{N} \rho_i(\boldsymbol{r} - \boldsymbol{r}_i)$ where N is the number of atoms in the unit cell, $\rho_i(\boldsymbol{r})$ is the electron density and $\boldsymbol{r}_i$ is the position of the i^{th} atom in the unit cell. This is called the independent atom model, and it is the most widely used for structure modeling. Using Equation (2.3) the scattering factor for the unit cell is found to be:

$$\begin{aligned} F(\boldsymbol{S}) &= \int \sum_{i=1}^{N} \rho_i(\boldsymbol{r} - \boldsymbol{r}_i) \exp(2\pi i \boldsymbol{S} \cdot \boldsymbol{r}) d\boldsymbol{r} \\ &= \sum_{i=1}^{N} f_i(\boldsymbol{S}) \exp(2\pi i \boldsymbol{S} \cdot \boldsymbol{r}_i) \end{aligned} \tag{2.5}$$

where $f_i(\boldsymbol{S})$ is the atomic form factor for the i^{th} atom (Giacovazzo 2000).

Scattering of a crystal

A three dimensional (3D) infinite lattice can be represented by the lattice function

$$L(\boldsymbol{r}) = \sum_{u,v,w=-\infty}^{+\infty} \delta(\boldsymbol{r} - \boldsymbol{r}_{u,v,w})$$

where δ is the Dirac delta function and $\boldsymbol{r}_{u,v,w} = u\boldsymbol{a} + v\boldsymbol{b} + w\boldsymbol{c}$ where u, v and w are integers. An infinite 3D periodic crystal structure can then be constructed by a convolution of the lattice with the unit cell

$$\rho_{cr}(\boldsymbol{r}) = \rho_{uc}(\boldsymbol{r}) * L(\boldsymbol{r})$$

and it follows that the scattering factor for the whole crystal is

$$\begin{aligned} F_{cr}(\boldsymbol{S}) &= T[\rho_{cr}(\boldsymbol{r})] = T[\rho_{uc}(\boldsymbol{r})] \cdot T[L(\boldsymbol{r})] \\ &= F(\boldsymbol{S}) \cdot \frac{1}{V} \sum_{h,k,l=-\infty}^{+\infty} \delta(\boldsymbol{S} - \boldsymbol{S}_{h,k,l}) \end{aligned} \tag{2.6}$$

where V is the unit cell volume and $\boldsymbol{S}_{h,k,l} = h\boldsymbol{a}^* + k\boldsymbol{b}^* + l\boldsymbol{c}^*$. If the scatterer is non-periodic, as in the case of the contents of a single unit cell, the scattering factor can be non-zero for any value of $\boldsymbol{S}$. In cases where the scatterer is a periodic crystal, the above equations show that non-zero intensity of the scattered beam will only be observed when $\boldsymbol{S}$ coincide with a reciprocal lattice point. The same conclusion was reached in the previous section, based on a lattice of point scatterers. In general all the conclusions made in Section 2.2.1 are true for any periodic electron density.

A diffraction experiment ideally determines the intensities $I(hkl)$ of the scattering related to reciprocal lattice points $h\boldsymbol{a}^* + k\boldsymbol{b}^* + l\boldsymbol{c}^*$, for all possible values of h, k and l. And, consequently, the relative sizes of the amplitudes $|F(hkl)|$ are known, but the phase information that is necessary for reconstructing the electron density is not. To obtain the phase information, all the atomic positions in the unit cell must be known (See Equation 2.5). This is the well-known phase problem in crystallography. To solve a structure the crystallographer therefore has to propose a physically and chemically reasonable structure model, which results in a convincing agreement between calculated and observed structure factor amplitudes.

2.4 Superspace crystallography

Since the beginning of the structural crystallography, at the beginning of 20th century, crystals were considered to be three-dimensionally periodic. It was only several decades later that crystals with long-range order, but with a lack of periodicity, were discovered. Not before 1974 was the first quantitative description of the structure of incommensurately modulated crystals published (de Wolf 1974). The method used for the structure description is based on embedding the aperiodic structures into a higher-dimensional space (called superspace), where the periodicity of the structure can be recovered. This method has since gained a widespread acceptance and is today used almost routinely to describe the structures of aperiodic crystals.

Figure 2.3 Incommensurate modulated structures, with atomic displacements defined by the modulation function $u = A\sin(2\pi \boldsymbol{q} \cdot \boldsymbol{r})$, with the wave vector $\boldsymbol{q} = 0.311\,\boldsymbol{c}^*$. A) The amplitude $A = 0.3\,\boldsymbol{c}$ results in a longitudinal modulation. B) An amplitude of $A = 0.3\,\boldsymbol{a}$ results in a transversal modulation. The lattice represent atom positions of the unmodulated structure, also called the average structure. The figure is reproduced from Van Smallen (1995) figure 2. Numbers marked on atoms are related to figure 2.6

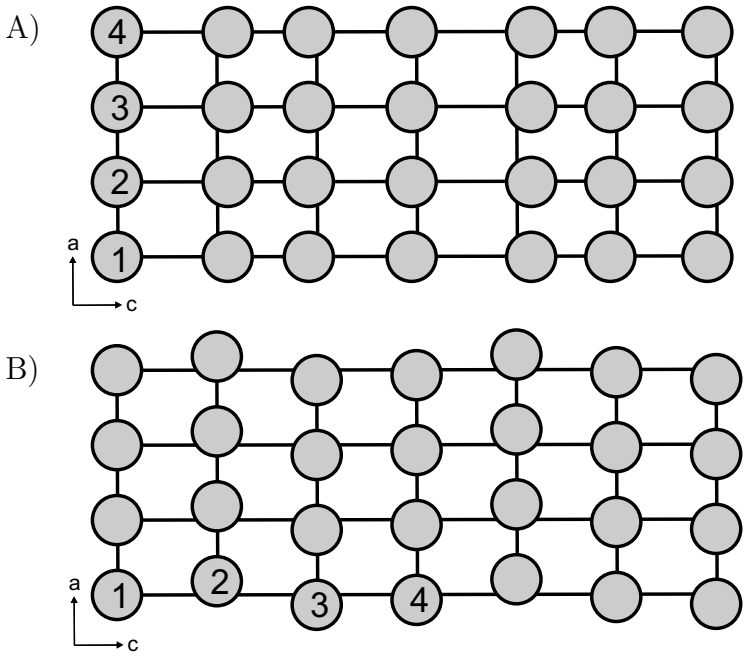

2.4.1 Aperiodic structures

Elemental incommensurate modulated structures are relative simple, comprising an average structure and low order harmonic modulations (Figure 2.3). Because modulated structures have an average structure, with corresponding intense Bragg reflections, it is the observation of weaker satellite reflections that reveal the structure as being incommensurate (Figure 2.4A). If all observed reflections fit onto a 3D lattice the structure would be described as a commensurate modulated structure and only when this is not the case will the structure be considered aperiodic.

It was shown in Section 2.3, that the Fourier transform of a three dimensionally periodic electron density results in a structure factor that is indexable by three integers. In general the Fourier transform of a n-dimensional peri-

Figure 2.4 Construction of a superspace reciprocal lattice. A) A schematic diffraction pattern of a modulated structure in 3D space with the modulation wave vector $\boldsymbol{q} = 0.311\,\boldsymbol{c}^*$. The positions of diffraction spots are therefore representative for both structures if figure 2.3, and only the intesity distribution will reveal the type of modulation. B) Section through the periodic 4D superspace reciprocal lattice.

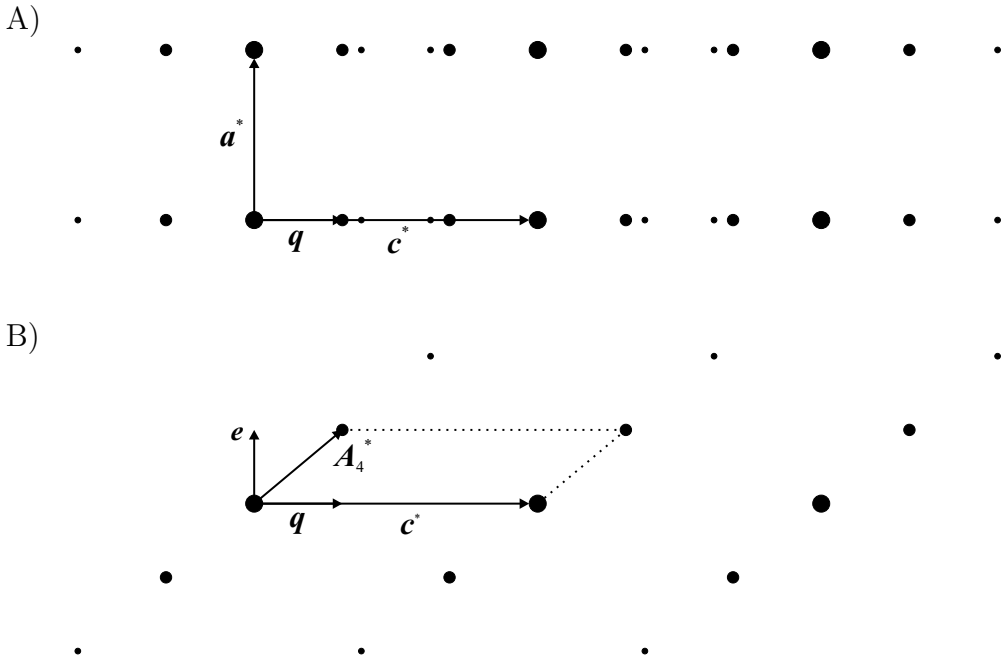

odic electron density forms a discrete lattice indexable by n integers, and vice versa - any function indexable by n integers must be a Fourier transform of a n-dimensionally periodic function. An elegant solution, where aperiodic structures could be described as periodic in higher dimensional space, was therefore proposed (de Wolf 1974).

2.4.2 Reciprocal superspace

The idea behind the construction of a higher dimensional periodic reciprocal lattice is both elegant and relative simple. Only four dimensional structures will be studied in this thesis, so the following discussions will be limited to the four-dimensional case. The main reflections of a aperiodic structure can be indexed based on the three normal reciprocal lattice vectors $\boldsymbol{a}^*$, $\boldsymbol{b}^*$ and $\boldsymbol{c}^*$, corresponding to the average structure. A characteristic property of the reflection distribution

from an aperiodic crystal is that the satellite reflections are observed symmetrical around main reflections, with first order reflections at an distance d and higher order satellites at the distance nd. The satellite reflections can therefore be indexed based on their relative position to a main reflection.

$$S = h\boldsymbol{a}^* + k\boldsymbol{b}^* + l\boldsymbol{c}^* + m\boldsymbol{q} \quad \text{where} \quad \boldsymbol{q} = q_1\boldsymbol{a}^* + q_2\boldsymbol{b}^* + q_3\boldsymbol{c}^*$$

resulting in four integers $(hklm)$ for unique indexing of reflections (Figure 2.4A). Reflections with m=0 are main reflections and reflections with $m = n$ are n^{th} order satellites.

The basic idea in the superspace approach is to create a 4D reciprocal lattice consisting of the three basis vectors of the lattice spanning the main reflections, and a fourth lattice vector which is a sum of the $\boldsymbol{q}$ vector and a unit vector $\boldsymbol{e}$ which is perpendicular to real-space:

$$\boldsymbol{A}_1^* = \boldsymbol{a}^* \quad \boldsymbol{A}_2^* = \boldsymbol{b}^* \quad \boldsymbol{A}_3^* = \boldsymbol{c}^* \quad \boldsymbol{A}_4^* = \boldsymbol{e} + \boldsymbol{q}$$

This construction results in a periodic lattice in four dimensions, where the arrangement of diffraction spots in real-space can be reconstructed by a simple projection (Figure 2.4B).

2.4.3 Direct superspace

The transformation between direct and reciprocal superspace is a direct generalization of the corresponding transformation in the 3D space:

$$\boldsymbol{A}_i \cdot \boldsymbol{A}_j^* = \delta_{ij} \quad \text{where} \quad i, j = 1, 2, 3, 4$$

Using the superspace reciprocal vectors, and the fact that the components of the $\boldsymbol{q}$ vector transforms as described in Equation 2.1, it is straightforward to show, that the basis vectors in direct superspace is described by:

$$\boldsymbol{A}_i = \boldsymbol{a}_i - q_i\boldsymbol{e}\,, \quad i = 1, 2, 3 \qquad \text{and} \qquad \boldsymbol{A}_4 = \boldsymbol{e}$$

The geometry of the superspace base vectors relative to real-space base vectors can be seen in Figure 2.5, which shows that real-space ($\boldsymbol{c}$) is a section through

Figure 2.5 The superspace atomic coordinates x_{s3}, x_{s4} of an atom at position $(0, 0, z)$ in real-space, decomposed in the superspace coordinates $\bar{x}_{s3}, \bar{x}_{s4}$ of the average structure position $(0, 0, \bar{z})$ and the contribution of the modulation u_z.

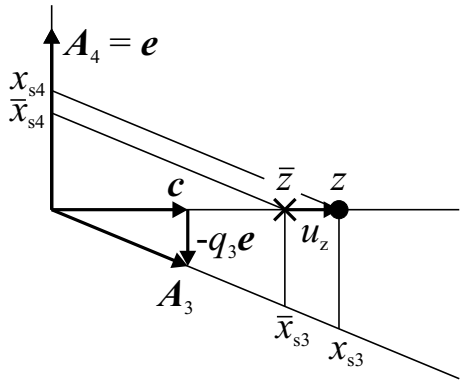

superspace perpendicular to the $\boldsymbol{A}_4$ superspace vector.

Coordinates in superspace

Figure 2.5 also illustrates that an atom in superspace with coordinates $(x_{s1}, x_{s2}, x_{s3}, x_{s4})$ will have the real-space coordinates (x, y, z), where

$$x_{si} = x_i \quad \text{for} \quad i = 1, 2, 3$$

independently of the x_{s4} coordinate. For an atom on the $\boldsymbol{c}$-axis and for a general wavevector $\boldsymbol{q}$ its value is $x_{s4} = q_3 z$ (see figure 2.5), and for an atom with general position it is $x_{s4} = \boldsymbol{q} \cdot \boldsymbol{r}$

In normal 3D structures only the atomic positions ($\boldsymbol{r}_0$) within a reference unit cell is considered, but since equivalent atoms related by lattice translations are displaced differently in a modulated structure, it is necessary to calculate the displacement ($\boldsymbol{u}$) for all atoms, that is for all lattice translations $\boldsymbol{L}$, separately.

$$\begin{pmatrix} \bar{x} \\ \bar{y} \\ \bar{z} \end{pmatrix} = \begin{pmatrix} L_x \\ L_y \\ L_z \end{pmatrix} + \begin{pmatrix} x_0 \\ y_0 \\ z_0 \end{pmatrix} \quad \text{or} \quad \bar{\boldsymbol{r}} = \boldsymbol{L} + \boldsymbol{r}_0$$

Atomic positions in the modulated structure are described as a sum of the average

structure atomic position ($\bar{\boldsymbol{r}}$) and the displacement.

$$\begin{aligned} x &= \bar{x} + u_x(\bar{x}_4) \\ y &= \bar{y} + u_y(\bar{x}_4) \\ z &= \bar{z} + u_z(\bar{x}_4) \end{aligned} \tag{2.7}$$

where the superspace coordinate $\bar{x}_{s4}$ is the phase of the modulation. Any periodic modulation function can be expressed by a Fourier expansion.

$$u_i = \sum_{n=1}^{\infty} A_{n,i} \sin(2\pi n \bar{x}_4) + B_{n,i} \cos(2\pi n \bar{x}_4) \quad \text{where} \quad i = x, y, z \tag{2.8}$$

This means that, for every order (n) of harmonics that are included in the description there will in general be six fourier coefficients to refine per atom in the basic structure. Symmetry will often constrain most of the coefficients to zero.

Atomic domains

The superspace is periodic in four dimensions, and the electron density of the superspace unit cell can therefore be constructed from the atomic positions of the modulated structure, by superspace lattice translations (Figure 2.6).

In both of the cases, presented in Figure 2.6, an atom with no phase shift has been chosen as the reference atom (marked by number 1). Any atom can be chosen as the reference, which corresponds to adding an offset phase to all atoms: $\bar{x}_4 = t + \boldsymbol{q} \cdot \bar{\boldsymbol{r}}$. This is equivalent to a shift t of real-space along the A_4 direction. Each basic unit cell anywhere in the structure can be mapped onto a section of a single reference super-space unit cell with a shift $t \in (0, 1)$. Thus all structural properties like bond distance, atom displacement etc. can be expressed as a function of t. Characterization of any structural property in the interval $t \in (0, 1)$ is equivalent to full characterization of the property in the whole structure.

2.4.4 Composite structures

Incommensurate composite structures of the type shown in Figure 2.7A can be described as an inter-growth of two periodic structures (the host and the guest)

Figure 2.6 Construction of the atomic domain in superspace. The atoms are shifted from their average positions (crosses) to the modulated positions (circles) along the real space according to the modulation function $u = A\sin(2\pi \boldsymbol{q}\cdot\boldsymbol{r})$, with the wave vector $\boldsymbol{q} = 0.311\,\boldsymbol{c}^*$. Atoms can be brought to the equivalent position in the reference superspace unit cell (thick outline) by superspace lattice translations (dotted lines). If all atoms of the structure are translated into the reference unit cell (green circles), they form the superspace electron density, also called the atomic domain. A) Rows of atoms along the c-axis starting with atoms marked with 1-4 in Figure 2.3A ($A = 0.3\,\boldsymbol{c}$) all plot on top of each other when moved into the shown superspace section using A_1 superspace lattice translations. A_3 and A_4 superspace lattice translations create the atomic domain in the reference unit cell. B) Rows of atoms along the a-axis starting with atoms marked with 1-4 in Figure 2.3B ($A = 0.3\,\boldsymbol{a}$) do not translate to the same position in the shown section. Red circles mark atoms that have been translated along A_3. The row starting with atom 2 has been translated once, the row starting with atom 3 has been translated twice and so on. A_1 and A_4 superspace lattice translations create the atomic domain in the reference unit cell.

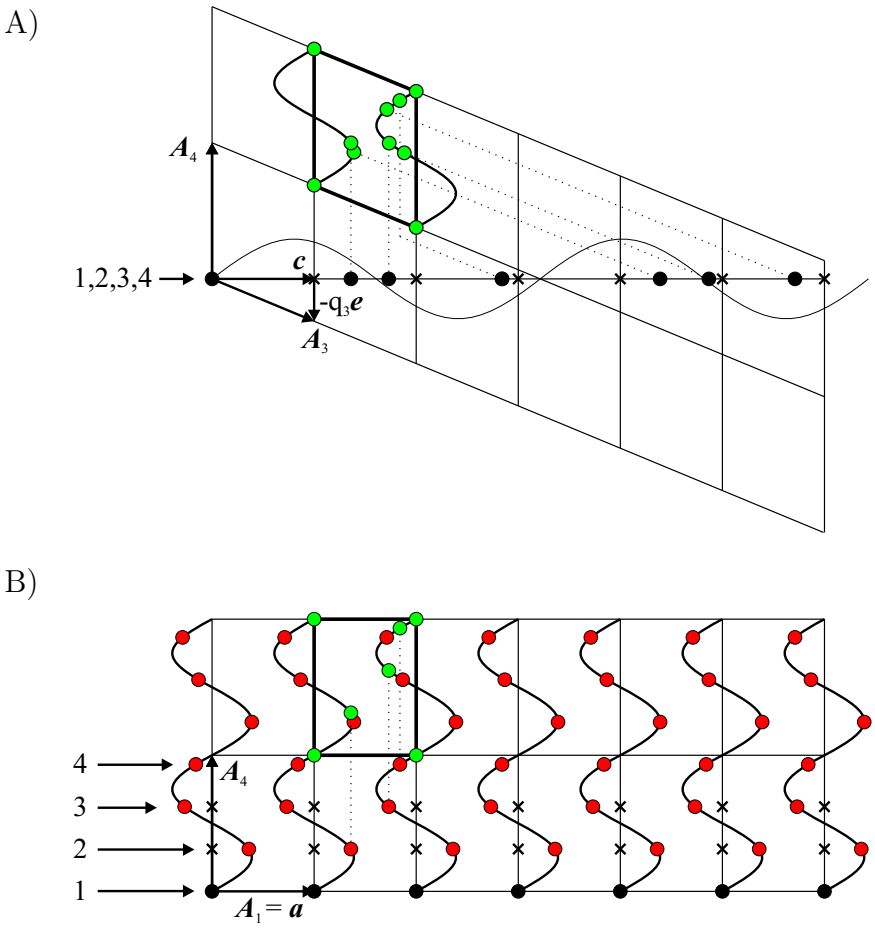

Figure 2.7 A) An incommensurate composite structure with two subsystems, labelled h and g respectively. The grid is the lattice of subsystem h. The figure is a modified version of Van Smallen (1995) Figure 3. B) Electron density map in the a-c plane of the g subsystem (grey) with the repeat distance c_g and the h subsystem (black). The ratio c_g/c_h is not a rational number, making the structure incommensurate - that is, there is no periodic repeat along the c-axis. This figure is a modified version of Heine (2000) Figure 1.

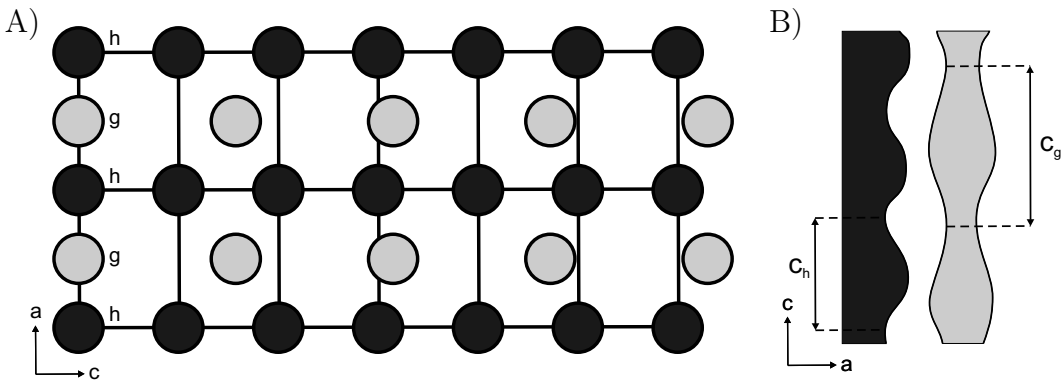

commensurate with each other in two directions, and incommensurate in the third direction. There will always be interactions with atoms in the first coordination shell, so the two subsystems will interact, resulting in a modulation of the two subsystems. The modulation function of subsystem 1 will have the periodicity of subsystem 2, and the modulation function of subsystem 2 will have the periodicity of subsystem 1 (Figure 2.7B). One of the consequences of this is that satellite reflections of the two subsystems will overlap, and even main reflections of one subsystem can be indexed as satellites of the other system.

All reflections can be indexed by choosing one of the subsystems as the reference lattice:

$$\boldsymbol{S}_h = h\boldsymbol{a}^* + k\boldsymbol{b}^* + l\boldsymbol{c}_h^* + m\boldsymbol{q}_h \quad \text{where} \quad \boldsymbol{q}_h = \frac{c_h}{c_g}\,\boldsymbol{c}_h^*$$

or

$$\boldsymbol{S}_g = h\boldsymbol{a}^* + k\boldsymbol{b}^* + l\boldsymbol{c}_g^* + m\boldsymbol{q}_g \quad \text{where} \quad \boldsymbol{q}_g = \frac{c_g}{c_h}\,\boldsymbol{c}_g^*$$

In this study the host structure has been chosen as the reference structure, so main host reflections will index $(hkl0)$, main guest reflections index $(hk0m)$ and satellite reflections index $(hklm)$. A satellite reflection $(hk12)$ can be considered

Figure 2.8 The diamond anvil cell. A) Pressure generating mechanism in a DAC. B) Section through the Merrill-Bassett type DAC (Merrill & Bassett 1974).

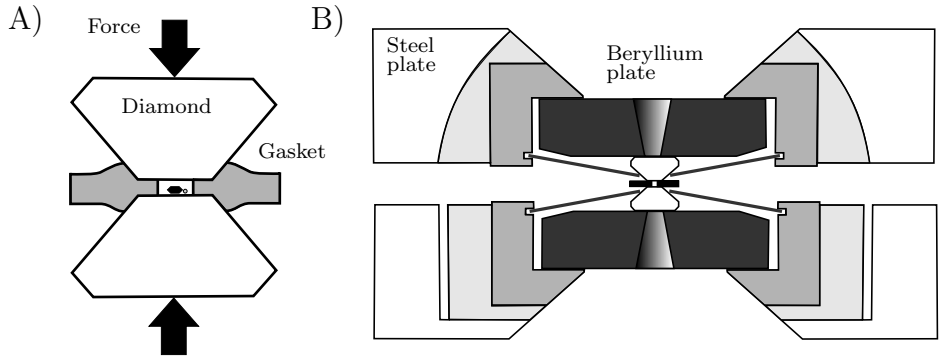

a first order satellite of the guest or a second order satellite of the host, but the satellite order is defined as $\min(|l|, |m|)$ and the given example would therefore be a first order reflection.

2.5 The Diamond Anvil Cell

The invention of the diamond anvil cell (Weir et al. 1959) revolutionized the field of high-pressure research. The DAC design is based on the opposed anvil principle, developed by Percy Williams Bridgman earlier in the century, with the main difference being that the tungsten carbide anvils used by Bridgman were replaced by diamond single-crystal anvils (Figure 2.8). The extreme hardness of diamond made it possible to reach much higher pressures, and the transparency of diamond to a wide range of electromagnetic radiation opened up for a new range of *insitu* experimental techniques which previously only were available to quenched samples. Among these techniques are visual observation, raman and infrared spectroscopy, Mossbauer spectroscopy, inelastic X-ray scattering, angle dispersive powder and single-crystal X-ray diffraction (Miletich et al. 2000).

2.5.1 Access to reflections

The X-ray absorbing steel body of the DAC only gives limited access to reciprocal space, which is strongly dependent on the opening angle α (Figure 2.9). A large opening angle ($> 45°$) will give access to more reflections, but it will result in a less

Figure 2.9 The X-ray absorbing steel body of a DAC with opening angel $\alpha = 40°$ only allow access to the light grey shaded area of reciprocal space. The DAC is rotation symmetric around the normal ($\boldsymbol{n}$) so the grey shaded area forms a torus shaped volume in reciprocal space. The dark grey shaded area is the volume that can be accessed with a $\alpha = 20°$ opening angle. The grey part of the detector shaded by the DAC.

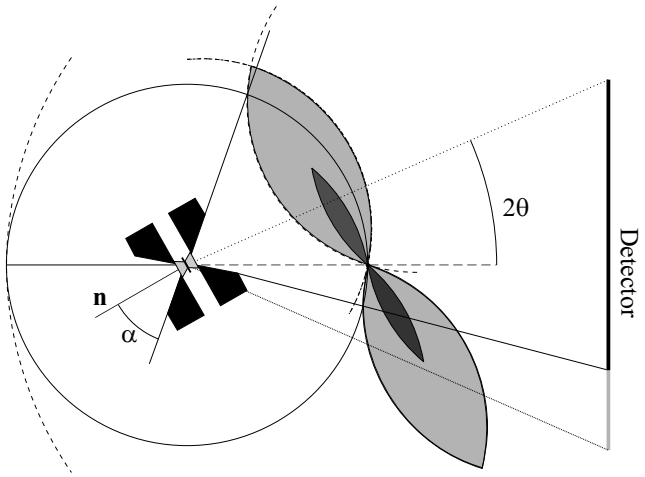

stable DAC, which can only reach low pressures. Pressure cells that can reach a 100 GPa (∼1 megabar) usually have opening angles less than 20°, resulting in extremely limited access to reciprocal space (Miletich et al. 2000). A new diamond cuelet and seat design was invented recently (Boehler & De Hantsetters 2004), which is reported to be capable of producing a megabar with a 40° opening angle (Boehler 2006), which opens up the exciting possibility of solving and refining structures of single-crystal diffraction data collected above a megabar. Access to reciprocal space is especially limited in the direction normal ($\boldsymbol{n}$) to the DAC (Figure 2.9), and the quality of the data set can therefore depend on the orientation of the crystal inside the DAC. Because of the the high symmetry of cubic crystals the orientation is not important, but for tetragonal or a hexagonal crystals the unique *c*-axis should be parallel to the diamond culets for access to the most symmetry independent reflections.

For the experimental work presented in this thesis Merril-Bassett type DAC's (Merrill & Bassett 1974) have been used with a $\alpha = 40°$ opening angle, allowing access to reflections with scattering angles up to $2\theta = 80°$. For a wavelength of 0.4 Å this corresponds to a *d*-spacing resolution of: $d = \lambda/(2\sin\theta) = 0.31$Å. This

Figure 2.10 Schematic drawing showing the effect of wavelength tuning on access to reciprocal space for a DAC with opening angle 40°. The circles with thick outline indicate a 0.9 Å data resolution. V_a and V_d is the accessible and the total reciprocal volume within this resolution. A) The limiting situation $\theta = \alpha$ at long wavelength where the maximum accessible resolution is 0.9 Å. B) The situation at shorter wavelength where the maximum accessible resolution is much smaller than 0.9 Å. Red circles indicate reflections that are accessible at both wavelengths. Yellow and green circles represent reflections that are only accessible at the short wavelength.

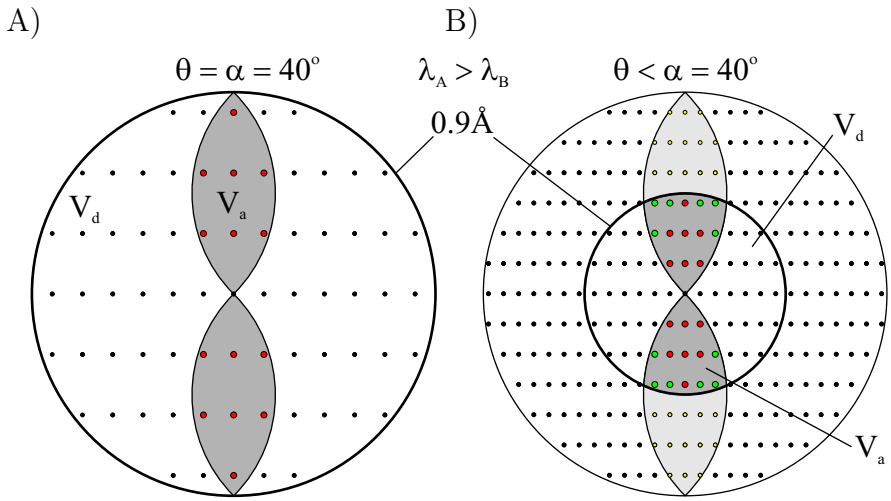

resolution is much higher than what is needed for normal structure solving and refinement, and only in cases of detailed charge density studies is a resolution of more than 0.9 Å typically needed. This can be realized when considering that the atomic electron distribution is almost perfectly spherical symmetric with a diameter of more than 1.3 Å for all elements except hydrogen. In case of Rb at 20 GPa the atomic radius is close to 3.0 Å.

It was mentioned above that it is important to collect as many symmetry independent reflections as possible, but some reflections are more important than others. Considering the reflection distribution within the torus shaped volume of access (Figure 2.10B), it follows that all reflections with d-spacings higher than 0.9 Å are to some extent redundant information because they only add resolution in a direction that is already well resolved (yellow reflection in Figure 2.10B), whereas any extra reflections that can be accessed further along the direction of the DAC normal ($\boldsymbol{n}$) are very important for improving resolution in this direction (green

Figure 2.11 Completeness V_a/V_d of data set as a function of opening angle α and wavelength λ. Full and dotted lines indicate completeness for 0.9 Å and 1.1 Å resolution respectively. A) Completeness as a function of opening angle. B) Completeness as a function of wavelength. The line $\theta = \alpha$ represent the limiting case (see figure 2.10A) where the full accessible volume is included in calculation of the completeness.

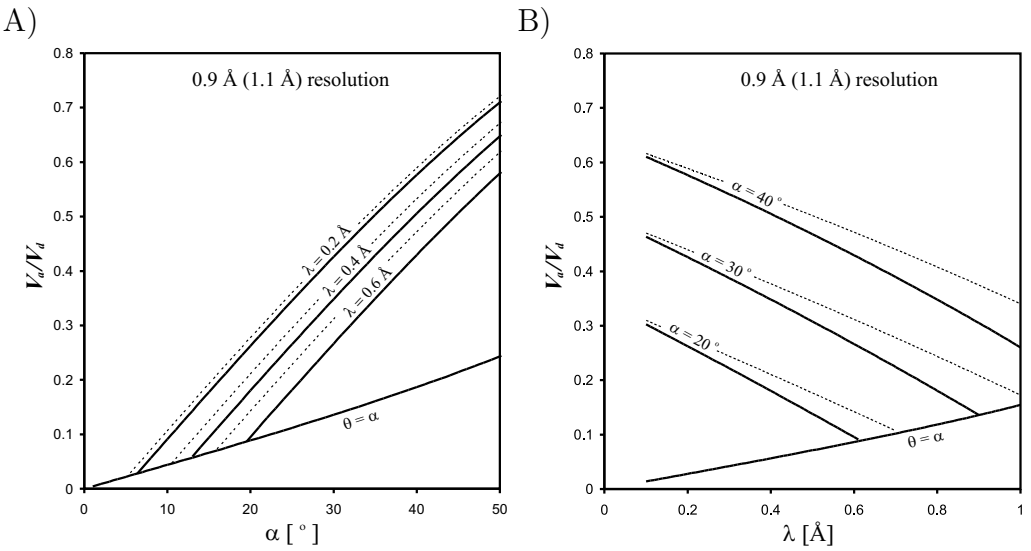

reflection in Figure 2.10). Using a shorter wavelength x-ray beam has several advantages, e.g. less absorption from sample and DAC components, but, most importantly, it improves the resolution along the DAC normal (Figure 2.10).

Merrill & Bassett (1974) derived an equation that gives the ratio between the accessible volume V_a and the total volume V_θ of reciprocal space with scattering angle less than θ. But θ only gives information on the quality of the data if the wavelength is also known. It is more instructive to consider the ratio between the accessible volume V_a and the total volume V_d within a given resolution d:

$$\frac{V_a}{V_d} = \frac{3}{4}\left[\sin(\alpha-\theta) + \frac{\sin\alpha}{2\sin^3\theta}(\theta - \sin\theta\cos\theta)\right]$$

where $(0 \leq \theta \leq \alpha)$ and $\theta = \arcsin(\lambda/(2d))$ (Figure 2.10). Using this equation the two plot in Figure 2.11, showing the effect of opening angle and wavelength on the completeness of the data set, was prepared.

Figure 2.11A shows that using the wavelength 0.4 Å and a 17° opening angle[1]

[1]This is the opening angle of a typical megabar DAC with standard tungsten carbide seats.

will result in a 10% completeness within 0.9 Å resolution, while an opening angle of 34° would result in a 40% completeness. In this case a factor four was gained in data completeness by increasing the opening angle by a factor two. In this thesis where DAC's with 40° opening angle is used, an increase from 42% to 57% can be achieved by changing the wavelength from 0.6 Å to 0.2 Å(Figure 2.11B). In conclusion the largest possible opening angle and the shortest possible wavelength should be used for high pressure single crystal data collections.

Chapter 3

Order-disorder transition in Rb-IV

The sequence of rubidium phases with increasing pressure is known to above 50 GPa at room temperature, but at high temperature the phase boundaries are only known up to 14 GPa as shown in Figure 3.1 (Yu. Tonkov & Ponyatovsky 2005).

At ambient conditions rubidium is a crystalline solid with a body-centered cubic (bcc) atomic arrangement (spacegroup #229: $Im\bar{3}m$, a = 5.703 Å, Wyckoff position: 2a). At 7 GPa rubidium undergoes a transition into the close packed face-centered cubic (fcc) atomic arrangement (spacegroup #225: $Fm\bar{3}m$, a = 5.224 Å at 11.9 GPa, Wyckoff position: 4a) (McMahon & Nelmes 2006). At 14.3 GPa rubidium transforms to the complex phase Rb-III (spacegroup #20: $C222_1$, a=7.886 Å, b=11.240 Å and c=18.431 at 14.3 GPa) with 52 atoms in the unit cell (Nelmes et al. 2002). At 16.2 GPa, Rb-III transforms into the host guest structure of Rb-IV (McMahon et al. 2001) which on further compression to 20 GPa transforms into Rb-V (spacegroup #141: $I4_1/amd$, a=2.883 Å and b=10.760 Å at 28 GPa, Wyckoff position: 4a) (Olijnyk & Holzapfel 1983). At 48 GPa Rb-V transforms into Rb-VI (spacegroup #64: Cmca, a=9.372 Å, b=5.550 Å and c=5.528 Å at 48.1 GPa, Wyckoff position: 8f and 8d with coordinates (0,0.1704,0.3177) and (0.2107,0,0) respectively) (Schwarz et al. 1999b). No structural studies of rubidium have been reported above 50 GPa (McMahon & Nelmes 2006).

The alkali metals behave as nearly-free-electron metals at ambient conditions, where they all adopt the bcc structure, and with increasing pressure they display the phase transition series 'bcc→fcc→series of complex structures' with a signif-

Figure 3.1 Pressure-temperature (P-T) phase diagram of solid rubidium up to 21 GPa as known from literature (Yu. Tonkov & Ponyatovsky 2005). Dotted lines mark the phase boundaries as determined by (Boehler & Zha 1986). The question mark indicate the area of the P-T phase diagram of interest for this study.

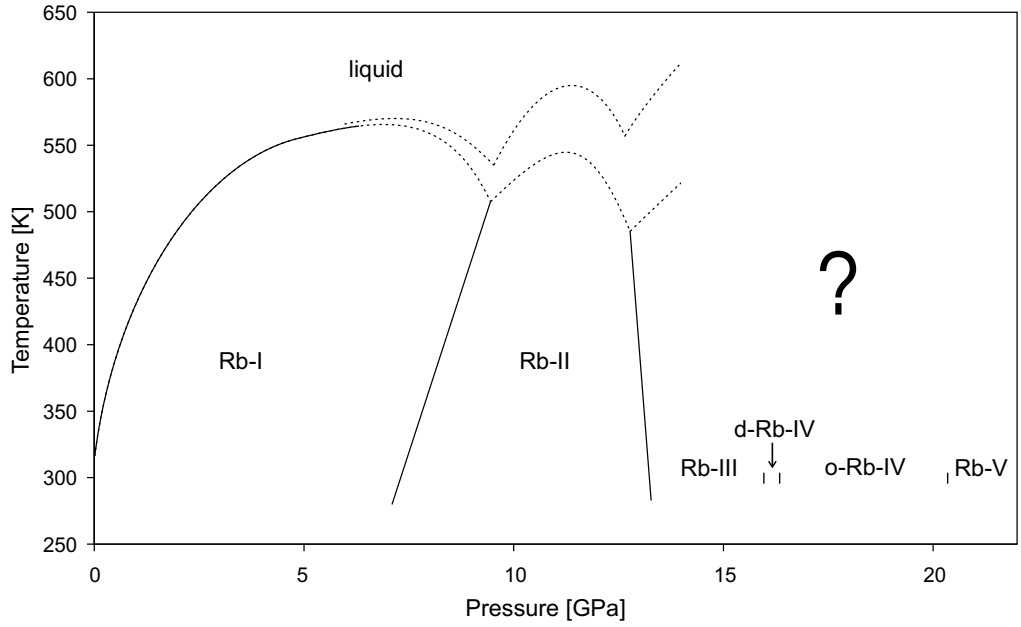

icant decrease in the atomic coordination number from 12 in the fcc phase to coordination numbers in the range 6-11 in the complex phases (Schwarz 2004). These changes in structure and coordination of the solid have long been attributed to an s-to-d electronic transition, or, in some cases, to dsp^3 hybridization of the electronic orbitals (Takemura et al. 1982, McMahan 1984, Takemura & Syassen 1985, Abd-Elmeguid et al. 1994) where it is argued that the complex structures exists because of directional bonding caused by the partial occupation of d-orbitals.

The melting curve of Rb is known from literature up to 14 GPa, but because of a large scatter in data at pressures between 6 GPa and 14 GPa, an upper and a lower estimate for the melting curve has been given (Boehler & Zha 1986).

3.1 Experimental Details

All experiments were done with high-purity (99.95+%) samples of Rb obtained from the Aldrich Chemical Company, using resistively heated gas membrane diamond-anvil pressure cells with tungsten gaskets. The Rb was loaded in a dry oxygen-free atmosphere (<1 ppm O_2 and <1 ppm H_2O) to prevent oxidation of the samples. No pressure transmitting medium was used. The sample pressure was measured using the SrB_4O_7:Sm^{2+} flourescence technique (Datchi et al. 1997) and the temperature was measured using a thermocouple in contact with one of diamond anvils. Diffraction data were collected on beamlines ID09 and ID27 at the European Synchrotron Radiation Facility, Grenoble, using an incident x-ray wavelength of ∼0.4 Å and a beamsize of 20 μm × 20 μm. The diffraction data were collected on an image-plate detector placed approximately 350 mm from the sample, and two-dimensional diffraction images were integrated using FIT2D (Hammersly 2005) to give standard diffraction profiles. The exposure time for each image was typically 3 s during which the sample was rotated ±3° around the vertical axis. Diffraction patterns of the low-pressure bcc and fcc phases showed no discernible contaminant peaks, confirming that the samples were pure rubidium.

3.2 Visual observations

One of the samples was taken up in pressure and temperature into the Rb-V phase, while a picture were taken at each pressure-temperature step using the pressure measuring system (Fig. 3.2, panel 1-16). At 3.6 GPa Rb-I has a highly reflecting metallic surface. The bcc (Rb-I) to fcc (Rb-II) transtion at 7.3 GPa was accompanied by a clear discontinuous drop in the optical reflectivity of the sample (panel 4-5), in contrast to the near-infrared reflectivity ($\hbar\omega = 0.7eV$) where no such discontinuity in reflectivity was observed (Takemura & Syassen 1982). Further discontinous optical changes in reflectivity was observed at the Rb-II→Rb-III, Rb-III→Rb-IV and Rb-IV→Rb-V transitions, where it was observed to increase, decrease and increase respectively. Diffraction patterns were collected at a few points where mixed phases were observed, to confirm that the mixed phase interpretation based on visual observation was correct. It is also observed that the reflectivity within the phases I-IV, respectively, is continuously decreas-

Figure 3.2 Visual changes in rubidium with increasing pressure. For each panel 1-16 the observed rubidium phases are indicated in the top corners, and the pressure and temperature are indicated in the bottom corners. In the case of mixed phases, each phase has been marked by an arrow. The five dark spots in the lower left quadrant of the sample volume are crystallites of SrB_4O_7:Sm^{2+} used for pressure measurement.

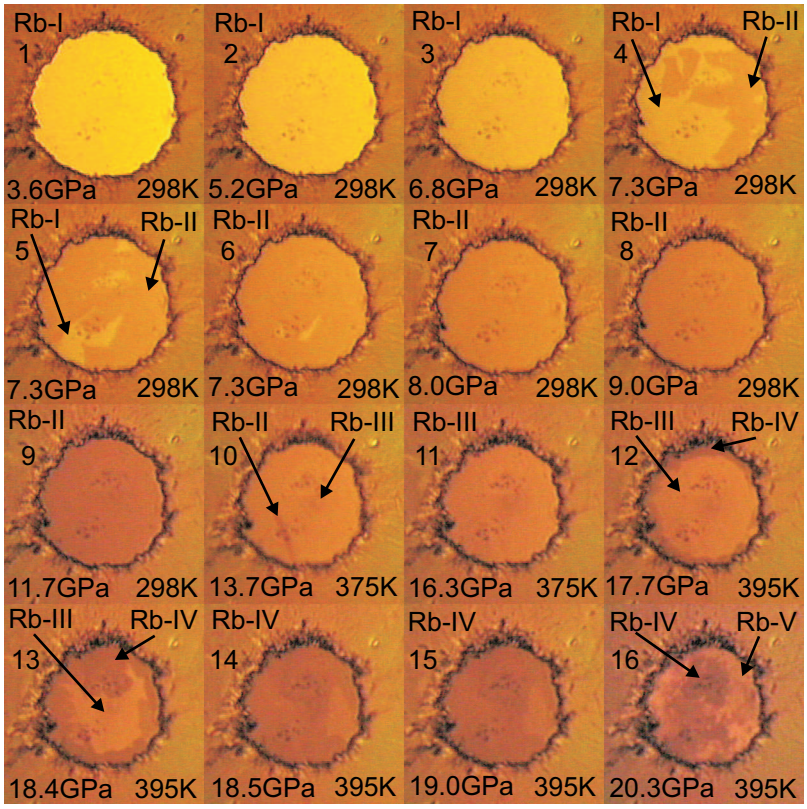

ing with increasing pressure. Finally it is observed that the Rb-III to Rb-IV transition is very sluggish, even at 395 K, with mixed phases over a 1.3 GPa pressure range (panel 12-13). This observation is consistent with observations on the Rb-III→Rb-IV transition at room temperature, but it is in contrast to the Rb-I→Rb-II transition, where the full transition happens at constant pressure (panel 4-6). These visual observations will later be used when constructing the P-T phase diagram of rubidium, where they are very useful for constraining the Rb-III→Rb-IV and Rb-IV→Rb-V phase boundaries (panel 12 and 16).

3.3 Diffraction observations

Rb-III starts to transform into Rb-IV at 16.2 GPa at 300 K on pressure increase, but the transition is not completed before the pressure reaches 16.8 GPa, which means that mixed phases are observed in this pressure range on pressure increase. Because of overlap between Rb-III peaks and the guest peaks in Rb-IV it is not possible to determine from a powder sample if Rb-IV is ordered or disordered as long Rb-III is present in the sample. Therefore, at room temperature, d-Rb-IV can only be observed on pressure decrease using powder samples. Once a single phase sample of o-Rb-IV was obtained, the pressure was carefully decreased in steps of $\sim$0.2 GPa until d-Rb-IV was obtained at 16.5 GPa. 16.7 GPa was the lowest pressure observation of o-Rb-IV on pressure decrease, and on subsequent pressure increase o-Rb-IV was again observed at 16.7 GPa, which means there is no significant hysteresis at this transition even at room temperature. These observations are consistent with what was observed by McMahon & Nelmes (2004*a*).

Temperature and pressure were then alternatingly increased in small steps between diffraction experiments, to map out the P-T dependence of the order-disorder transition, as illustrated in Figure 3.3. This Figure shows the transformation from d-Rb-IV (profile 1) to the o-Rb-IV (profile 2) on increasing the pressure by 0.22 GPa at 321 K, and the transformation back to d-Rb-IV (profile 3) on increasing the temperature by 19 K at the constant pressure of 17.4 GPa. Using four different samples, the phase boundary was crossed 20 times up to the maximum pressure and temperature of 20 GPa and 550 K, respectively. The P-T path taken for each of the four samples is shown in Figure 3.4. In addition, further data were collected in order to get constraints on the liquid$\rightleftharpoons$solid, Rb-III$\rightleftharpoons$d-Rb-IV and o-Rb-IV$\rightleftharpoons$Rb-V phase boundaries at high pressure and temperature (Figure 3.4).

The data points in the P-T phase diagram seems to indicate a discontinuity in the o-Rb-IV$\rightleftharpoons$d-Rb-IV phase boundary close to 400 K. The P-T phase boundary between two phases is expected to be continuous with a slope described by the Clausius-Clapeyron equation $dP/dT = \Delta S/\Delta V$. Any discontinuity in the P-T phase boundary therefore indicate that either the high- or the low-pressure phase has transformed into a new phase at higher temperature. No differences could be seen visually in the integrated powder profiles above and below 400 K, but a more quantitative analysis is necessary to evaluate the structural changes as a

Figure 3.3 A) MAR345 image of disordered Rb-IV. Top left insert (1) is showing the area marked by the black box. The center insert (2) is showing the appearance of Bragg peaks from the guest component of the sample, when pressure is increased by 0.22GPa. The final insert (3) is showing the disappearance of guest Bragg peaks, when temperature is increased by 19K at constant pressure. B) Integrated powder profiles corresponding to the data shown in inserts 1-3. Arrows in profile (2) mark the Bragg peaks from the ordered guest structure two of which are indexed.

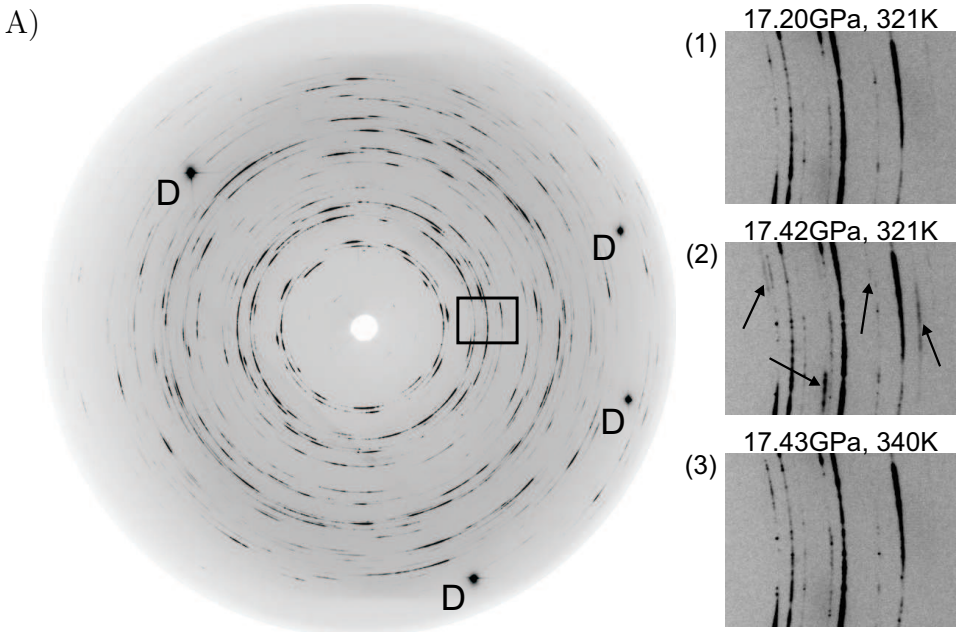

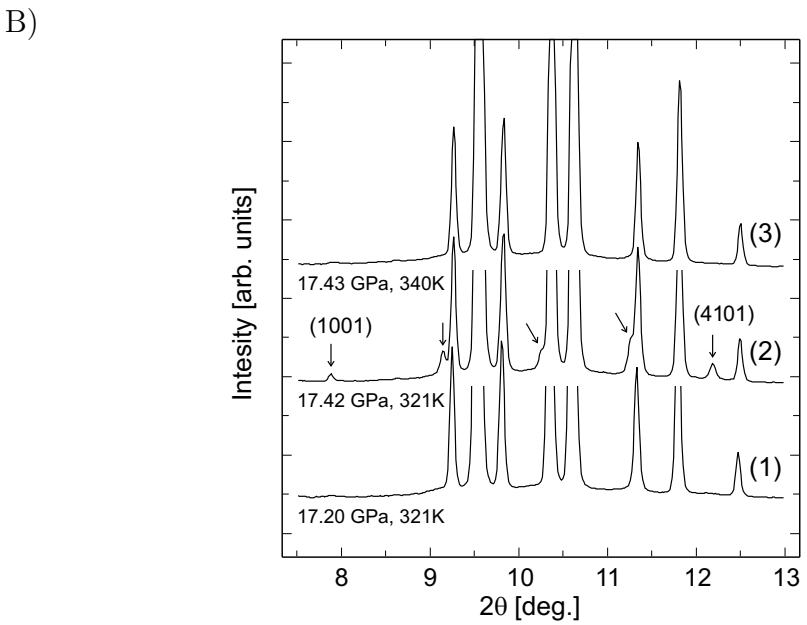

Figure 3.4 Red, blue, green and yellow lines represent the pressure-temperature path used for collecting data on sample 1, 2, 3 and 4 respectively. Arrows indicate the direction in which the data were collected. Additional data points constraining the liquid⇌solid, Rb-III⇌d-Rb-IV and o-Rb-IV⇌Rb-V phase boundaries are also shown. Dotted lines are guides for the eye to show approximate phase boundaries. Data points obtained by visual observation of the phase transition are shown with black crosses. Data point marked with 1, 2 and 3 correspond to the data points marked with 1, 2 and 3 in Figure 3.6

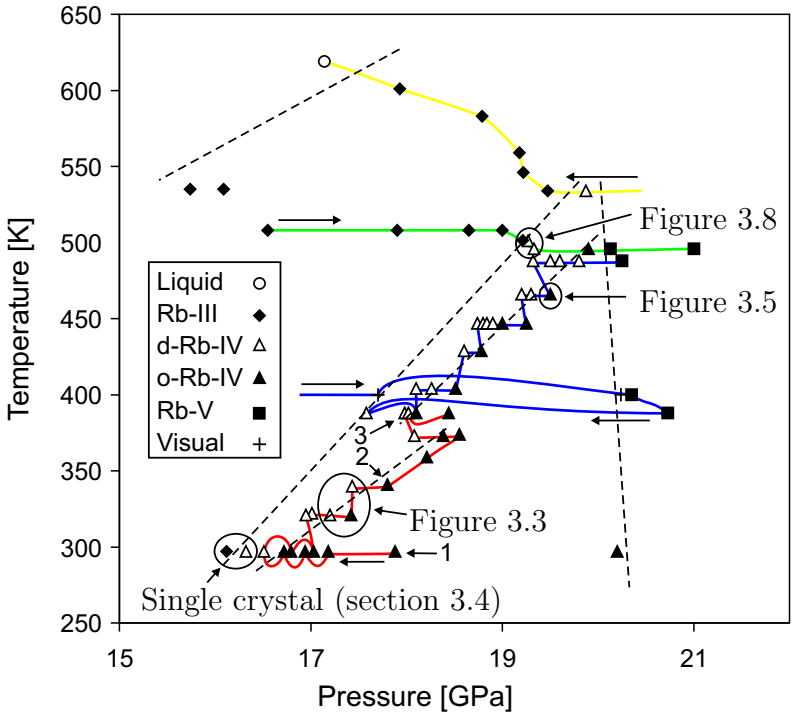

function of pressure and temperature.

As can be seen from Figure 3.3 the samples are very poor quality powders and the data does therefore not contain precise information on the relative intensity distribution between Bragg reflections, making full structural characterization using Rietweld analysis impossible. For qualitative structural analysis LeBail profiles were fitted to all Rb-IV data. A LeBail fit freely refines the intensity of each Bragg peak so it does not result in any information on the atomic positions, but instead it gives precise information on lattice parameters, and the possibility to evaluate the fit between the observed data and the structure model, defined by the refined lattice and the chosen space-group.

Figure 3.5 shows a LeBail fit of o-Rb-IV at 466 K and 19.5 GPa using the

Figure 3.5 LeBail fit of o-Rb-IV at 466 K and 19.5 GPa. The only two non-overlapped guest reflections are indexed. Tick marks below the powder profile indicate the positions of main host and guest reflections and the bottom line shows the difference between the LeBail fit and the observed data. There is a small contribution of diffraction from the rhenium gasket. Rhenium peaks marked by the grey boxes have been excluded from the fitting.

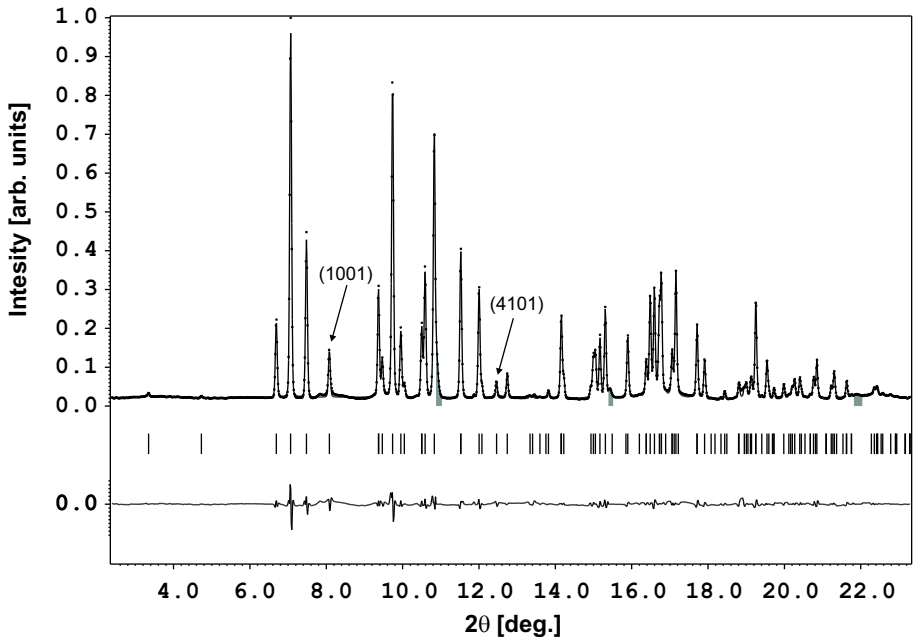

same structure model as at room temperature. The fit is very good so it is concluded that there are no structural transition in o-Rb-IV at high temperature. The LeBail fit of the host structure in d-Rb-IV also fits very well at all temperatures and even the diffuse scattering caused by the disordered guest chains shows no sign of change with increasing temperature (The diffuse scattering will be discussed in more detail in the next section). It is therefore concluded that there are no structural transitions in Rb-IV at 400K, and the observed discontinuity needs a different explanation.

It is noted that the discontinuity is observed at 400 K where four data points were collected from two different samples. The observations from the two samples are not inconsistent at this temperature, but at the same time it is noted that the order-disorder transition pressure is poorly constrained by data points from the two samples separately. The low-temperature data from sample 1 and the

high-temperature data from sample 2 are inconsistent though, when the phase boundary for each of the two data sets are considered separately. This clearly indicate there have been a systematic error in the determination of pressure or temperature in one or both of these samples.

The host and guest unit cell volumes as determined by the LeBail fits have been plotted as a function of pressure in Figure 3.6. The high temperature data (run 1, triangles and run 2, circles) have been plotted together with room temperature data (tick marks), that were used in the publication McMahon & Nelmes (2004*a*). First it is observed that the room temperature data collected in run 1 lies on the same line as the high temperature data collected in run 1 (See data points marked 1, 2 and 3 in Figure 3.6), which implies that the volume reduction is almost purely a pressure effect, and the thermal expansion will therefore be ignored for the rest of this discussion.

Next it is observed that the pressure dependence of the unit cell volume observed in run 1 is significantly different from that observed in the reference data. It is always expected to observe identical unit cell volumes at identical P-T conditions, and because it was concluded that the thermal expansion of Rb-IV is very small, it is very likely that the observed systematic volume error is an effect of a systematic error in the pressure determination. The low pressure data would only need a pressure correction of -0.2 GPa but the high pressure data of run 1 would need a correction of -0.7 GPa to make it consistent with the reference data. Run 2 would need a much smaller correction especially at the highest pressure where no correction is needed.

There are two self-consistency checks that can be made following the above considerations. The order-disorder transition is a pressure marker that at room temperature is observed at 16.5 GPa. The data from run 1 constrained this transition to the pressure range 16.5 - 16.7 GPa, but after a pressure correction of -0.2 GPa this constraint would still be consistent with a transition at 16.5 GPa. Applying pressure correction to all Rb-IV data points would also result in a much smaller discontinuity at 400 K. It is therefore reasonable to conclude that systematic errors in the data are likely to be caused by pressure gradients in the sample, resulting in pressure offsets between the pressure callibrant and the sample volume exposed during the diffraction experiments. Pressure gradients of 0.7 GPa in a soft material like Rb is more than what would normally be expected,

Figure 3.6 Unit cell volume of the host A) and the guest B) as a function of pressure. Empty and filled symbols correspond to d-Rb-IV and o-Rb-IV respectively. Data collected in the first run are marked using triangles and the second run is marked using circles. Data points marked with horizontal lines are room temperature data that several times have been shown to be reproducible, and they are therefore used as a reference to compare with the high temperature data. Trend lines are guides for the eye. Data are not corrected for thermal expansion so the fact that the points marked with 1, 2 and 3 (See Figure 3.4) lie on the same trend line show that thermal expansion of Rb-IV is very small and will be ignored.

A)

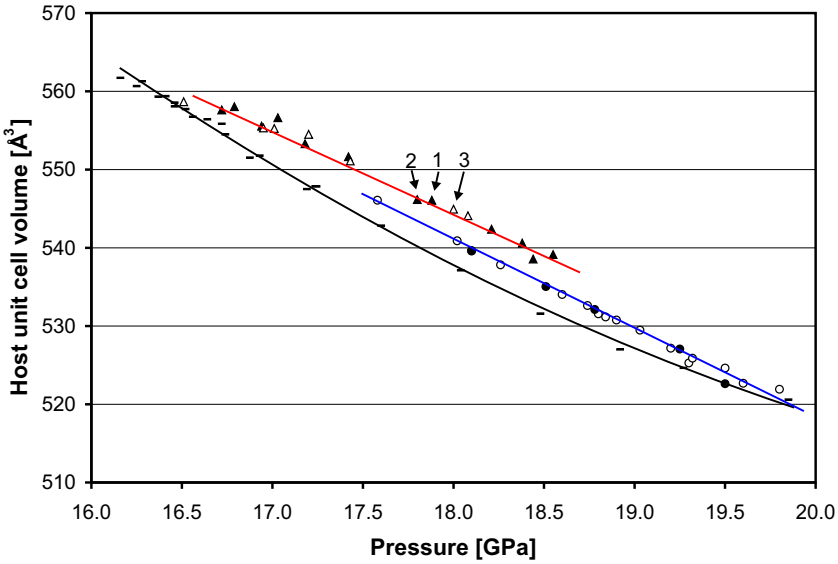

B)

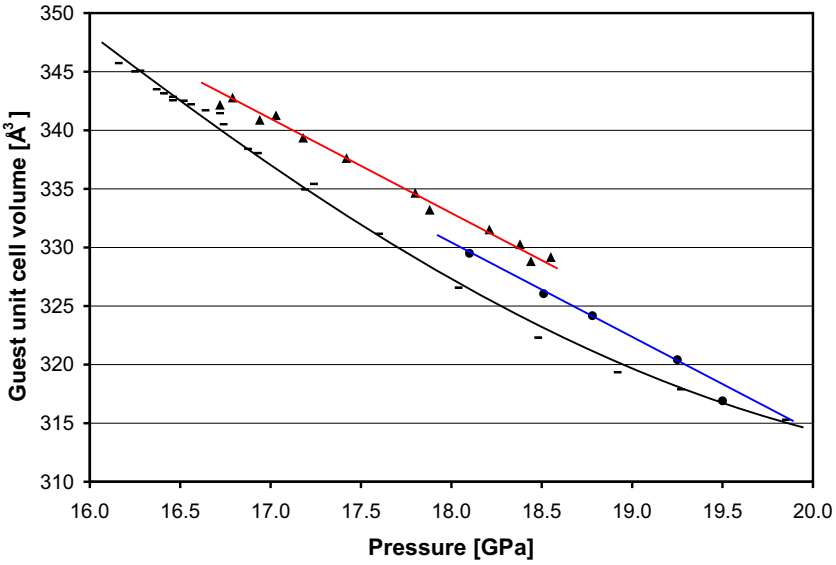

Figure 3.7 First $(hk1)_g$ and second $(hk2)_g$ layer of guest main reflections at 18.5GPa, 16.7GPa and 16.3GPa. A) Sharp Bragg peaks are seen in both layers. B) Just above the order-disorder transition, intense Bragg peaks are still observed in the first layer, although diffuse disks a developing (marked with arrows) around the sharp peaks. Second layer peaks are now very weak at this pressure. C) In the disordered phase all Bragg peaks have disappeared. Only broad diffuse features are observed in the first layer, and the second layer is a completely homogeneous diffuse layer.

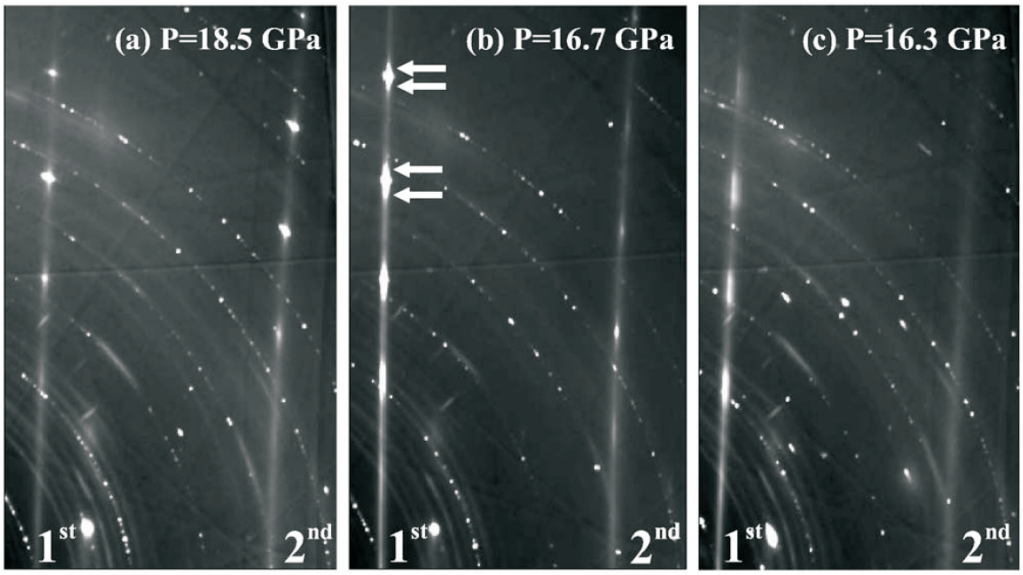

and it is not clear why they develop in this case.

Considering the systematic errors that have been identified it can only be justified to fit a straight line as phase boundary, which is constrained at 16.5 GPa at room temperature and fitted to the highest pressure data which have been shown to suffer the least from the systematic errors. The resulting o-Rb-IV⇌d-Rb-IV phase boundary can be seen in Figure 3.9.

3.4 Information from single crystals

The study by McMahon & Nelmes (2004*a*) concluded that the disordered phase is not completely disordered, because a broad diffuse peak is observed at the position of the (101) guest peak to the lowest pressure (16.2 GPa). This conclusion was based on that reflection alone, all other guest reflections completely disappear

Figure 3.8 Diffraction image (top half) of mixed phase Rb-III and a d-Rb-IV single crystal collected at 19.2 GPa and 501 K (Figure 3.4). The sample was rotated ±3° around the *c*-axis. The first and second order diffuse layers from the guest atoms in d-Rb-IV are clearly visible in the upper picture while the close up of the first order layer shows broad diffuse features.

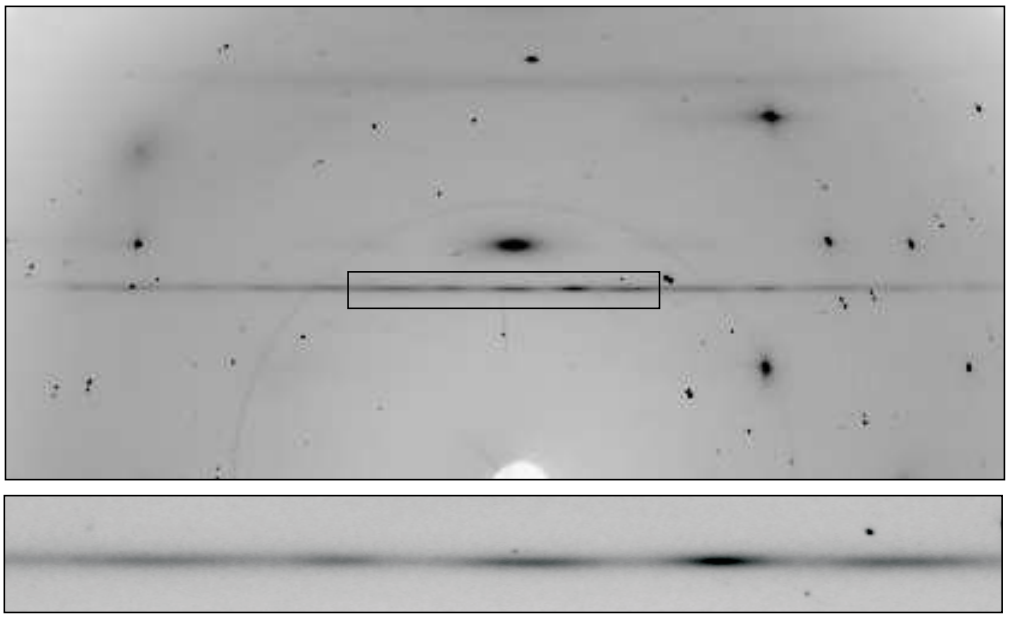

below the order-disorder transition.

In parallel to the current high-temperature powder diffraction study, an effort was made to grow high-quality single crystals of Rb-IV necessary for the full structure refinement which will be described in detail in Chapter 4. Several of these crystals were of sufficient quality for a study of the diffuse scattering in Rb-IV (Falconi et al. 2006)(See Appendix B), and this study gave a much clearer picture of the non-homogeneous distribution of the diffuse scattering within the layers of guest reflections (Fig. 3.7). In contrast to the powder data these images clearly show broad diffuse features centered on all the reciprocal lattice point of the first guest layer $(hk1)_g$. This study gives strong evidence in support of the conclusion that the disordered phase never becomes completely disordered at room temperature even at the lowest pressure.

The broad diffuse (1001) peak was not observed in the powder diffraction studies at high temperature. Even after a temperature increase of only 23°C above room temperature, no clear evidence of any diffuse scattering was observed

(Figure 3.3 profile 1). One explanation could be that the guest phase is fully disordered at these temperatures, or the diffuse (1001) peak has just become too weak to be observed using powder techniques. The question as to whether a fully disordered liquid-like chain state is observed at high pressure and temperature therefore had to be determined using single crystals. Fortuitously, on increasing pressure at 501 K, we obtained a split single crystal of Rb-III which partially transformed, at 19.2 GPa and 501 K, into a high quality single crystal of d-Rb-IV (Figure 3.8) which gave clearly visible layers of diffuse scattering. An enlarged view of the diffuse scattering from this mixed-phase sample shows the diffuse scattering to be strongly non-uniform, showing that the guest chains are not fully disordered on the Rb-III→d-Rb-IV phase boundary at 19.2 GPa and 501 K. A definitive demonstration that a fully disordered state is not obtained at the highest temperature of the Rb-IV stability field will require further single-crystal data under these conditions. However, the present data suggest that it is unlikely that such a fully disordered phase exists.

As stated earlier, a determination of the Rb-III⇌d-RB-IV phase transition at 300 K is greatly hindered by the sluggishness of the transition, which prevent the identity of Rb-IV (whether o- or d-) being determined until the pressure is increased above 16.7 GPa, by which time the sample is o-Rb-IV. However, by slowly increasing the pressure at 300 K on a sample of Rb-III such that only a few intense single-crystal reflections of Rb-IV appeared at 16.2 GPa we were able to observe the (1001) guest reflection, directly on the area detector image, without hindrance from Rb-III reflections. At 16.3 GPa this reflection was elongated along the diffuse lines. On further pressure increase to 16.5 GPa, this elongation was reduced, and the diffuse scattering was decreased in intensity. These observations strongly suggest that Rb-III transform to d-Rb-IV at 16.2 GPa, as plotted in Fig. 3.9.

3.5 Revised phase diagram of rubidium

The P-T phase diagram for rubidium can now be constructed based on the visual observations and the powder and single-crystal diffraction data.

The d-Rb-IV⇌o-Rb-IV phase boundary has been determined by a weighted least-squares fit of a line constrained to 16.5 GPa at room temperature. Run 1 is

Figure 3.9 New P-T phase diagram of solid rubidium in the pressure range 15-21 GPa. Solid lines represent phase boundaries well constrained by the data, and dashed lines are extrapolated phase boundaries.

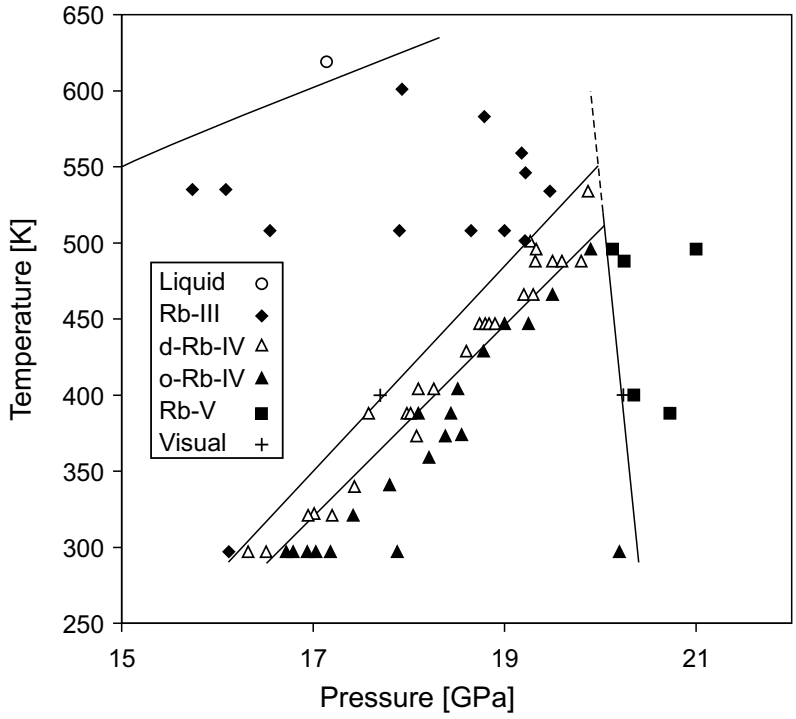

not included in the fit because it was shown to be strongly affected by systematic errors. Points used for fitting are the pressure average between two constraining points at the same temperature, and the weight is inversely proportional to the size of the pressure step between them. The resulting gradient of the order-disorder phase boundary is $dT_c/dP = 63(2)$ K/GPa.

The Rb-III⇌d-Rb-IV phase boundary is also well constrained by the data especially when the visual observations are included, and it enables the gradient of the phase boundary to be determined as $dT/dP = 67.5$ K/GPa. Also, the o-Rb-IV→Rb-V phase boundary is relatively well constrained by the data but only up to 500 K. The o-Rb-IV→Rb-V transition is very sluggish with a hysterises in the order of 1.5 GPa. The phase boundary shown in Figure 3.9 is determined by the first appearance of Rb-V on pressure increase. Extrapolation of this phase boundary to higher temperatures strongly indicates that Rb-IV does not exist all the way up to the melting curve and that Rb-III will transform directly into Rb-V at 20 GPa above 550 K. This transition was never directly observed so further

Figure 3.10 Complete P-T phase diagram of solid rubidium up to 21 GPa combining the phase diagram know from literature with figure 3.10. Open circles indicate liquid and black squares and rhombs indicate RbII and RbIII respectively. An upper and a lower estimate of the melting curve were given by Boehler & Zha (1986) but data from this study are only consistent with the lower temperature estimate.

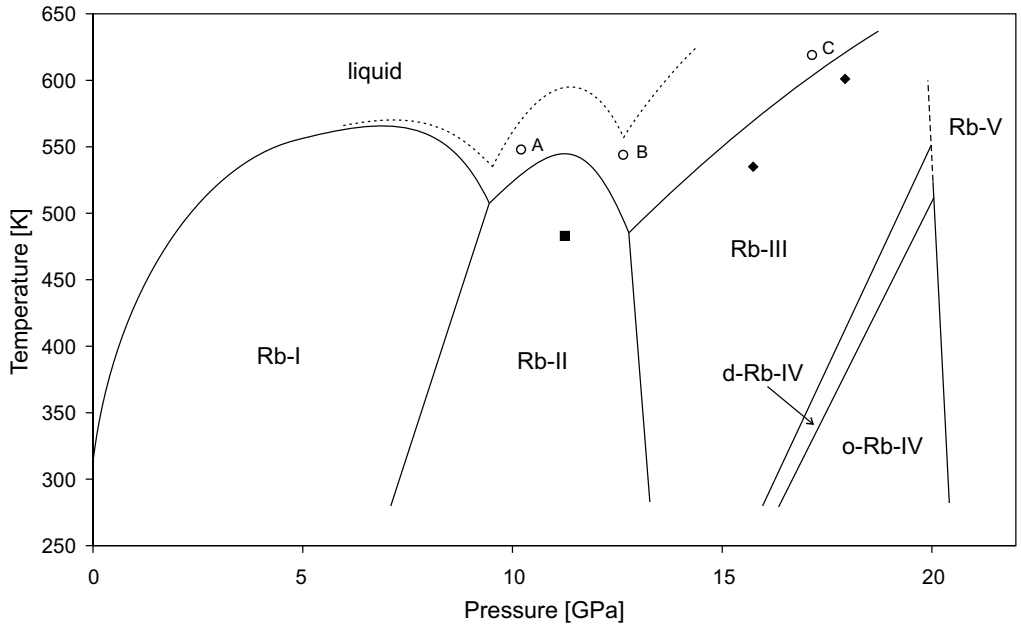

data are needed for a determination of the Rb-III⇌Rb-V phase boundary.

The final P-T phase diagram is shown in figure 3.10. It is important to note that the dips at the Rb-I : liquid : Rb-II and Rb-II : liquid : Rb-III triple points were observed reproduceably in different samples by Boehler & Zha (1986), but the absolute position of the melting curve would vary between samples. The data collected for this study are only consistent with the low temperature estimate of the melting curve (Figure 3.10), but they do not give strong constraints on the triple points. A detailed study of the melting curve of rubidium above 5 GPa is therefore still necessary.

Liquid rubidium

This subsection is not directly related to the structural changes in Rb-IV that are being studied in this thesis, but it has been included for a complete discussion of the phase diagram.

Figure 3.11 Liquid rubidium as observed in the pressure range 10-17 GPa just above the melting curve. Profiles A, B and C represent the data points marked A, B and C in figure 3.10. The background caused by th compton scattering from diamond anvils have not been subtracted. The intensity drop above 20° in 2θ is caused by the limited opening angle of the DAC.

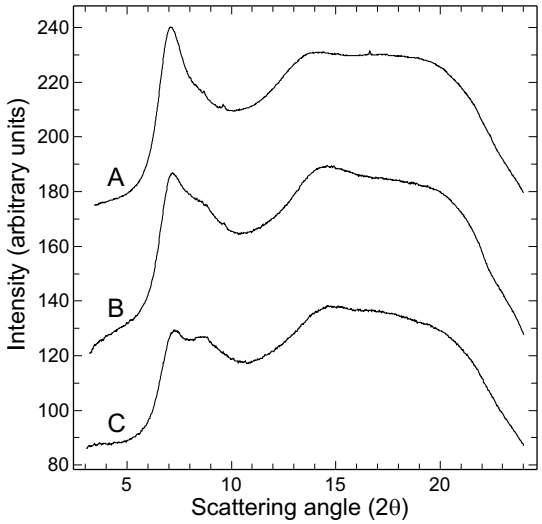

The radially integrated intensity distribution profiles of the liquid data are shown in Figure 3.11. These three profiles show an evolution from a sharp almost symmetric first peak, which at higher pressure develops a shoulder and at the highest pressure turns into a split peak. Very similar diffraction patterns were observed by Falconi et al. (2005) (see Appendix B) in liquid cesium in the pressure range 2 to 6 GPa. It was concluded by Falconi et al. (2005) that the changes in the diffraction patterns were caused by a phase transition, transforming a simple liquid into a non-simple liquid at increasing pressure, with a corresponding change in coordination number from about 12 to 8. This closely mirrors the transition observed in the solid, at almost the same pressure, where the coordination number changes from 12 to 8 or 9 when the solid transforms from the simple Cs-II (fcc) phase into the complex Cs-III structure. It was therefore concluded that the liquid phase transition was caused by a dsp^3 electronic hybridization equivalent to that reported for the solid (Falconi et al. 2005). High quality structural data are needed to show whether the low-pressure phase of liquid rubidium can be explained by a simple liquid model, but if that is the case, the dsp^3 electronic hybridization would also be a reasonable explanation for the transition observed

in liquid rubidium. For a detailed structural analysis of the liquid, data are needed to much higher scattering angles, but at least it is clear from the present data that the split first peak in the non-simple liquid rubidium is different from that observed in the non-simple liquid cesium, and a study of liquid rubidium would therefore be of great interest.

3.6 Conclusion

The phase diagram of rubidium has been studied in detail in the temperature range 298 - 600 K and the pressure range 15 - 21 GPa. Combined with what is known from the literature, the complete phase diagram of solid rubidium is now known up to 21 GPa. A direct transformation from Rb-III to Rb-V was not observed but by extrapolating the determined Rb-III$\rightleftharpoons$d-Rb-IV and o-Rb-IV$\rightarrow$Rb-V phase boundaries by only 10 K and 50 K respectively it is concluded that Rb-IV does not exists above 550 K.

The most remarkable feature of the new phase diagram of rubidium is the strong temperature dependence of, and the parallel nature of, the Rb-III$\rightleftharpoons$d-Rb-IV and d-Rb-IV$\rightleftharpoons$o-Rb-IV phase boundaries. This suggests that d-Rb-IV may be a necessary intermediate phase between Rb-III and o-Rb-IV. It is noted that amongst the elements having host-guest structures, only in rubidium is the incommensurate phase obtained from a complex (52-atom) composite structure.

Finally it is concluded, based on single crystal data, that the guest chains in d-Rb-IV keeps, the short range order observed at room temperature up to at least 501 K. In fact, the structured diffuse scattering observed at room temperature looks identical to that observed at 501 K, so by extrapolation, it is very unlikely that d-Rb-IV has truly disordered chains at any temperature above room temperature.

Chapter 4

The modulated structure of Rb-IV

In this chapter the full modulated structure of Rb-IV will be described resulting in new detailed information on the host-guest interactions.

Guest chains in Rb-IV are more than 7 Å apart and direct interaction between these are effectively screened by the host framework structure. The long range order observed between guest chains in o-Rb-IV is therefore not a result of direct interactions between guest chains, but happens through a deformation of the host structure. The disorder observed in d-Rb-IV is a result of weak interactions between the guest chains and the host framework. The transition from d-Rb-IV to o-Rb-IV is caused by increasing host-guest interactions with increasing pressure, and it is therefore expected to observe the strongest host-guest interactions at the high-pressure end of the Rb-IV stability field (16.2 - 20.5 GPa).

The main challenge in the study of the modulated structure of Rb-IV, will be to observe satellite reflections for the first time and to extract the intensity of these extremely weak reflections, using single-crystal techniques.

Satellite reflection intensities increases with increasing host-guest interactions, and it is therefore expected to observe the most intense satellite reflections at the high-pressure end of the Rb-IV stability field. For that reason it will be attempted to grow a high quality single crystal from the melt at 20 GPa by heating up the pressure cell at constant pressure. As shown in the previous chapter a single crystal Rb-III can be grown from the melt, and at high temperature this will transform into a single crystal of Rb-IV (See Figure 3.8).

4.1 Crystal growth

Single crystals of Rb-IV were grown in standard Merrill-Bassett type pressure cells with Be diamond support disks and 400 μm diamond culets. A 200 μm thick tungsten foil were preindented to 30 μm and a 100 μm hole were drilled using a spark eroder. A few small ruby fragments for pressure measurement (Mao et al. 1986), were attached to one of the diamond culets using the smallest possible amount of vacuum grease. The use of vacuum grease is important because it minimizes the risk of the ruby fragments getting covered by the soft Rb metal when sealing the DAC. To prevent contamination, the pressure cells were left in an oxygen- and water-free atmosphere (<1 ppm O_2 and <1 ppm H_2O) for at least two hours before loading the high purity (99.996%) Rb metal (Aldrich Chemical Company). Finally, the DAC's were pressurized to between 18 and 19 GPa and then heated to 650 K and slowly cooled down to room temperature (12 hours), using a time and temperature programmable oven. Often the pressure would drift during heating and crystals of the wrong phase (Rb-III or Rb-V) would be grown. In this case the pressure cell must be repressureized and re-heated. In other cases several crystals of Rb-IV were grown, but if there were too many crystallites, or they were of too poor quality the pressure cell were re-heated. Re-heating crystals of poor-quality crystals almost never resulted in any improvements in quality, and a new loading had to be prepared. About 50 loadings were needed to grow one very high quality single crystal of Rb-IV at 19.6 GPa. A single-crysta data collection for checking crystal quality of this sample showed that the tetragonal c-axis was parallel to the diamond cuelet, which is the optimal orientation giving access to most symmetry independent reflections (See section 2.5.1.)

4.2 Preliminary studies

After a number of preliminary data collections using lab and synchrotron based diffractometers, it was clear there were a number of problems that had to be solved before reliable reflection intensities for structure refinement could be extracted.

4.2.1 In house

There are two single crystal diffractometers available in School of Physics, University of Edinburgh: a CCD-equipped Bruker difractometer, and a point detector eqiupped CAD-4, both using Mo tubes as x-ray sources. The Bruker is ideal for screening crystal quality, and for determining crystal orientation from intense host and guest reflections, but no modulation reflections could be observed on this instrument. A point detector equipped with a collimator has the advantage over CCD detectors, in that Be scattering and Compton scattering from diamonds can be significantly reduced. But after hours of scanning of the strongest satellite reflections nothing was observed on the CAD-4, which lead to the conclusion the satellite reflections have less than 0.1% of the intensity of the main host reflections.

4.2.2 SRS 9.8

The diffractometer on SRS station 9.8, Daresbury, is, in principle, identical to the Bruker difractometer in Edinburgh. The most important difference is the x-ray source, which in this case is a superconductong wiggler, producing a beam that is approximately a factor 1000 times more intense than the Mo x-ray tube.

A data collection using a one second exposures per frame, resulted in clearly visible modulation reflections, but almost all main host and guest reflections were saturated and therefore useless for integration. On the other hand, if the primary beam was attenuated such that the most intense Bragg reflection would be just below the saturation limit of the CCD-detector, non of the modulation reflections could be observed ($F_{obs} > 3\sigma$). The limited dynamic range of the CCD detector is, in itself, not a serious problem, because a series of data collections could be collected with different degrees of attenuation and finally the integrated data could be scaled to form a complete data set.

The real problem is the contaminating scatter from DAC components such as diamond anvils, tungsten gasket and beryllium backing disks. Diamond reflections and the smooth powder rings from the tungsten gasket impose the less serious problem. Sample reflections overlapping with one of the few very intense diamond reflections can easily be identified as outliers and subsequently be deleted from the resulting list of reflections. The smooth, slowly changing powder

Figure 4.1 A single CCD image (0.2° scan width, one second exposure) from a data set collected on station 9.8 at SRS. Host and guest reflections are marked by H and G respectively. Smooth powder lines from the tungsten gasket are marked with W, and broad spotty powder diffraction lines from the polycrystalline beryllium backing disks are marked with Be.

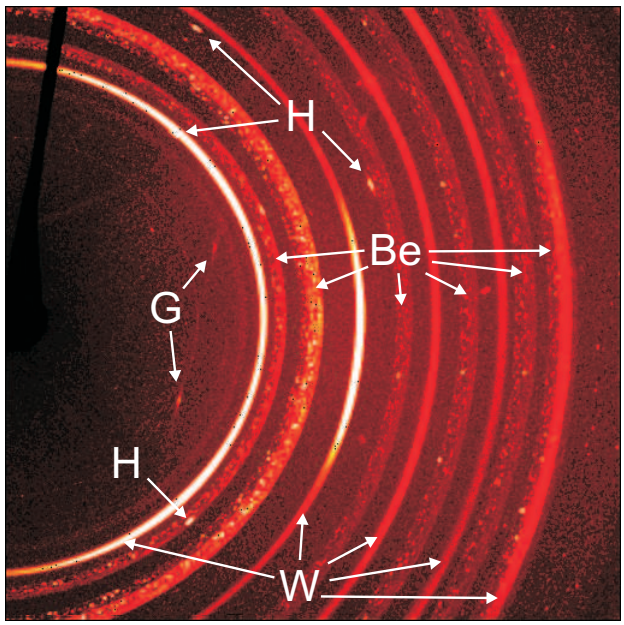

rings from the tungsten gasket are effectively included in the background that is calculated and subtracted from each frame during integration. By far the most serious problem is caused by the spotty powder rings from the polycrystalline beryllium backing disks. Beryllium has the hcp structure resulting in many diffraction rings and because the backing disks are several mm thick each ring is very broad. The result is that a very large percentage of the CCD detector will be affected by beryllium rings (Figure 4.1). When sample reflections are much stronger than the beryllium diffraction, as in the case of main host-guest reflections, reliable reflection intensities can be obtained. When sample reflections are only as strong as, or weaker than, the diffraction spots from individual beryllium crystallites, integration of reliable reflection intensities become impossible. This is the case for Rb-IV satellite reflections.

Figure 4.2 Three peak profiles collected on station D3, DORISIII, Hamburg. The peak profiles are representative of all the data collected during the beam time, i.e. intense host reflection, intermediate intensity guest reflections and non-observed modulation reflections.

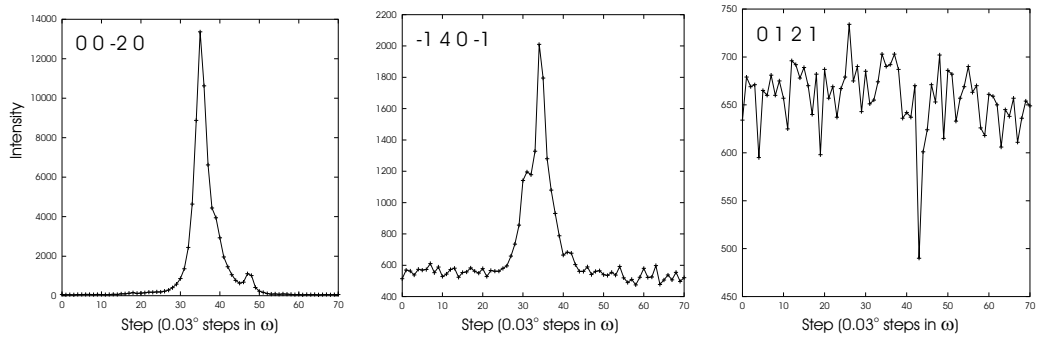

4.2.3 Hasylab

The next step was therefore to collect data using a point detector equipped diffractometer at a synchrotron facility ($\lambda = 0.450$ Å). Two days of beam time for testing were obtained on station D3, on the DORISIII synchrotron in Hamburg. The crystal orientation was refined by scanning 12 host reflections, and subsequently the orientation was checked by driving the diffractometer to the position of randomly chosen reflections. The predicted positions were perfectly centered on observed reflections of both host and guest reflections, confirming that the orientation was well refined and that the correct q value (q=1.646) was used.

The ($hklm$) indices of the strongest modulation reflections were known from the SRS 9.8 data, but none of them could be observed (Figure 4.2). The beam on this station is produced by a bending magnet and is therefore significantly less intense compared that produced by the superconducting wiggler on station 9.8 at SRS. Even though, it seems surprising, the beam was just not intense enough to observe the modulation reflections.

4.2.4 ESRF ID09 and ID27

From previous experience we knew that the stations ID09 and ID27, even though designed and optimized for collecting high-pressure powder diffraction data, had the potential to also collect very high quality single crystal data. The experimental setup on these stations is very simple, consisting of a single vertical motorized

Table 4.1 Comparison of experimental setup at station 9.8 and ID09/27

	9.8	ID09/27
Beam size	300/200μm	50-5μm
Detector type	ApexII CCD	MAR345 Imageplate
Detector area	Square: 10 mm×10 mm	Circular: 356 mm diameter
Typical detector dist.	70mm	360mm
Sample stage	3-circle goniometer (Fixed χ)	Vertical ω axis
Sphere of confusion	>100μm	<5μm
Wavelength	1.4 - 0.4 Å	1 - 0.1 Å

rotation axis and a MAR345 image plate (IP) detector centered on the direct beam (2θ=0) at a distance of ∼360 mm from the sample stage rotation axis. This setup has both important advantages, and a few disadvantages, compared to station 9.8 at SRS. The most important differences in experimental setup are summarized in Table 4.1.

As discussed in Section 2.5.1, access to reflections is very limited when studying samples in a DAC, but the number of accessible reflections can be increased by using a shorter wavelength incident beam. So, in principle, the shortest wavlength possible would be preferred for data collection. On station 9.8, choosing the wavelength of 0.41 Å does give acess to more reflections compared to the 0.68 Å wavelength routinely used, but it also results in much lower quality data. The reason is that at 0.68 Å the highly absorbing tungsten gasket acts like a pinhole blocking most of the primary beam not hitting the sample. At 0.41 Å, the linear absorption coefficient of tungsten is much smaller and a much higher percentage of the incident beam will penetrate the gasket (Figure 4.3). This not only leads to much stronger gasket powder lines, but it also leads to a stronger Compton background, and diffraction from the diamond and beryllium backing disk on the detector side of the DAC.

On station ID09/27, the incident beam can be focused to a size smaller than the sample (Figure 4.3C). Using this setup the optimal ratio between the intensity of the sample reflections and the intensity of the contaminating scattering is always achieved. And consequently, a shorter wavelength beam can be used, resulting in access to more reflections without lowering the data quality. This experimental setup also results in data with no contaminating scatter from the

Figure 4.3 Schematic drawing showing the effect on a 300μm collimated incident beam A) at long wavelengths where the tungsten gasket acts like a pinhole and B) at shorter wavelengths where the beam penetrates the gasket. C) On the right is shown the situation where the incident beam is focused to 20μm.

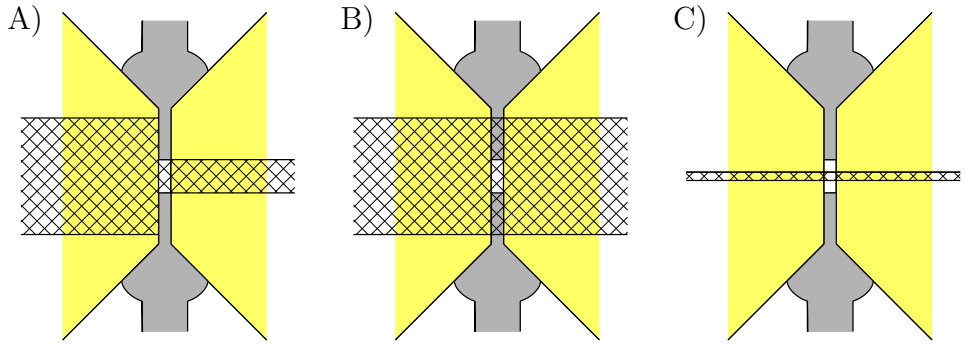

gasket, simply because the gasket is not exposed by the finely focused incident beam.

Both the APEXII CCD and the MAR345 IP are pixelated detectors, where each of the pixels can be considered as point detector. The number of photons that each pixel will receive from the evenly distributed Compton scattering is approximately proportional to $1/d^2$ where d is the detector distance. The number of photons received by a pixel on a powder diffraction line is proportional to $1/(d \cdot \tan 2\theta)$ where 2θ is the scattering angle for a given powder line, but in case of single-crystal reflections there will be no decrease in the observed intensity. This means that a significant improvement in the ratio between the intensity of the sample reflections and the intensity of the contaminating scattering can be made by increasing the sample-detector distance from 70 mm to 360 mm. This means that the ID09/27 experimental setup should be able to collect better quality data compared to data collected at station 9.8, because of the much larger detector distance.

All of this was confirmed during the ID09 beam time awarded for studying diffuse scattering caused by disorder in Rb-IV guest chains (See Appendix B). Not only the diffuse scattering was observed but also satellite reflections sitting on a very low background.

Although the MAR345 IP detector collects excellent quality data the readout time is ∼2min per frame, which result in a data collection time of 9 hours for a

single 90° ω-scan using a 0.2° frame width. Even though the dynamic range of the MAR345 detector is better compared to the APEXII CCD it is still far from high enough to collect intensities on both main host-guest and satellite reflections at the same time. Ideally a full data set would be collected on ID09/27, but because of the slow data collection and the limited access to the ID09/27 beam lines, it was decided that, to obtain a full data set, the modulation reflection intensities would be collected at station ID09/27 and the host-guest reflections intensities would be collected at station 9.8. The only problem using this approach is that there is no software available to analyze the high-pressure single crystal data collected with the MAR345 detector. There are several single crystal software packages supporting the MAR345 format but they have all been optimized for analyzing data collected from complex crystals on a fiber at ambient pressure. Considerable effort had been made at the ESRF, by the ID27 beamline staff, to use the software packages **Automar** and **XDS** but without any success. The goal of this study is to make a structure refinement of Rb-IV, but the preliminary studies has shown that it is necessary to develop new techniques for extracting intensities from MAR345 data.

4.3 Experimental setup and data collection

Data sets were collected on stations 9.8 at SRS and ID09 at the ESRF on the same single crystal of Rb-IV at 19.6 GPa.

4.3.1 SRS 9.8

Data were collected on a Bruker diffractometer equipped with an APEXII CCD detector, using a wavelength of 0.6713 Å (Cernik et al. 1997). A series of scans about the diffractometer ω-axis (Figure 4.4), were optimized to collect all accessible reflections, avoiding as much shading caused by the DAC steel body as possible (Table 4.2). The beam was heavily attenuated, using 2 mm of aluminium, such that the strongest sample reflections was just under the saturation limit of the detector. The sample was aligned to the goniometer center optically, using a laser to align the diamond table perpendicular to the optical axis of the microscope. Centering along the optical axis was centered using the focal plane of the microscope.

Figure 4.4 Goniometer circles and directions as defined in the Bruker software. When the goniometer is in the shown position relative to the laboratory system (X_L,Y_L,Z_L) the three angles χ, ω and 2θ are zero.

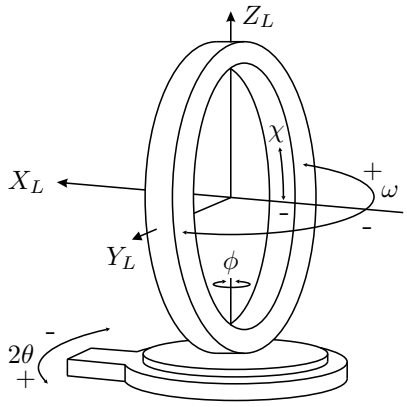

4.3.2 ESRF ID27

A data set was collected on beamline ID09 at the ESRF. Alignment of the sample onto the direct beam and onto the rotation axis is achieved by a set of automated scans of the gasket and sample across the direct beam, exploiting the contrast in x-ray absorption between the Rb-IV sample and the tungsten gasket.

The *c*-axis of the Rb-IV crystal was aligned parallel to the vertical sample stage rotation axis (the ω-axis), and a fine sliced (0.2° width) scan covering the full DAC opening angle (±40°) was collected. An exposure time of one second per. frame and an undulator gap of 5 mm (no attenuation of the beam) was chosen because it resulted in clearly observed first order satellite reflections (Figure 4.5) and a few of the weak guest reflections under the saturation limit of the detector. The guest reflections are important for determination of a scale factor when merging the data set with the SRS data.

4.4 Data reduction

The data reduction process is often a highly automated process for data collected from a good quality crystal mounted on a fiber, where the user only has to be careful in choosing the correct symmetry. In the case of high-pressure data, the contaminating scatter and the shading caused by the DAC's steel body, means

Figure 4.5 (A) A single 0.2° scan width image from the data set collected on ID27, showing intense host reflections and guest reflections connected by horizontal layers of diffuse scattering. (B) Expanded view of the area marked by a black box in (A). First order satellite reflections are clearly visible.

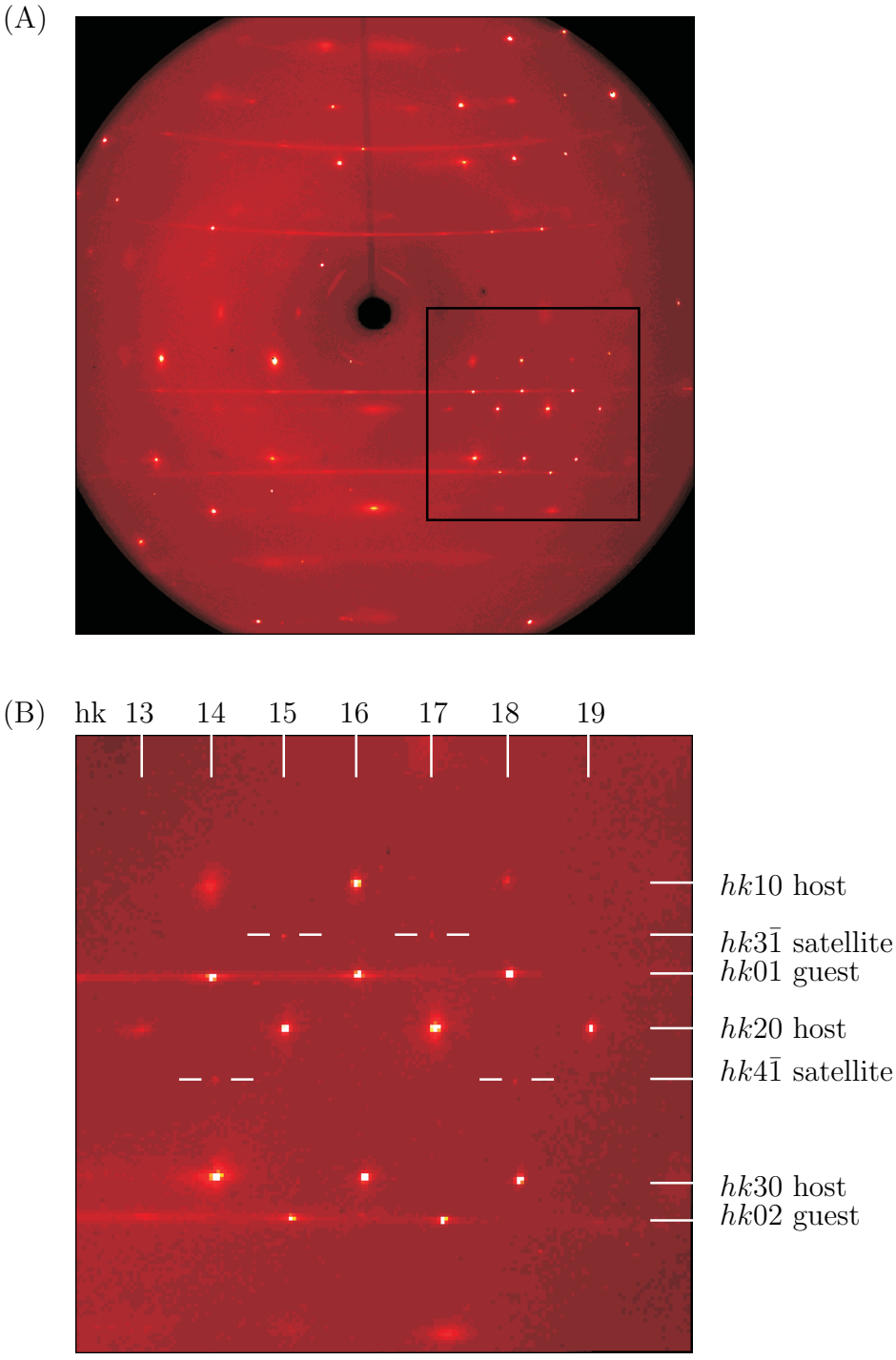

Table 4.2 Multirun used for single crystal data collection on station 9.8. Angles and directions are defined in Figure 4.4. This multi run is optimized for collecting data from a DAC with 40° opening angle.

Scan	2θ	ω	ϕ	χ	width	time	sweep	direction
ω	28		0	54.734	0.2	1	30	neg
ω	-28		0	54.734	0.2	1	50	neg
ω	28		180	54.734	0.2	1	30	neg
ω	-28		180	54.734	0.2	1	50	neg
ω	28		0	54.734	0.2	1	50	neg
ω	-28		0	54.734	0.2	1	30	neg
ω	28		180	54.734	0.2	1	50	neg
ω	-28		180	54.734	0.2	1	30	neg
ω	-40		0	54.734	0.2	1	20	neg
ω	-40		180	54.734	0.2	1	20	neg
ω	0		0	54.734	0.2	1	32	neg
ω	0		0	54.734	0.2	1	32	neg

that the data reduction process requires much more input from the user.

4.4.1 APEX and MAR345 format to SMART format conversion

Station 9.8 uses Bruker's new **APEX** software package for diffractometer control and data analysis. We have found this software to be ill suited for data analysis of our high-pressure data, mainly because it does not offer the possibility to hand pick sample reflections, which is essential because the automatic reflection picking procedure cannot handle the contaminating background scatter in the data. The program **FrmUtility**, which is a part of the Bruker software package, is therefore used to convert the data into the old Bruker format supported by the program **SMART**v.5.62 (Bruker 2000), which has the flexibility that is needed.

Because the **SMART** software is our preferred program for data analysis, the MAR345 data must also be converted into the old Bruker format. It has not been possible to find a program that would do this, so a conversion program had to be written. The conversion from the 3450×3450 pixel MAR345 IP format to the 512×512 pixel Bruker CCD format, is done by cutting away 189 rows of pixels from each of the four sides leaving a 3072×3072 frame format (Figure 4.6).

Figure 4.6 MAR345 to Bruker format conversion. MAR345 frames have a pixel resolution of 3450×3450 while Bruker frames have a 512×512 pixel resolution. Pixels inside the small box are used for conversion, while pixels outside are not used. The white circle in the large box shows the active area of the MAR345 detector, so the pixels not used for conversion only includes a small number of active pixels.

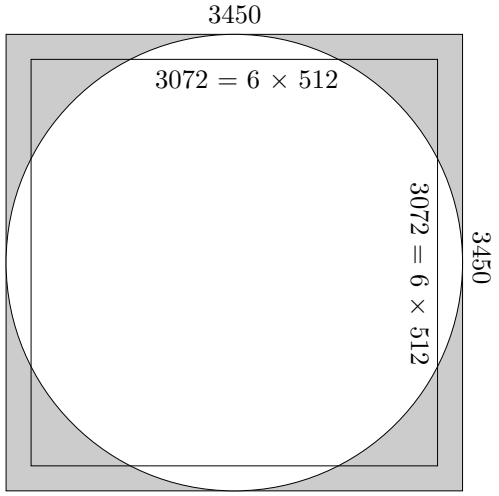

These pixels are then grouped into 6×6 squares where the new pixel value is the average of the 36 original pixel values, except when one of the original pixels is saturated, in which case the new pixel will be given the saturation limit value ($2^{16} - 1 = 65535$) as well. The program also writes a bruker format frame header to each file, containing information on goniometer angles, and scan width and direction, as defined in Figure 4.4. This is not information found in the MAR345 frames, but it is information the user has to provide the conversion program, based on how the data were collected.

4.4.2 Hand picking and Rlatt

The Rb-IV single crystal was of very high quality, resulting in sharp, round diffraction spots on the frames and 0.3° (FWHM) rocking curves that showed no splitting. When browsing through the frames it is easy visually to tell the difference between sample reflection and contaminating scatter. A sample reflection is present in two to three successive frames, with the same position in each. Reflections from the diamond anvils are in general much more intense, and because

Figure 4.7 Rb-IV host reflections visualized in Rlatt. Reflections have been handpicked using SMART and picked reflections not belonging to the host have been manually deleted using Rlatt.

the diamond anvils are strained and not centered on the scan axis, reflections will be broad, present in 6 to 7 frames and be shifted in position from frame to frame. Also, reflections from beryllium crystallites in the backing disks are easy to identify because they are only present in a single frame. These distinguishing features make it straightforward to manually pick only sample reflections.

The picked reflections are then visualized in reciprocal space using the program ***Rlatt*** (Bruker 2000), where any accidently picked non-sample reflections can easily be identified, as outliers not fitting a simple lattice (Figure 4.7). Removing non-sample reflections makes the automatic indexing procedure much more reliable.

Host and guest lattice parameters were determined independently in both ESRF and SRS data, and in all cases the results were a body-centered tetragonal lattice, with a satisfying agreement between determined lattice parameters (Table 4.3).

Table 4.3 Lattice parameters of Rb-IV as determined from the SRS and the ESRF data. The large uncertainty in the parameters determined from the ESRF data is caused by small deviations in the geometry of the experimental setup from that assumed by the software used for analyzing the data. The lattice parameters determined from the SRS data are of better quality and will be used in the rest of this thesis.

	SRS	ESRF
a_{host}	10.153(1)	10.16(2)
c_{host}	5.122(1)	5.14(1)
a_{guest}	10.154(2)	10.16(3)
c_{guest}	3.111(1)	3.13(1)
$q = c_h/c_g$	1.646	1.635

4.4.3 Frame masking

It is very important to identify reflections that are blocked by the DAC steel body, and make sure that these reflections are not included in the final (hkl) list. Because the DAC has rotational symmetry around the axis normal to the diamond tables ($\mathbf{n}$), the problem is to identify and remove reflections with an angle to $\mathbf{n}$ larger than the DAC opening angle. This is a geometric problem and can be solved from the following considerations.

The goniometer geometry used for data collection at both the SRS and the ESRF has the HUBER 4-circle geometry as shown in Figure 4.4. The DAC is aligned such that the DAC normal ($\mathbf{n}$) is parallel to the incident beam, when the ϕ-angle and the ω-angle are both zero. Because the ϕ-angle is fixed at 0° or 180° during experiments, the DAC normal ($\mathbf{n}$) is always in the plane with its normal parallel to the ω-axis (This plane is defined by the (X_L, Y_L) plane in Figure 4.9), and the ω-angle is therefore equal to the angle between the DAC normal and the incident beam direction.

The detector distance D and the detector center (x_0, y_0) are refined from a data set collected on a standard crystal and these parameters are constant during an experiment. Using the $\omega, 2\theta, \phi, \chi$ goniometer position angles and the position (x, y) for each reflection on the detector, the angle v between the diffracted beam and the DAC normal ($\mathbf{n}$) is determined by the product $\mathbf{r} \cdot \mathbf{n} = \cos v$, where $\mathbf{r}$ is a unit vector in the direction of the diffracted beam with the components

Figure 4.8 A single MAR345 IP image (0.2° scan width) collected using an empty DAC. The Compton scattering from the diamond anvils result in a homogeneous background in which the shaded area, caused by the absorbing steel body of the DAC, can clearly be seen. Two diamond Bragg reflections can also be seen in the image.

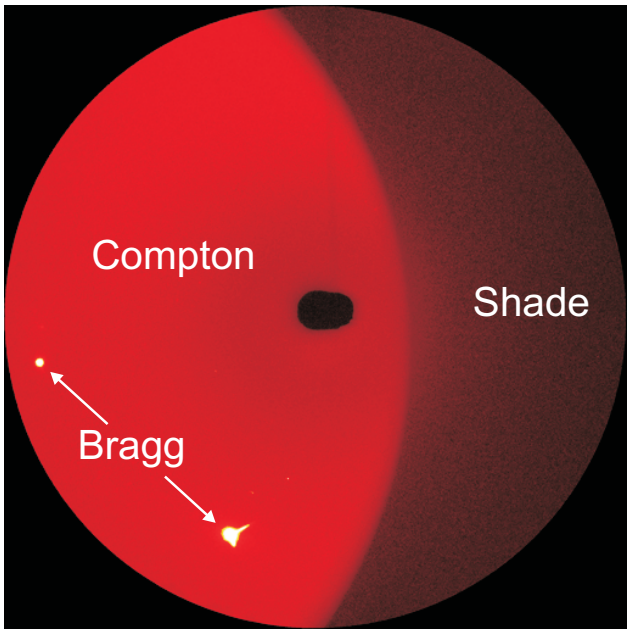

$\big(\cos(2\theta+\alpha)\cos\beta, \sin(2\theta+\alpha)\cos\beta, \sin\beta\big)$ and the DAC normal unit vector ($\mathbf{n}$) has the components $\big(\cos\omega, \sin\omega, 0\big)$. The α and β angles as defined in Figure 4.9 are:

$$\alpha = \arctan\left\{\frac{x_0 - x}{D}\right\} \qquad \text{and} \qquad \beta = \arctan\left\{\frac{(y - y_0)\cos\alpha}{D}\right\} \tag{4.1}$$

The angle v can therefore be expressed as a function of detector position and goniometer setting angles:

$$\cos v = \cos\beta\big\{\cos\omega\cos(2\theta+\alpha) + \sin\omega\sin(2\theta+\alpha)\big\} \tag{4.2}$$

Initially, a program that would simply identify and remove shaded reflection from the integration output was written and used. However, a much better approach to the problem where shaded reflections are identified and omitted during the integration process was developed recently (Parsons 2004, Dawson et al. 2004). For each data frame a mask frame is calculated, in which the pixel

Figure 4.9 Geometry of the single-crystal diffraction experiment. The laboratory (X_L, Y_L, Z_L) and the detector (x, y) coordinate systems are shown. This figure is showing the experimental setup as viewed from above, with the sample at the origin of the laboratory system and the incident X-ray beam coming from the left along the X_L axis. Goniometer setting angles (ω and θ) are defined in Figure 4.4. **n** is the unit vector normal to the diamond culets and **r** is the unit vector in the direction of the diffracted beam.

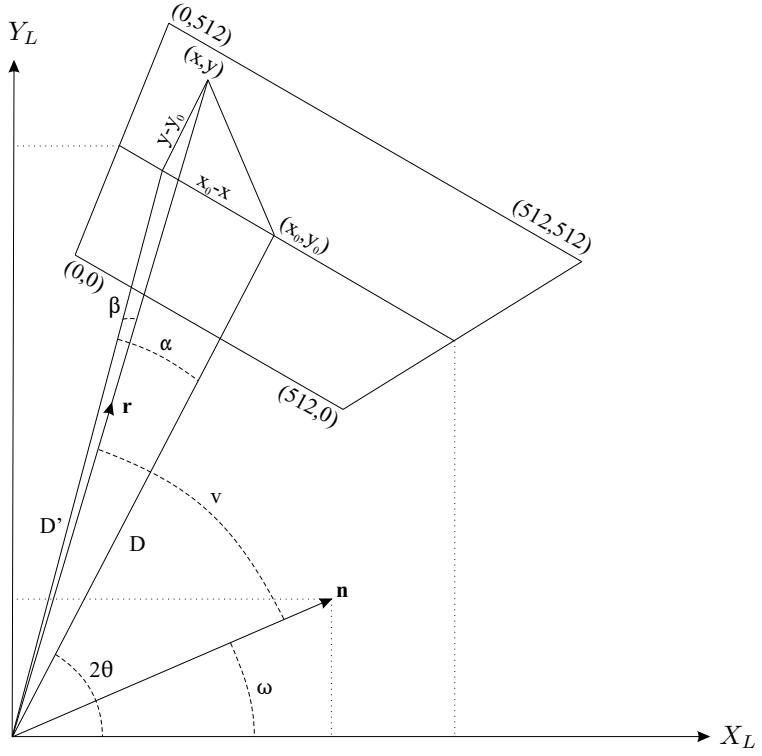

values are 0 for non-shaded pixels and 64 for shaded pixels. The **SAINT** integration software will read in both data frame and mask frame and omit pixels that are masked (Bruker 2000). Using this approach, a program, based on Equation 4.2, was written that would calculate mask frames for DAC's of any opening angle, and the possibility of removing pixels in user defined 2θ ranges, i.e. allowing for masking the corners of MAR345 IP frames, or masking strong powder lines from beryllium disks and gasket. The frame masking approach results in a more stable intensity integration process, and more reliable intensities can be extracted.

4.4.4 Visual inspection of data

Because the high-pressure incommensurate Rb-IV data are non-standard data for the Bruker software it is very important that every single step in the data reduction process is checked carefully. The first thing to do, after conversion of the Mar3450 IP data into Bruker format, is to check all the frames visually in **Smart**. Because the c-axis of the crystal was aligned to be parallel to the ω-axis, a number of layers perpendicular to the c-axis were clearly visible (Figure 4.5).

Layers of host reflections are observed with l indices up to ± 6, and for guest reflections layers with m indices up to ± 3 are observed. If a satellite reflection $(hklm)$, indexed using the 4D approach, was indexed based on the host lattice, it would index (hkl_{host}), where $l_{host} = l + m \cdot q_h$. From this it is straight forward to determine all first and second order satellite reflections that are possible to observe in the range $-6 < l_{host} < 6$, and the result is shown in Table 4.4 where the satellite reflections has been sorted after the l_{host} index. Using the transformation matrix explained in Table 4.4, all 27 layers of satellite reflections were checked visually, and it was observed that while most first-order reflections were visible, only one layer of 2nd order satellite reflections were visible.

4.4.5 Integration of intensities

The next step in the data reduction process was the integration of reflection intensities. Previous versions of **SAINT+** could integrate intensities from incommensurate modulated structures but only the newest version of the software (**SAINT+**v.7.12A) will integrate intensities from incommensurate composite crystals. Both the SRS and the ESRF data sets were integrated including first order modulation reflections, and the resulting intensity distribution is shown in Figure 4.10.

In the heavily attenuated SRS data, strong main reflections are observed, while only very low integrated intensities are observed at the positions of the satellites. No satellite reflections could be seen visually in the frames of this data set, so the low satellite intensity ($|F|^2 < 3\sigma$) is an indication of a successful integration. In general, the integration of this data set looked very good: all the reflections are observed at the position where they are expected, and all intense

Table 4.4 Observed satellite reflections in Rb-IV at 19.6 GPa. General $(hklm)$ satellite reflections are grouped based on their l and m indices, e.g. $l = -3$ and $m = 2$ represents all satellite reflections with indices $hk\bar{3}2$ and $hk3\bar{2}$. l_{host} is the l index based on the host lattice ($l_{host} = l + 1.646 \cdot m$). The $l + m$ column shows whether the sum of the l and m indices are even or odd. The 3x3 transformation matrix, transforming the host UB matrix into a matrix that will predict the position of modulation reflections, is an identity matrix I where the 1 at position I_{33} has been replaced by the number in the transform column. The number in the transform column is the inverse of l_{host} and the modulation reflections will be at the predicted positions of the $hk1$ and $hk\bar{1}$ reflections. The obs column shows if the modulation reflections are observed, where '-' indicates not observed and the number of +'s indicate relative intensities of observed modulation reflections. The $h + k$ column shows if the the sum of the the h and k index of observed reflections is even or odd. The type column indicates if the reflections are of first (1) or second (2) order, where type=min($|l|, |m|$).

l	m	l_{host}	$l+m$	transform	obs	$h+k$	type
-3	2	0.30	o	3.3333	-	-	2
2	-1	0.35	o	2.8571	++	o	1
-1	1	0.65	e	1.5385	++	e	1
4	-2	0.70	e	1.4286	-	-	2
-2	2	1.30	e	0.7692	-	-	2
3	-1	1.35	e	0.7407	+	e	1
5	-2	1.70	o	0.5882	-	-	2
-1	2	2.30	o	0.4348	-	-	1
4	-1	2.35	o	0.4255	+	o	1
1	1	2.65	e	0.3776	++	e	1
6	-2	2.70	e	0.3704	-	-	2
-2	3	2.95	o	0.3390	-	-	2
5	-1	3.35	e	0.2985	-	-	1
2	1	3.65	o	0.2740	+++	o	1
7	-2	3.70	o	0.2703	-	-	2
-1	3	3.95	e	0.2531	-	-	1
1	2	4.30	o	0.2326	-	-	1
6	-1	4.35	o	0.2299	-	-	1
-2	4	4.60	e	0.2174	-	-	2
3	1	4.65	e	0.2151	+	e	1
8	-2	4.70	e	0.2128	-	-	2
2	2	5.30	e	0.1887	+	e	2
7	-1	5.35	e	0.1869	-	-	1
-1	4	5.60	o	0.1786	-	-	1
4	1	5.65	o	0.1770	+	o	1
9	-2	5.70	o	0.1754	-	-	2
1	3	5.95	e	0.1681	-	-	1

Figure 4.10 Identification of outliers. Both the SRS and the ESRF data were sorted into main reflections and satellites, and each of these groups was sorted into subgroups depending on their l_{host} index (See Table 4.4). Within each of the subgroups the reflections are sorted with increasing intensity. This type of plot is very useful for identifying outliers. A) Two suspected outlier reflections in the SRS data marked with 1 and 2 is shown to be pure sample reflections. B) Several suspected outlier reflections in the ESRF data (marked 1 to 6), were all shown to result from partially overlap with diamond reflections or artifacts of the integration process, and were therefore deleted.

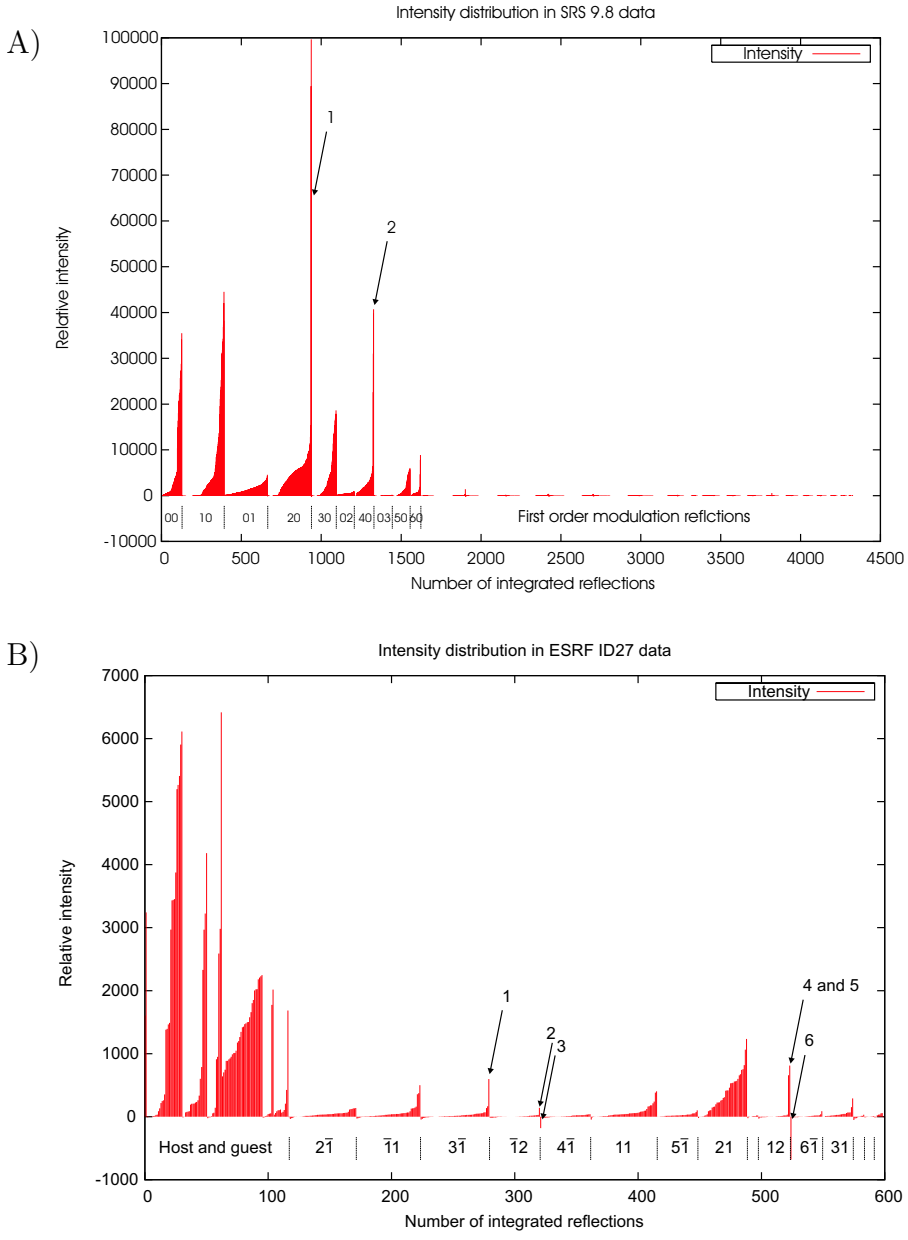

reflections have very similar peak shapes. Only the internal R-factor[1] (R_{int}=0.16) is slightly high compared to R_{int} values observed in data collected at ambient conditions. R_{int} values up to 0.2 are not unusual for data collected in a DAC, and is caused by sample absorption, absorption by DAC components, diamond dips and gasket shadowing (Loveday et al. 1990, Miletich et al. 2000). There are a few reflections (marked with arrows in Figure 4.10A) which are significantly more intense than other reflections in the same layer. These reflections can be found in the integration output file, which contains information on which frame the reflections was observed, making it possible to go back to the raw data and check if these reflections are pure sample reflection or if they are overlapped with diamond reflections. The reflection marked with 1 in Figure 4.10A is the $00\bar{2}0$ host reflection, and the reflections marked with 2 are the 0040 and $00\bar{4}0$ host reflections. They all represent pure sample reflections. A total of 1581 host and guest reflections were observed, including reflections observed several times (redundant observations). After merging of redundant observations and symmetry equivalent reflections these reduced to 168 unique reflections.

4.4.6 Identification of outliers

The integrated intensities of the ESRF data are shown in Figure 4.10B. These data are converted from Mar345 IP data into the Bruker format using the program written for this study. This approach has not been tested before, so it is therefore very important that these intensities are evaluated carefully. Most important is to check if the integrated satellite intensities agrees with the visual observation.

A direct comparison of Table 4.4 and Figure 4.10B, shows a very good agreement, except for a few outliers marked with arrows, confirming that reliable satellite reflection intensities have been extracted from the ESRF data. The low internal R-factor (R_{int}=0.10) also indicates a good quality data set. Outlier reflections 1 and 4 were partially overlapping with diamond reflections. The reflection pairs 2,3 and 5,6 are artifacts of the integration process. No sample intensity is observed at the positions of these reflections, but the two reflections in each pair are spatially so close to each other that the integration program allows one

[1]The internal R-factor is defined as the sum of the differences of all intensities from the average value of symmetry equivalent reflection intensities divided by the sum of all intensities: $R_{int} = \sum_{hkl} \sum_i |I_i(hkl) - \overline{I(hkl)}| / \sum_{hkl} \sum_i I_i(hkl)$

reflection to have a positive intensity and the other to have an equal negative intensity, averaging out to zero intensity, consistent with what is observed in the experiment. All of these reflection were deleted from the data set and the internal R value decreased to R_{int}=0.09. A total of 477 satellite reflections were observed and these resulted in 275 unique satellite reflections after merging of symmetry equivalent reflections.

A scale factor of 2.8(2) were estimated from 12 reflections that were present in both data sets, which means that the SRS data (Figure 4.10A) must be multiplied by 2.8 to bring the two data sets onto the same intensity scale.

4.5 Structure refinement

The most widely used method of structure refinement is the least-squares method. And two of the most widely used refinement programs based on this method, are **SHELX** and **JANA2000**, for normal commensurate and incommensurate structure refinements respectively. These are our preferred refinement programs.

4.5.1 Host-guest refinement

The first step in the refinement process is the refinement of the basic host and guest structures separately. Setting up a structure refinement in **JANA2000** is not trivial, so to check that the initial **JANA2000** refinement is set up correctly, the host and guest structures were refined in both **SHELX** and **JANA2000**. The host and gueset structures were refined using only unique host ($hkl0, l \neq 0$) and guest ($hk0m, m \neq 0$) reflections respectively, and anisotropic atomic displacement parameters (ADP) were include for both structures. The two programs result in almost identical fits to the observed data (Table 4.5), and the refined parameters are identical within error (Table 4.6), confirming a high degree of reproducibility between the two refinement programs.

The refined values of the host-structure atomic coordinates (for the 16k site (x,y,0) of the space group I4/mcm) are (0.4166(2), 0.2922(2), 0), and the guest structure has atoms on the Wyckoff 2a site of the space group I4/mmm, in agreement with the previously reported structure (McMahon et al. 2001).

The anisotropic ADP's of the host structure are almost perfectly isotropic (Table 4.6)(U_{iso}=0.0243(4)Å^2) and this displacement parameter value is inter-

Table 4.5 Agreement between structure model and experimental data. The fit is quantified using the crystallographic R-factor. The R-factor (residual factor) is a measure of the agreement between the crystallographic model and the experimental X-ray diffraction data. It is defined by $R = \sum ||F_{obs}| - |F_{calc}|| / \sum |F_{obs}|$, where F_{calc} is the structure factor calculated based on the model structure and the criteria for an observed reflection is $|F|^2 > 3\sigma$. The sum is over all measured reflections.

		# reflections obs. (all)
SHELX		
R_{host}	0.0428	81 (104)
R_{guest}	0.0626	42 (64)
JANA		
R_{host}	0.0424	76 (104)
R_{guest}	0.0626	40 (64)

Table 4.6 Refined structure parameters as refined in **SHELX** and **JANA2000**. Atomic positios and modulation amplitudes are in relative coordinates and ADP's are in units of Å^2.

	SHELX	**JANA2000**
Host	I4/mcm	(x,y,0)
x	0.4166(2)	0.4166(2)
y	0.2921(2)	0.2922(2)
U_{11}	0.025(1)	0.0248(1)
U_{22}	0.024(1)	0.0239(1)
U_{33}	0.0266(9)	0.0266(1)
U_{12}	0.001(1)	0.0009(9)
Guest	I4/mmm	(0,0,0)
U_{11}	0.024(2)	0.023(1)
U_{33}	0.093(5)	0.096(5)

preted as an effect of thermal vibration. The ADP's of the guest structure are strongly anisotropic, where the displacement parameters perpendicular to the chains (U_{11}=U_{22}=0.023(1)Å^2) are equal to the ADPs' observed in the host structure, while the APD along the chain is a factor 4 larger (U_{33}=0.096(5)Å^2, see Table 4.6). The ADP's observed perpendicular to the chain are interpreted as a thermal vibration consistent with the thermal vibration observed in the host structure. Considering the weak interaction between host and guest structures, it is expected to observe a large thermal vibration along the chain direction, but the observed U_{33} does not arise only from thermal vibration. The chains are incommensurately modulated, and the displacements caused by this modulation cannot be described in a normal 3D structure refinement, so the modulation along the chains is seen as a disorder, resulting in a larger U_{33}. The most important step in setting up a modulated structure refinement is the decoupling of the thermal vibration and the static charge density. A modulated structure refinement should result in a thermal vibration along the chain that is smaller than U_{33} observed in the un-modulated refinement.

4.5.2 Modulated structure refinement

The superspace group of Rb-IV can be derived from the symmetry elements of the average host and guest structures (See Appendix A). As described in the introduction the average host and guest structures were determined from powder diffraction data, and the superspace group X4/mcm(00g)s000 was derived, where X denotes the centering $(\frac{1}{2}\frac{1}{2}\frac{1}{2}\frac{1}{2})$(McMahon & Nelmes 2004*b*). Modulation reflections have never been observed in Rb-IV until this single-crystal study, so it is very satisfying to see that satellite reflections has systematic absent reflections (reflection condition: $h+k+l+m=2n$) as predicted by the 4D body centered superspace group (See Table 4.4).

There are two symmetry independent atoms in the Rb-IV host-guest structure. Rb1 is a host at the average position (0.4166,0.2922,0) and Rb2 is a guest atom at the average position (0.5,0,0); all other atoms are related to these two by symmetry (Figure 4.11). The next step in the structure refinement is to add periodic modulation functions to the average atomic coordinates (as described in section 2.4.3). Adding only first order harmonic modulations to the Rb1 and Rb2 will result in 12 refinable Fourier coefficients (See Equation 2.8), but all 6

Figure 4.11 The average host structure is described relative to the host lattice and the average guest structure is described relative to the guest lattice. These two lattices can glide relative to each other along the *c*-axis (corresponding to a phase shift), so the z=0 plane of the two lattices do not coincide in general. The phase t is defined as zero when the z=0 plane of the two lattices coincide. This figure shows the z=0 plane of the average host structure (red circles) and the average guest structure (blue circles) at the phase t=0. White circles indicate guest atoms that have positions $\frac{1}{2}c_g$ above the plane. The host atom Rb1 and the guest atom Rb2 are symmetry independent; all other atoms in the Rb-IV structure are related to these two atoms by symmetry.

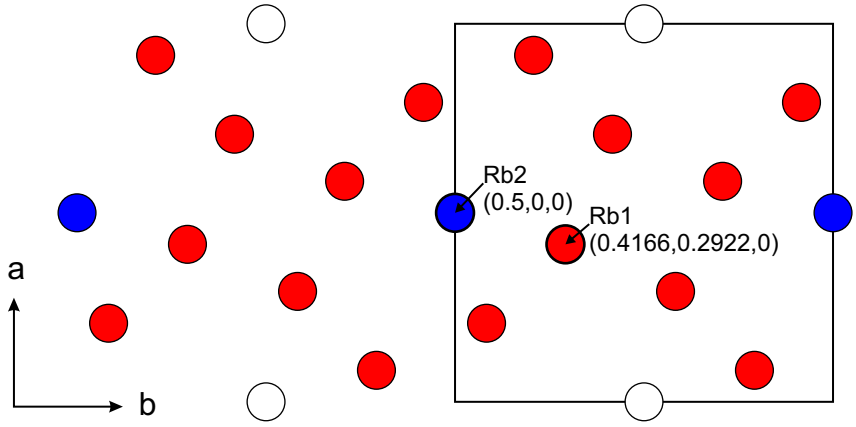

coefficients related to the modulation of Rb2 and 3 coefficients related to Rb1 are constrained to 0 by symmetry. There is an extensive mathematical theory for symmetry in superspace, which could be used to show why this is the case (Van Smallen 1995), but it can also be understood from the considerations presented in Figure 4.12.

The starting model, and the simplest possible model for the modulated structure, includes a first order harmonic modulation of Rb1, and a second order harmonic modulation of Rb2. A least squares refinement of this model resulted in a satellite R-factor of $R_{satell.}$=0.191, indicating that the refined modulation already fits the observed data quite well, but inspection of the guest super-space atomic domain, with the modulation function superimposed on top, shows that the atomic domain does not display the same simple harmonic modulation as the model function (Figure 4.13A). It is therefore necessary to add higher order harmonic functions to model the complex shape of the atomic domain.

Including fourth order harmonics to the Rb2 modulation function, resulted in

Figure 4.12 Symmetry of the modulation functions. A) The guest chains are modulated by interactions with the host structure, so the modulation function must have the symmetry of the host structure. The guest atoms are positioned on a 4_2 rotation axis of the host structure, along which interactions with the host structure only will have half the periodicity compared to the host structure itself. All odd order harmonics will therefore be constrained to zero. Even order harmonics are allowed, but because symmetry is constraining the guest atoms to the 4_2 rotation axis there can be no displacements in the x any y directions, and the $A_{nx}, B_{nx}, A_{ny}, B_{ny}$ Fourier coefficients are therefore constrained to zero for all n (See Equation 2.8 for a definition of the Fourier coefficients). Finally the mirror plane through each layer of host atoms perpendicular to the c-axis, constrains guest atoms placed on one side of the mirror plane to be displaced in the opposite direction from atoms placed on the other side of the mirror plane. Consequently only sin shaped modulations are allowed and B_{nz} is constrained to zero for all n. B) The host atoms have general positions relative to the guest structure, resulting in a modulation function with the periodicity of the guest structure. All orders of harmonics are therefore allowed but the mirror plane through the guest atoms perpendicular to the c-axis will only allow cos components for displacement in the a and b directions, while only sin components are allowed for displacements in the c direction, resulting in A_{nx}, A_{ny}, B_{nz} being constrined to zero for all n.

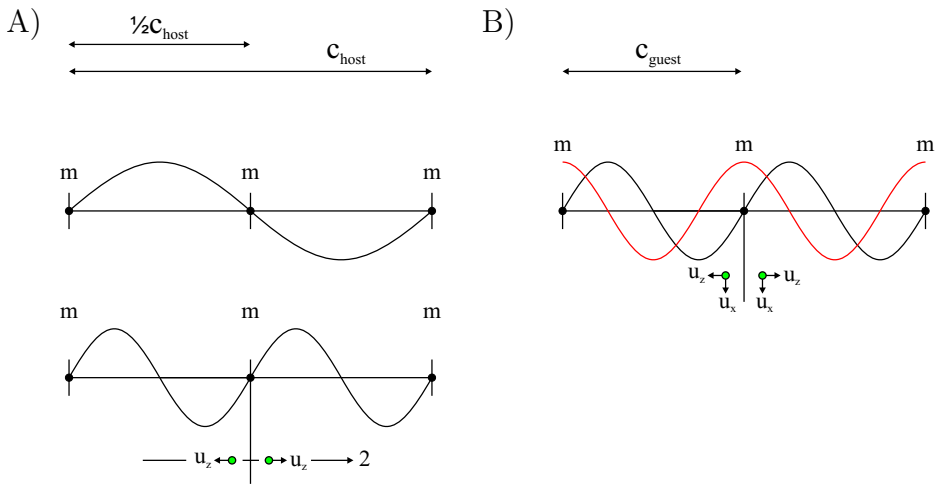

Figure 4.13 Atomic domains of the guest atom Rb2 at position (0.5,0,0) and the fitted modulation function are shown when A) using second order harmonics, B) using fourth order harmonics, and C) when using a sawtooth function. The chosen 2D section shows the atomic modulation in the *c*-direction. D) is showing the atomic domain of the host atom Rb1 at position (0.4166,0.2922,0) (See Figure 4.11). The chosen 2D section shows the atomic modulation in the *b*-direction. These figures are closely related to those presented in Figure 2.6

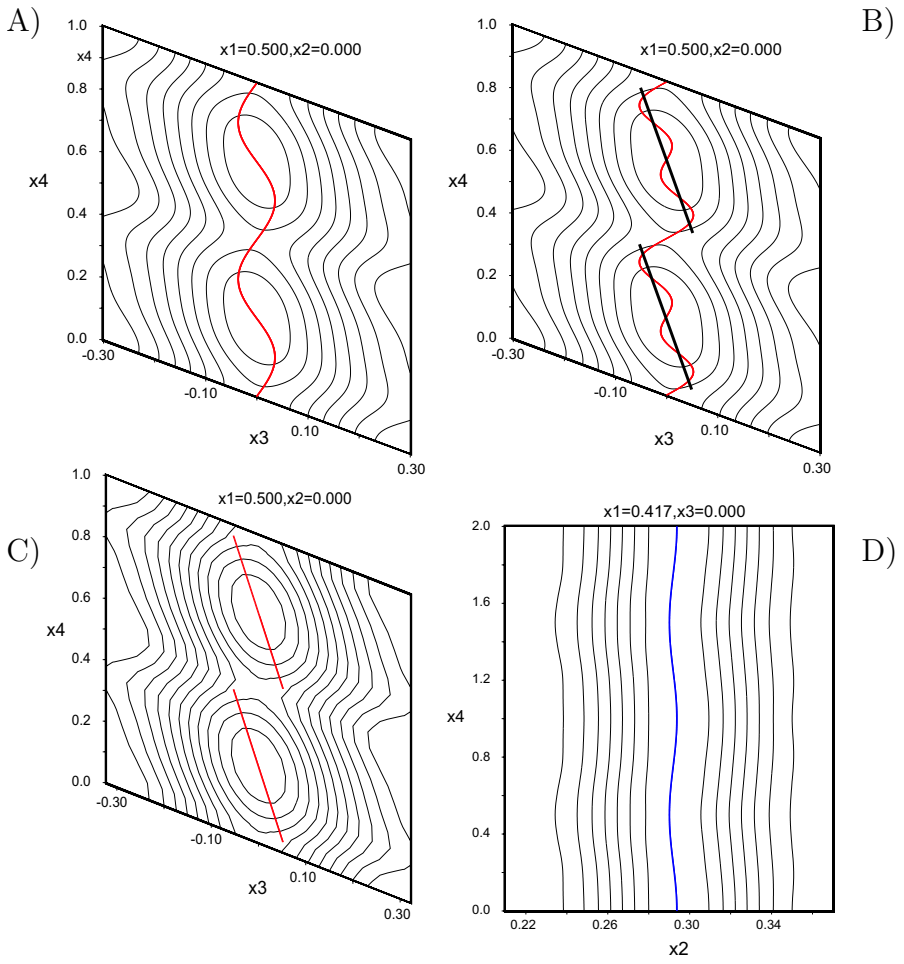

Figure 4.14 Definition of the sawtooth function with periodicity Δ and amplitude A_{saw}.

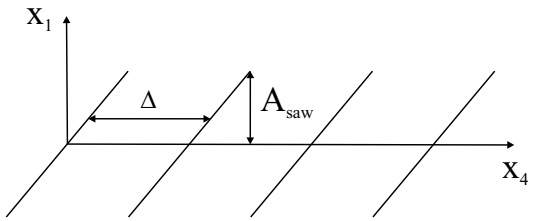

a slightly better fit to the observed satellite intensities ($R_{satell.}$=0.188). The modulation function also has an improved fit to the atomic domain (Figure 4.13B), but there are clearly sections ($x_4 \in (0.1, 0.4)$) where the model function is oscillating and the atomic domain is showing a simple linear behavior.

The observed modulation function strongly resembles a sawtooth function defined as shown in Figure 4.14. The harmonic function describing the modulation of Rb2 along the c direction was therefore removed and a sawtooth function was added instead. The periodicity of a modulation function is constrained to $c_h/2$, and the sawtooth function is therefore fully described by the amplitude A_{saw} alone.

Even though reducing the number of refinable parameters the fit to the observed satellite intensities improved significantly ($R_{satell.}$=0.164). The sawtooth modulation has a satisfying fit when projected on the guest atomic domain, and also the first order harmonic function describing the modulation of the host atom Rb1 in the b direction fits very well (Figure 4.13C and D). Several models were tested using higher harmonics, but none of them resulted in a better fit, only when exchanging the sin shaped modulation function of Rb1 in the c-direction, with a sawtooth function did the fit to the satellite improve slightly ($R_{satell.}$=0.162). The final modulated structure model for Rb-IV includes first order harmonic functions for displacements of the host atom (Rb1) in the a and b directions, and sawtooth functions for displacements in the c direction of both the host (Rb1) and the guest (Rb2) atom. The final model parameters are presented in Table 4.7 and 4.8.

Table 4.7 Agreement between the final sawtooth structure model for Rb-IV and experimental data. R-factors from the structure refinement of the average host and guest structures have been included. The sawtooth modulated of guest atoms results in a improved fit to the observed guest reflections ($hk0m, m \neq 0$). Only a very small improvement in the fit to the observed host reflections ($hkl0, l \neq 0$) is achieved, which is reasonable because the host structure is weakly modulated.

	host	guest	host-guest sawtooth	# reflections obs. (all)
JANA				
R_{all}			0.0524	176 (468)
R_{host}	0.0424		0.0414	76 (104)
R_{guest}		0.0626	0.0513	40 (64)
$R_{comm.}$			0.0423	24 (25)
$R_{satell.}$			0.1622	36 (275)

Table 4.8 Refined parameters for the sawtooth structure model of Rb-IV. The shown parameters are refined in the superspace group X4/mcm(00g)s000 using the program **JANA2000**. Atomic positios and modulation amplitudes are in relative coordinates and ADP's are in units of Å^2.

	host	guest	host-guest sawtooth	displacement absolut values
Rb1	(x,y,0)			
x	0.4166(2)		0.4168(1)	
y	0.2922(2)		0.2920(1)	
U_{11}	0.0239(1)		0.0229(7)	
U_{22}	0.0248(1)		0.0238(7)	
U_{33}	0.0266(1)		0.0262(6)	
U_{12}	-0.0009(9)		-0.0005(8)	
B_{1x}			-0.00033(6)	0.003Å
B_{1y}			0.00182(6)	0.018Å
$A_{saw,z}$			0.0020(1)	0.010Å
Rb2	(0.5,0,0)			
U_{11}		0.023(1)	0.0227(9)	
U_{33}		0.096(5)	0.080(2)	
$A_{saw,z}$			-0.052(1)	0.150Å

Figure 4.15 The modulated structure of Rb-IV. A) The structure in projection along the c-axis. B) Part of the structure, defined by the black rectangular box in A), in projection perpendicular to the c-axis. The modulation of the guest chains results in groupings of four and five guest atoms. C) Closeup of a section including a long guest-guest distance. Long guest-guest inter atomic distances develop where two host layers are intersected. Inter atomic distances between 3.0 and 3.2 Å are indicated by white cylinders ($c_g = 3.111(1)$Å).

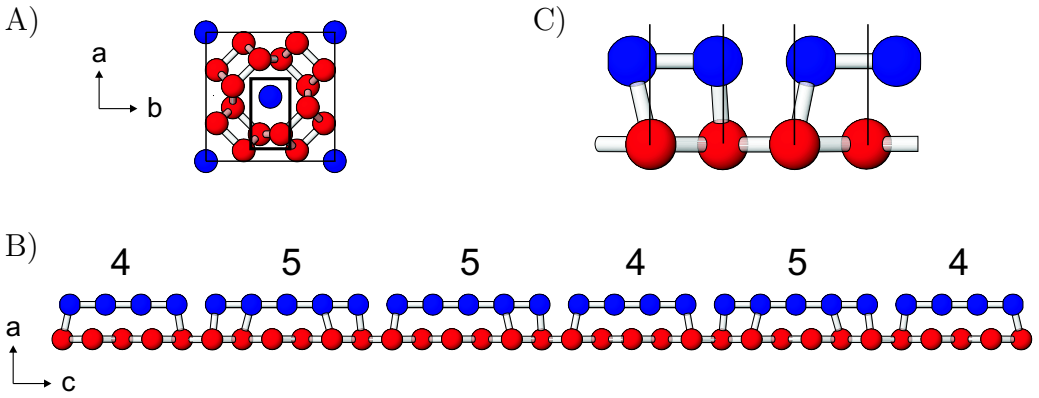

4.6 The sawtooth structure model

Having established the sawtooth model as the structure resulting in the best fit to the observed data, the next step is a detailed analysis of the structure which should lead to a better understanding of the mechanism causing the modulation.

4.6.1 Modulation of guest chains

A drawing of the refined structure immediately reveals groupings of guest atoms with short inter atomic distances which are separated by longer distances (Fig. 4.15). A direct consequence of the pure sawtooth modulation is that the long distances (3.366(4) Å) between groups are all the same and short distances (3.040(4) Å) within groups are all the same (Figure 4.16). These are significant variations from the inter atomic distance ($c_g = 3.111(1)$ Å) between guest atoms in the average structure.

With the establishment of the sawtooth shaped modulation function, the determination of the average number of atoms per group (N) is reduced to a purely

Table 4.9 Number of guest atoms per group, at commensurate values of c_g/c_h, assuming a sawtooth modulation of the guest chains. The guest structures at $c_g/c_h = 1$ and at $c_g/c_h = 0.5$ both have a simple undistorted body-centered arrangement of atoms.

c_h/c_g	c_g/c_h	N	short dist.	long dist.
1.000	1	1	$= c_g$	$= c_g$
1.333	3/4	2	$< c_g$	$> c_g$
1.500	4/6	3	$< c_g$	$> c_g$
1.600	5/8	4	$< c_g$	$> c_g$
1.666	6/10	5	$< c_g$	$> c_g$
1.714	7/12	6	$< c_g$	$> c_g$
⋮	⋮	⋮	⋮	⋮
2.000	1/2	∞=1	$= c_g$	$= c_g$

geometric problem, and the following equations can be deduced from Figure 4.16.

$$\text{In general} \quad N = \frac{0.5}{c_g/c_h \bmod 0.5} \quad \text{or} \quad N = \frac{0.5}{c_g/c_h - 0.5} \quad \text{for} \quad c_g/c_h \in (0.5, 1)$$

It is also clear from Figure 4.16 that N has to be achieved by a combination of groups containing four or five atoms only: $N = a4 + b5$. With $c_g/c_h = 0.608$ it follows that $N = 4.63$ and that 63% of the groups have five atoms and 37% of the groups have four atoms. Integer values of N are found at commensurate values of c_g/c_h (See table 4.9), and in these cases chains will only consist of groups with N atoms in each.

4.6.2 Modulation of host structure

The largest displacement of the host atom Rb1 away from its average position (0.4166,0.2921,0.000) is observed at the phase shifts t=0 and t=0.5 (Figure 4.17). From Figure 4.18 and Figure 4.19 it is clear that these phase shifts corresponds to the situation where Rb1 have the shortest and the longest atomic distances respectively to the nearest guest atom in the average structure.

Three dimensional structures are usually visualized by a simple drawing of the unit cell content, whereas it is much more difficult to visualize the four dimen-

Figure 4.16 A) The positions of the guest atoms along the chain are given by the intersections between the horizontal real-space with the sawtooth shaped modulation in superspace. At t=0.00 the guest atom at position $(0.5, 0, 1)$ is part of a five atom group and at t=-0.01 (equivalent to t=0.99) it is part of a four atom group. B) Close up of the area marked with dotted lines, showing the geometry in details. C) is showing the distances from the guest atom Rb2 $(0.5, 0, 0)$ to its nearest neighbor guest atoms at average positions $(0.5, 0, \bar{1})$ and $(0.5, 0, 1)$. The pure sawtooth modulation of the guest chains, leads to two nearest neighbor distances within the chains; one shorter (S) and one longer (L) than c_g. The short distances are found within groups of guest atoms, and the long distances separate them.

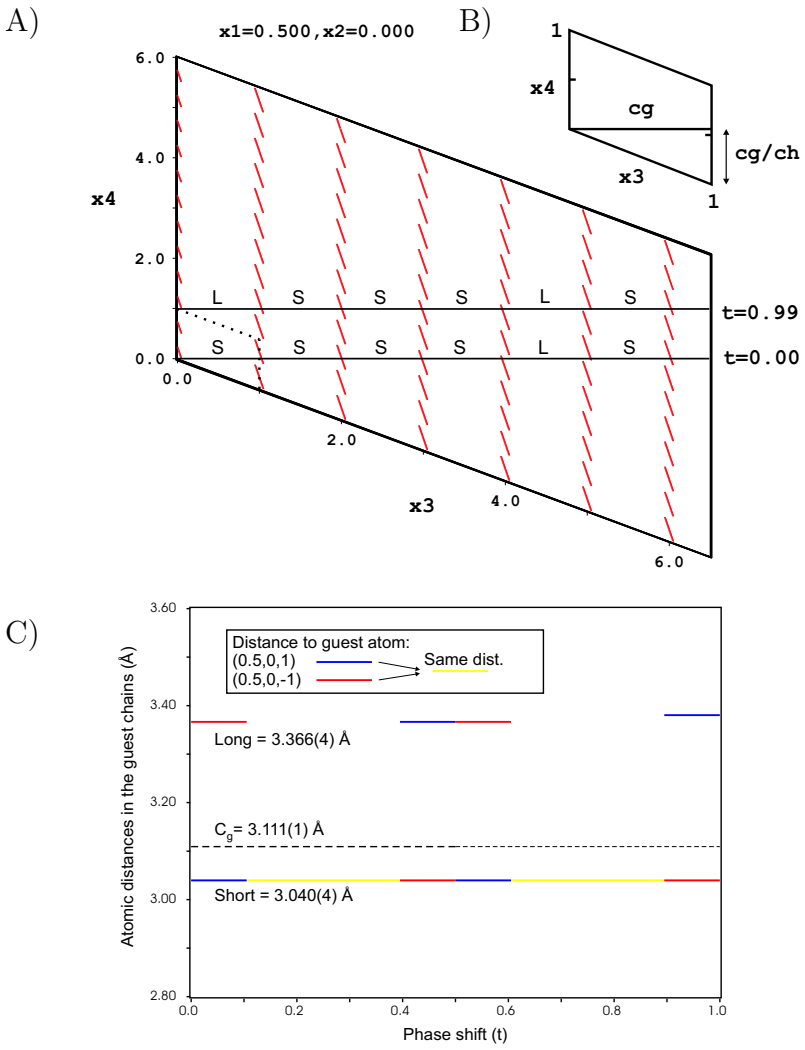

Figure 4.17 Displacements of the host atom Rb1 away from its average position (0.4166,0.2922,0) as function of the phase shift t. Displacements in the crystallographic a, b and c directions are shown with black, blue and green lines respectively.

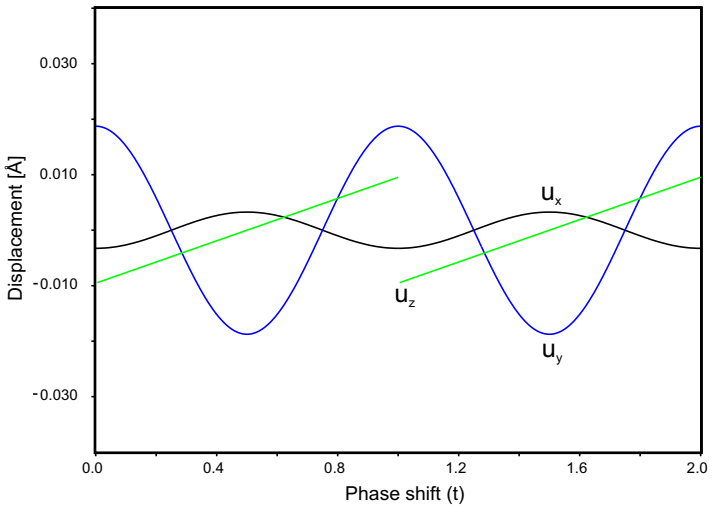

Figure 4.18 Displacements of host atoms (red) in the z=0 plane at t=0. The arrows indicate the direction of displacement, but the amplitude has been multiplied by a factor 30 for clarity. The modulation is shown relative to the average guest structure, so blue circles indicate guest chains with an atom in the a-b plane and white circles indicate guest chains that are shifted by $\frac{1}{2}c_g$ relative to the blue guest chains, in accordance with the body-centering of the guest structure.

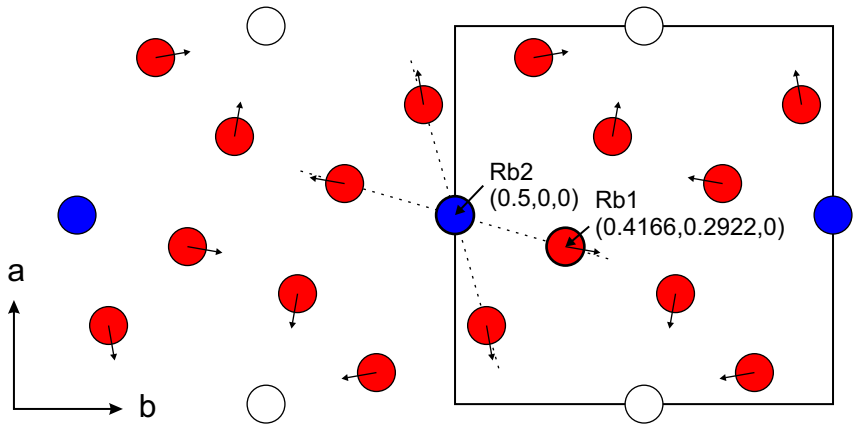

sional unit cell of an incommensurate structure. In principle an infinite number of 3D sections are needed for full structural characterization, which is equivalent to showing the continuous changes of the content of the basic unit cell as a function of the phase shift $t \in (0, 1)$. An animation of the basic unit cell, using the phase shift as a time parameter, is therefore a very effective way of visualizing the full structural details of an incommensurate structure.

If choosing the host structure as the reference structure, a phase shift corresponds to a sliding of the guest lattice relative to the host along the c-direction. An animation showing the displacement of the host atoms in the $z = 0$ layer (see Figure 4.18) as the guest chains are sliding along the c-axis has been prepared[2]. This animation shows how host and guest atoms are displaced as guest atoms are pushed trough the host structure, but it does not show the formation of groups along the guest chains because only one host layer has been included.

4.7 Interpretation of the modulated structure

It follows from the sawtooth modulation of the guest chains that guest atoms are never found in the plane defined by host layers. In fact, the guest atoms never come closer than 0.15 Å to the layers. One interpretation could be that the guest atom is being pushed away by the host atoms when it gets to close. This simple interpretation makes sense, also when the modulation of the host structure is considered. It is clear from Figure 4.18, and from the animation, that the host atoms are being displaced radially *away* from the axis of guest chains when guest atoms are approaching the host layers, and they are displaced radially *towards* the guest chains when guest atoms are moving away from the layers. One of the consequences is that the shortest host-guest atomic distance is longer in the modulated structure compared to that of the average structure (Figure 4.19).

The atomic displacements correspond pushing a too large ball through the hole of a torus shaped balloon. Force has to be added until the balloon expands radially and the ball jumps through. Even the modulation of the host structure in the direction of the c-axis is consistent with this simple interpretation, because the sign of the sawtooth modulation of the host structure is such that the host atoms

[2]The animation can be obtained by download from http://www.ph.ed.ac.uk/∼s0349214/share/ or by emailing the author

Figure 4.19 Bond distances from the host atom Rb1 to the nearest guest atoms as a function of the phase t. Red, black and blue lines correspond to distances to the guest atoms at the average positions $(0.5, 0, \bar{1})$, (0.5,0,0) and (0.5,0,1) respectively. Full lines and dashed lines correspond to bond distances in the modulated and the average structure model respectively.

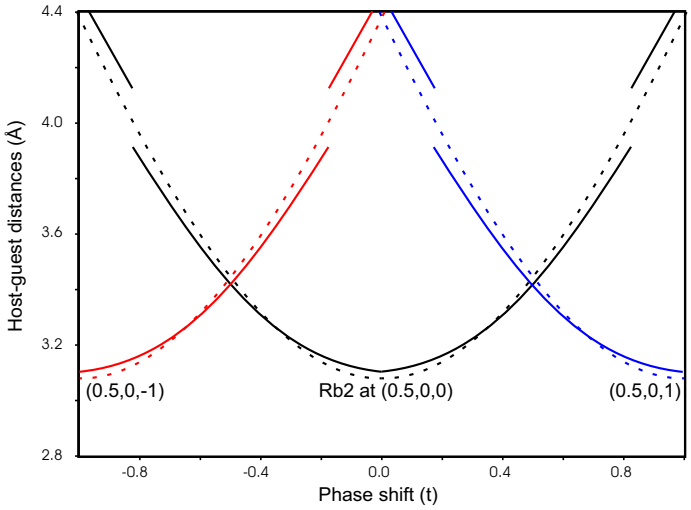

jumps in the opposite direction as a reaction to guest atom jumping through the layer. The amplitude of the host sawtooth modulation is much smaller (0.01 Å) compared to that of the guest chains (0.15 Å), because the host forms a rigid framework structure. The conclusion is that the modulation happens as a result of a bottleneck effect at the position where guest chains intersect host layers, and the strongest host-guest interaction is a repulsive force when they get too close.

The situation where guest atoms have to cross layers of host atoms is in principle identical in all other elemental host-guest structures. The simple bottleneck effect causing the modulation in Rb-IV is therefore proposed for all other host-guest structures. The average number of guest atoms per group can then be calculated from published c_h/c_g values: $N = 4.04$ for K-III ($c_h/c_g = 1.603$), $N = 1.89$ for Bi-III ($c_h/c_g = 1.309$), $N = 1.90$ for Sb-II ($c_h/c_g = 1.310$), $N = 1.88$ for As-III ($c_h/c_g = 1.305$),$N = 2.27$ for Ba-IVa ($c_h/c_g = 1.388$) and $N = 2.36$ for Sr-V ($c_h/c_g = 1.404$) (McMahon & Nelmes 2004*b*, McMahon et al. 2006b).

4.8 Conclusion

New techniques in growing single-crystals of Rb-IV have lead to the observation of satellite reflections for the first time. New experimental developments, taking advantages of the high energy and fine focused X-ray beam available at third generation synchrotron facilities, and new data reduction techniques, have made it possible to extract reliable intensities of these extremely weak reflections. The result is the full modulated structure refinement of Rb-IV giving new insight on the host-guest interactions.

The single-crystal technical developments alone are quite exciting. The experimental setup used in this study for collecting satellite intensities results in an optimal ratio between sample and background scattering. This means that weakly scattering samples that could not previously be studied using standard high-pressure single-crystal diffraction techniques (because of the high background scattering shown in Figure 4.1), can now be studied using the new techniques. Examples of new opportunities are single-crystal diffraction studies of the high-pressure phases of solid hydrogen, or the study of single-crystals of sodium above 100 GPa (It was shown recently that single crystals of two high pressure phases of sodium could be grown above 100 GPa (Gregoryanz et al. 2005)).

Further more the existence of high-quality single-crystals of Rb-IV also opens the exciting possibility of conducting the first ever study of the dynamics in an incommensurate element at high pressure. This will be the topic of the next chapter.

Chapter 5

Inelastic studies of Rb-IV

Inelastic x-ray scattering (IXS) was pioneered at HASYLAB in the early 80's, and today IXS with meV energy resolution has become an important tool in the investigation of dynamical properties in a wide range of materials including liquids, amorphous materials, powders and single crystals. IXS is complementary to the well established neutron inelastic scattering (INS) technique because these two techniques cover different regions in energy-momentum transfer space, but IXS has a very important advantage over INS techniques when studying materials under high pressure. The small beam size and divergence on third generation synchrotron sources makes it possible to study materials with sample volumes as small as 10^{-5}mm^3. This makes IXS ideal suited for studying materials loaded into daimond anvill cells, and phonon dispersion curves has been determined above 100 GPa (Krisch 2003).

In this chapter the lattice dynamics in incommensurate composite Rb-IV will be investigated by IXS. The focus will be on the longitudinal acoustic (LA) excitations along the direction of the incommensurate wavevector (parallel to the guest-atom chains), which calculations (Radulescu et al. 2002, Currat et al. 2002, Axe & Bak 1982, Finger & Rice 1982, Finger & Rice 1983, Theodorou & Rice 1978) predict to reflect the incommensurability most clearly. These model calculations were all made in the context of more complex incommensurate composite systems such as $Hg_{3-\delta}AsF_6$ (Hastings et al. 1977, Heilmann et al. 1979). The 1D, monoatomic nature of the elemental host-guest structures offers the possibility of studying the lattice dynamics in a much simpler composite system.

Figure 5.1 The monoatomic linear chain model. A) A finite number of atoms with mass m are connected by perfect springs with spring constant K. The equilibrium inter atomic distance is c, and the equilibrium position of atom number n is therefore nc. B) Atomic displacements, described by equation 5.1, at $Q = 0$ and $Q = 2\pi/c$ at $t = 0$. Crosses indicate equilibrium positions. C) The corresponding displacement waves $u(nc)$ for $Q = 0$ (red line) and $Q = 2\pi/c$ (black line). D) Atomic displacements at $Q = \pi/c$ and $Q = 3\pi/c$ at $t = 0$ E) The corresponding displacement waves $u(nc)$ for $Q = \pi/c$ (red line) and $Q = 3\pi/c$ (black line).

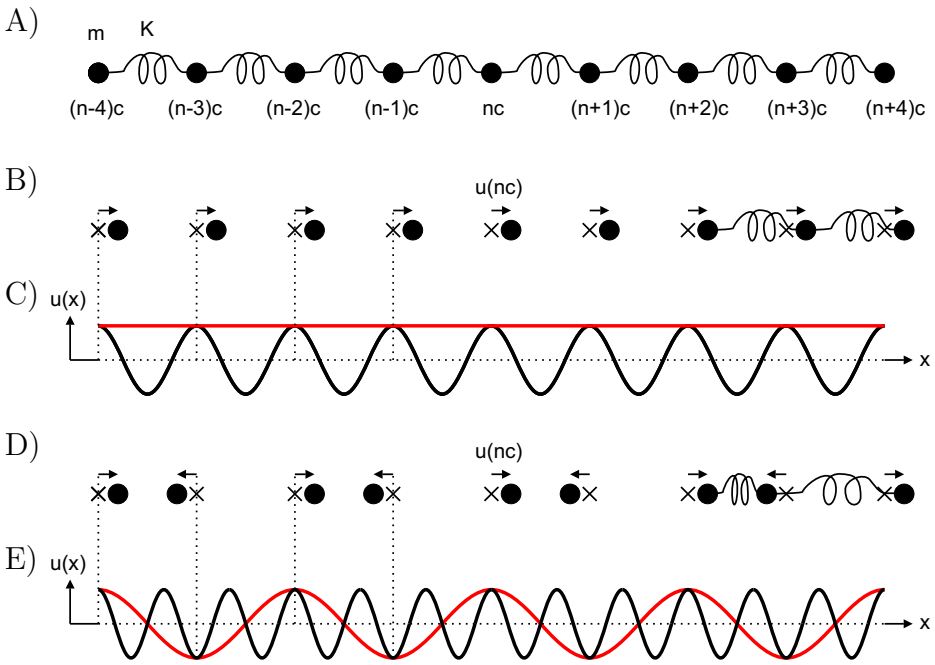

5.1 The monoatomic linear chain model

To introduce logitudinal acoustic phonons and the properties of the related dispersion curve, it is usefull to consider the monoatomic linear chain model. This is a purely classical system, with only nearest neighbor interactions modeled by a perfect spring with spring constant K (Figure 5.1). The equation of motion, for a chain with a finite number of atoms where the first and the last atom of the chain has been constrained to move as if they were connected by a spring with spring constant K, has the harmonic wave solution:

$$u(nc, t) \propto \sin(Qnc - \omega t) \tag{5.1}$$

where $u(nc, t)$ is the displacement of atom number n at position nc as a function of time, and where the harmonic angular frequency ω is a function of the wave number Q described by the dispersion curve:

$$\omega(Q) = 2\omega_0 |\sin(Qc/2)| \tag{5.2}$$

shown in figure 5.2 (Ashcroft & Mermin 1976).

The translation and inversion symmetry of the dispersion curve can be understood from the following considerations. The angular frequency only depends on the elastic properties of the crystal and the wavelength ($\lambda = 2\pi/Q$) of the displacement wave traveling through the crystal. At time $t = 0$ the displacement of atom n is identical for wave numbers Q and $Q + 2\pi/c$ or any integer multiples of $2\pi/c$ added to Q (according to equation 5.1), and the system is therefore identical at these wave numbers (Figure 5.1C and E). The angular frequency must be identical for identical systems, and consequently the angular frequency ω(Q) is periodic with the periodicity $2\pi/c$. It follows that the atomic displacements will be identical, independent of the time, for Q and $Q + 2\pi/c$. This means that solutions with wave numbers above π/c are just alternative mathematical descriptions of a system that can equally well be described using a wave number in the interval $Q \in (-\pi/c, \pi/c)$. The inversion symmetry is a result of the fact, that two wave numbers with opposite signs correspond to two identical waves traveling in opposite directions along the atomic chain. As a result of these symmetries the dispersion curve is fully described in the interval $Q \in (0, \pi/c)$.

It is instructive to consider the properties of the dispersion curve at the long wavelength limit ($Q \approx 0$) and the short wavelength limit ($Q - \pi/c \approx 0$). As a result of the sine-shaped dispersion curve, the angular frequency becomes linear dependent on the wavenumber for very long wavelengths ($Q \approx 0$):

$$\omega(Q) \approx c\omega_0 Q \tag{5.3}$$

and for wavelengths close to $Q = \pi/c$ the angular frequency is independent of the wave number:

$$\omega(Q) \approx 2\omega_0 \tag{5.4}$$

The infinite wavelength ($Q = 0$) corresponds to a harmonic displacement of the whole chain (Fig. 5.1B), and $Q = \pi/c$ corresponds to a standing wave where

Figure 5.2 Phonon dispersion curve for a monoatomic linear chain (solid line) with a inter atomic distance c and only nearest neighbor interactions. Note that the dispersion curve has translation symmetry $\omega(Q) = \omega(Q+2\pi/c)$ and inversion symmetry $\omega(Q) = \omega(-Q)$. The phonon dispersion curve along the unique c-axis of a body-centered tetragonal lattice structure is shown with the dashed line. The body-centered lattice leads to a periodicity that is two times the periodicity of the primitive lattice (See section 5.2)

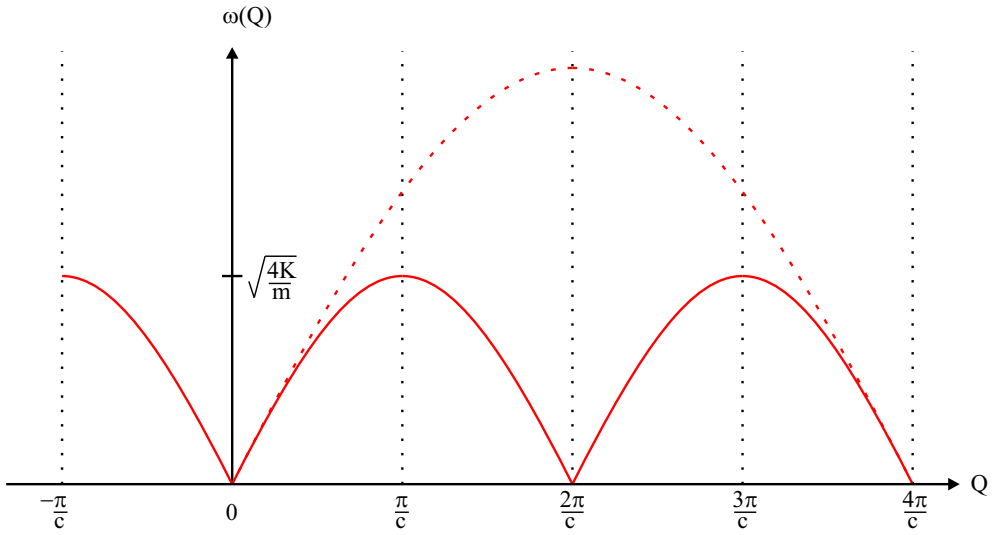

neighboring atoms are oscillating in anti-phase (Fig. 5.1D). In this situation, an atom displaced by $u(nc)$ will have a force equal to $F = -4Ku(nc)$ acting on it, with the angular frequency:

$$\omega = 2\sqrt{\frac{K}{m}} \quad \Rightarrow \quad \omega_0 = \sqrt{\frac{K}{m}}$$

showing that ω_0 in equation 5.3 and 5.4 is the angular frequency of a simple harmonic oscillator with mass m and spring constant K.

Speed of sound

Equation 5.1 describe waves propagating along the chain with phase velocity $v_p = \omega/Q$, and group velocity $v_g = d\omega/dQ$. The group velocity at the long wavelength limit is the speed of sound (Ashcroft & Mermin 1976). The group velocity of a wave in the short wavelength limit of the linear chain model is

therefore $v_g = 0$, consistent with the conclusion made earlier that the short wavelength limit corresponds to a standing wave. The velocity of a sound wave v_s traveling along the chain direction is:

$$v_s = c\sqrt{\frac{K}{m}} \tag{5.5}$$

showing that the speed of sound is independent of frequency. This is true only because sound waves have frequencies in the Hz to MHz range, and these frequencies all belong to the long wavelength limit for any natural material.

5.2 Dispersion curve for three dimensional lattice

The simplest example of a three dimensional extended solid is the case where atom positions define a simple primitive orthogonal lattice. In this case the dispersion curve of longitudinal acoustical phonon in the three main crystallographic directions(a, b and c) will be identical to that of the momoatomic linear chain, where the interatomic distance in the phonon propagation direction is given by the a, b and c lattice parameters respectively (Ashcroft & Mermin 1976).

The body-centered lattice structure has a different dispersion curve from that of the primitive lattice. This can be realized when considering that the deformation wave ($Q = 2\pi/c$) in the primitive lattice will produce atomic displacements equivalent to that found in the long wavelength limit, but i case of the body-centered lattice it will produce a standing wave where primitive and body-centered atoms will oscillate in anti-phase (Figure 5.3). Only the deformation wave with half the wavelength ($Q = 4\pi/c$) will in case of the body-centered lattice produce atomic displacements equivalent to that found in the long wavelength limit.

This can be generalized to the situation where atom positions are not coinciding with lattice nodes. The analytical solution to the equation of motion for a harmonic solid with a body centered lattice and one atom in the primitive unit cell results in the LA phonon dispersion curve:

$$\omega(Q) = 2\omega_0 |\sin(Qc/4)| \tag{5.6}$$

Figure 5.3 Atomic displacements in a body-centered lattice structure. Black circles represent atoms defining a primitive lattice and red circles represent atoms in the body-centered position relative to the primitive lattice. Atomic displacements in the body-centered lattice by the deformation wave $Q = 2\pi/c$ in A) and $Q = 4\pi/c$ in B).

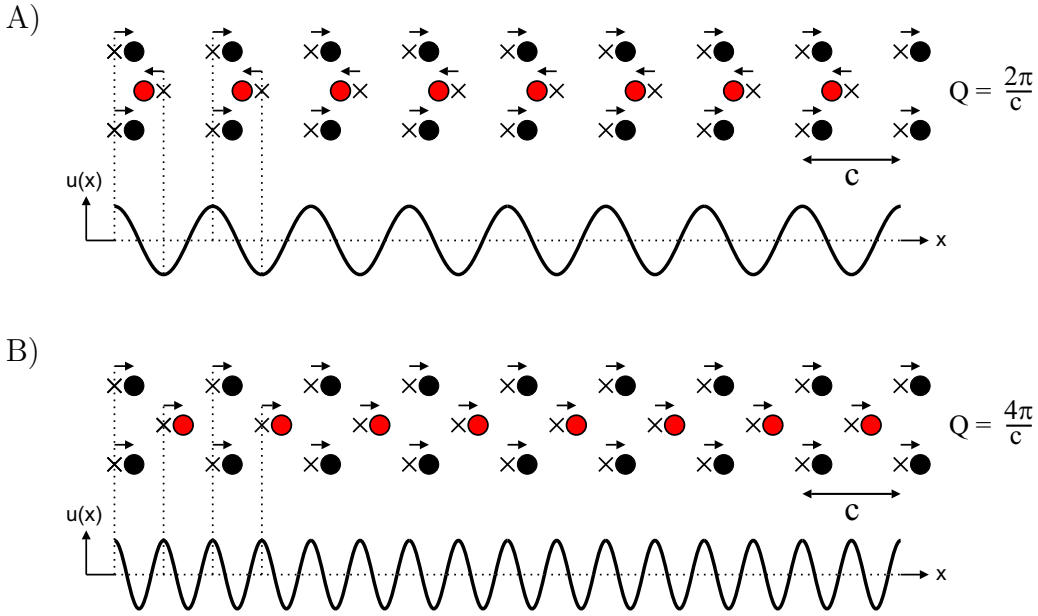

where c is the lattice parameter of the crystallographic main direction of interest. The dispersion curve has got the same shape as in the case of the primitive lattice, with the only difference that the periodicity is twice as large (shown as the dotted line in figure 5.2). In general the dispersion curve will be periodic with the periodicity equal to the width of the first Brillouin zone in the direction of interest (Fig. 5.4)(Ashcroft & Mermin 1976).

5.3 Photon - phonon interactions

In this study phonons are probed by the use of X-rays. Consider a photon of momentum $\boldsymbol{p}_1 = \hbar\boldsymbol{k}_1$ and energy $E_1 = \hbar\omega_1 = \hbar 2\pi c/\lambda_1$ that is incident on the crystal. The photon will interact with electrons in the crystal and emerge with the momentum $\boldsymbol{p}_2 = \hbar\boldsymbol{k}_2$ and energy $E_2 = \hbar\omega_2 = \hbar 2\pi c/\lambda_2$, where c is the speed of light and $\boldsymbol{k}_1$ and $\boldsymbol{k}_2$ are the wave vectors for the incoming and the scattered

Figure 5.4 First Brillouin zone, defined in reciprocal space as the volume enclosed by the surfaces at the same distance from the origin of the lattice and its neighboring lattice points, of a primitive A) and a body-centered B) tetragonal direct lattice. Only the intersection of Brillouin zone with the h0l layer is shown here.

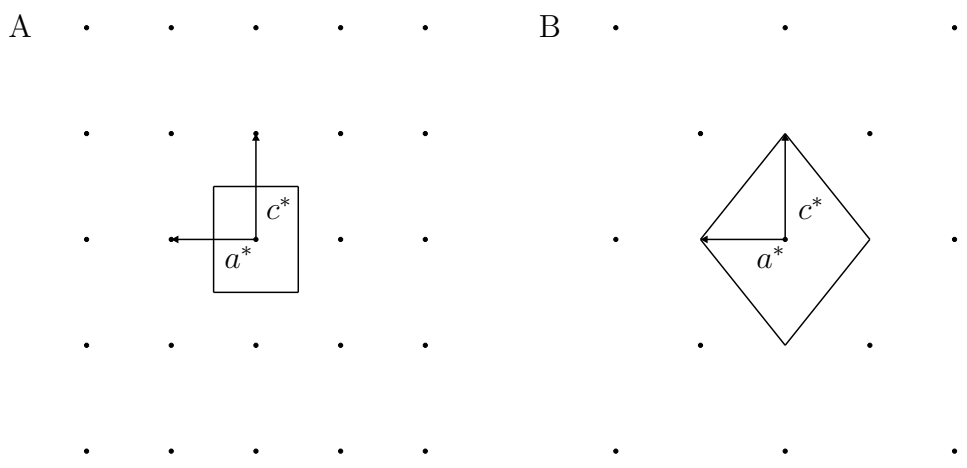

beam.

Conservation of energy

The phonon dispersion curves were discussed in the previous section based a classical mechanical system, even though a phonon is defined as the quantum of a lattice vibration, with energy $E = \hbar\omega(\boldsymbol{Q})$. The energy conservation law for creation of a phonon is therefore:

$$E_1 = E_2 + \hbar\omega(\boldsymbol{Q}) \tag{5.7}$$

where E_1 and E_2 is the energy of the incident and the scattered X-ray photons respectively. The plus sign is exchanged with a minus sign in the case where a phonon is annihilated by a photon. The phonon angular frequency, as a function of the incident and the scattered beam wavelength, is given by:

$$\omega(\boldsymbol{Q}) = 2\pi\, c \left(\frac{1}{\lambda_1} - \frac{1}{\lambda_2}\right) \tag{5.8}$$

where c is the speed of light.

Figure 5.5 Inelastic scattering experiment setup. A) Schematic drawing showing the main components of an inelastic experimental setup. B) Both monochromator and analyzer are setup in the backscattering geometry using a perfect silicon single crystal aligned on the (111) face.

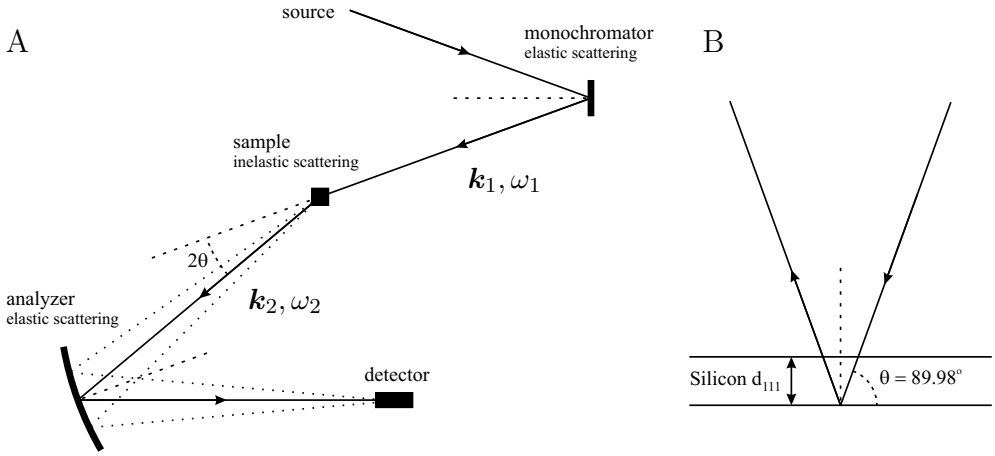

Conservation of crystal momentum

It is a general result of quantum theory that symmetry of the Hamiltonian describing a system will lead to a conservation law (Ashcroft & Mermin 1976). The Hamiltonian of a crystal interacting with a photon possesses a symmetry, closely related to the translation symmetry of the crystal lattice, that leads to the conservation law known as the conservation of crystal momentum:

$$\boldsymbol{p}_1 = \boldsymbol{p}_2 + \hbar \boldsymbol{Q}$$

i.e. the momentum of the incoming phonon, must the sum of the momentum of the scattered phonon and the crystal momentum of the phonon that has been created. Also in this case is the plus sign exchanged with a minus sign when a phonon is annihilated by a photon. The crystal momentum law can then be used to represent the phonon wave vector $\boldsymbol{Q}$ in terms of the wavelength and direction of the incident and scattered photons:

$$\boldsymbol{Q} = \boldsymbol{k}_1 - \boldsymbol{k}_2 = 2\pi \left(\frac{\boldsymbol{s}_1}{\lambda_1} - \frac{\boldsymbol{s}_2}{\lambda_2} \right) \tag{5.9}$$

5.4 Experimental details

The inelastic X-ray scattering experiment was performed on beam line ID28 at the ESRF, Grenoble. See Figure 5.5 for presentation of the experimental setup. The incident radiation was monochromatized at a photon energy of 17.794 keV corresponding to the wavelenght $\lambda = 0.6968$ Å using the (999) reflection of a Si monochromator. Two grazing-incidence mirrors focused the X-rays onto the sample with a focal size of 25 x 60 μm^2 . The spectrum of the scattered radiation was analyzed by a high-resolution spherical crystal (Si) analyzer resulting in an overall energy resolution of 3 meV (Figure 5.6). The momentum resolution was set to 0.03 $Å^{-1}$ by placing slits in front of the analyzer crystals (Figure 5.7), and the IXS spectra were collected in the energy-scanning mode. A detailed account of the IXS setup has been given elsewhere (Krisch 2003).

The energy scans are performed by varying the monochromator temperature (with sub-mK precession) while the temperature of the analyzer and all diffractometer setting angles are kept fixed (Figure 5.6). Because of the thermal expansion of silicon the monochromator crystal will have slightly different lattice parameters relative to the analyzer, and consequently the wavelength of the monochromated beam (λ_1) will be slightly different from that of the analyzed beam (λ_2). The energy for a given wavelength difference is given by Equation 5.7 and 5.8.

Constant Q scans

Not only the energy, but also the crystal momentum $\hbar\boldsymbol{Q}$ will change as a function of the incident beam wavelength (See equation 5.9). Consider now an experimental setup with an very small opening of the slits. In this case the directions of the incident beam $\boldsymbol{s}_1$ and the scattered beam $\boldsymbol{s}_2$ and the wavelength λ_2 of the analyzed beam are well know and constant during a scan. Only the wavelength of the incident beam is varying during a scan. According to equation 5.9 the resulting variation in the momentum transfer is given by:

$$\delta\boldsymbol{Q} = \boldsymbol{Q}_{T_1} - \boldsymbol{Q}_{T_2} = 2\pi\left(\frac{1}{\lambda_{1T_1}} - \frac{1}{\lambda_{1T_2}}\right) \tag{5.10}$$

$$\sim 2\pi\left(\frac{\delta\lambda_1}{{\lambda_1}^2}\right) \quad \text{when} \quad \delta\lambda_1 \ll \lambda_1 \tag{5.11}$$

Figure 5.6 A) Energy profile of the analyzed beam (full line) and after the monochromated beam (dashed line). The analyzer and monochromator crystals have the temperatures T and $T + \Delta T$ respectively. B) The discrete energy levels of the elastically scattered photons (center line) and photons that have created or annihilated a phonon in the scattering process. C) The scattered beam is a convolution of the energy profile of the incident beam with the discrete energy levels involved in the scattering process. D) Data are collected by counting the number of photons hitting the detector in a given time interval at a fixed monochromator temperature. This is repeated at a number of increasing monochromator temperatures, enough to cover the energy range of interest and in steps fine enough to resolve the shape of the energy profile (black squares represent a fictive data set). The energy profile observed at the detector is the convolution of the energy profiles of the scattered beam and the analyzed beam.

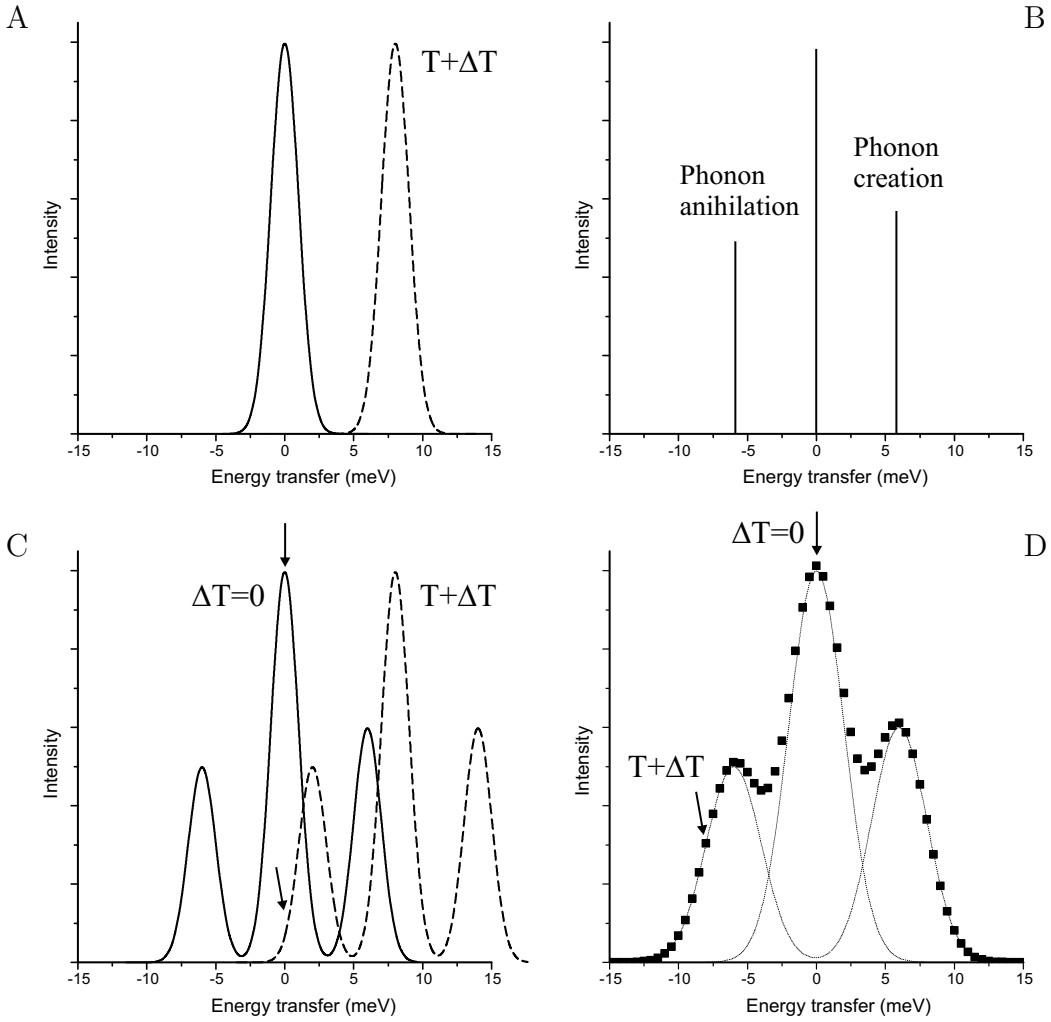

Figure 5.7 Momentum resolution of the experimental setup. The energy profiles of the monochromated, the scattered and the analyzed sections of the beam path is shown. Each of the three shown scattered beams will contain elastic and inelastic scattering corresponding to the three shown wave vectors. By adjusting the opening width of the slits in front of the analyzer crystal, the experimental momentum transfer resolution $\hbar\Delta\boldsymbol{Q}$ is chosen. Slit position 1 correspond to a high momentum transfer resolution but long data acquisition times, because only a few photons is passing through the slits. Slit position 2 correspond to lover resolution and faster data aqusition.

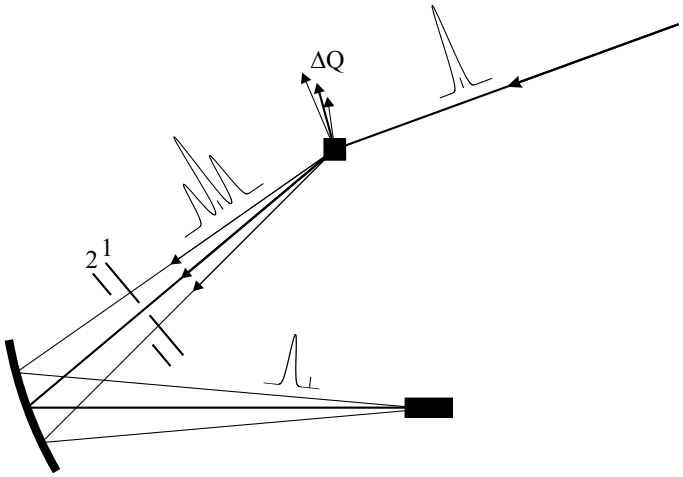

See also figure 5.8.

A typical ±20 meV energy scan corresponds to a incident wavelength variation $\delta\lambda_1$ of approximately $\pm 10^{-6}$ Å. According to equation 5.10 this will result in a wave vector variation of $\delta\boldsymbol{Q} \sim 10^{-5}$ Å^{-1} which is farbelow the instrumental resolution, so the energy scans can therefore be considered as constant Q scans. This is equivalent to saying that the scattering geometry of the inelastic experiment is identical to elastic scattering geometry (for $\lambda = 0.6968$ Å) within experimental resolution (Figure 5.8).

Elastic scattering geometry

Because the momentum transfer Q, within instrument resolution, is independent of the wavelength changes, it can simply be described as a linear combination of

Figure 5.8 Geometry of an inelastic energy scan performed by varying the monochromator temperature. The wavelength change and consequently $\delta\boldsymbol{Q}$ have been exaggerated in this schematic drawing.

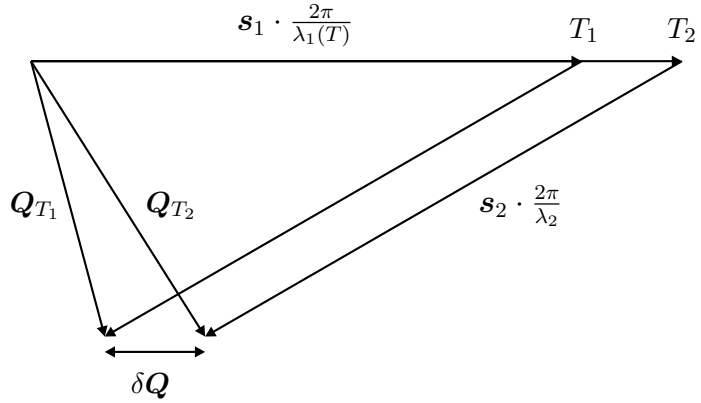

the reciprocal lattice vectors of the single crystal being studied:

$$\boldsymbol{Q} = h\boldsymbol{a}^* + k\boldsymbol{b}^* + l\boldsymbol{c}^* \tag{5.12}$$

where h,k and l are real numbers. For diffraction the Laue conditions has to be satisfied resulting in integer h,k and l values. For general elastic scattering the Laue conditions does not have to be satisfied and consequently h,k and l can be any real number.

As mentioned in the introduction to this section, we will in this study concentrate on the phonon dispersion behavior along the crystallographic c axis of Rb-IV, and because it has tetragonal symmetry the above equation can be formulated as:

$$Q = lc^* = \frac{2\pi}{c}l \tag{5.13}$$

when using the definition of reciprocal space used in most solid state physics books:

$$\boldsymbol{a}_i \cdot \boldsymbol{a}_j^* = 2\pi\,\delta_{ij} \quad \text{where} \quad i,j = 1,2,3$$

This definition scales reciprocal space by a factor 2π relative to the reciprocal space used in crystallographic literature (See section 2.2.1). Equation 5.13 is the conversion between reciprocal space units and the momentum transfer. For setting up the experiment and data collection it is much more convenient to to

think in terms of reciprocal space units instead of momentum transfer, because it makes it straight forward to determine the position relative to the first Brillouin zone. In the rest of this chapter the momentum transfer will mainly be expressed in reciprocal space units.

For elastic scattering the norm of the momentum transfer vector Q, can be also expressed as a function of the scattering angle:

$$Q = \frac{4\pi}{\lambda} \sin\theta \tag{5.14}$$

which is a general case of the Bragg equation. From this it follows that the momentum transfer is uniquely determined by the scattering angle.

The elastic scattering geometry makes setting up the experiment very simple, once an orientation matrix has been determined for the single crystal sample. First a point in reciprocal space is chosen for the experiment. The momentum transfer for that point is then calculated using Equation 5.13, and from that the position of the analyzer arm is calculated using Equation 5.14. By rotating the sample crystal, the momentum transfer vector $\boldsymbol{Q}$ is placed in the the bisecting position between the incident beam direction and the direction of the analyzer arm. This completes the experimental setup, and an energy scan is performed. This is repeated for all points in reciprocal that are being measured.

5.5 Results and discussion

One Rb-IV crystal was investigated at a pressure of 18.4 GPa, while a second was studied at 17.3, 17.0, and 16.3 GPa. As discussed in the introduction of this chapter the focus will be on the LA excitations along the chain direction of Rb-IV, which in practice means that inelastic spectra with momentum transfer vectors Q parallel to the crystal c axis are collected (Figure 5.9).

Figure 5.10 shows selected IXS spectra recorded from Rb-IV at 17.3 GPa for three different momentum transfers Q. Despite the small size of the sample in the pressure cell (scattering volume $\approx 2 \cdot 10^{-5}$ mm^3), high-quality spectra were obtained in $\sim$90 mins. The spectra exhibit a clear Q-dependence, and comprise one or two inelastic features of varying energy and intensity in addition to the elastic line. Figure 5.10 also shows the decomposition of the measured

Figure 5.9 Reciprocal lattice of Rb-IV. Only main reflections from host and guest subsystems are shown here, and the reciprocal lattices of the two subsystems are indicated with dashed and dotted lines respectively. For this study inelastic scattering spectra were collected at positions between $(0\ 0\ 2.1)_h$ and $(0\ 0\ 3.54)_h$.

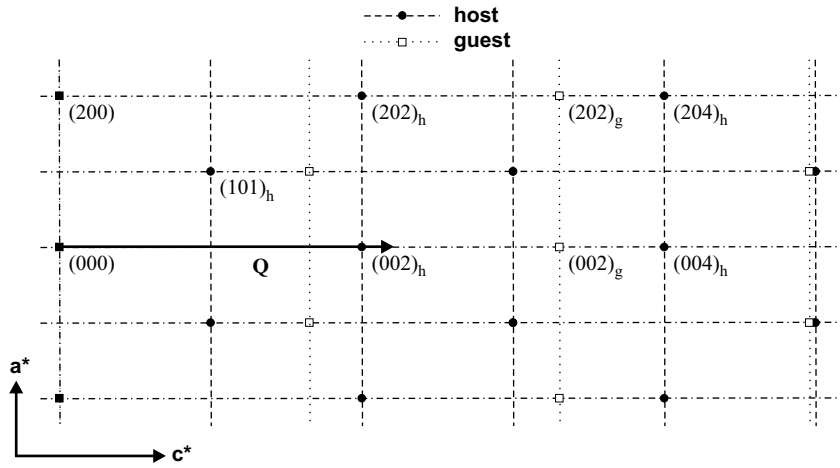

spectra into the elastic line, the excitation peaks, and a constant background that were obtained by least-squares fitting (*Computer program: FIT28* 2006). All contributions were modeled by Lorentzian profiles and the stokes/anti-stokes pairs were constrained to have the same peak width.

5.5.1 Phonon dispersion curves

The principal information resulting from the least squares fitting are the energies of the excitation peaks. When the energies of all the observed excitation peaks are plotted against the momentum transfer for all four pressures the plots in Figure 5.11 are obtained. The data points clearly defines two separate LA-type branches, both of which are very well described by the LA phonon dispersion curve derived for a simple harmonic solid with nearest neighbor interactions only:

$$\omega(Q) = 2\omega_0 |\sin(l\pi/2)| \tag{5.15}$$

(derived from Equations 5.6 and 5.13). The observed dispersion curves have the periodicities $2l_h$ (filled circles) and $2l_g$ (empty circles) and are therefore interpreted as LA-type phonon dispersion curves of the host and guest components respectively.

Figure 5.10 Inelastic X-ray scattering spectra of Rb-IV at 17.3 GPa ($T = 297K$). Spectra were recorded at different momentum transfers Q. l_h refers to the reciprocal lattice of the host, with a periodicity of c_h=5.1527 Å along the c direction. The circles indicate the measured intensities, the lines denote the fitted spectra and the contributing components. Note the different intensity scales for the three spectra. A slightly modified version of this figure were used in the publication Loa et al. 2007, see Appendix B.

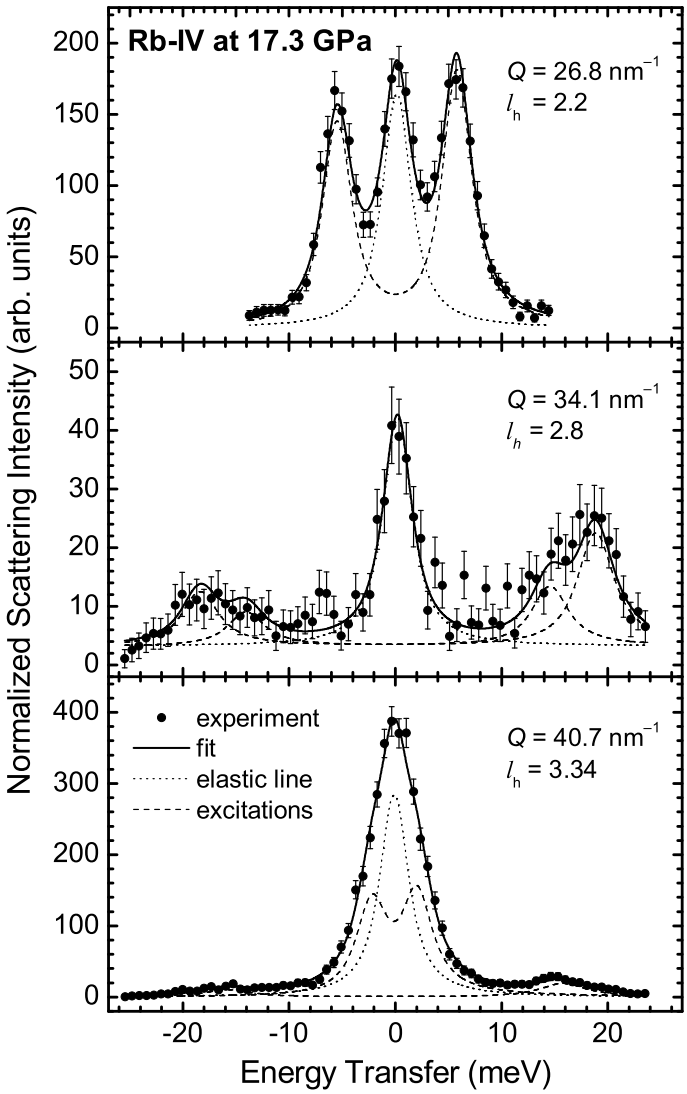

Figure 5.11 Dispersion relations of longitudinal lattice excitations in Rb-IV at all four collected pressures. The two branches are attributed to lattice excitations of the host (solid symbols) and the guest (open symbols), respectively. The lines indicate phonon dispersion relations of the type $\omega(l) = 2\omega_0|\sin(l\pi/2)|$ fitted to the data.

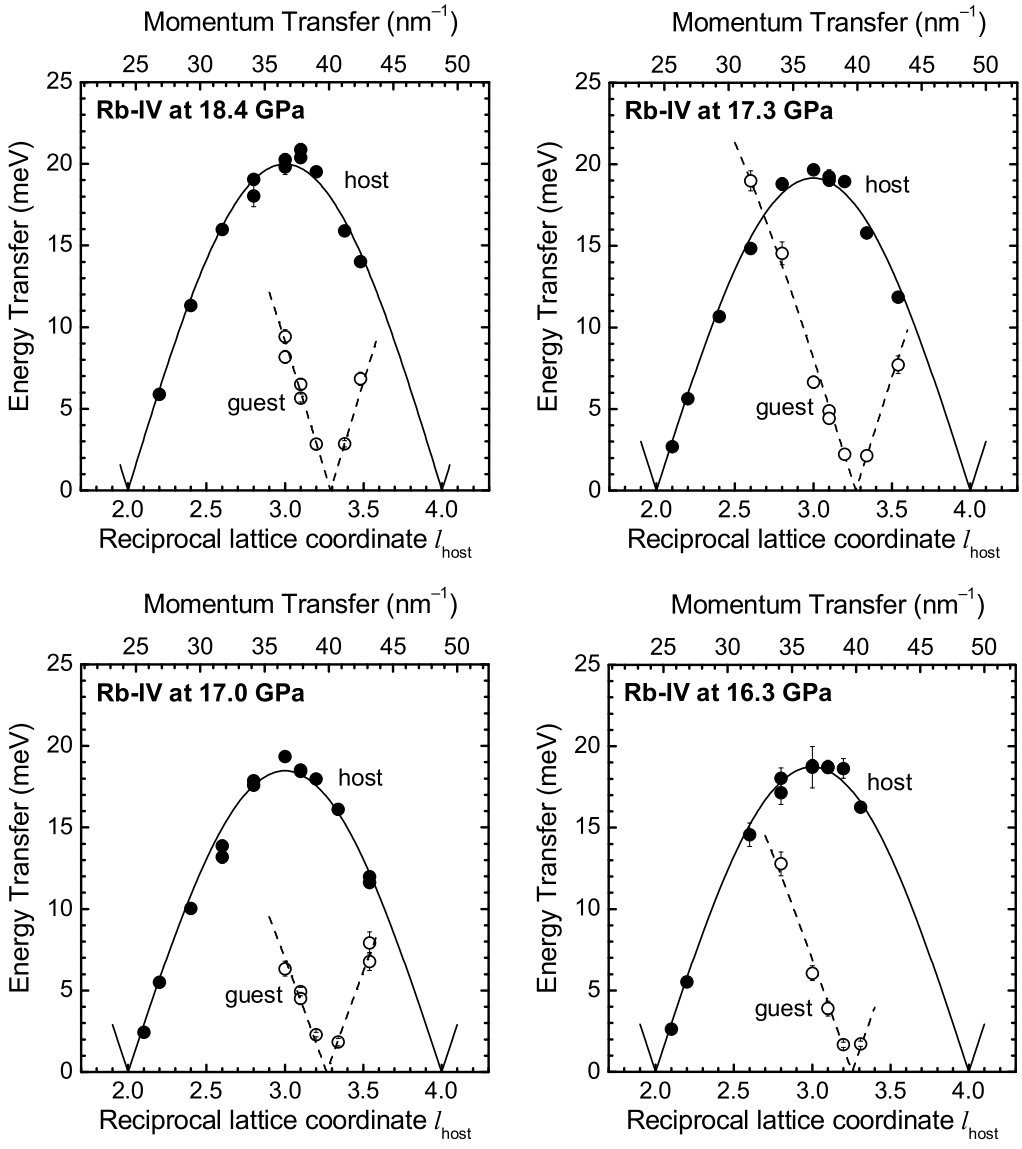

The lattice dynamics of incommensurate composite systems have been the topic of several theoretical studies, and it has been shown that the existence of two separate LA-type phonon dispersion curves in certain crystallographic directions is a unique property of these systems (Axe & Bak 1982, Finger & Rice 1982, Finger & Rice 1983, Theodorou & Rice 1978). But in the infinity wavelength limit these composite systems will only have a single LA mode corresponding to a translation of the entire crystal plus a phason mode corresponding to sliding of the two components in opposite directions along the chain direction (Finger & Rice 1982). In the case of $Hg_{3-\delta}AsF_6$, the crossover from the two separate LA-type dispersion curves observed at high energies to a single LA mode and a phason mode at low energies were estimated to occur at $\approx 10^{-5}$ meV (Finger & Rice 1982). There is no evidence of the crossover in the Rb-IV data, but this is expected since the energy resolution of the IXS instrument (3meV) is much higher than the expected crossover energy.

Other studies have shown that two separate LA-type dispersion curves only exists in the limiting case where the interactions between the two components are very weak, and that stronger interactions will lead to (pseudo-)gaps in the dispersion curves caused by an effect described as zone-folding (Radulescu et al. 2002, Luo et al. 1997, Brussaard et al. 2001).

A host-guest system of the Rb-IV type with no host-guest interactions along the chain direction would correspond to a situation where the two components can freely glide relative to each other in this direction. Each of the two components will be periodic along the chain direction and will therefore each have a well defined Brillouin Zone. Interactions between the two components along the chain direction will result in modulations of the two components as described in Chapter 4 and the two Brillouin Zones are therefore no longer well defined. The effect on the dispersion curves with increasing interaction strength is a gradual change from the two separate LA-type dispersion curves, to the intermediate case where the original dispersion curves are still recognizable but with energy gaps in the previous continuous dispersion curves, to the extreme case where strong interactions will force a lock in transition. In this case the upper parts of the original LA-type dispersion curves will have developed into optical phonon branches, and the lowest part will be the single LA phonon branch with a periodicity corresponding to the new super cell periodicity.

Figure 5.12 Pressure dependences of the sound velocities of the longitudinal acoustic excitations along the c directions of the host and the guest subsystem of Rb-IV. The solid lines represent linear regressions to the experimental data. The star and the dashed line indicate the estimated sound velocity and its pressure dependence in a monatomic linear chain of Rb. This figure was also used in the publication Loa et al. 2007, see Appendix B.

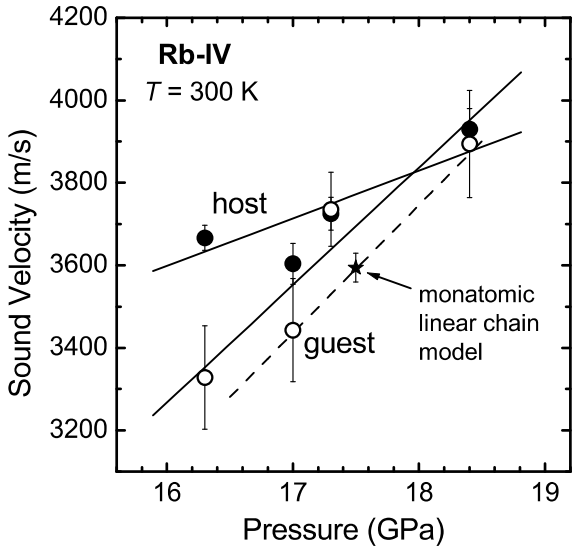

The Rb-IV data do not show any deviation from two ideal LA-type dispersion curves (Figure 5.11). It can therefore be concluded that the host-guest interaction, that was shown to exists in Chapter 4, is too weak to result in any detectable (pseudo-)gaps, and it raises the question if zone-folding effects is of any importance in any of the elemental composite phases.

5.5.2 Sound velocities

As discussed in Section 5.1 the sound velocity is the group velocity in the long wavelength limit:

$$v_s = \omega(Q)\frac{d}{dQ}\bigg|_{Q=0} = \frac{\omega_0 c}{2} = \frac{Ac}{4\hbar}$$

where A is the amplitude of the dispersion curves fitted to the energy transfer data shown i Figure 5.11. The resulting high frequency sound velocities (above the crossover) of the host and the guest, are shown in Figure 5.12. There is

no clear evidence of a discontinuous change in the sound velocity of the guest component at the order-disorder transition pressure (16.7 GPa) and a line has been fitted to these data over the studied pressure range (16 GPa - 19 GPa). The host sound velocity data could support an interpretation where the velocity shift to lower values at the order-disorder transition on pressure increase and above the transition the velocities would be almost identical to those observed in the guest component. But this interpretation is not consistent with the X-ray diffraction data, where detailed investigations using powder and single-crystal techniques never have resulted in any evidence of structural changes in the host component at the order-disorder transition. It it therefore unlikely that the sound velocity of the host would change discontinuously at this pressure and a line has therefore also been fitted to these data over the studied pressure range (Figure 5.12).

By interpolation the host and guest velocities are found to be equal at a pressure of 18 GPa, $v_h = v_g = 3840(100)$ m/s). The pressure dependence of the sound velocity in the guest chains is $dv_g/dP = 280(80)$ m/s GPa^{-1}, and a significantly lower pressure dependence is observed in the host component, $dv_h/dP = 140(60)$ m/s GPa^{-1}. The sound velocities determined here for the guest chains are $\sim$10% lower than the velocities recently estimated from the layers of diffuse scattering observed in disordered chain phase of Rb-IV (Falconi et al. 2006, see Appendix B). This is a good agreement considering the substantial difficulties in collecting high quality diffuse scattering from a sample in a DAC, and it therefore gives support to the analysis and model used by Falconi et al. (2006).

5.5.3 The monoatomic linear chain model

What will be presented in this section is mainly the work of Dr. Ingo Loa, but it has been included for a complete discussion of the IXS results.

The very weak coupling between the incommensurate host and the guest in Rb-IV raises an interesting question. Can the 1D chains of guest atoms in Rb-IV be considered a realization of the monatomic linear chain treated in textbooks (Ashcroft & Mermin 1976) to introduce the concepts of crystal lattice dynamics? In order to calculate the sound velocity according to $v_s = c_g\sqrt{K_g/m}$ (eq. 5.5) in the linear chain model, one needs to determine the force constant K_g and the atomic spacing c_g of the guest chains. K_g can be derived from the lattice

Figure 5.13 The c_{guest} lattice parameter as function of pressure.

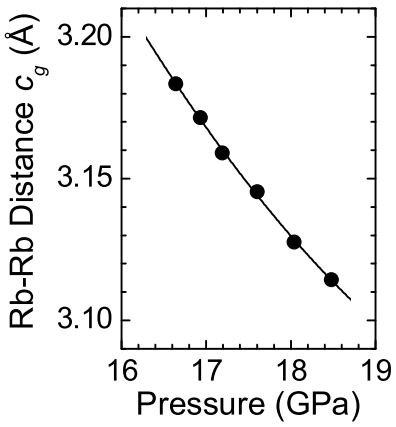

parameter c_g measured as a function of pressure by X-ray diffraction (Figure 5.13). One assumption needs to be made in order to calculate forces from c_g versus pressure, namely, on the effective cross sectional area of the chains. At 17.5 GPa, the minimum chain-host distance and the average distance between atoms in the chains are 3.11 and 3.15 Å, respectively, and the smallest tabulated value for the Rb^+ ionic radius is 1.48 Å (Shannon 1976). We have therefore chosen an effective radius of R = 1.50 Å for the Rb chains. From X-ray diffraction measurements of the intrachain Rb-Rb distances, that is c_g, in the pressure range 16.6−18.5 GPa (Figure 5.13), a force constant of $K_g = -\pi R^2 dP/dc_g = 18.5(4)$ N/m is determined for the guest chains at 17.5 GPa. With $c_g = 3.1480(7)$ Å at the same pressure, one obtains a sound velocity of $v_g = 3594(35)$ m/s in the guest chains at P = 17.5 GPa, in excellent agreement with the guest sound velocity of 3700(100) m/s obtained by interpolating the measured data as shown in Figure 5.12.

The success of the linear chain model encouraged us to estimate also the pressure dependence of v_g. The limiting factor in calculating this is the accuracy of the pressure derivative of K_g, since this requires the second pressure derivative of the lattice parameter c_g. As high-precision values of c_g could only be obtained from the diffractograms of single-phase and fully ordered Rb-IV between 16.6 and 18.5 GPa (Figure 5.13), d^2c_g/dP^2 is not very well constrained by the experiment. With $d^2c_g/dP^2 = 0.0038(14)$ Å/GPa^2, an estimate of $dv_g/dP = 310(140)$ m/s

GPa^{-1} is obtained, as indicated by the dashed line in Figure 5.12, which is in good agreement with the measured pressure dependence, $dv_g/dP = 280(80)$ m/s GPa^{-1}. It can thus be concluded that the guest-atom chains in the composite Rb-IV structure do indeed represent a realization of the monatomic linear chain model with regard to the LA phonons.

5.6 Conclusion

In summary, this chapter have presented the first experimental investigation of the lattice dynamics in an element with a composite crystal structure. Two well-defined LA-type phonon branches are observed in Rb-IV along the direction of the incommensurate wave vector, which are assigned to separate LA-type phonons of the host and the guest sublattices. The LA phonons in the chains are well described by the classic monoatomic linear chain model.

It is interesting to note that the observation of a simple sin-shaped dispersion curve for each of the host and the guest components, is in contrast to what was predicted by theoretical studies, where zone folding was believed to cause a multitude of dispersion branches separated by (pseudo-) gaps. Because Zone folding effects are expected to be less important for weakly interacting systems it is possible that any additional spectral weight is just too weak to be observed in this study of Rb-IV.

It would therefore be of great interest to repeat the experiment on an elemental host-guest phase with strong host-guest interactions. Bi-III and Sb-II both have readily observable satellite reflections in powder diffraction data, indicating strong host-guest interactions, but where it has been proven possible to grow single-crystals of B-III it has also proven to be much more difficult to grow single-crystals of Sb-II (McMahon et al. 2007). Bi-III would therefore be the preferred phase for testing whether Zone folding effects are of any importance in elemental host-guest structures.

Chapter 6

Conclusion

Conclusions for each of the three experimental chapters are summarized below, followed by a short overall conclusion.

- The complete P-T phase diagram of solid rubidium up to 21 GPa has been determined. A direct transformation from Rb-III to Rb-V was not observed but by extrapolating the determined Rb-III⇌d-Rb-IV and o-Rb-IV→Rb-V phase boundaries by only 10 K and 50 K respectively it was concluded that Rb-IV does not exists above 550 K. A remarkable feature of the new phase diagram of rubidium is the strong temperature dependence of ($\sim dT/dP = 65$ K/GPa), and the parallel nature of, the Rb-III⇌d-Rb-IV and d-Rb-IV⇌o-Rb-IV phase boundaries. It was concluded, that the guest chains in d-Rb-IV keeps the short range order observed at room temperature up to at least 501 K. In fact, the structured diffuse scattering observed at room temperature looks identical to that observed at 501 K, so by extrapolation, it is very unlikely that d-Rb-IV has truly disordered chains at any temperature above room temperature.

- New techniques in growing single-crystals of Rb-IV have lead to the observation of satellite reflections for the first time. New experimental developments, and new data reduction techniques, have made it possible to extract reliable intensities of these extremely weak reflections, allowing the full modulated structure refinement of Rb-IV. Based on the refined structure model it was concluded that the modulation happens as a result of a bottleneck effect at the position where guest chains intersect host lay-

ers, and that the strongest host-guest interaction is a repulsive force when host-guest distances are less than ~ 3.2 Å.

- Longitudinal-acoustic (LA) phonons have been studied by inelastic X-ray scattering in the high-pressure incommensurate host-guest system Rb-IV in the pressure range of 16.3 to 18.4 GPa. Two LA-like phonon branches are observed along the direction of the incommensurate wave vector, which are attributed to separate lattice vibrations in the host and guest subsystems. The derived sound velocities for the host and the guest, v_h and v_g, respectively, are similar in magnitude [$v_h = v_g = 3840(100)$ m/s at 18 GPa], but our results indicate different pressure dependencies of dv_h/dP=140(60) m/s GPa^{-1} and dv_g/dP= 280(80) m/s GPa^{-1}. The observations for the 1D guest chains are reproduced quantitatively on the basis of the monoatomic linear chain model and the measured compressibility of the chains.

This thesis have contributed to significant new knowledge on the modulated structure of Rb-IV and on the interactions between the host-guest components. Furthermore the newly available high-pressure IXS techniques have proven very useful for determination of dynamical properties of incommensurate elemental systems. But the main result of this thesis is the development of new high-pressure single-crystal diffraction techniques. These techniques have been shown to be superior to standard techniques when reliable intensities from very low intensity reflections are needed. These techniques also have the potential to make single-crystal structure refinements possible above 100 GPa.

Until now the highest pressures at which structures have been refined from single-crystal data are 29 GPa (Yamanaka et al. 2002) and 33 GPa (Zhang et al. 1998). The technical developments presented in this thesis have very recently enabled a single-crystal structure refinement at 108 GPa (See Appendix B) which is more than three times the pressure of any previous single-crystal structure refinement.

Appendix A

Superspace symmetry

Figure A.1 Solid lines outline the host unit cell with the I4/mcm symmetry and dashed lines outline the guest unit cell when described in the standard I4/mmm space group.

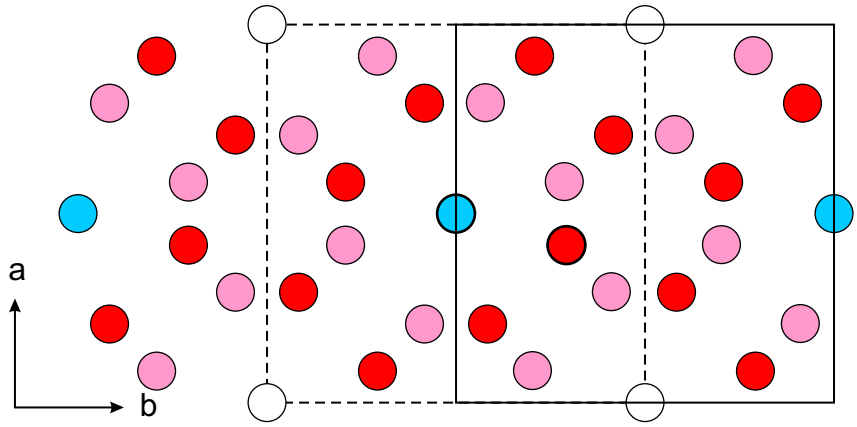

The average host structure of Rb-IV can be described in the space group I4/mcm and the average guest structure can be described in the in the space group I4/mmm, but using the standard origin choice results in half a lattice translation along the b direction between the two unit cells (Figure A.1). The two unit cells will therefore overlap in projection along the c direction after a guest unit-cell translation by $(0\frac{1}{2}0)$. The superspace group symmetry elements are constructed by taking the two first columns of coordinates from either I4/mmm ($(0\frac{1}{2}0)$ origin shift) or I4/mcm space group symmetry elements (they are identical) and then adding the third column of these space groups as the third and fourth column

of the superspace symmetry elements. The resulting symmetry elements are the symmetry elements of the superspace group X4/mcm(00g)s000 (Table A.1).

Table A.1 Symmetry elements of the space groups used for describing the Rb-IV host-guest structure. $\bar{1}$ indicate the presence of an inversion center at the origin and $\frac{1}{2}\frac{1}{2}\frac{1}{2}$ (or $\frac{1}{2}\frac{1}{2}\frac{1}{2}\frac{1}{2}$) indicate the presence body-centering translation symmetry.

Host I4/mcm

x_1	x_2	x_3
$-x_1$	$-x_2$	x_3
$-x_2$	x_1	x_3
x_2	$-x_1$	x_3
$-x_1$	x_2	$\frac{1}{2}-x_3$
x_1	$-x_2$	$\frac{1}{2}-x_3$
x_2	x_1	$\frac{1}{2}-x_3$
$-x_2$	$-x_1$	$\frac{1}{2}-x_3$
$+\bar{1}$	$+\frac{1}{2}\frac{1}{2}\frac{1}{2}$	

Guest I4/mmm

x_1	x_2	x_3
$-x_1$	$-x_2$	x_3
$-x_2$	x_1	x_3
x_2	$-x_1$	x_3
$-x_1$	x_2	$-x_3$
x_1	$-x_2$	$-x_3$
x_2	x_1	$-x_3$
$-x_2$	$-x_1$	$-x_3$
$+\bar{1}$	$+\frac{1}{2}\frac{1}{2}\frac{1}{2}$	

Guest in host lattice
I4/mmm (Origin shift $(0\frac{1}{2}0)$)

x_1	x_2	x_3
$-x_1$	$-x_2$	x_3
$-x_2$	x_1	$\frac{1}{2}+x_3$
x_2	$-x_1$	$\frac{1}{2}+x_3$
$-x_1$	x_2	$-x_3$
x_1	$-x_2$	$-x_3$
x_2	x_1	$\frac{1}{2}-x_3$
$-x_2$	$-x_1$	$\frac{1}{2}-x_3$
$+\bar{1}$	$+\frac{1}{2}\frac{1}{2}\frac{1}{2}$	

RbIV super space group
X4/mcm(00g)s000

x_1	x_2	x_3	x_4
$-x_1$	$-x_2$	x_3	x_4
$-x_2$	x_1	x_3	$\frac{1}{2}+x_4$
x_2	$-x_1$	x_3	$\frac{1}{2}+x_4$
$-x_1$	x_2	$\frac{1}{2}-x_3$	$-x_4$
x_1	$-x_2$	$\frac{1}{2}-x_3$	$-x_4$
x_2	x_1	$\frac{1}{2}-x_3$	$\frac{1}{2}-x_4$
$-x_2$	$-x_1$	$\frac{1}{2}-x_3$	$\frac{1}{2}-x_4$
$+\bar{1}$	$+\frac{1}{2}\frac{1}{2}\frac{1}{2}\frac{1}{2}$		

Appendix B

Published and submitted papers

The author of this PhD thesis has contributed to a number of scientific publications, based on work performed within the Edinburgh, School of Physics, High-pressure Group. They are all based on experiments combining diamond anvil cells and synchrotron X-ray sources, but they cover a range of experimental techniques such as powder and single-crystal diffraction, high-temperature diffraction, inelastic scattering and techniques for studying liquids and diffuse scattering of materials under high-pressure. The papers listed below have been attached to this thesis after the bibliography.

- M. I. McMahon, E. Gregoryanz, L. F. Lundegaard, I. Loa, C. Guillaume, R. J. Nelmes, A. K. Kleppe, M. Amboage, H. Wilhelm and A. P. Jephcoat '*Structure of Sodium above 100GPa by Single-Crystal X-ray Diffraction*' **PNAS** accepted Sep (2007).

- I. Loa, L. F. Lundegaard, M. I. McMahon, S. R. Evans, A. Bossak and M. Krisch '*Lattice Dynamics of Incommensurate Composite Rb-IV and a Realization of the Monatomic Linear Chain Model*' **Phys. Rev. Lett.** (2007) 99:035501.

- C. Hejny, S. Falconi, L. F. Lundegaard and M. I. McMahon '*Phase transitions in tellurium at high pressure and temperature*' **Phys. Rev. B** (2006) 74:174119.

- L. F. Lundegaard, G. Weck, M. I. McMahon, S. Desgreniers and P. Loubeyre '*Observation of an O8 molecular lattice in the epsilon phase of solid oxygen*' **Nature** (2006) 443: 201-204.

- S. Falconi, M. I. McMahon, L. F. Lundegaard, C. Hejny, R.J. Nelmes and M. Hanfland '*X-ray diffraction Study of Diffuse Scattering in Incommensurate Rb-IV*' **Phys. Rev. B** (2006) 73:214102.

- M. I. McMahon, L. F. Lundegaard, C. Hejny, S. Falconi and R. J. Nelmes '*Different incommensurate composite crystal structure for Sc-II*' **Phys. Rev. B** (2006) 73:134102.

- S. Falconi, L. F. Lundegaard, C. Hejny and M. I. McMahon '*X-ray diffraction study in liquid Cs up to 9.8GPa*' **Phys. Rev. Lett.** (2005) 94:125507.

- C. Hejny, L. F. Lundegaard, S. Falconi, M. I. McMahon and M. Hanfland '*Incommensurate sulfur above 100 GPa*' **Phys. Rev. B** (2005) 71:020101.

- M. I. McMahon, C. Hejny, J. S. Loveday, L. F. Lundegaard and M. Hanfland '*Confirmation of the incommensurate nature of Se-IV at pressures below 70 GPa*' **Phys. Rev. B** (2004) 70:054101.

Bibliography

Abd-Elmeguid, M. M., Pattyn, H. & Bukshpan, S. (1994), 'Microscopic observation of the s→d transition in metallic cesium under high pressure', *Phys. Rev. Lett.* **72**, 502 – 505.

Ashcroft, N. W. & Mermin, N. D. (1976), *Solid State Physics*, Holt Saunders.

Axe, J. D. & Bak, P. (1982), 'Long-Wavelength Excitations in Incommensurate Intergrowth Compounds with Application to $Hg_{3-\delta}AsF_6$', *Phys. Rev. B* **26**(9), 4963–4973.

Benna, P., Nestola, F., Boffa-Ballaran, T., Balic-Zunic, T., Lundegaard, L. F. & Bruno, E. (2007), 'The high-pressure structural configurations of $Ca_{0.2}Sr_{0.8}Al_2Si_2O_8$ feldspar: The $I\bar{1} - I2/c$ and $I2/c - P2_1/c$ phase transitions', *American Mineralogist* **92**, 1190–1199.

Boehler, R. (2006), 'New diamond cell for single-crystal x-ray diffraction', *Review of Scientific Instruments* **77**, 115103.

Boehler, R. & De Hantsetters, K. (2004), 'New anvil designs in diamond-cells', *High Pressure Research* **24**(3), 391–396.

Boehler, R. & Zha, C. S. (1986), 'Systematics in the melting behavior of the alkali metals from DAC measurements', *Physica B* **140**, 233–236.

Bruker (2000), 'SMART, SAINT+ and XPREP.', *Bruker AXS Inc., Madison, Wisconsin.* .

Brussaard, L. A., Fasolino, A. & Janssen, T. (2001), 'Phason mode in inclusion compounds', *Phys. Rev. B* **63**, 214302.

Cernik, R. J., Clegg, W., Catlow, C. R. A., Bushnell-Wye, G., Flaherty, J. V., Greaves, G. N., Burrows, I., J., T. D., Teat, S. J. & Hamichi, M. (1997), 'A new high-flux chemical and materials crystallography station at the SRS Daresbury .1. Design, construction and test results', *J. Synchrotron Radiat.* **4**(5), 279–286.

Computer program: FIT28 (2006), ESRF.

Currat, R., Kats, E. & Luk'yanchuk, I. (2002), 'Sound modes in composite incommensurate crystals', *Eur. Phys. J. B* **26**, 339–347.

Datchi, F., LeToullec, R. & Loubeyre, P. (1997), 'Improved calibration of the SrB_4O_7:Sm^{2+} optical pressure gauge: Advantages at very high pressures and high temperatures', *J. Appl. Phys.* **81**(8), 3333–3339.

Dawson, A., Allan, D. R., Parsons, S. & Ruf, M. (2004), 'Use of a CCD diffractometer in crystal structure determination at high pressure', *J. Appl. Cryst.* **37**, 410–416.

de Wolf, P. M. (1974), 'The Pseudo-Symmetry of Modulated Crystal Structures', *Acta Cryst. A* **30**, 777–785.

Degtyareva, O., McMahon, M. I. & Nelmes, R. J. (2004), 'Pressure-induced incommensurate-to-incommensurate phase transition in antimony', *Phys. Rev. B* **70**(18), 184119.

Falconi, S., Lundegaard, L. F., Hejny, C. & McMahon, M. I. (2005), 'X-ray Diffraction Study of Liquid Cs up to 9.8 GPa', *Phys. Rev. Lett.* **94**, 125507.

Falconi, S., McMahon, M. I., Lundegaard, L. F., Hejny, C., Nelmes, R. J. & Hanfland, M. (2006), 'X-ray diffraction study of diffuse scattering in incommensurate rubidium-IV', *Phys. Rev. B* **73**(21), 214102.

Finger, W. & Rice, T. M. (1982), 'Theory of the Crossover in the Low-Frequency Dynamics of an Incommensurate System, $Hg_{3-\delta}AsF_6$', *Phys. Rev. Lett.* **49**(7), 468–470.

Finger, W. & Rice, T. M. (1983), 'Long-wavelength phonons in incommensurate systems', *Phys. Rev. B* **28**(1), 340–358.

Fujihisa, H., Akahama, Y., Kawamura, H., Gotoh, Y., Yamawaki, H., Sakashita, M., Takeya, S. & Honda, K. (2005), 'Incommensurate composite crystal structure of scandium-II', *Phys. Rev. B* **72**(13), 132103.

Fujihisa, H., Akahama, Y., Kawamura, H., Ohishi, Y., Gotoh, Y. & Yamawaki, H. (2007), 'Incommensurate Structure of Phosphorus Phase IV', *Phys. Rev. Lett.* **98**, 175501.

Giacovazzo, C. (2000), The Diffraction of X-rays by Crystals, *in* C. Giacovazzo, ed., 'Fundamentals of Crystallography', Oxford University Press, pp. 141–228.

Gregoryanz, E., Degtyareva, O., Somayazulu, M., Hemley, R. J. & Mao, H. K. (2005), 'Melting of Dense Sodium', *Phys. Rev. Lett.* **94**(18), 185502.

Hammersly, A. (2005), 'FIT2D Version 12.073', ESRF.

Hastings, J. M., Pouget, J. P., Shirane, G., Heeger, A. J., Miro, N. D. & MacDiarmid, A. G. (1977), 'One-Dimensional Phonons and "Phase-Ordering" Phase Transition in $Hg_{3-\delta}AsF_6$', *Phys. Rev. Lett.* **39**(23), 1484–1487.

Heilmann, I. U., Axe, J. D., Hastings, J. M., Shirane, G., Heeger, A. J. & MacDiarmid, A. G. (1979), 'Neutron investigation of the dynamical properties of the mercury-chain compound $Hg_{3-\delta}AsF_6$', *Phys. Rev. B* **20**(2), 751–762.

Heine, V. (2000), 'As weird as they come', *Nature* **403**, 836–837.

Hejny, C., Lundegaard, L. F., Falconi, S., McMahon, M. I. & Hanfland, M. (2005), 'Incommensurate sulfur above $100GPa$', *Phys. Rev. B* **71**(2), 020101.

Hejny, C. & McMahon, M. I. (2003), 'Large Structural Modulations in Incommensurate Te-III and Se-IV', *Phys. Rev. Lett.* **91**(21), 215502.

Krisch, M. (2003), 'Status of Phonon Scattering Studies at High Pressure by Inelastic X-Ray Scattering', *J. Raman Spectr.* **34**, 628–6320.

Loveday, L. S., McMahon, M. I. & Nelmes, R. J. (1990), 'The effect of diffraction by the diamonds of a diamond-anvil cell on single-crystal sample intensities', *J. Appl. Crystallogr.* **23**, 392–396.

Lundegaard, L. F., Makovicky, E., Boffa-Ballaran, T. & Balic-Zunic, T. (2005), 'Crystal structure and cation lone electron pair activity of Bi_2S_3 between 0 and 10 GPa', *Phys Chem Minerals* **32**, 578–584.

Lundegaard, L. F., Weck, G., McMahon, M. I., Desgreniers, S. & Loubeyre, P. (2006), 'Observation of an O_8 molecular lattice in the ϵ phase of solid oxygen', *Nature* **443**, 201–204.

Luo, N. S., Wu, S. Y. & Jayanthi, C. S. (1997), 'Exotic features in the lattice dynamics of an incommensurate overlayer/substrate structure as modeled via the Frenkel-Kontorova system', *Phys. Rev. B* **55**(17), 11300.

Mao, H. K., Xu, J. & Bell, P. M. (1986), 'Calibration of the ruby pressure gauge to 800kbar under quasi-hydrostatic conditions', *J. Geophys. Res.* **91**(B5), 4673.

Yu. Tonkov, E. & Ponyatovsky, E. G. (2005), *Phase Transformations of Elements Under High Pressure*, CRC Press, Boca Raton.

McMahan, A. K. (1984), 'Alkali-metal structures above the s-d transition', *Phys. Rev. B* **29**(10), 5982 – 5985.

McMahon, M. I., Bovornratanaraks, T., Allan, D. R., Belmonte, S. A. & Nelmes, R. J. (2000a), 'Observation of the incommensurate barium-IV structure in strontium phase V', *Phys. Rev. B* **61**(5), 3135 – 3138.

McMahon, M. I., Degtyareva, O. & Nelmes, R. J. (2000b), 'Ba-IV-Type Incommensurate Crystal Structure in Group-V Metals', *Phys. Rev. Lett.* **85**(23), 4896–4899.

McMahon, M. I., Degtyareva, O., Nelmes, R. J., van Smaalen, S. & Palatinus, L. (2007), 'Incommensurate modulations of Bi-III and Sb-II', *Phys. Rev. B* **75**, 184114.

McMahon, M. I., Hejny, C., Loveday, J. S., Lundegaard, L. F. & Hanfland, M. (2004), 'Confirmation of the incommensurate nature of Se-IV at pressures below 70 GPa', *Phys. Rev. B* **70**(5), 054101.

McMahon, M. I., Lundegaard, L. F., Hejny, C., Falconi, S. & Nelmes, R. J. (2006a), 'Different incommensurate composite crystal structure for Sc-II', *Phys. Rev. B* **73**(13), 134102.

McMahon, M. I. & Nelmes, R. J. (2004*a*), 'Chain Melting in the Composite Rb-IV Structure', *Phys. Rev. Lett.* **93**(5), 055501.

McMahon, M. I. & Nelmes, R. J. (2004*b*), 'Incommensurate crystal structures in the elements at high pressure', *Z. Kristallogr.* **219**, 742–748.

McMahon, M. I. & Nelmes, R. J. (2006), 'High-pressure structures and phase transformations in elemental metals', *Chem. Soc. Rev.* **35**, 943–963.

McMahon, M. I., Nelmes, R. J., Schwarz, U. & Syassen, K. (2006b), 'Composite incommensurate K-III and a commensurate form: Study of a high-pressure phase of potassium', *Phys. Rev. B* **74**, 140102.

McMahon, M. I., Rekhi, S. & Nelmes, R. J. (2001), 'Pressure Dependent Incommensuration in Rb-IV', *Phys. Rev. Lett.* **87**(5), 055501.

Merrill, L. & Bassett, W. A. (1974), 'Miniature diamond anvil pressure cell for single crystal x-ray diffraction studies', *Rev. Sci. Instrum.* **45**(2), 290–294.

Miletich, R., Allan, D. R. & Kuhs, W. F. (2000), High-Pressure Single-Crystal Techniques, *in* R. M. Hazen & R. T. Downs, eds, 'High-Temperature and High-Pressure Crystal Chemistry', Vol. 41 of *Reviews in Mineralogy and Geochemistry*, The Mineralogical Society of America, pp. 445–519.

Nelmes, R. J., Allan, D. R., McMahon, M. I. & Belmonte, S. A. (1999), 'Self-Hosting Incommensurate Structure of Barium IV', *Phys. Rev. Lett.* **83**(20), 4081–4084.

Nelmes, R. J. & McMahon, M. I. (1994), 'High-Pressure Powder Diffraction on Synchrotron Sources', *J. Synchrotron Radiat.* **1**, 9–73.

Nelmes, R. J., McMahon, M. I., Loveday, J. S. & Rekhi, S. (2002), 'Structure of Rb-III: Novel Modulated Stacking Structures in Alkali Metals', *Phys. Rev. Lett.* **88**(15), 155503.

Oganov, A. R. & Glass, C. (2006), 'Crystal structure prediction using ab initio evolutionary techniques: Principles and applications', *J. Chem. Phys.* **124**, 244704.

Olijnyk, H. & Holzapfel, W. B. (1983), 'Phase transitions in K and Rb under pressure', *Phys. Lett. A* **99**(8), 381–383.

Parsons, S. (2004), 'Shade', *Univ.of Edinburgh, Scotland.* .

Radulescu, O., Janssen, T. & Etrillard, J. (2002), 'Dynamics of modulated and composite aperiodic crystals', *Eur. Phys. J. B* **29**, 385–398.

Schwarz, U. (2004), 'Metallic high-pressure modifications of main group elements', *Z. Kristallogr.* **219**, 376–390.

Schwarz, U., Grzechnik, A., Syassen, K., Loa, I. & Hanfland, M. (1999a), 'Rubidium-IV: A High Pressure Phase with Complex Crystal Structure', *Phys. Rev. Lett.* **83**(20), 4085–4088.

Schwarz, U., Syassen, K., Grzechnik, A. & Hanfland, M. (1999b), 'The crystal structure of rubidium-VI near 50 GPa', *Solid State Commun.* **112**(6), 319–322.

Shannon, R. D. (1976), 'Revised Effective Ionic Radii and Systematic Studies of Interatomie Distances', *Acta Cryst.* **A**(32), 751.

Smith, H. G. & Lander, G. H. (1984), 'Neutron scattering α-uranium in the charge-density-wave state', *Phys. Rev. B* **30**(10), 5407–5415.

Takemura, K., Minomura, S. & Shimomura, O. (1982), 'X-ray diffraction study of electronic transitions in cesium under high pressure', *Phys. Rev. Lett.* **49**, 1772 –1775.

Takemura, K., Sato, K., Fujihisa, H. & Onoda, M. (2003), 'Modulated structure of solid iodine during its molecular dissociation under high pressure', *Nature* **423**, 971–974.

Takemura, K. & Syassen, K. (1982), 'High-pressure equation of state of rubidium', *Solid State Communications* .

Takemura, K. & Syassen, K. (1985), 'High pressure structural investigation of cesium above 10 GPa', *Phys. Rev. B* **32**(4), 2213 – 2217.

Theodorou, G. & Rice, T. M. (1978), 'Statics and dynamics of incommensurate lattices', *Phys. Rev. B* **18**(6), 2840–2856.

Van Smallen, S. (1995), 'Incommensurate crystal structures', *Cryst. Rev.* **4**(2), 79–202.

Weir, C. E., Lippincott, E. R., Van Valkenburg, A. & Bunting, E. N. (1959), 'Infrared Studies in the 1- to 15-Micron Region to 30,000 Atmospheres', *J. Res. Natl. Bur. Stand.* **63A**, 55–62.

Yamanaka, T., Fukuda, T., Komatsu, Y. & Sumiya, H. (2002), 'Charge density analysis of SiO2 under pressures over 50 GPa using a new diamond anvil cell for single-crystal structure analysis.', *J. Phys.: Condens. Matter* **14**, 10545 – 10551.

Zhang, L., Ahsbahs, H. & Kutoglu, A. (1998), 'Hydrostatic compression and crystal structure of pyrope to 33 GPa', *Phys. Chem. Minerals* **25**, 301 – 307.

Structure of sodium above 100 GPa by single-crystal x-ray diffraction

M. I. McMahon*†, E. Gregoryanz*†, L. F. Lundegaard*, I. Loa*, C. Guillaume*, R. J. Nelmes*, A. K. Kleppe‡, M. Amboage‡, H. Wilhelm‡, and A. P. Jephcoat‡§

*Scottish Universities Physics Alliance, School of Physics and Centre for Science at Extreme Conditions, The University of Edinburgh, Mayfield Road, Edinburgh EH9 3JZ, United Kingdom; ‡Diamond Light Source Ltd., Harwell Science and Innovation Campus, Didcot, Oxfordshire OX11 0QX, United Kingdom; and §Department of Earth Sciences, University of Oxford, Parks Road, Oxford OX1 3PR, United Kingdom

Communicated by Russell J. Hemley, Carnegie Institution of Washington, Washington, DC, October 1, 2007 (received for review August 14, 2007)

At pressures above a megabar (100 GPa), sodium crystallizes in a number of complex crystal structures with unusually low melting temperatures, reaching as low as 300 K at 118 GPa. We have utilized this unique behavior at extreme pressures to grow a single crystal of sodium at 108 GPa, and have investigated the complex crystal structure at this pressure using high-intensity x-rays from the new Diamond synchrotron source, in combination with a pressure cell with wide angular apertures. We confirm that, at 108 GPa, sodium is isostructural with the *cI*16 phase of lithium, and we have refined the full crystal structure of this phase. The results demonstrate the extension of single-crystal structure refinement beyond 100 GPa and raise the prospect of successfully determining the structures of yet more complex phases reported in sodium and other elements at extreme pressures.

alkali metals | crystal structure | high pressure

At ambient pressure the alkali metals are simple metals; i.e., they can be described as nearly-free-electron metals that are characterized by a weak interaction between their single valence electron and the atomic core (1, 2). At ambient conditions the alkali metals all crystallize in the close-packed body-centered cubic (*bcc*) structure. However, under sufficient compression, they undergo a series of structural phase transitions. At pressures ranging from 2.2 GPa in cesium to 65 GPa in sodium, they transform from the *bcc* to the face-centered-cubic (*fcc*) structure (3–5). Further compression leads to the formation of a wide variety of lower-symmetry and often very complex crystal structures (6, 7), which range from distorted variants of the *bcc* structure in lithium and sodium (5, 8, 9) to an incommensurate composite or "host–guest" crystal structure in rubidium (10, 11). The discovery of a whole series of these symmetry-lowering transitions over the last decade—not only in the alkali metals, but also in various other elements (6, 7, 9)—had been unexpected because it often involves a reduction in coordination number, which is opposite to the usual trend for pressure-induced phase transitions. The experimental discoveries have been complemented by computational studies, but the physical mechanisms that lead to the formation of the complex phases are not yet fully understood, and their physical properties not yet known in detail.

Because of the low x-ray scattering power and relatively high transition pressures of sodium, it is only recently that it has become possible to investigate its high-pressure behavior. A number of high-pressure phases have been identified above 100 GPa (ref. 12 and M. Hanfland, K. Syassen, N. E. Christensen, and D. L. Novikov, unpublished data—see ref. 5), and the melting line was discovered to be very unusual: it first rises close to 1,000 K at ≈30 GPa and then falls to room temperature (≈300 K) at 118 GPa (12) (see Fig. 1). Previous x-ray diffraction studies have shown that, with increasing pressure at room temperature, sodium transforms first from the *bcc* phase to *fcc* at 65 GPa, as said, and then to a more complex body-centered cubic structure with 16 atoms in the unit cell (*cI*16) at 103 GPa (5, 9). Further studies up to higher pressures have revealed at least two more transitions (ref. 12 and M. Hanfland, K. Syassen, N. E. Christensen, and D. L. Novikov, unpublished data—see ref. 5), and theoretical calculations (9, 13) have suggested these phases may have the tetragonal β-Sn-type structure of cesium phase IV (7) (*tI*4 in Pearson's notation; ref. 14) and the orthorhombic C-face-centered (*oC*8) structure of α-gallium (7). Theoretical studies have explored the possibility of the onset of superconductivity in the solid phases (15, 16), and suggest the possible onset of a dimerized phase at pressures >200 GPa (13, 17). Here we are concerned with the crystal structure of the *cI*16 phase. It is the first of the complex phases in sodium; however, although its symmetry and density are known (9) and some calculations have been performed (13, 15), the experimental determination of its structure has remained incomplete.

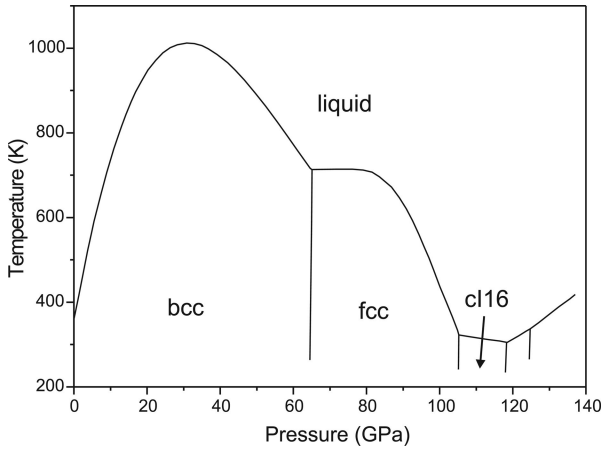

Fig. 1. The phase diagram of Na to 140 GPa (adapted from ref. 12), showing the stability fields of the *bcc*, *fcc*, and *cI*16 phases, and the remarkable decrease in the melting temperature observed above 30 GPa.

The *cI*16 structure has already been determined in lithium, which exists in this phase above 40 GPa at 180 K (8). The structure is shown in Fig. 2 and has space group $I\bar{4}3d$ with 16 atoms on a 16*c* site, (x, x, x). Refinements of powder diffraction data for Li give a value of 0.055(1) for the variable atomic coordinate x at 46 GPa and 180 K (8). The value of x was found to vary between 0.054 at 45 GPa and 0.060 at 50 GPa (both at 180 K), and a value of 0.046 was obtained on pressure decrease

Author contributions: M.I.M. and E.G. designed research; M.I.M., E.G., L.F.L., I.L., C.G., R.J.N., A.K.K., and M.A. performed research; A.K.K., M.A., H.W., and A.P.J. contributed new reagents/analytic tools; L.F.L. analyzed data; and M.I.M., E.G., I.L., and R.J.N. wrote the paper.

The authors declare no conflict of interest.

†To whom correspondence may be addressed. E-mail: mim@ph.ed.ac.uk or e.gregoryanz@ed.ac.uk.

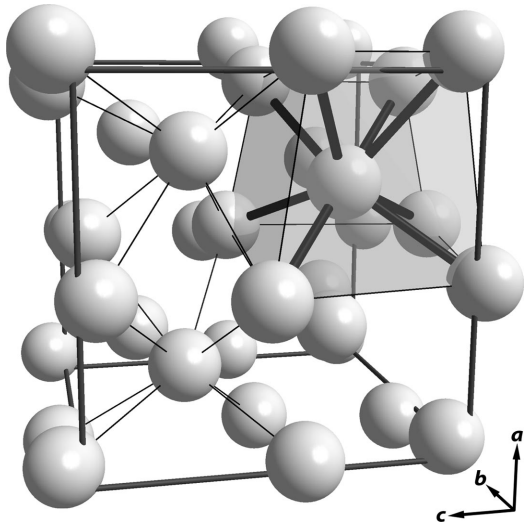

Fig. 2. The *cI*16 crystal structure. It can be regarded as a distorted $2 \times 2 \times 2$ superstructure of the *bcc* structure. One of the eight distorted-*bcc* subunits is highlighted, and the local coordination is indicated for two further subunits. The atoms occupy the 16*c* Wyckoff site, (*x*, *x*, *x*), of space group $I\bar{4}3d$ and positions are shown for $x = 0.044$.

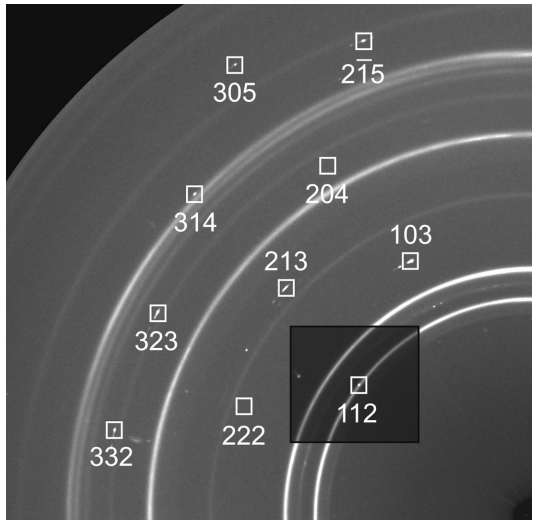

Fig. 3. One quadrant of a composite image of five superimposed Mar345 images selected from the overall 14° scan range to show representative data. Eight observed reflections are marked. As discussed in the text, the (204) and (222) reflections are absent. Weak intensity just to the left of the (103) reflection arises from a second crystal; reflections from this are ≈10 times weaker than from the main crystal. The powder diffraction rings are from the rhenium gasket and from some tantalum included with the sample as a pressure marker. One part of the image has been enhanced to reveal the (112) reflection on one of the rhenium diffraction rings. Other small diffraction spots in the image are of a different appearance from the sample reflections, and are not from the sample.

in an experiment at 100 K where the phase was observed down to 37.5 GPa—well below the pressure at which the phase first appears on pressure increase at 180 K, probably due to hysteresis effects. The structure would be *bcc* for $x = 0$, and it is a simple distortion of *bcc* in which atoms are displaced along the body-diagonal directions of the cubic unit cell (8).

Here we report a determination of the structure of *cI*16 sodium at 108(1) GPa using single-crystal x-ray diffraction techniques. Details of experimental techniques are given in *Materials and Methods*. At pressures <90 GPa, the diffraction patterns from the sample were powder-like and contained a number of Debye–Scherrer rings. However, above that pressure, the sample became more textured and single-crystal like because of the proximity of the experimental conditions to the melting curve (Fig. 1), and the diffraction patterns contained a number of strong Bragg reflections. The single-crystal nature of the sample became still more evident once the pressure was increased into the *cI*16 phase at 108 GPa, and the sample quality was improved by careful annealing just below the melting curve at 40°C.

Fig. 3 shows some of the diffraction data, which were collected on an image-plate detector in a sequence of contiguous ±0.25° oscillations over a total scan range of 14° around the vertical axis. The short x-ray wavelength (0.3444 Å) and the 50° aperture in the pressure cell, which is significantly larger than in typical megabar cells currently in use, were chosen to allow us to extend the accessible part of reciprocal space and thereby increase considerably the number of observable reflections. Inspection of the data revealed reflections from a much smaller second crystal with a slightly different orientation from the main one, and an intensity ratio between the two of ≈10:1. Evidence of the weaker (≈10%) component can be seen just to the left of the box around the main (103) reflection in Fig. 3. The difference in orientation made it straightforward to fit an orientation matrix and obtain accurate integrations of the data from the main crystal alone.

The lattice parameter of the sodium at 108(1) GPa was refined from the measured reflection *d*-spacings as 5.461(1) Å. This corresponds to an atomic volume of 10.18 $Å^3$ (a V/V_0 of 0.258 and a density of 3.76 gcm^{-3}), in good agreement with the value shown in ref. 9 for the same pressure of 108 GPa.

The orientation matrix showed that 31 different allowed reflections, consistent with a body-centered cubic lattice, had passed completely through the reflection condition in the range of the scans. These were averaged over symmetry equivalents to give 15 unique reflections, six of which were observed as having no detectable intensity at a level below 0.02% of the strongest reflections. Five of these six have (*hkl*) indices that break some general conditions for allowed reflections in space group $I\bar{4}3d$: $2h + l = 4n$ for (*hhl*) or $h = 4n$ for (*h*00). An example is the absent (222) reflection in Fig. 3. The remaining absent reflection is the (204) reflection seen in Fig. 3, which has indices that break the special conditions for atoms in the 16*c* sites: $h + k + l = 4n$ or $h = 2n + 1$. Two of the allowed reflections were omitted from the least-squares refinement because they were saturated on the detector. The final refinement converged to an *R* factor of 3.3% and a goodness of fit (χ^2) of 1.37.

The isotropic atomic displacement parameter refined to 0.03(1) $Å^2$ and the value of the variable atomic coordinate *x* refined to 0.044(1), giving a displacement of the atoms from the *bcc* structure of 0.42(1) Å. The fractional distortion from the *bcc* structure is smaller than the 0.054 observed at the onset of the *cI*16 phase in lithium at 180 K, and even slightly less than the value of 0.046 found at the limit of existence of the phase on pressure decrease at 100 K (8). At the V/V_0 of 0.258 for sodium at 108 GPa, Christensen and Novikov (13) calculated *x* to be 0.028 (figure 7 of ref. 13). Our value is significantly larger, but is in quite close agreement with the calculations of Neaton and Ashcroft at the same V/V_0, as estimated from the values for the ionic radius, r_s, given in ref. 15.¶

At temperatures below 35 K at atmospheric pressure, *bcc*-Na transforms to one or more rhombohedral structures, the exact

¶V/V_0 values can be estimated from the ambient-pressure value of $r_s = 3.78$ given in ref. 15, and the calculated values of r_s at high pressure, which are given in footnote 21 of that paper along with the corresponding calculated values of *x*.

nature of which is unclear (18, 19). Because *cI*16 is a *bcc*-like structure, there is the interesting possibility of a corresponding transition to a lower-symmetry structure at low temperatures. Nothing is currently known about the structural behavior of sodium at 100 GPa and low temperatures, and further studies would be worthwhile.

Single-crystal techniques at high pressure have been significantly developed over the past decade, and have been successfully applied to solving many highly complex structures that had defied solution with powder diffraction methods (7). The data are best collected with monochromatic techniques, but then a wide-angle aperture is needed in the pressure cell to collect complete data. Suitable pressure cells for work in the range up to ≈50 GPa have been available for some time; however, for work over a megabar (100 GPa), cells have typically had apertures with (full) angles no larger than ≈35°. That size of aperture, even with the short x-ray wavelength used here, would have occluded most of the reflections seen in Fig. 3: only the (222), (112), and (103) reflections would have been completely measurable. It is not just that the aperture is restricted but that reflection *d* spacings are reduced by the very high pressure, thus moving reflections to higher scattering angles, 2θ. For example, sodium at 108 GPa is approximately four times denser than at ambient pressure ($V/V_0 \approx 0.25$), and so average *d* spacings are reduced by ≈37%. The *cI*16 structure is not particularly complex, but it could not have been satisfactorily determined by single-crystal methods with previously existing limits on the scattering angle. In principle, a reduced aperture can be overcome partially by using even shorter x-ray wavelengths, but then integrated intensities fall as λ^3 and other limitations may arise, including weak scattering from low-Z samples or lack of resolution in the diffraction pattern. Large apertures will always allow for more options in solving the most challenging structural problems.

Extension of single-crystal structure refinement beyond a megabar opens up the prospect of successful structural studies of intriguing complex phases already believed to exist in elements in this range, including in sodium (refs. 9, 12, and 13, and M. Hanfland, K. Syassen, N. E. Christensen, and D. L. Novikov, unpublished data—see ref. 5).

Materials and Methods

Sodium with a stated purity of 99.95% was loaded into the diamond anvil cell in a dry argon atmosphere to prevent oxidation of the sample. The pressure cell was equipped with beveled Boehler–Almax-type diamond anvils and seats (20), which provided a conical aperture (full angle) of 50°. The diamond anvils were 1.70 mm thick, and had a girdle diameter of 3.10 mm, with 100-μm-diameter culets beveled to 300 μm at an angle of 8°. The initial sample chamber in the rhenium gasket was 30 μm in diameter and preindented to ≈15 μm in thickness. Three or four grains of polycrystalline tantalum (grain size 2–3 μm) were enclosed with the sodium for pressure measurement via the Ta equation of state (21). Because sodium itself has been identified as an excellent quasihydrostatic pressure medium (21), no other pressure-transmitting medium was added. Diffraction patterns of the low-pressure *bcc* and *fcc* sodium phases showed no discernible contaminant peaks, confirming that the sample was pure. The sharpness of the diffraction peaks observed from both the sodium and Ta at pressures above 100 GPa confirms that sodium is indeed quite hydrostatic in this pressure range where the melting curve is close to room temperature (12).

The pressure cell was placed in an oven and gently heated at 40°C, very close to the melting curve at 108 GPa (12), for ≈30 min. This resulted in the production of a good quality single crystal ≈25 μm in diameter and ≈2.5 μm thick. Diffraction data were collected on the Extreme Conditions Beamline (I15) at the Diamond Light Source (www.diamond.ac.uk/Beamlines/Beamlineplan/I15/TechSpecs.htm) using an x-ray wavelength of 0.3444 Å (36 keV) from a double-bounce Si monochromator. The incident beam was collimated to a beam size of 50 μm. The distance from the sample to the Mar345 image-plate detector and the detector tilt angles were determined with a Si standard. The sample pressure was determined from the tantalum diffraction pattern and its known equation of state (21) as 108(1) GPa, and the single-crystal diffraction data were collected at 300 K. The intensities of the reflections were integrated by using the SAINT+ program (22), and the structure was refined on squared structure factors (F^2) using SHELXL97 (23). (No absorption corrections were applied because these will be negligible for such a small sodium sample with 36 keV x-rays.) The three variable parameters refined were an overall scale factor and the isotropic atomic displacement factor and fractional coordinate of the sodium atom.

This work is supported by a research grant from the U.K. Engineering and Physical Sciences Research Council and facilities made available by Diamond Light Source Ltd.

1. Wigner E, Seitz F (1934) *Phys Rev* 43:804–810.
2. Wigner E, Seitz F (1934) *Phys Rev* 46:509–524.
3. Bridgman PW (1938) *Proc Am Acad Arts Sci* 72:207–225.
4. Bardeen J (1938) *J Chem Phys* 6:372–378.
5. Hanfland M, Loa I, Syassen K (2002) *Phys Rev B* 65:184109.
6. Schwarz U (2004) *Zeit fur Kristallogr* 219:376–390.
7. McMahon MI, Nelmes RJ (2006) *Chem Soc Rev* 35:943–963.
8. Hanfland M, Syassen K, Christensen NE, Novikov DL (2000) *Nature* 408:174–178.
9. Syassen K (2002) in *High Pressure Phenomena*, Proceedings of the International School of Physics, eds Hemley RJ, Chiarotti GL, Bernasconi M, Ulivi L (IOS Press, Amsterdam), pp 266–268.
10. McMahon MI, Rekhi S, Nelmes RJ (2001) *Phys Rev Lett* 87:055501.
11. Schwarz U, Grzechnik A, Syassen K, Loa I, Hanfland M (1999) *Phys Rev Lett* 83:4085–4088.
12. Gregoryanz E, Degtyareva O, Somayazulu M, Hemley RJ, Mao H-K (2005) *Phys Rev Lett* 94:185502.
13. Christensen NE, Novikov DL (2001) *Solid State Commun* 119:477–490.
14. Villars P, Calvert LD (1991) *Pearson's Handbook of Crystallographic Data for Intermetallic Phases* (Am Soc Microbiol, Materials Park, OH), 2nd Ed.
15. Neaton JB, Ashcroft NW (2001) *Phys Rev Lett* 86:2830–2833.
16. Christensen NE, Novikov DL (2006) *Phys Rev B* 73:224508.
17. Angilella GGN, Siringo F, Pucci R (2003) *Eur Phys J B* 32:323–327.
18. Berliner R, Smith HG, Copley JRD, Trivisonno J (1992) *Phys Rev B* 46:14436–14447.
19. Schwarz W, Blaschko O, Gorgas I (1992) *Phys Rev B* 46:14448–14452.
20. Boehler R, De Hantsetters K (2004) *High Press Res* 24:391–396.
21. Hanfland M, Syassen K, Köhler J (2002) *J Appl Phys* 91:4143–4148.
22. Bruker (2000) SAINT+ (Bruker AXS, Madison, WI).
23. Sheldrick GM (1997) SHELXL97 (Univ of Göttingen, Göttingen, Germany).

Lattice Dynamics of Incommensurate Composite Rb-IV and a Realization of the Monatomic Linear Chain Model

I. Loa,[1,*] L. F. Lundegaard,[1] M. I. McMahon,[1] S. R. Evans,[1] A. Bossak,[2] and M. Krisch[2]

[1]*SUPA, School of Physics and Centre for Science at Extreme Conditions, The University of Edinburgh, Mayfield Road, Edinburgh, EH9 3JZ, United Kingdom*

[2]*European Synchrotron Radiation Facility, BP 220, 38043 Grenoble Cedex, France*

(Received 12 September 2006; published 19 July 2007)

Longitudinal-acoustic (LA) phonons have been studied by inelastic x-ray scattering in the high-pressure incommensurate host-guest system Rb-IV in the pressure range of 16.3 to 18.4 GPa. *Two* LA-like phonon branches are observed along the direction of the incommensurate wave vector, which are attributed to separate lattice vibrations in the host and guest subsystems. The derived sound velocities for the host and the guest, v_h and v_g, respectively, are similar in magnitude [$v_h = v_g = 3840(100)$ m/s at 18 GPa], but our results indicate rather different pressure dependences of $dv_h/dP = 140(60)\,\mathrm{m/s\,GPa^{-1}}$ and $dv_g/dP = 280(80)\,\mathrm{m/s\,GPa^{-1}}$. The observations for the one-dimensional Rb guest chains are reproduced quantitatively on the basis of the monatomic linear chain model and the measured compressibility of the chains.

DOI: 10.1103/PhysRevLett.99.035501 PACS numbers: 63.20.Dj, 61.44.Fw, 62.50.+p, 78.70.Ck

In recent years, a number of surprisingly complex crystal structures has been discovered in the elements at high pressures, in particular, incommensurately modulated structures and incommensurate host-guest composite structures (see reviews [1] for an overview and references). The high-pressure phase rubidium-IV [2,3] shown in Fig. 1(a) belongs to the group of incommensurate host-guest structures that have also been observed in K, Ba, Sr, Sc, As, Sb, and Bi. Although considerable progress has been made in determining the detailed crystal structures of the complex metallic phases at high pressure, little is known about their other physical properties [4]. And while they have been investigated in theoretical studies [5], the mechanisms that lead to their formation and stability are not yet fully understood. The lattice dynamics of composite systems, which lack a conventional Brillouin zone due to the loss of translational symmetry along one or more crystal directions, have been addressed in model calculations [6–11], but only in the context of more complex incommensurate systems such as $Hg_{3-\delta}AsF_6$ [12,13]. The 1D, monatomic nature of composite structures observed in the elements at high pressures offers the possibility of studying the lattice dynamics in much simpler systems.

Here we investigate the lattice dynamics in incommensurate composite Rb-IV by inelastic x-ray scattering (IXS). In particular, we focus on the longitudinal-acoustic (LA) phonons along the direction of the incommensurate wave vector (parallel to the guest-atom chains), which the calculations [6–11] predict to reflect the incommensurability most clearly. Rb-IV is stable from 16 to 20 GPa at room temperature. Above 16.7 GPa, both host and guest components exhibit long-range order, and the interchain long-range order is presumably mediated via minute distortions of the host lattice. Below 16.7 GPa the interchain correlation length decreases rapidly and is only ~40 Å at 16.1 GPa [14,15]. The breakdown of interchain correlations below 16.7 GPa suggests that the host-guest interactions in Rb-IV are particularly weak. This view is supported by the fact that x-ray diffraction on Rb-IV yields extremely weak modulation reflections (which arise from the host-guest interactions), whereas they are readily observed in Sb-II, Sb-IV, and Bi-III [16].

The present study demonstrates that there are *two* well-defined LA-type phonon branches along the chain direction that can be attributed to separate LA excitations in the host and the guest sublattices. From the measured dispersion curves we have determined the sound velocities of these host and guest excitations as a function of pressure from 16.3 to 18.4 GPa. We find that the sound velocity

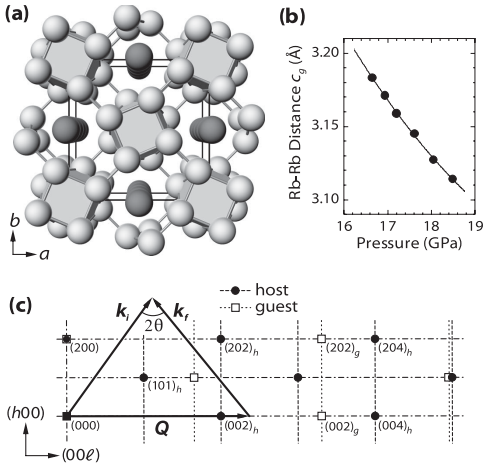

FIG. 1. (a) Crystal structure of Rb-IV [2,3]. It comprises a framework of "host" Rb atoms (light gray) with 1D channels that accommodate chains of "guest" Rb atoms (dark gray). The periodicities of the host and guest sublattices along the chain direction are incommensurate with each other. (b) Intrachain Rb-Rb distance vs pressure, $c_g(P)$. (c) The IXS scattering geometry. The circles and squares indicate the Bragg reflections, $\boldsymbol{k}_i$ and $\boldsymbol{k}_f$, are the incoming and scattered photon wave vectors, and $\boldsymbol{Q}$ denotes momentum transfer vector.

along the guest-atom chains, and its pressure dependence, is in excellent agreement with that calculated using the monatomic linear chain model utilized in solid-state physics textbooks to introduce the concepts of lattice dynamics.

The IXS experiments were performed on beam line ID28 at the ESRF, Grenoble. The incident radiation was monochromatized at a photon energy of 17.794 keV. Two grazing-incidence mirrors focused the x rays onto the sample with a focal size of $25 \times 60\ \mu\text{m}^2$. The spectrum of the scattered radiation was analyzed by a high-resolution spherical crystal (Si) analyzer to yield an overall energy resolution of 3 meV. The momentum resolution was set to 0.3 nm^{-1} and the IXS spectra were collected in the energy-scanning mode. The scattering geometry is shown in Fig. 1(c). A detailed account of the IXS setup has been given elsewhere [17].

An essential prerequisite for the present study was the ability to grow high-quality single crystals of Rb-IV in a diamond anvil cell (DAC), as described previously [15]. One Rb-IV crystal was investigated at a pressure of 18.4 GPa, while a second was studied at 17.3, 17.0, and 16.3 GPa. X-ray diffraction was used to confirm that both samples of Rb-IV were single crystals and to determine their crystal orientations within the DACs. The lattice parameters (a, $c_{\text{host}} \equiv c_h$, $c_{\text{guest}} \equiv c_g$) were determined *in situ* at the IXS beam line by scanning across three Bragg reflections. The sample pressures were derived from c_h and c_g on the basis of their previously measured pressure dependences [2,18].

Figure 2 shows selected IXS spectra recorded from Rb-IV at 17.3 GPa for three different momentum transfers Q. Despite the smallness of the sample in the DAC (scattering volume $\approx 2 \times 10^{-5}$ mm^3), high-quality spectra were obtained in ~90 min. The spectra exhibit a clear Q dependence and comprise one or two inelastic features of varying energy and intensity in addition to the elastic line. We focus here on the LA excitations along the chain direction of Rb-IV by selecting momentum transfer vectors $\boldsymbol{Q}$ parallel to the crystal c axis [Fig. 1(c)] and taking advantage of the IXS selection rules. Also shown in Fig. 2 are decompositions of the measured spectra into the elastic line, the excitation peaks, and a constant background that were obtained by least-squares fitting [19]. The Stokes/anti-Stokes intensity ratios were assumed to be given by the Bose-Einstein population factors.

From the decompositions of the IXS spectra, the LA phonon energies were obtained as a function of momentum transfer (Fig. 3). The data points clearly separate into two dispersion branches. The first (solid symbols) exhibits the periodicity of the host lattice along the c direction. The apparent doubling of the periodicity originates from the body-centered nature of the host lattice. As shown by the solid line in Fig. 3, the dispersion relation is well modeled by a one-dimensional phonon dispersion relation of the type $\omega(q) = \sqrt{2\omega_0^2[1-\cos(q\pi)]} = 2\omega_0|\sin(q\pi/2)|$, where ω_0 is the free-oscillator frequency. The second $E(q)$ data

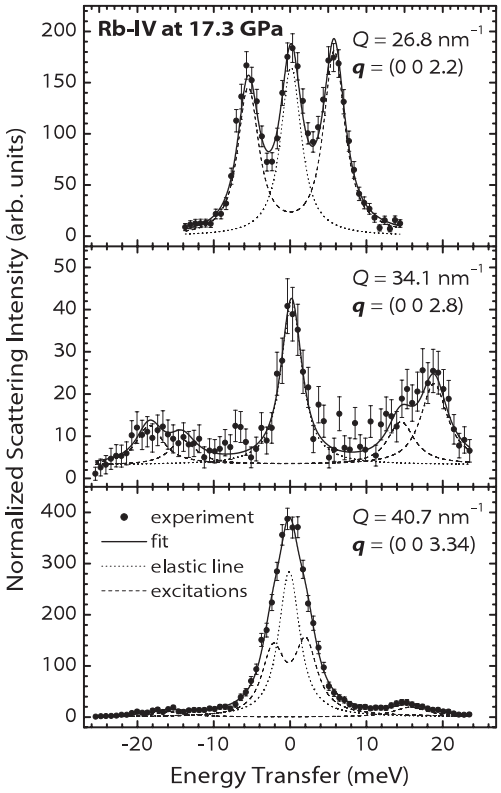

FIG. 2. IXS spectra of Rb-IV at 17.3 GPa ($T = 297$ K). Spectra were recorded at different momentum transfers Q. The reduced wave vector $\boldsymbol{q}$ refers to the reciprocal lattice of the host, with a periodicity of $c_h = 5.1527$ Å along the c direction. The circles indicate the measured intensities; the lines denote the fitted spectra and the contributing components. Note the different intensity scales for the three spectra.

set (open symbols) has a minimum at $(0\ 0\ 3.27)_h$ in the reciprocal lattice of the host, which corresponds to the $(002)_g$ lattice point of the guest structure. The intensity of these excitations decreases rapidly for momentum transfers away from the $(002)_g$ lattice point. The dominant features of the dynamical structure factor $S(\boldsymbol{Q}, \omega)$ are two dispersion branches with the periodicity of the host and the guest lattice, respectively. They are thus assigned to separate LA-type phonon branches of the host and the guest sublattices. Further IXS data of Rb-IV were collected at 18.4, 17.0, and 16.3 GPa, yielding spectra and dispersion curves very similar to those shown in Figs. 2 and 3.

The appearance of two LA-type phonon branches along a certain crystal direction is a unique property of an incommensurate host-guest crystal [8–11]. In an idealized system of a host framework with embedded incommensurate chains, the two subsystems can slide relative to each other. This allows separate longitudinal phonons in the two sublattices, with polarization along the chain direction. In the limit of infinite wavelength, however, a crystal can have only one longitudinal-acoustic mode along the chain direction, which corresponds to a rigid translation of the entire crystal. In an incommensurate composite crystal, there exists a second mode with zero or nearly zero energy,

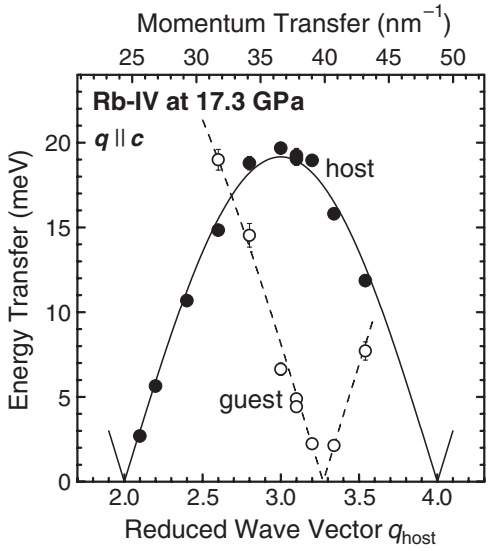

FIG. 3. Dispersion relations of LA lattice excitations in Rb-IV at 17.3 GPa. The reduced wave vector $\boldsymbol{q}$ (parallel to the chains) refers to the reciprocal lattice of the host. The two branches are attributed to lattice excitations of the host (solid symbols) and the guest (open symbols), respectively. The lines indicate phonon dispersion relations of the type $\omega(q) = \sqrt{2\omega_0^2[1 - \cos(q\pi)]}$ fitted to the data.

the phason, which corresponds to a rigid relative displacement of the two subsystems in opposite directions along the chains. There is thus a crossover from two separate LA-type phonon branches at high frequencies to two coupled excitations (the longitudinal-acoustic mode and the phason) at very low energies near the Brillouin zone center. In the case of $Hg_{3-\delta}AsF_6$, the crossover was estimated to occur at frequencies of the order of 1 MHz ($\approx 10^{-5}$ meV) [9], i.e., several orders of magnitude below the energy range accessible by IXS.

The theoretical aspects of the lattice dynamics of incommensurate composite systems have been studied in detail [6–11] in the context of the prototype host-guest compound systems $Hg_{3-\delta}AsF_6$ and alkane/urea, while experimental investigations have remained scarce. Recent numerical studies of various model systems with finite interaction between the subsystems indicate a complex structure of the dynamical structure factor $S(\boldsymbol{Q}, \omega)$ [6,20,21]: zone folding is believed to cause a multitude of dispersion branches that are separated by (pseudo-) gaps.

The dynamical structure factor of Rb-IV presented here is dominated by separate LA-like phonon branches of the host and the guest. Only a few of the IXS spectra indicate the possible existence of additional spectral weight that does not originate from the main phonon branches. These features were, however, extremely weak thus preventing their study in detail. Much stronger interaction between the host and guest is presumably required to observe deviations from the two-LA-branch scenario.

The high-frequency sound velocities (i.e., above the crossover from coupled to separate longitudinal modes) in the host and guest structures (Fig. 4) were determined from the initial slopes of the fitted phonon dispersion relations. The sound velocities of the host and the guest, v_h and v_g, respectively, are rather similar in magnitude and their interpolated values are equal at a pressure of 18 GPa, $v_h = v_g = 3840(100)$ m/s. The speed of sound in the chains increases linearly at a rate of $dv_g/dP = 280(80)$ m/s GPa^{-1}, while the present data indicate a lower pressure dependence for the host, $dv_h/dP = 140(60)$ m/s GPa^{-1}. The sound velocities determined here for the guest chains are ~10% lower than the estimate derived recently from diffuse x-ray scattering of the disordered chains in the pressure range 16.2–16.4 GPa [15]. In view of the substantial challenges posed by the analysis of diffuse x-ray scattering data from a sample in a DAC, this is a good agreement, and it corroborates the analysis and model used in Ref. [15].

The present data provide no evidence of a significant change in the sound velocity along the chains below 16.7 GPa, the pressure at which the interchain correlation length begins to decrease rapidly [14,15]. As for the sound velocity in the host subsystem, we consider it unlikely that there is an anomaly at this pressure, given the lack of any measurable change in the crystal structure of the host at 16.7 GPa [18]. However, the results in Fig. 4 are not conclusive in this respect and further studies at a greater number of pressures would be needed to address these questions definitively.

As for the difference between the pressure dependences of the sound velocities of the host and the guest (while their absolute values are rather close), a simple ball-and-spring model of Rb-IV with one single spring constant for all nearest-neighbor interactions (without host-guest interaction) reproduces this situation semiquantitatively, including the larger compressibility of the chains. This suggests that the *ratios* of (i) the host and guest sound velocities along c, (ii) their pressure dependences, and (iii) the compressibilities along c are determined largely by geometrical factors, i.e., by the spatial arrangement of the atoms rather than details of the chemical bonding in the two subsystems.

The very weak coupling between the incommensurate host and the guest in Rb-IV raises a rather interesting question. Can the 1D chains of guest atoms in Rb-IV be considered a realization of the "monatomic linear chain" treated in textbooks (e.g., Ref. [22]) to introduce the concepts of crystal lattice dynamics? In order to calculate the sound velocity according to $v = d\sqrt{K_g/M}$ in the linear chain model, one needs to determine the force constant K_g and the atomic spacing $d \equiv c_g$ of the guest chains. K_g can be derived from the lattice parameter c_g measured as a function of pressure by x-ray diffraction [Fig. 1(b)]. One assumption needs to be made in order to calculate forces from c_g versus pressure, namely, on the effective cross sectional area of the chains. At 17.5 GPa, the minimum chain-host distance and the average distance between atoms in the chains are 3.11 and 3.15 Å, respectively, and

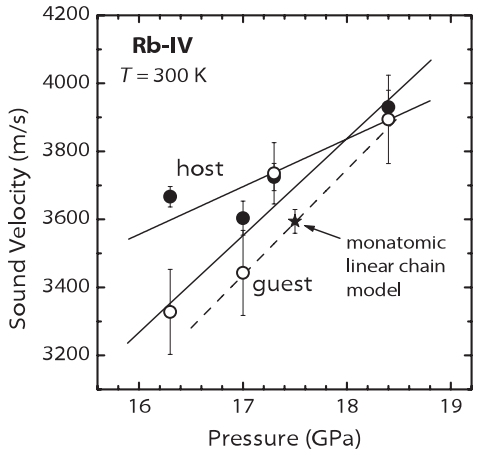

FIG. 4. Pressure dependences of the sound velocities of the LA phonons along the c directions of the host and the guest subsystem of Rb-IV. The solid lines represent linear regressions to the experimental data, and the error bars are derived from the uncertainties determined in the least-squares fitting of the phonon dispersion curves. The star and the dashed line indicate the estimated sound velocity and its pressure dependence in a monatomic linear chain of Rb.

the smallest tabulated value for the Rb^+ ionic radius is 1.48 Å [23,24]. We have therefore chosen an effective radius of $R = 1.50$ Å for the Rb chains. From x-ray diffraction measurements of the intrachain Rb-Rb distances, that is c_g, in the pressure range 16.6–18.5 GPa [Fig. 1(b)], a force constant of $K_g = -\pi R^2 dP/dc_g = 18.5(4)$ N/m is determined for the guest chains at 17.5 GPa. With $c_g = 3.1480(7)$ Å at the same pressure, one obtains a sound velocity of $v_g = 3594(35)$ m/s in the guest chains at $P = 17.5$ GPa, in excellent agreement with the guest sound velocity of 3700(100) m/s obtained by interpolating the measured data as shown in Fig. 4.

The success of the linear chain model encouraged us to estimate also the pressure dependence of v_g. The limiting factor in calculating this is the accuracy of the pressure derivative of K_g, since this requires the *second* pressure derivative of the lattice parameter c_g. As high-precision values of c_g could only be obtained from the diffractograms of single-phase and fully ordered Rb-IV between 16.6 and 18.5 GPa [Fig. 1(b)], d^2c_g/dP^2 is not very well constrained by the experiment. With $d^2c_g/dP^2 = 0.0038(14)$ Å/GPa^2, an estimate of $dv_g/dP = 310(140)$ m/s GPa^{-1} is obtained, as indicated by the dashed line in Fig. 4, which is in good agreement with the measured pressure dependence, $dv_g/dP = 280(80)$ m/s GPa^{-1}. It can thus be concluded that the guest-atom chains in the composite Rb-IV structure do indeed represent a realization of the monatomic linear chain model with regard to the LA phonons.

In summary, we have reported the first experimental investigation of the lattice dynamics in an element with a composite crystal structure. Two well-defined LA-type phonon branches are observed in Rb-IV along the direction of the incommensurate wave vector, which are assigned to separate LA-type phonons of the host and the guest sublattices. The LA phonons in the chains are well described by the classic monatomic linear chain model. The present observations motivate further studies in search for zone-folding effects and gaps in the dynamical structure factor $S(\boldsymbol{Q}, \omega)$, which are predicted by theory but have not been observed in the present work.

This work was supported by grants from EPSRC.

*Corresponding author.
I.Loa@ed.ac.uk

[1] U. Schwarz, Z. Kristallogr. **219**, 376 (2004); M. I. McMahon and R. J. Nelmes, Chemical Society Reviews **35**, 943 (2006).
[2] M. I. McMahon, S. Rekhi, and R. J. Nelmes, Phys. Rev. Lett. **87**, 055501 (2001).
[3] U. Schwarz *et al.*, Phys. Rev. Lett. **83**, 4085 (1999).
[4] E. Yu. Tonkov and E. G. Ponyatovsky, *Phase Transformations of Elements Under High Pressure* (CRC Press, Boca Raton, 2005).
[5] S. K. Reed and G. J. Ackland, Phys. Rev. Lett. **84**, 5580 (2000); U. Häussermann, K. Söderberg, and R. Norrestam, J. Am. Chem. Soc. **124**, 15 359 (2002); G. J. Ackland and I. R. Macleod, New J. Phys. **6**, 138 (2004); G. J. Ackland and H. Fox, J. Phys. Condens. Matter **17**, 1851 (2005).
[6] O. Radulescu, T. Janssen, and J. Etrillard, Eur. Phys. J. B **29**, 385 (2002).
[7] R. Currat, E. Kats, and I. Luk'yanchuk, Eur. Phys. J. B **26**, 339 (2002).
[8] J. D. Axe and P. Bak, Phys. Rev. B **26**, 4963 (1982).
[9] W. Finger and T. M. Rice, Phys. Rev. Lett. **49**, 468 (1982).
[10] W. Finger and T. M. Rice, Phys. Rev. B **28**, 340 (1983).
[11] G. Theodorou and T. M. Rice, Phys. Rev. B **18**, 2840 (1978).
[12] J. M. Hastings *et al.*, Phys. Rev. Lett. **39**, 1484 (1977).
[13] I. U. Heilmann *et al.*, Phys. Rev. B **20**, 751 (1979).
[14] M. I. McMahon and R. J. Nelmes, Phys. Rev. Lett. **93**, 055501 (2004).
[15] S. Falconi *et al.*, Phys. Rev. B **73**, 214102 (2006).
[16] M. McMahon and R. Nelmes, Z. Kristallogr. **219**, 742 (2004).
[17] M. Krisch, J. Raman Spectrosc. **34**, 628 (2003).
[18] M. I. McMahon and L. F. Lundegaard *et al.* (to be published).
[19] Computer program FIT28, ESRF.
[20] N. S. Luo, S. Y. Wu, and C. S. Jayanthi, Phys. Rev. B **55**, 11 300 (1997).
[21] L. A. Brussaard, A. Fasolino, and T. Janssen, Phys. Rev. B **63**, 214302 (2001).
[22] N. W. Ashcroft and N. D. Mermin, *Solid State Physics* (Saunders College Publishing, Fort Worth, 1976).
[23] M. F. C. Ladd, Theor. Chim. Acta **12**, 333 (1968).
[24] R. D. Shannon, Acta Crystallogr. Sect. A **32**, 751 (1976).

Phase transitions in tellurium at high pressure and temperature

C. Hejny,* S. Falconi, L. F. Lundegaard, and M. I. McMahon
SUPA, School of Physics and Centre for Science at Extreme Conditions, The University of Edinburgh, Mayfield Road, Edinburgh, EH9 3JZ, United Kingdom

(Received 20 December 2005; revised manuscript received 28 August 2006; published 22 November 2006)

The structural phase transitions in tellurium have been studied up to 21 GPa and 743 K using powder-diffraction techniques. We find the incommensurate Te-III phase to be stable up to at least 743 K, and have determined the *P-T* dependence of the incommensurate wave vector q. We also find that the rhombohedral β-Po phase of Te, Te-IV, previously reported to exist at room temperature, is stable only above 315 K.

DOI: 10.1103/PhysRevB.74.174119 PACS number(s): 61.50.Ks, 62.50.+p

Incommensurately modulated structures have recently been found to be a well established and frequently encountered phenomenon in the elements at high pressure.[1] In contrast to the simple structures they adopt at ambient pressure, K, Rb, Sr, Ba, As, Sb, Bi, and Sc all have an incommensurate host-guest composite structure at high pressure, comprising a tetragonal "host" framework with channels along the c axis.[1–8] Contained within these channels are one-dimensional chains of atoms that form a "guest" structure, which is incommensurate with the host along their common c axis.[1] It has been proposed that phosphorous also has a composite host-guest structure,[9] or an incommensurately modulated structure,[10] above 100 GPa, but this has not yet been confirmed experimentally.

Recently, we have reported that the group VI*a* elements S, Se, and Te possess noncomposite incommensurate structures at high pressure,[11–13] and incommensurate structures have also been reported in I and Br.[14,15] At room temperature, the incommensurate phase of Te, Te-III, is stable from 4.5(2) to 29.2(7) GPa, where it transforms into the body-centered cubic (bcc) structure, Te-V.[11,16] In Se and S, the incommensurate phases (Se-IV and S-III) are stable from 41 to ~80 GPa and from 75 to 153(5) GPa, respectively,[12,13,17,18] and in both cases they transform to the rhombohedral β-Po structure. The same structure is not observed in Te at room temperature.[11] In Se, there is a further known transition to the bcc structure at 140(3) GPa,[17,18] while the β-Po phase of sulfur is known to be stable to at least 212 GPa.[19]

The incommensurate structures of S-III, Se-IV, and Te-III are the same and four unit cells of the structure are shown in Fig. 1. The basic unmodulated structure is body-centered monoclinic (bcm), spacegroup $I2/m$, with two atoms per unit cell. The modulated structure has superspacegroup $I'2/m(0q0)s0$, where I' denotes the centering $(\frac{1}{2},\frac{1}{2},\frac{1}{2},\frac{1}{2})$ in superspace, and the modulation wave vector is $q=0.287(1)$ in Te-III at 8.5 GPa.[11] The modulation wave vector is strongly pressure dependent in Te-III at 300 K, varying from its maximum value of 0.314(2) at 5 GPa, just above the Te-II→Te-III transition, to a minimum value of 0.274(2) at 15.5(2) GPa, before increasing again to a value of 0.287(2) at 26.5 GPa.[11] Similar strong pressure dependence is found in Se-IV and S-III.[12,13] A peculiarity of the pressure dependence of Te is that the rhombohedral β-Po structure is not observed at room temperature, in contrast to Se and S, where this phase is found to be stable over wide pressure ranges of 60 GPa and at least 59 GPa, respectively.[17,18] (We believe that previous reports of a transition in Te to the β-Po structure at 10.6 GPa[16] arose because the poorer resolution of the previous diffraction studies was unable to distinguish diffraction patterns of Te-III from those of the proposed β-Po structure above this pressure.)

Although they are known to be stable over wide pressure ranges at 300 K, there have, as yet, been no *in situ* studies of the stability of *any* of the composite or modulated phases of the elements at elevated temperatures. Nor is there any information on the temperature dependence of their incommensurate wave vectors q. In this paper we describe the first such study, with a high-pressure high-temperature (HP-HT) diffraction study of the modulated structure of Te-III up to 7.9 GPa and 743 K. We find that the incommensurate phase is stable up to the highest temperatures investigated, and have determined the *P-T* dependence of q. We also find that a phase of Te with the rhombohedral β-Po structure (Te-IV), which was not observed previously at room temperature,[11] is stable over a wide range of P and T above 315 K, and we have determined the gradients of both the III→IV and IV→V phase boundaries.

Angle-dispersive x-ray diffraction data from powdered Te were obtained on beamline ID09 at the European Synchrotron Radiation Facility (ESRF), Grenoble, France. Preliminary HP-HT studies were also conducted on station 9.1 at the Synchrotron Radiation Source, Daresbury Laboratory, UK. The sample was prepared from starting material of 99.9999% purity obtained from the Aldrich Chemical Company. Diffraction profiles collected at ambient pressure revealed only peaks from the known trigonal phase, Te-I. Two samples were loaded into resistively heated WCMA diamond-anvil cells[20] with a small amount of $SrB_4O_7:Sm^{2+}$ and Mo for pressure measurement.[21,22] The uncertainty in pressure measurements was determined from repeated measurements of the pressure both before and after the collection of the diffraction data and was typically 0.2 GPa, or less.

In order to collect data into the liquid phase above 730 K at 2.8 GPa, a third sample was loaded into a lever-arm pressure cell equipped with both internal and external heaters. This enabled a maximum temperature of 793 K to be reached. The temperatures of the samples were measured with a thermocouple placed inside the cells in contact with the gasket and confirmed by measuring the temperature of the back of one of the diamond anvils. The two temperatures agreed to within 5 K. Diffraction data were collected on both

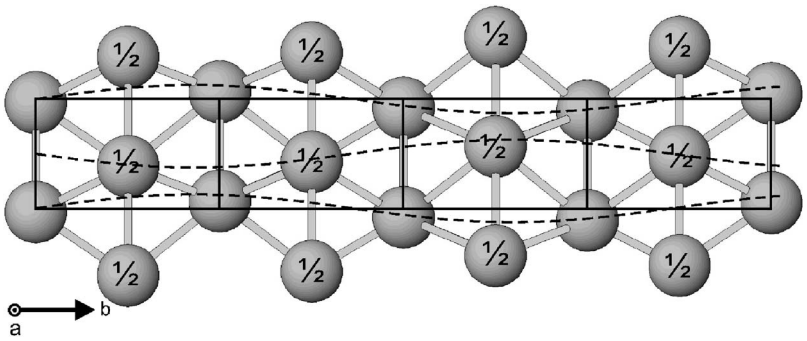

FIG. 1. A view down the *a* axis of four unit cells of Te-III at 8.5 GPa. The six nearest-neighbor contact distances for each atom are shown, and those atoms at the body centers are labeled with "$\frac{1}{2}$." The modulation wave with $q=0.287(1)$ is indicated by the dotted lines. Note: The displacements of the atoms labeled "$\frac{1}{2}$" were shown incorrectly in Refs. 1, 11, 12, and 17 and 18, though the description in terms of structural parameters was correct. These atoms are displaced in antiphase to those at the corners of the unit cell, and not in phase as previously shown.

pressure increase and decrease, and the *P-T* paths followed by the three different samples are shown in Fig. 2. The diffraction measurements were made using an x-ray wavelength of 0.410 11 Å and an incident beam size of 20 μm $\times$20 μm. The exposure time for each image was typically 20 s, during which the sample was oscillated by ±3° to improve the powder averaging. The diffraction data were collected on a MAR345 image-plate detector placed approximately 370 mm from the sample, and the two-dimensional diffraction images were integrated using FIT2D (Ref. 23) to give standard diffraction profiles. Rietveld refinement of these profiles was performed within the formalism of four-dimensional superspace[24] using JANA2000.[25]

No pressure transmitting medium was utilized in the study, as the commonly used methanol:ethanol:water mixture was found to react with Te at elevated temperatures. The absence of a pressure medium, and the resulting nonhydrostatic environment, can produce deviatoric stresses and lattice distortions in the sample, giving *hkl*-dependent peak shifts. Analysis of the peak positions across the full 2θ range of the diffraction profiles revealed that the observed and calculated peak positions (*d* spacings) agreed within 0.0003 Å at all pressures. Furthermore, analysis of the two-dimensional diffraction images with FIT2D revealed that none of the Debye-Scherrer rings had any deviation from circular symmetry. Despite the absence of a pressure medium, therefore, we observed no evidence of any lattice distortions produced by deviatoric stress.

Figure 3 shows the diffraction profiles collected on pressure increase at 473 K. At 8.7 GPa, numerous satellite peaks arising from the incommensurate modulation are visible, as marked with asterisks in the inset to Fig. 3. The intensity of the modulation peaks decreases with increasing pressure, as observed previously at room temperature,[11] and on pressure increase from 22.0 to 23.0 GPa they all disappeared, and the diffraction profile at 23.0 GPa contained only intense peaks. In addition, some of the intense peaks, which were clearly separated at 22.0 GPa and below, became singlets above this pressure. All of the diffraction peaks at 23.0 GPa and 473 K can be fitted by the previously reported Te-IV β-Po structure, spacegroup $R\bar{3}m$, with $a_h=4.6873(3)$ Å and $c_h=3.5474(2)$ Å in the hexagonal setting [$a_r=2.9533(2)$ Å, $\alpha_r=105.042(2)°$ in the rhombohedral setting[26]], and an atom

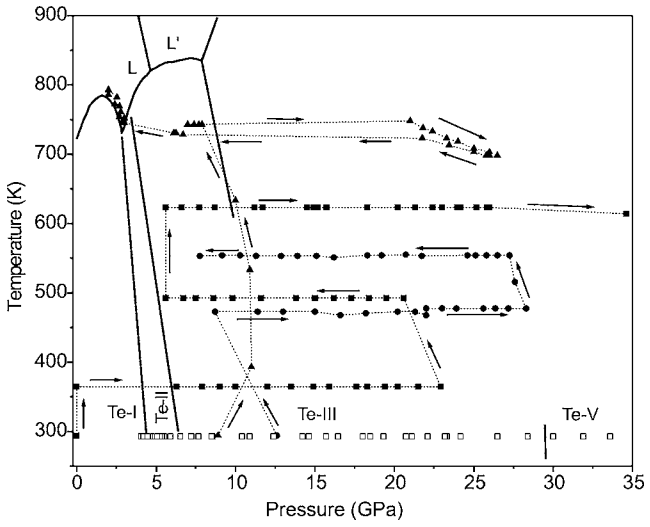

FIG. 2. The reported *P-T* phase diagram of Te (Ref. 28), showing the *P-T* paths taken by the three samples. The data points plotted with unfilled symbols at room temperature are from Refs. 11 and 29.

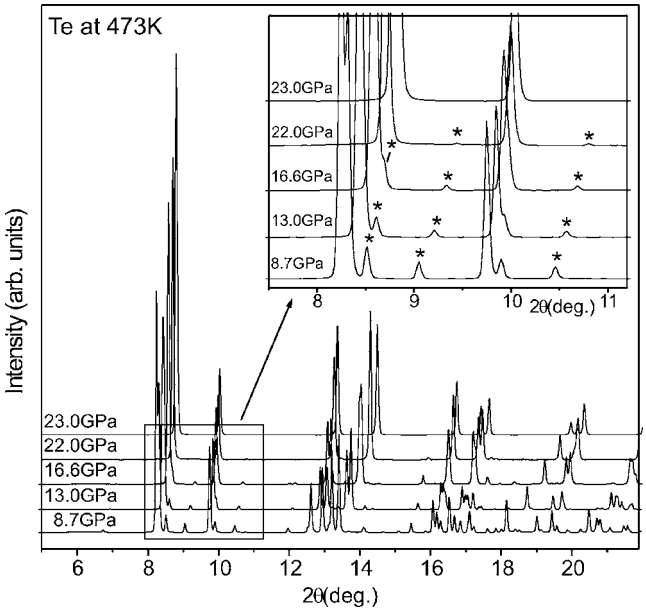

FIG. 3. Diffraction profiles collected from Te as a function of pressure at 473 K, showing the transition from monoclinic Te-III to rhombohedral Te-IV between 22.0 and 23.0 GPa. The inset shows an enlarged view of the low-angle part of the profiles. Those diffraction peaks arising from the incommensurate modulation in Te-III are identified in the inset with asterisks.

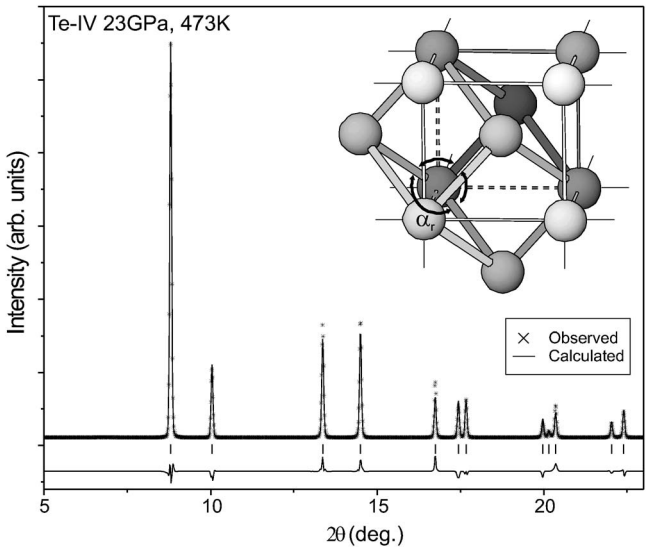

FIG. 4. Rietveld refinement of the rhombohedral β-Po structure of Te-IV at 23 GPa and 473 K. The tick marks below the profile show the calculated peak positions, and the difference between the observed and calculated profiles is shown below the tick marks. The inset shows the relationship between the β-Po structure and the body-centered cubic structure. The rhombohedral angle α_r is indicated.

on the 3*a* site at (0,0,0). A Rietveld refinement of the Te-IV profile obtained at 23.0 GPa and 473 K is shown in Fig. 4. Te-IV, which is not observed on compression at room temperature,[11] is thus found to be a stable phase of tellurium at elevated temperatures.

The pressure dependence of the lattice parameters of Te-III and Te-IV at 473 K (both indexed on the monoclinic unit cell of Te-III to enable comparison through the phase transition[27]) is shown in Fig. 5. As in the bcm$\rightarrow\beta$-Po transitions in Se and S (Refs. 17 and 18) there is no measurable discontinuity in any of the lattice parameters at the Te-III $\rightarrow$Te-IV phase transition [see Figs. 5(a) and 5(b)], and no measurable discontinuity in the atomic volume [Fig. 5(c)]. Furthermore, a plot (Fig. 6) of the pressure dependence of the monoclinic distortion away from rhombohedral symmetry – $D=(\sin\beta - b/\sqrt{3}c)$ – again shows that there is no discontinuity within the uncertainties. The Te-III$\rightarrow$Te-IV transition thus appears to be continuous.

Because of its close relationship to the primitive cubic structure of α-Po, the rhombohedral β-Po structure type is normally regarded as being a primitive cubic structure that has been compressed along the body diagonal. As a result, the hexagonal setting of the β-Po rhombohedral unit cell has a c/a ratio that is smaller than the value of 1.225 it would have in a primitive cubic cell. Furthermore, if the c/a ratio is decreased to 0.612, then the β-Po structure becomes body-centered cubic, with the structural relationship shown in the inset to Fig. 4. Depending on the c/a ratio, therefore, the β-Po structure may be regarded as either a primitive cubic structure compressed along the body diagonal ($c/a<1.225$), or as a body-centered cubic structure elongated along the body diagonal ($c/a>0.612$). In the group VIa elements S, Se, and Te, the c/a ratio of their β-Po structures lies between

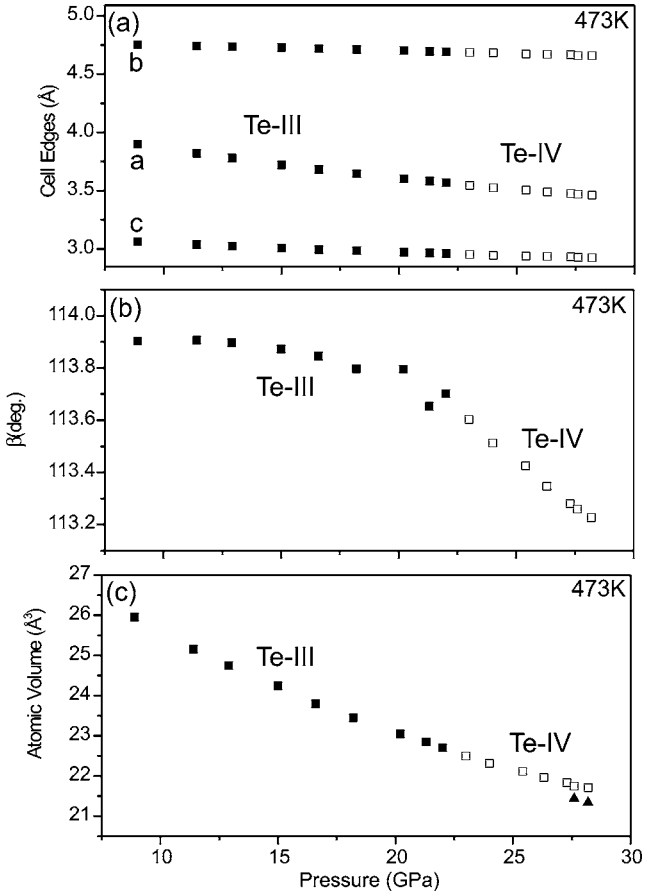

FIG. 5. Pressure dependence of (a) the unit-cell edges, (b) the monoclinic angle β, and (c) the atomic volume, of monoclinic Te-III (filled symbols), and rhombohedral Te-IV (indexed on the same monoclinic unit cell as Te-III and plotted with unfilled symbols) as a function of pressure at 473 K. In all three plots, the uncertainties are smaller than the symbols used to plot the data. Plot (c) also shows two data points for the atomic volume of bcc Te-V (plotted with filled triangles), illustrating the first-order nature of the Te-IV$\rightarrow$Te-V transition at 27.7(5) GPa.

0.74 and 0.8, depending on the pressure, and these structures can therefore all be regarded as a distortion of the body-centered cubic structure. For example, in Se-IV at 110 GPa and 300 K, $c/a=0.7449$ (Ref. 18) while in S-V at 160 GPa and 300 K the value is 0.7969.[18] Figure 7 shows the pressure dependence of the c/a ratio of Te-IV at three different temperatures, showing that in all cases c/a has a value of 0.74–0.77 and, like the equivalent structures in Se and S, Te-IV is much closer to having a bcc structure than a primitive cubic structure. Furthermore, since c/a decreases with pressure, the Te-IV structure becomes more bcc-like at higher pressures. However, the transition from rhombohedral Te-IV to bcc Te-V at 27.7(5) GPa and 473 K is first order, with a volume discontinuity ($\Delta V/V_{trans}$) of 1.5(1)%, where V_{trans} is the atomic volume of Te-IV at the transition [Fig. 5(c)].

The inset to Fig. 7 shows an enlarged view of part of the Te-IV diffraction profiles collected as a function of pressure at 473 K. At 23 GPa, the (003) reflection is at a lower 2θ value than the $(42\bar{0})$ reflection and thus $c/a>0.75$. However, with increasing pressure, the two reflections move

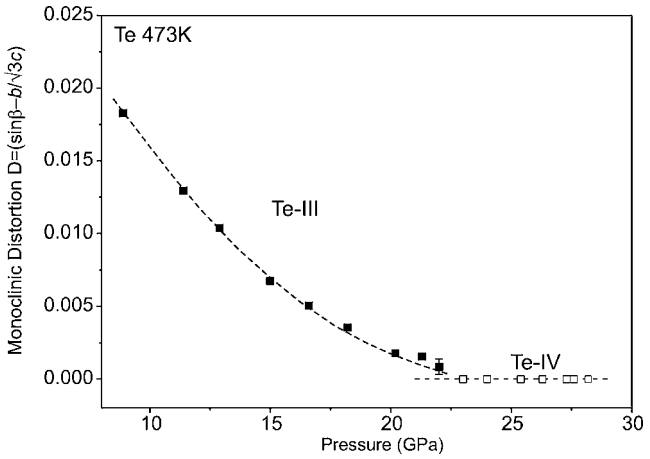

FIG. 6. Pressure dependence of the distortion away from rhombohedral symmetry, $D=(\sin\beta - b/\sqrt{3}c)$, in Te-III and Te-IV. Where no error bars are shown the uncertainties are smaller than the symbols used to plot the data. The lines through the data are guides to the eye.

closer together, as a result of the decrease in the c/a ratio with pressure, and at 25.4 GPa, where $c/a=0.75$, the two reflections overlap, resulting in a further simplification of the diffraction profile. However, at higher pressures, where c/a becomes <0.75, the two reflections again separate, but with the (003) reflection having a higher 2θ value than the $(4\bar{2}0)$ reflection.

Analysis of the 122 diffraction profiles collected from the three samples of Te (Fig. 2) revealed that they could all be indexed on either the Te-I, Te-II, Te-III, Te-IV, or Te-V structures, as a mixture of these phases, or from the liquid phase. The phase boundaries between the various phases were then

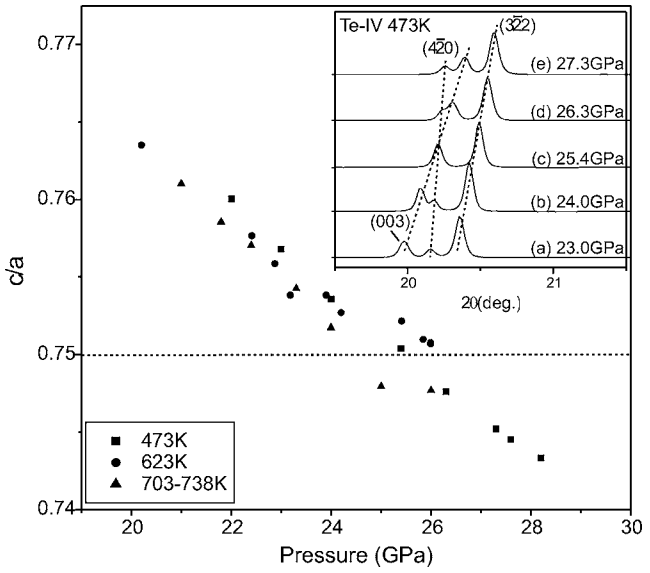

FIG. 7. Pressure dependence of the c/a ratio of rhombohedral Te-IV as a function of pressure at three different temperatures. The inset shows the diffraction profiles obtained as a function of pressure at 473 K, showing the overlap of the (003) and $(4\bar{2}0)$ reflections at 25.4 GPa when $c/a=0.75$.

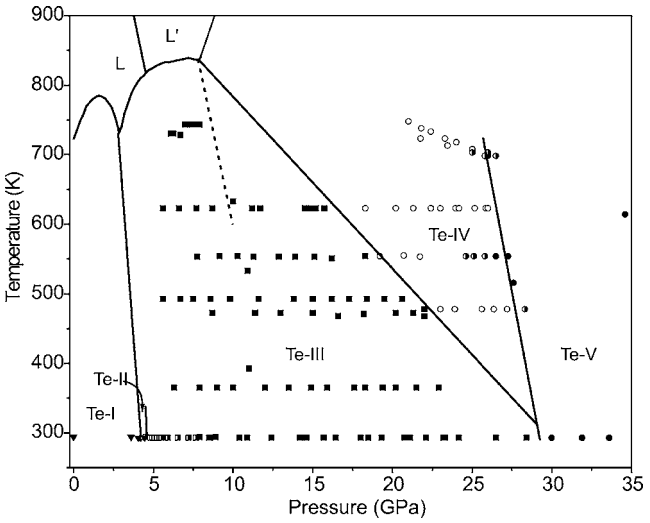

FIG. 8. Phase diagram of Te to 35 GPa and 900 K. The melting curve, the phase boundary between the two liquid phases (L and L'), and the Te-I→Te-II phase boundary are taken from Ref. 28. Half-filled symbols denote mixed-phase profiles. The Te-III→Te-IV and Te-IV→Te-V phase boundaries were determined from the first appearance of the higher-pressure phase on pressure increase—compare Fig. 2. The dashed line shows the Te-III→Te-IV phase boundary reported in Ref. 28.

located by determining the pressure at which the higher-pressure phase first appeared on compression. In determining the Te-III→Te-IV (III→IV) phase line, we also used the fact that Te-IV is not observed at room temperature, and therefore that this phase boundary must intercept that of the IV→V transition above room temperature. Extrapolation of the phase boundary consistent with this constraint, and the pressures at which Te-IV first appears on compression at 473 and 623 K, suggests that the triple point previously identified by Brazhkin *et al.* at 7.6 GPa and 835 K (Ref. 28) is between the L', Te-III, and Te-IV phases. Our proposed III→IV phase boundary was thus chosen to terminate at this triple point. The resulting phase diagram for Te is shown in Fig. 8. The gradients of the III→IV and IV→V transition lines are $-25(5)$ K GPa^{-1} and $-112(9)$ K GPa^{-1}, respectively. Although Brazhkin *et al.* did identify the 7.6 GPa/835 K triple point as being between the L', Te-III, and Te-IV phases, their determination of the III→IV phase line, shown in Fig. 8 as a dashed line terminating at the triple point, is inconsistent with the results of this diffraction study. The most notable feature of the new phase diagram of Te is the stability field of rhombohedral Te-IV, which is found to be the equilibrium phase at temperatures above the III-IV-V triple point at 29.0 GPa and 315 K. The stability field of Te-IV increases rapidly with increasing temperature, becoming more than 10 GPa wide above 620 K.

Although the transition pressures for the I→II and II→III transitions are well determined as 4.0 and 4.5 GPa at 300 K (Refs. 11 and 29), (Fig. 8), and the temperature dependence of the I→II transition has been followed up to the liquid-I-II triple point at 2.9 GPa and 718 K (Refs. 28 and 30), the temperature dependence of the II→III phase boundary is less well determined. Previous studies of the slope of

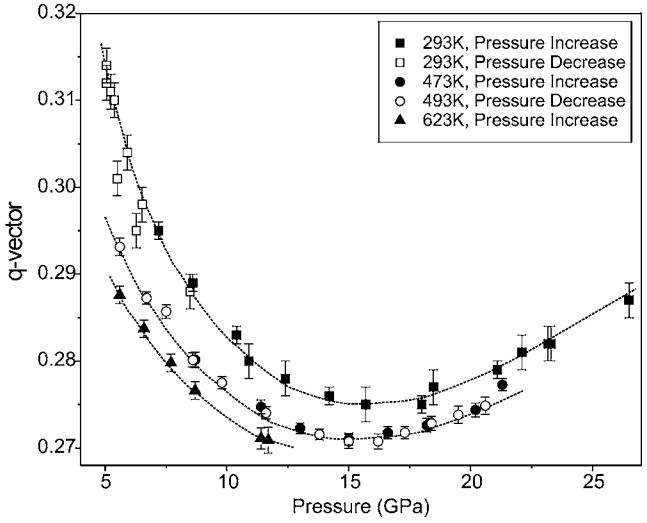

FIG. 9. Pressure dependence of the incommensurate wave vector q in Te-III at room temperature, 473/493 K, and at 623 K. The dashed lines drawn through the data points are guides to the eye.

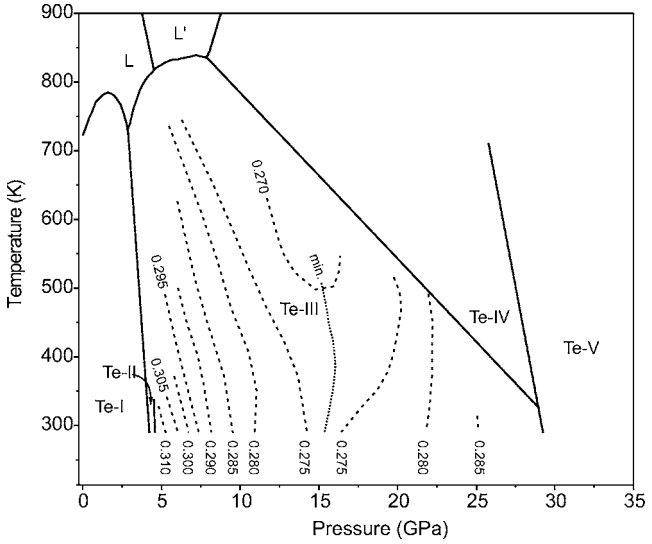

FIG. 10. Phase diagram of Te to 35 GPa and 900 K showing the P-T dependence of the incommensurate wave vector q within the Te-III phase. The dashed lines mark contours of constant q, in increments of 0.005. These contours were determined from the average value of q obtained on pressure increase and decrease. The dotted line marked "min." denotes the position of the minimum value of q obtained at each temperature.

this boundary at high temperatures[28,30,32] have been consistent with the room-temperature transition pressure of 7 GPa reported by Bridgman,[31] rather than our significantly lower value of 4.5 GPa. However, one of these previous studies[30] noted that the II↔III transition was difficult to detect, and reported that they could see no evidence of it below 573 K. We have previously reported that although diffraction peaks from Te-III first appear at 4.5 GPa on compression at room temperature, single-phase profiles of Te-III are observed only above 8 GPa.[11,29] The higher pressures reported for the II→III transition[28,31] may then be a consequence of the insensitivity of these (nondiffraction) studies to the small amounts of Te-III that exist below 7 GPa. Because of this uncertainty in the II→III phase boundary, we have shown it only near 300 K in Fig. 8.

The large number of Te-III diffraction profiles has enabled us to determine the P-T dependence of the incommensurate wave vector q. Attempts to also determine the P-T dependence of the amplitude of the incommensurate modulation were unsuccessful, as the recrystallization of the sample that occurred at high temperatures resulted in peak intensities that were inconsistent both from pressure to pressure, and between different samples. Despite therefore being unable to obtain quantitative results, and thus to establish the relationship between the amplitude of the incommensurate modulation and the monoclinic distortion away from rhombohedral symmetry (see Fig. 6), qualitative analysis of the Te-III profiles shows that the amplitude of the modulation clearly decreases with increasing temperature, but that incommensurate satellite reflections are still visible at 7.9 GPa at 743 K, the highest P and T at which data were collected within the Te-III stability field (see Fig. 8).

Figure 9 shows the pressure dependence of q at room temperature,[11] at 473/493 K on pressure increase/decrease, and at 623 K on pressure increase. The previous room temperature results[11] are also shown for comparison. q is clearly strongly dependent on both P and T. As reported previously, q initially decreases on compression at room temperature before reaching a minimum and then increasing again. Similar behavior is observed on compression at higher temperatures. q is also strongly temperature dependent, and decreases with increasing temperature, with the change being largest at lower pressures. We have previously noted the close relationship of the triclinic Te-II structure to the (commensurate) Te-III structure obtained when the q vector is $(0,\frac{1}{3},0)$, and thus when the b axis of Te-III is tripled in length.[29] At room temperature, the value of q at 5 GPa, just above the II→III phase transition, is 0.314(2) (Fig. 9), close to the commensurate value of $\frac{1}{3}$. However, on increasing the temperature at constant pressure, q decreases sharply; from 0.314 to ~0.290 on increasing the temperature from room temperature to 623 K at 5 GPa (Fig. 9). If the III→II transition occurs when q is close to $\frac{1}{3}$, then this suggests that the transition pressure may decrease with increasing temperature. Extrapolation of the data at 473 and 623 K in Fig. 9 suggests that q will have a value of 0.314 at ~3.1 GPa at 473 K, and at ~2.5 GPa at 623 K. Both of these pressures are below the I↔II phase boundary shown in Fig. 7, suggesting that the transition to Te-II may occur with q being more discrepant from $\frac{1}{3}$ at higher temperatures.

Finally, Fig. 10 shows the P-T dependence of q, illustrated using contours of constant q. The contours were determined by interpolating between the measured values of q, and by averaging over data collected on pressure increase and decrease. The weakness of the incommensurate satellite peaks at the highest pressures and temperatures prevented us determining q above 12 GPa at 623 K and above 7 GPa at 743 K, even though satellite peaks were visible to 7.9 GPa at 743 K. The range of values of q clearly decreases with increasing temperature, principally as a consequence of the reduced stability field of Te-III, but also because of the de-

crease in q with increasing T at lower pressures. And while the location of the minimum in q remains almost unchanged with temperature, the minimum deepens, and extrapolation suggests that q values as small as 0.26 might be obtained near the L'-III-IV triple point.

The reasons *why* incommensurate structures should be stable at high pressures and high temperatures is still unclear, as the very thing that makes them so intriguing, their incommensurate nature, also prevents exact electronic structure calculations of their properties. However, calculations have been made on commensurate analogues as approximations, and these have provided some insight into the incommensurate composite structures, reproducing their reported transition sequence[33–35] and suggesting that in Ba-IV, the host and guest atoms have different electronic structures,[33] with the host and guest atoms being more *s*- and *d*-like, respectively. However, such differences were not found in calculations of the composite structures in the group V*a* elements (As, Sb, and Bi), which suggested, rather, that the stability of the composite structures arises from the interplay of band and electrostatic energies.[34] The stability of the composite phases has also been analyzed within the Hume-Rothery mechanism,[37,38] which suggests that an interaction between the Fermi surface and the Brillouin zone results in the opening of a pseudogap and a reduction in the overall electronic energy of the structure. Recent calculations have also given insight into the Te-III-like modulated phase of sulfur.[36] Calculations of the topology of the Fermi surface at 100 GPa show that it exhibits parallel zones, indicating Fermi surface nesting, characterized by a wave vector that is very similar to that observed experimentally.[36] And calculations of phonon dispersion at the same pressure show a softening at the same wave vector as the nesting vector, indicating that the incommensurate phase in metallic sulfur at megabar pressures — and therefore probably in isostructural Se-IV and Te-III — may be due to a charge-density wave. Te-III offers the best opportunity for confirming this experimentally, since the availability of single-crystal samples of the incommensurate phase[11] will enable the use of inelastic x-ray-scattering techniques to investigate the lattice dynamics, and search for the predicted phonon softening.

In conclusion, the structural phase transitions in tellurium have been studied as a function of pressure and temperature up to 21 GPa and 743 K, the first time the stability of an elemental high-pressure incommensurate phase has been studied *in situ*. We find that incommensurate Te-III is stable up to at least 7.9 GPa and 743 K, and have determined the P-T dependence of the incommensurate wave vector q. We find that the rhombohedral β-Po phase of tellurium, Te-IV, is stable only above 315 K, but that the stability field increases strongly with increasing temperature. Both the Te-III-Te-IV and Te-IV-Te-V phase boundaries have been determined to 27 GPa, and the III-IV-V triple point has been located at 315 K and 29.0 GPa.

We thank Dr. M. Hanfland of the ESRF for assistance in setting up the ID09 beam line, and Dr. M. Roberts and Dr. A. Lennie of Daresbury Laboratory for assistance in setting up the 9.1 beam line. This work was supported by grants from EPSRC, funding from CCLRC, and facilities provided by European Synchrotron Radiation Facility and Daresbury Laboratory.

*Present address: Institute of Mineralogy and Petrography, University of Innsbruck, Innrain 52, A-6020 Innsbruck, Austria.

[1] M. I. McMahon and R. J. Nelmes, Z. Kristallogr. **219**, 742 (2004).
[2] R. J. Nelmes, D. R. Allan, M. I. McMahon, and S. A. Belmonte, Phys. Rev. Lett. **83**, 4081 (1999).
[3] M. I. McMahon, T. Bovornratanaraks, D. R. Allan, S. A. Belmonte, and R. J. Nelmes, Phys. Rev. B **61**, 3135 (2000).
[4] M. I. McMahon, S. Rekhi, and R. J. Nelmes, Phys. Rev. Lett. **87**, 055501 (2001).
[5] M. I. McMahon, O. Degtyareva, and R. J. Nelmes, Phys. Rev. Lett. **85**, 4896 (2000).
[6] O. Degtyareva, M. I. McMahon, and R. J. Nelmes, Phys. Rev. B **70**, 184119 (2004).
[7] H. Fujihisa, Y. Akahama, H. Kawamura, Y. Gotoh, H. Yamawaki, M. Sakashita, S. Takeya, and K. Honda, Phys. Rev. B **72**, 132103 (2005).
[8] M. I. McMahon, L. F. Lundegaard, C. Hejny, S. Falconi, and R. J. Nelmes, Phys. Rev. B **73**, 134102 (2006).
[9] F. J. H. Ehlers and N. E. Christensen, Phys. Rev. B **69**, 214112 (2004).
[10] T. Ishikawa, H. Nagara, K. Kusakabe, and N. Suzuki, Phys. Rev. Lett. **96**, 095502 (2006).
[11] C. Hejny and M. I. McMahon, Phys. Rev. Lett. **91**, 215502 (2003).
[12] M. I. McMahon, C. Hejny, J. S. Loveday, L. F. Lundegaard, and M. Hanfland, Phys. Rev. B **70**, 054101 (2004).
[13] C. Hejny, L. F. Lundegaard, S. Falconi, M. I. McMahon, and M. Hanfland, Phys. Rev. B **71**, 020101(R) (2005).
[14] K. Takemura, K. Sato, H. Fujihisa, and M. Onoda, Nature (London) **423**, 971 (2003).
[15] T. Kume, T. Hiraoka, Y. Ohya, S. Sasaki, and H. Shimizu, Phys. Rev. Lett. **94**, 065506 (2005).
[16] G. Parthasarathy and W. B. Holzapfel, Phys. Rev. B **37**, 8499 (1988).
[17] O. Degtyareva, E. Gregoryanz, H. K. Mao, and R. J. Hemley, High Press. Res. **25**, 17 (2005).
[18] O. Degtyareva, E. Gregoryanz, M. Somayazulu, H. K. Mao, and R. J. Hemley, Phys. Rev. B **71**, 214104 (2005).
[19] H. Luo, R. G. Greene, and A. L. Ruoff, Phys. Rev. Lett. **71**, 2943 (1993).
[20] Diacell Products Ltd., 54 Ash Tree Road, Oadby, Leicester LE2 5TD, UK.
[21] F. Datchi, R. LeToullec, and P. Loubeyre, J. Appl. Phys. **81**, 3333 (1997).
[22] Y. Zhao, A. C. Lawson, J. Zhang, B. I. Bennett, and R. B. Von Dreele, Phys. Rev. B **62**, 8766 (1997).
[23] A. P. Hammersley, S. O. Svensson, M. Hanfland, A. N. Fitch, and

D. Hausermann, High Press. Res. **14**, 235 (1996).
[24] S. van Smaalen, Crystallogr. Rev. **4**, 79 (1995).
[25] V. Petricek, M. Dusek and L. Palatinus, *The Crystallographic Computing System JANA2000* (Institute of Physics, Praha, Czech Republic, 2000).
[26] The relationship between the lattice parameters in the rhombohedral (r) and hexagonal (h) settings of the β-Po unit cell are $a_r = \frac{1}{3}\sqrt{3a_h^2+c_h^2}$ and $\sin\frac{\alpha_r}{2} = \frac{3}{2\sqrt{3+(c_h/a_h)^2}}$.
[27] The relationship between the lattice parameters of monoclinic Te-III (a_m, b_m, c_m, β_m) and those of the hexagonal and rhombohedral settings of Te-IV are $a_m = a_r(3+6\cos\alpha_r)^{1/2} = c_h$, $b_m = a_r(2-2\cos\alpha_r)^{1/2} = a_h$, $c_m = a_r$, and $\beta_m = \arccos[-(1/3+2/3\cos\alpha_r)^{1/2}]$ [Ref. 18].
[28] V. V. Brazhkin, R. N. Voloshin, S. V. Popova, and A. G. Umnov, J. Phys.: Condens. Matter **4**, 1419 (1992).
[29] C. Hejny and M. I. McMahon, Phys. Rev. B **70**, 184109 (2004).
[30] F. A. Blum, Jr. and B. C. Deaton, Phys. Rev. **137**, A1410 (1965).
[31] P. W. Bridgman, Phys. Rev. **60**, 351 (1941); Proc. Am. Acad. Arts Sci. **74**, 425 (1942).
[32] D. L. Ball, in *Proceedings of General Motors Research Laboratories Symposium, September 1963* (Elsevier Publishing Company, New York, 1964).
[33] S. K. Reed and G. J. Ackland, Phys. Rev. Lett. **84**, 5580 (2000).
[34] U. Haüssermann, K. Söderburg, and R. Norrestam, J. Am. Chem. Soc. **124**, 15359 (2002).
[35] A. Ormeci and H. Rosner, Z. Kristallogr. **219**, 370 (2004).
[36] O. Degtyareva, R. Caracas, E. Gregoryanz, R. Cohen, H. K. Mao, and R. J. Hemley, Acta Crystallogr., Sect. A: Found. Crystallogr. **A61**, C467 (2005).
[37] V. F. Degtyareva, Phys. Usp. **49**, 369 (2006).
[38] G. J. Ackland and I. D. Macleod, New J. Phys. **6**, 138 (2004).

LETTERS

Observation of an O_8 molecular lattice in the ε phase of solid oxygen

Lars F. Lundegaard[1], Gunnar Weck[2], Malcolm I. McMahon[1], Serge Desgreniers[3] & Paul Loubeyre[2]

Of the simple diatomic molecules, oxygen is the only one to carry a magnetic moment. This makes solid oxygen particularly interesting: it is considered a 'spin-controlled' crystal[1] that displays unusual magnetic order[2]. At very high pressures, solid oxygen changes from an insulating to a metallic state[3]; at very low temperatures, it even transforms to a superconducting state[4]. Structural investigations of solid oxygen began in the 1920s and at present, six distinct crystallographic phases are established unambiguously[1]. Of these, the ε phase of solid oxygen is particularly intriguing: it exhibits a dark-red colour, very strong infrared absorption, and a magnetic collapse[1]. It is also stable over a very large pressure domain and has been the subject of numerous X-ray diffraction[5–7], spectroscopic[8–11] and theoretical studies[12–14]. But although ε-oxygen has been shown to have a monoclinic *C*2/*m* symmetry[5–7,15] and its infrared absorption behaviour attributed to the association of oxygen molecules into larger units[9,14], its exact structure remains unknown. Here we use single-crystal X-ray diffraction data collected between 13 and 18 GPa to determine the structure of ε-oxygen. We find that ε-oxygen is characterized by the association of four O_2 molecules into a rhombohedral molecular unit, held together by what are probably weak chemical bonds. This structure is consistent with existing spectroscopic data, and further validated by the observation of a newly predicted Raman stretching mode.

X-ray studies of solid oxygen began in the 1920s, and, at present, six solid crystallographic modifications are unambiguously established[1]. The α, β and γ phases exist at ambient pressure and low temperature. Under pressure at $T = 295$ K, oxygen solidifies into the β phase at 5.4 GPa, then transforms into the 'orange' δ phase at 9.6 GPa, which in turn undergoes a strongly first-order transition to the 'red' ε phase at 10 GPa. Above 96 GPa, the ε phase transforms into the metallic ζ phase[3,4]. The α, β, δ phases are layered structures, and the non-magnetic rhombohedral β phase is an optimal packing of diatomic molecules possessing a small quadrupole moment. A small deformation of this structure due to the magnetic interaction results in the monoclinic or orthorhombic structures of the magnetic α and δ phases, respectively[1]. The ε phase was discovered[16] in 1979 with the first loading of oxygen in a diamond anvil cell. Drastic changes occur at the δ–ε transition: a significant volume discontinuity (~7%), the appearance of a strong infrared absorption, new Raman and infrared modes, a dramatic colour change to dark red, and a magnetic collapse[1,17]. Optical and X-ray powder-diffraction studies have suggested that the ε phase retains the layered nature of the α, β and δ phases, with the O_2 molecules remaining aligned parallel to each other. Johnson *et al.*[5] proposed that the ε phase has monoclinic *C*2/*m* symmetry with eight molecules in the unit cell, but although subsequent powder[6,15] and single-crystal[7] diffraction experiments confirmed the *C*2/*m* space group, the positions of the molecules remained elusive. To explain the infrared absorption of the ε phase, a molecular association into O_4 units has been proposed[9], and density functional calculations suggest a larger association of molecules, with the formation of herringbone-type chains of O_2 molecules[14]. We demonstrate here that an association of molecules does indeed take place in the ε-phase, but into units containing four O_2 molecules (and hence eight atoms).

The growth of a single crystal of the ε phase directly from the melt is difficult, and the *C*2/*m* space group was determined previously from a sample consisting of at least seven crystals[5]. However, the ability to grow high-quality single crystals of the ε phase in a helium hydrostatic pressure medium now makes it possible to perform detailed structural studies of oxygen at high pressure. The first synchrotron X-ray diffraction study of such a crystal was made with the energy dispersive technique[7] and, although the *C*2/*m* space group was confirmed, the number of peaks was insufficient to determine the structure. However, high-pressure single-crystal diffraction techniques using charge-coupled device (CCD) area detectors and synchrotron radiation are ideally suited to determining complex structures using such samples[18], and we have therefore used this technique to determine the structure of ε-oxygen between 13.2 and 17.6 GPa.

Two different ε-oxygen crystals were studied. For crystal 1, data were collected at 17.5 GPa and these revealed that the alignment of the crystal relative to the pressure cell was unfavourable, resulting in the measurement of only 33 unique reflections. The crystal was therefore re-grown in a more favourable orientation that enabled the measurement of 55 unique reflections at 17.6 GPa. After collecting data at this pressure, the pressure was reduced and further data were collected from crystal 2 at 15.6 GPa and 13.2 GPa. Figure 1a illustrates the combination of techniques used: the micrograph shows crystal 2 of ε-oxygen in helium at 17.6 GPa, and the diffraction pattern comprises 13 individual CCD images from the data collected at 17.6 GPa.

Both crystals were found to be twinned, but with different twin laws, and diffraction data from only a single twin component was used in each case (see Supplementary Information). Indexing of the observed reflections confirmed the symmetry of the ε phase as *C*-centred monoclinic at all pressures, while the systematic absences showed the space group to be *C*2, *Cm* or *C*2/*m*, in perfect agreement with the previous single-crystal diffraction study[5]. The lattice parameters at 17.6 GPa were $a = 7.770(10)$ Å, $b = 5.501(5)$ Å, $c = 3.657(3)$ Å and $\beta = 116.4(1)°$, where the estimated standard deviations are indicated in parentheses. The structure of the ε phase was solved in the highest-symmetry *C*2/*m* spacegroup from the data collected from crystal 2 at 17.6 GPa, using the structure solution software SIR92 (see Methods), with trial refinements in the lower-symmetry *C*2 and *Cm* space groups showing no significant

[1]SUPA, School of Physics and the Centre for Science at Extreme Conditions, The University of Edinburgh, Edinburgh, EH9 3JZ, UK. [2]Département de Physique Théorique et Appliquée, Commissariat à l'Énergie Atomique, 91680 Bruyères-le-Châtel, France. [3]Department of Physics, University of Ottawa, Ontario K1N 6N5, Canada.

improvement in fit. The solved structure contains three symmetry-inequivalent atoms: two (oxygens O1 and O2) occupy 4*i* positions of the *C*2/*m* space group at (*x*,0,*z*), and the third (O3) an 8*j* position at (*x*,*y*,*z*). The refined structural coordinates of ε-oxygen from the two crystals at 17.5 and 17.6 GPa, along with the final *R*-factor, are given in Table 1 (see also Supplementary Information). When tested, previously proposed structures for the ε phase gave significantly poorer fits (see also Supplementary Information). The structure of the ε phase at 17.6 GPa, as viewed perpendicular to the *a*–*b* plane, is shown in Fig. 2. As in the high-pressure β[19] and δ[20] phases, ε-oxygen comprises layers of collinear O_2 molecules, the axes of which are oriented perpendicular to the layers which lie in the *a*–*b* plane. The striking feature of the structure is the association of four O_2 molecules into rhomb-shaped $(O_2)_4$ molecular units, which are symmetry equivalent and centred on the lattice points at (0,0,0) and (0.5,0.5,0). Within these molecular units, each molecule has two neighbours at a distance of 2.18(1) Å at 17.6 GPa and with inter-molecular angles of 96° and 84°. The $(O_2)_4$ units observed at 17.6 GPa are also present at both 15.6 and 13.2 GPa, and they are therefore formed at the δ-to-ε transition rather than through compression of the ε phase.

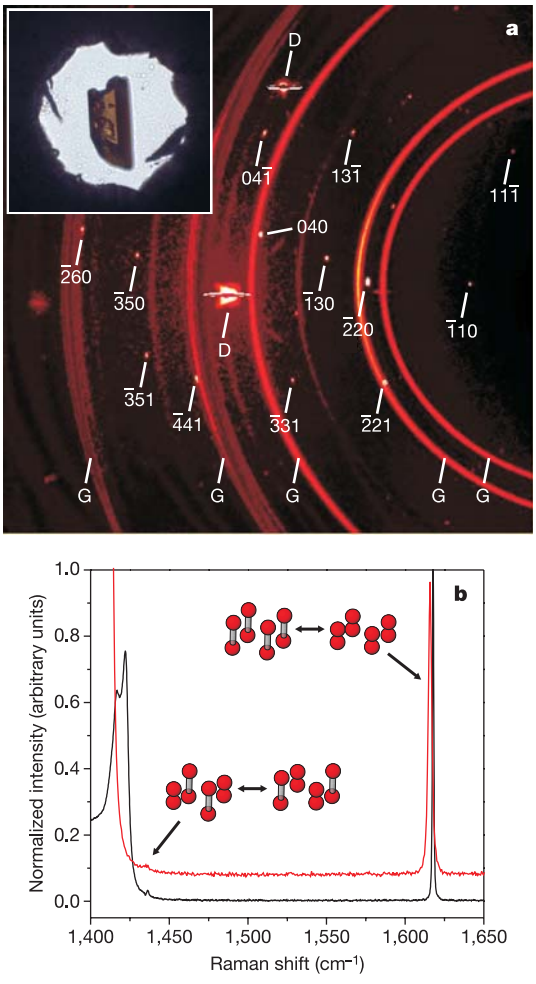

Figure 1 | X-ray and Raman measurements of ε-oxygen. a, Composite image of 13 individual CCD images showing the indexed Bragg peaks from the ε phase of oxygen. Diffraction features from the gasket and diamond anvils are marked G and D, respectively. The inset shows a micrograph of crystal 2 of ε-oxygen in helium at 17.6 GPa. **b**, Raman (red) and Fourier transform–Raman (black) spectra of two different crystals of ε-oxygen at 32.8 GPa and 33.4 GPa, respectively, showing the two stretching modes of the $(O_2)_4$ molecular unit. The motion of the atoms for the two modes is indicated.

The structural relationship between the β, δ and ε phases is illustrated in Fig. 3. The β and δ structures can both be described using the *C*-centred monoclinic cell of the α-phase, with the molecules remaining centred on the unit cell's lattice points[1,19,20]. Any changes in the intermolecular distances within the molecular layers can then arise only via deformation of this unit cell. In contrast, the δ–ε transition involves a doubling of the δ-phase unit cell in both the *a* and *b* directions, and the relative displacement of half the molecules in each layer along the $\pm a$ direction (Fig. 3c). As a result, there is a dramatic reduction in the nearest-neighbour intermolecular distance from 2.57 Å in the δ phase at 9.6 GPa (ref. 20) to 2.25 Å in the ε phase at 13.2 GPa; this reduction gives rise to the large volume contraction observed at the δ-ε transition.

While molecular units containing eight oxygen atoms have not previously been observed in any oxygen phase, gas-phase $(O_2)_2$ dimers with an equilibrium spacing of 3.5 Å between the two parallel O_2 molecules are known[21,22]. Pauling[23] proposed that the formation of such a dimer requires that the chemical spin–spin contribution should not be negligible, as confirmed recently[22]. The observed rhombohedral shape of the $(O_2)_4$ molecular units can probably also be explained by a bonding between open shell π^* orbitals, and $(O_2)_4$ and the gas-phase dimer $(O_2)_2$ should thus both be considered as chemically weakly bonded units. Indeed, while the O–O bond length within each O_2 molecule is unaltered by pressure, the inter-O_2 distances both within, and between, the $(O_2)_4$ groups compress at the same rate of 0.011(3)–0.014(3) Å GPa^{-1}, emphasizing the weakness of the interaction between the O_2 molecules that form the $(O_2)_4$ units. However, the intensity increase in the infrared modes of the ε phase up to 20–30 GPa has been taken as an indication that there is a progressive strengthening of the inter-O_2 bonds over this pressure range[9,10]. Further detailed diffraction studies to higher pressures will be required to address this.

An $(O_2)_4$ complex with the observed D_{2h} symmetry has a large number of allowed vibrational modes: nine Raman and seven infrared fundamental modes. The vibrational modes were calculated for an isolated $(O_2)_4$ complex with the same structure as that determined at 17.6 GPa, using the Spartan 5.1 program (an *ab initio* quantum mechanics software package for computing molecular

Table 1 | Data collection and refined structural parameters

Pressure (GPa)	Crystal 1 17.5	Crystal 2 17.6
Unit cell		
Space group	*C*2/*m*	*C*2/*m*
a (Å)	7.760(10)	7.770(10)
b (Å)	5.510(3)	5.501(5)
c (Å)	3.656(8)	3.657(3)
β (°)	116.5(1)	116.4(1)
Data collection		
Number of unique reflections	33	55
Number of observed reflections (with $\|F_{obs}\| > 4\sigma$)	25	46
$R_{int} = \sum\|F^2_{obs} - F^2_{obs}(mean)\|/\sum[F^2_{obs}]$	0.105	0.104
$R_\sigma = \sum[\sigma(F^2_{obs})]/\sum[F^2_{obs}]$	0.064	0.044
Refinement		
R ($\|F_{obs}\| > 4\sigma$)	0.069	0.038
R (for all)	0.083	0.062
Structure parameters		
O1 x	0.827(2)	0.826(1)
O1 z	0.173(5)	0.175(2)
O2 x	0.246(3)	0.247(1)
O2 z	0.190(6)	0.192(2)
O3 x	0.036(2)	0.0379(9)
O3 y	0.2673(5)	0.2666(6)
O3 z	0.180(4)	0.185(1)
O1 Uiso (Å^2)	0.013(2)	0.015(1)
O2 Uiso (Å^2)	0.014(2)	0.017(1)
O3 Uiso (Å^2)	0.013(1)	0.015(1)

Results are given for crystals 1 and 2 at 17.5 GPa and 17.6 GPa, respectively. The estimated standard deviations are indicated in parentheses. Details at other pressures are given in the Supplementary Information.

properties) with density functional theory[24]. This simple calculation does not take into account effects such as the crystal field; but it nevertheless allows for a semiquantitative comparison with the spectroscopic data, yielding mode frequencies that agree within a few tens of cm^{-1} with the observed modes. Three infrared modes were found to have significant absorption (B_{3u} at 1,500 cm^{-1}, B_{2u} at 1,443 cm^{-1} and B_{1u} at 292 cm^{-1}), in agreement with the reported infrared spectroscopic data[9,11]. In addition, four Ag Raman modes should also be measurable, three of which, at 1,600 cm^{-1}, 342 cm^{-1} and 161 cm^{-1} have already been observed[8]. The fourth Raman mode, at approximately 1,380 cm^{-1}, is a signature of the $(O_2)_4$ unit but has not been observed to date, perhaps because it lies very close to the Raman signal from the diamond anvils of the pressure cell. This fourth mode is also expected to be very weak owing to the antisymmetric stretching motion of the four O_2 molecules, coupled in diagonal pairs. Raman and Fourier-Transform Raman with excitation at 514.5 nm and 1,064 nm, respectively, were carried out to search specifically for this peak. In different samples, a weak Raman-active line was observed to emerge from the Raman signal from the diamond anvils at pressures above 30 GPa. At 33 GPa, the new Raman line was observed at 1,430 cm^{-1}, as illustrated in Fig. 1b. We interpret this new line to be the fourth Raman active mode of the $(O_2)_4$ molecular unit, and, given its weakness, it was best observed by performing Raman scattering on single-crystal samples with high-quality optical surfaces.

The rhomb-shaped $(O_2)_4$ molecular unit of the ε phase differs from the long-sought cyclooctaoxygen molecule, which would be the

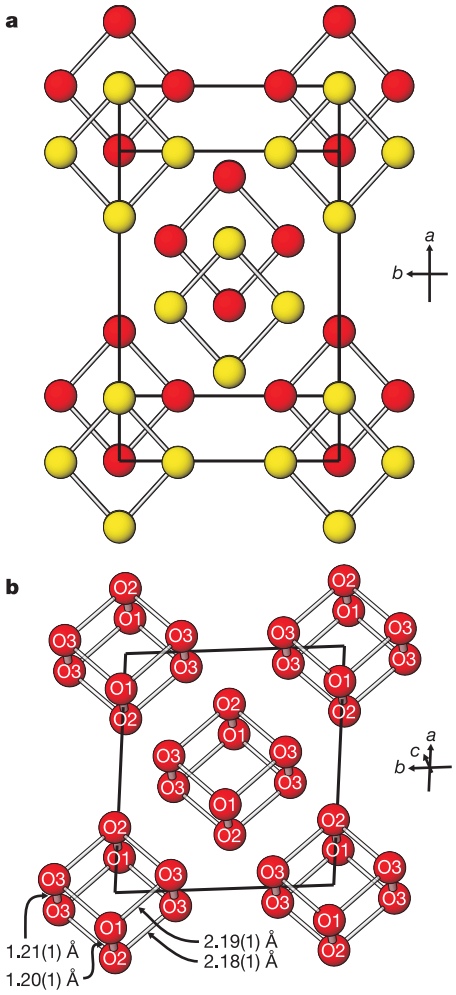

Figure 2 | The structure of ε-oxygen at 17.6 GPa. **a**, The structure as viewed perpendicular to the *a*–*b* plane. Red and yellow atoms lie in symmetry-equivalent molecular layers located at heights $z = 0$ and 1, respectively. The groups of molecules forming the $(O_2)_4$ units are connected by thick lines. An inclined view of the $z = 0$ molecular layer is shown in **b**. The layers comprise two types of O_2 molecules—those containing two symmetry-equivalent O3 atoms and the centres of which are constrained by symmetry to lie exactly in the *a*–*b* planes at $z = 0$ and 1, and those comprising symmetry-inequivalent O1 and O2 atoms, and the centres of which are unconstrained. The symmetry of the structure does not require that the O–O bond lengths of the O3–O3 and O1–O2 molecules be the same, nor that the molecules be oriented perpendicular to the *a*–*b* plane. However, the bond lengths of all the O_2 molecules are the same within error at all pressures, with a bond length of 1.20(3) Å and in good agreement with the O–O bond length in the gas phase (1.207 Å)[1]. Additionally, all the molecules are perpendicular to the *a*–*b* planes to within 1°.

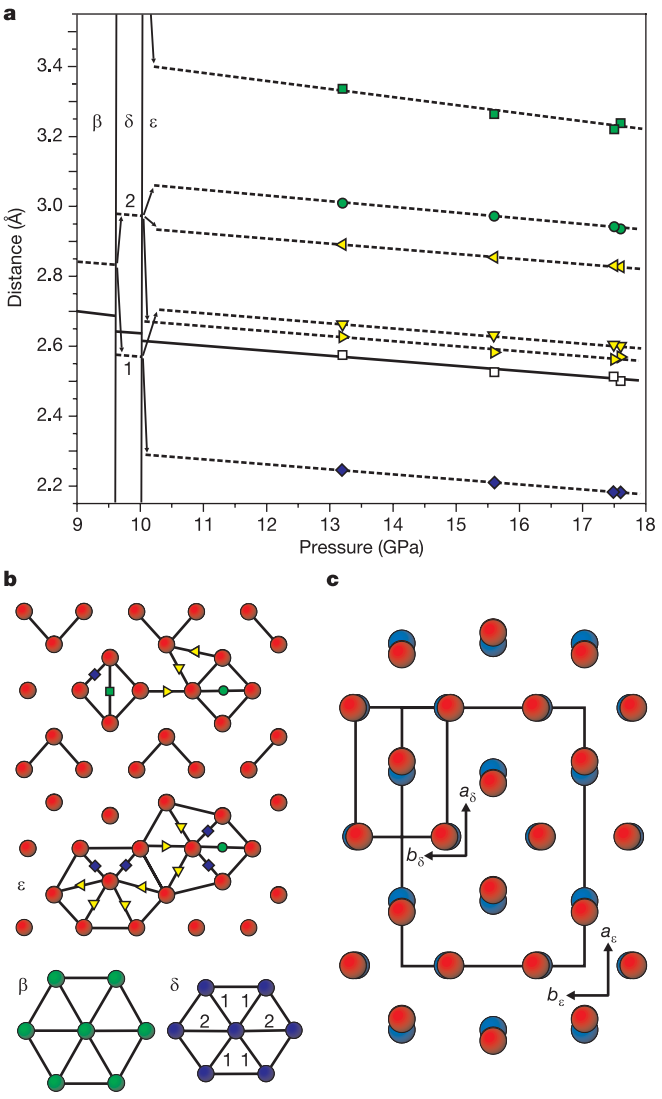

Figure 3 | Structural evolution of oxygen with pressure. **a**, Pressure dependence of the intermolecular distances within the molecular layers of the β, δ and ε phases of solid oxygen. The coloured symbols are identified in **b**. The shortest interlayer O–O distance in the ε phase is shown using unfilled squares, and the same distance is shown as a solid line for the β and δ phases. In the β phase, each molecule is surrounded within the layer by six others, all at the same distance[19]. The distortion within the molecular layer at the β–δ transition results in two different intermolecular distances in the δ phase[20], marked 1 and 2 in **a** and **b**. The larger unit cell and lower symmetry of the ε phase results in two symmetry-inequivalent coordination shells, and a wider range of intermolecular distances. **c**, The relationship between the locations of molecules within the molecular layers of the δ (blue atoms) and ε (red atoms) phases.

isoelectronic analogue of the S_8 rings in elemental sulphur[25]. As may be inferred from the fact that the structure of the ε-phase of oxygen reported here has not been predicted by various *ab initio* calculations, it presents a challenge to our understanding of dense oxygen, particularly of the nature of the interactions that develop to stabilize the $(O_2)_4$ unit. We also note that the observation of molecular association in oxygen under pressure may affect explanations of the spectroscopic data from other elemental molecular solids (interestingly, the increased infrared absorption of phase III of solid hydrogen[26] parallels the case of the ε phase of oxygen), and the miscibility of O_2 with other elements at high pressure[27].

METHODS

Crystals of ε-oxygen were grown from a 2.6 mol% O_2 in He mixture at 450 K and 22.5 GPa, as described previously[7]. The diamond anvil pressure cell was equipped with anvil support seats with full conical apertures that enabled 70° angular X-ray access to the sample without contaminating scatter. X-ray diffraction data were collected on station 9.8 at the SRS, Daresbury Laboratory, using an incident X-ray wavelength of 0.688 Å. The pressure was measured using the standard ruby fluorescence technique. Diffraction data were measured over the full angular ranges permitted by the cell, and at two azimuthal angles ($\chi = 0°$ and 90°) around the X-ray beam. No correction was made for the absorption of the sample and diamonds. Indexing and integration of the data were performed using the Bruker software suite[28]. The structure was solved using SIR92[29], and refined using SHELX[30].

Received 2 May; accepted 16 August 2006.

1. Freiman, Y. A. & Jodl, H. J. Solid oxygen. *Phys. Rep.* **401,** 1–228 (2004).
2. Goncharenko, I. N., Makarova, O. L. & Ulivi, L. Direct determination of the magnetic structure of the delta phase of oxygen. *Phys. Rev. Lett.* **93,** 055502 (2004).
3. Desgreniers, S., Vohra, Y. K. & Ruoff, A. L. Optical response of very high density solid oxygen to 132 GPa. *J. Phys. Chem.* **94,** 1117–1122 (1990).
4. Shimizu, K., Suhara, K., Ikumo, M., Eremets, M. I. & Amaya, K. Superconductivity in oxygen. *Nature* **393,** 767–769 (1998).
5. Johnson, S. W., Nicol, M. & Schiferl, D. Algorithm for sorting diffraction data from a sample consisting of several crystals enclosed in a sample environment apparatus. *J. Appl. Cryst.* **26,** 320–326 (1993).
6. Desgreniers, S. & Brister, K. E. in *High Pressure Science and Technology* (ed. Trzeciakowski, W. A.) 363–365 (World Scientific, Singapore, 1996).
7. Weck, G., Loubeyre, P. & LeToullec, R. Observation of structural transformations in metal oxygen. *Phys. Rev. Lett.* **88,** 035504 (2002).
8. Akahama, Y. & Kawamura, H. High-pressure Raman spectroscopy of solid oxygen. *Phys. Rev. B* **54,** R15602–R15605 (1996).
9. Gorelli, F. A., Ulivi, L., Santoro, M. & Bini, R. The ε phase of solid oxygen: Evidence of an O_4 molecule lattice. *Phys. Rev. Lett.* **83,** 4093–4096 (1999).
10. Akahama, Y. & Kawamura, H. High-pressure infra-red spectroscopy of solid oxygen. *Phys. Rev. B* **61,** 8801–8805 (2000).
11. Agnew, S. F., Swanson, B. I. & Jones, L. H. Extended interactions in the ε phase of oxygen. *J. Chem. Phys.* **86,** 5239–5245 (1987).
12. Serra, S., Chiarotti, G., Scandolo, S. & Tosatti, E. Pressure-induced magnetic collapse and metallization of molecular oxygen: the ζ-O_2 phase. *Phys. Rev. Lett.* **80,** 5160–5163 (1998).
13. Gebauer, R. *et al.* Noncolinear spin polarization from frustrated antiferromagnetism: A possible scenario for molecular oxygen at high pressure. *Phys. Rev. B* **61,** 6145–6149 (2000).
14. Neaton, J. B. & Ashcroft, N. W. Low-energy linear-structures in dense oxygen: implications for the ε-phase. *Phys. Rev. Lett.* **88,** 205503 (2002).
15. Akahama, Y., Kawamura, H., Häusermann, D., Hanfland, M. & Shimomura, O. New high-pressure structural transition of oxygen at 96 GPa associated with metallization in a molecular solid. *Phys. Rev. Lett.* **74,** 4690–4693 (1995).
16. Nicol, M., Hirsch, K. R. & Holzapfel, W. B. Oxygen phase equilibria near 298 K. *Chem. Phys. Lett.* **68,** 49–52 (1979).
17. Goncharenko, I. N. Evidence of magnetic collapse in the epsilon phase of solid oxygen. *Phys. Rev. Lett.* **94,** 205701 (2005).
18. McMahon, M. I., Nelmes, R. J. & Rekhi, S. Complex crystal structure of cesium-III. *Phys. Rev. Lett.* **87,** 255502 (2001).
19. Schiferl, D., Cromer, D. T. & Mills, R. L. Structure of O_2 at 5.5 GPa and 299 K. *Acta Crystallogr. B* **37,** 1329–1332 (1981).
20. Schiferl, D., Cromer, D. T., Schwalbe, L. A. & Mills, R. L. Structure of 'orange' $^{18}O_2$ at 9.6 GPa and 297 K. *Acta Crystallogr. B* **39,** 153–157 (1983).
21. Long, C. A. & Ewing, G. E. Spectroscopic investigation of van der Waals molecules. Infrared and visible spectra of $(O_2)_2$. *J. Chem. Phys.* **58,** 4824–4834 (1973).
22. Aquilanti, V. *et al.* Quantum interference scattering of aligned molecules: binding in O_4 and role of spin coupling. *Phys. Rev. Lett.* **82,** 69–72 (1999).
23. Pauling, L. *The Nature of the Chemical Bond* (Cornell Univ. Press, Ithaca, New York, 1964).
24. SPARTAN version 5.1 (Wavefunction Inc., Irvine, California, 1998).
25. Kim, K. S., Jang, J. H., Kim, S., Byung-Jin Mhin, B.-J. & Schaefer, H. F. Potential new high energy density materials: cyclooctaoxygen O_8, including comparisons with the well-known cyclo-S_8 molecule. *J. Chem. Phys.* **92,** 1887–1892 (1990).
26. Hanfland, M., Hemley, R. J. & Mao, H. K. Novel infrared vibron absorption in solid hydrogen at megabar pressures. *Phys. Rev. Lett.* **70,** 3760–3763 (1993).
27. Sihachakr, D. & Loubeyre, P. O_2/N_2 mixtures under pressure: A structural study of the binary phase diagram at 295 K. *Phys. Rev.* **70,** 134105 (2004).
28. *SMART, SAINT, ASTRO and XPREP: Data Collection and Processing Software for the SMART System* (Bruker Analytical X-ray Systems, Inc., Madison, Wisconsin, 1995).
29. Altomare, A., Cascarano, G., Giacovazzo, C. & Guagliardi, A. Completion and refinement of crystal structures with SIR92. *J. Appl. Cryst.* **26,** 343–350 (1993).
30. Sheldrick, G. M. *SHELX97 Programs for Crystal Structure Analysis (Release 97-2).* (Univ. of Göttingen, 1997)

Supplementary Information is linked to the online version of the paper at www.nature.com/nature.

Acknowledgements We acknowledge discussions with T. Balic-Zunic on the sample twinning. We gratefully acknowledge the assistance of J. Warren and T. Prior in using beamline 9.8 at SRS, Daresbury Laboratory. The work was supported by research grants from the EPSRC, and facilities and other support from Daresbury Laboratory and the CCLRC. S.D. acknowledges the financial support of CEA/DAM Île-de-France and NSERC.

Author Contributions P.L. and G.W. prepared the ε-oxygen crystals. L.F.L. and M.I.M. performed the X-ray measurements and the structural analysis. G.W. performed the calculations of the modes. S.D. and G.W. performed the Raman measurements. P.L. and M.I.M. wrote most of the paper.

Author Information Reprints and permissions information is available at www.nature.com/reprints. The authors declare no competing financial interests. Correspondence and requests for materials should be addressed to M.I.M. (mim@ph.ed.ac.uk) or P.L. (paul.loubeyre@cea.fr).

X-ray diffraction study of diffuse scattering in incommensurate rubidium-IV

S. Falconi, M. I. McMahon, L. F. Lundegaard, C. Hejny, and R. J. Nelmes
SUPA, School of Physics and Centre for Science at Extreme Conditions, The University of Edinburgh, Mayfield Road, Edinburgh, EH9 3JZ, United Kingdom

M. Hanfland
ESRF, BP 220, Grenoble Cedex, France

(Received 20 December 2005; revised manuscript received 17 April 2006; published 6 June 2006)

X-ray diffraction data have been collected from single crystals of incommensurate Rb-IV in order to study the sheets of diffuse scattering arising from the one-dimensional (1D) guest chains. Discontinuities in both the relative intensity and width of the diffuse sheets are observed on pressure decrease below 16.7 GPa, the pressure at which the interchain correlations begin to decrease rapidly. These changes in the diffuse scattering are accompanied by the progressive disappearance of the Bragg peaks from the guest chains. By modeling the diffuse scattering as coming from either a perturbed 1D lattice or a 1D harmonic liquid, we have determined the pressure dependence of the intrachain spacing of the guest atoms and the root-mean-square (RMS) fluctuation of the guest atoms from their unperturbed sites. We have also made estimates of the sound velocity along the guest-atom chains, and their effective Debye temperature.

DOI: 10.1103/PhysRevB.73.214102 PACS number(s): 64.70.Ja, 62.50.+p, 64.60.My, 64.70.Fx

I. INTRODUCTION

Recent studies of the high-pressure phase transitions in simple elements have revealed a number of surprisingly complex crystal structures, such as incommensurate host-guest composite structures,[1–8] incommensurately modulated structures,[9–12] and complex commensurate structures.[13–17] Many of these structural complexities arise through the pressure dependence of the electronic structure, and are accompanied by insulator-metal phase transitions, or the onset of superconductivity.[18,19] Among these phases, the behavior of the host-guest composite structure of Rb-IV, stable between 16 and 20 GPa, is unique.

Rb-IV has a 16-atom body-centered host framework (space group $I4/mcm$) with channels along the fourfold c-axis. Contained within these channels are one-dimensional (1D) chains of atoms that form the guest structure (space group $I4/mmm$) which is incommensurate with the host structure along their common c axis.[7,20] The 4D superspace group of the structure is $I'4/mcm(00\gamma)000s$, with $\gamma=1.631$ at 16.8 GPa.[7] Using both powders and small crystallites of Rb-IV, we have recently shown that at pressures below 16.7 GPa the interchain correlation length begins to decrease rapidly, leading to a gradual "melting" of the 1D guest chains.[7,20] The onset of this "melting" is accompanied by the elongation of the Bragg peaks from the guest structure perpendicular to the c axis, and the appearance of sheets of diffuse scattering from the increasingly disordered, perhaps liquid-like, 1D chains. At 16.2 GPa, the pressure at which Rb-IV transforms to Rb-III on pressure decrease at 300 K, the interchain correlation length is only $\sim$30 Å, or 4 times the interchain spacing.[20] Extrapolation of the interchain correlation length suggests that completely "melted" chains would occur at 300 K at pressures below $\sim$15.8 GPa.[20]

Previous studies of single- or quasisingle-crystal samples of the host-guest structures of Ba-IV,[1] Sr-V,[2] and Bi-III (Ref. 3) have revealed that diffuse scattering is also observed from these structures, although the guest structures are still crystalline. In Ba-IV, this diffuse scattering decreases in intensity on repeated passing through the Ba-IVa$\leftrightarrow$Ba-IVb intraphase transition at 12.5 GPa,[1] suggesting that, at least in this phase, the diffuse scattering arises from nonequilibrium disorder within the chains. It would clearly be of interest to make a detailed study of the diffuse scattering from all of the elemental composite structures in order to obtain information on the correlated motion of the chains, or their disorder. Studies of diffuse scattering in more complex 1D systems such as $Hg_{3-\delta}AsF_6$ (Refs. 21 and 22) and $DIPS(C_6H_5)_4(I_3)_{0.76}$ (Refs. 23–26) have provided information on intrachain correlation lengths, the sound velocity along the chains, and their effective Debye temperatures. In Rb-IV, it would be of particular interest to determine whether there is any diffuse scattering from the crystalline-chain state above 16.7 GPa (our previous studies from powders or individual sample crystallites of Rb-IV were not able to determine this) and to follow the scattering below 16.7 GPa to determine whether the chains are truly melting, so that they approach the state of a 1D liquid.

In this paper we describe such a study, using high-quality single crystals of Rb-IV grown by slow cooling from the melt. In Sec. II we describe the experimental setup and procedure, in Sec. III we give a qualitive description of the behavior of the Bragg peaks with pressure, in Sec. IV A we give a qualitative analysis of the diffuse scattering and in Sec. IV B we describe the two models used to analyze the diffuse data. Finally, in Secs. V–VII, we report and discuss the results of the analysis, and give conclusions.

II. EXPERIMENT AND EXPERIMENTAL DATA

Angle-dispersive x-ray diffraction data from single crystals of Rb-IV were obtained on beamline ID09 at the European Synchrotron Radiation Facility (ESRF), Grenoble. Preliminary studies were also conducted on station 9.1 at the

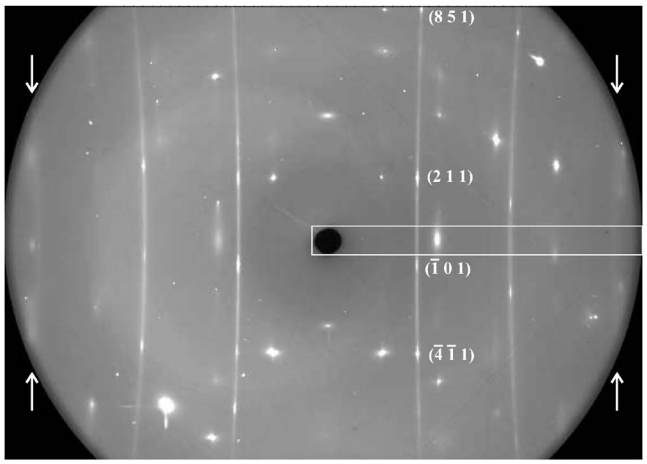

FIG. 1. 2D diffraction image from S2 of Rb-IV at 19.7 GPa. Three vertical lines of diffuse scattering are visible on each half of the pattern. The location of the very weak third-order line is identified by arrows, and indices are given for four of the guest Bragg reflections visible on the first-order diffuse line. The white rectangle shows the integration limits used in the azimuthal integration of the 2D images. The contrast of this image has been enhanced so as to make the very weak third-order diffuse line visible.

Synchrotron Radiation Source, Daresbury Laboratory. The initial sample material was commercial Rb with a stated purity of 99.96% purchased from the Aldrich Chemical Company. The two samples were loaded under a dry argon atmosphere into diamond anvil cells with tungsten gaskets and gasket holes of 100 μm initial diameter. A small piece of ruby or $SrB_4O_7:Sm^{2+}$ was included in each pressure cell for pressure measurement.[27] After loading, the samples were pressurized to 18–20 GPa and then heated in an oven at 350 °C for several hours before cooling slowly to room temperature. After this heating process the sample pressures were 16.7 GPa for sample 1 (S1) and 19.7 GPa for sample 2 (S2). Data collected on a single-crystal diffractometer confirmed that both samples were high-quality single crystals of Rb-IV.

The measurements on Rb-IV were performed using an x-ray wavelength of 0.4101 Å, and an incident beamsize of 20×20 μm. The 2D diffraction patterns were recorded using a MAR345 image plate placed either ~250 mm (S1) or ~360 mm (S2) from the sample, and the samples were aligned to have their tetragonal *c*-axes in the horizontal plane and perpendicular to the incident x-ray beam. The exposure time at each pressure was four minutes, during which the samples were kept stationary in order to reduce the number of Bragg peaks incident on the image plate from the sample and diamond anvils. A series of images were collected from S1 (Ref. 29) in ~0.2 GPa intervals, first on pressure increase to 18.7 GPa, and then on pressure decrease to 16.2 GPa, where the sample began to transform to Rb-III.

A diffraction image from S2 at 19.7 GPa is shown in Fig. 1. In addition to the strongly saturated Bragg peaks from the host and guest components of the structure, the diffraction patterns from both S1 and S2 clearly contained lines of much weaker (<0.1% of the intensity of the host Bragg peaks) diffuse scattering aligned perpendicular to the *c* axis which would have been too weak to observe in our previous study.[20] The positions of these lines correspond to sheets of diffuse scattering that are coplanar with the $hk\pm1$, $hk\pm2$, etc., reciprocal-lattice layers of the guest structure, exactly as observed previously in the composite structures of Ba-IV, Sr-V, and Bi-III.[1–3]

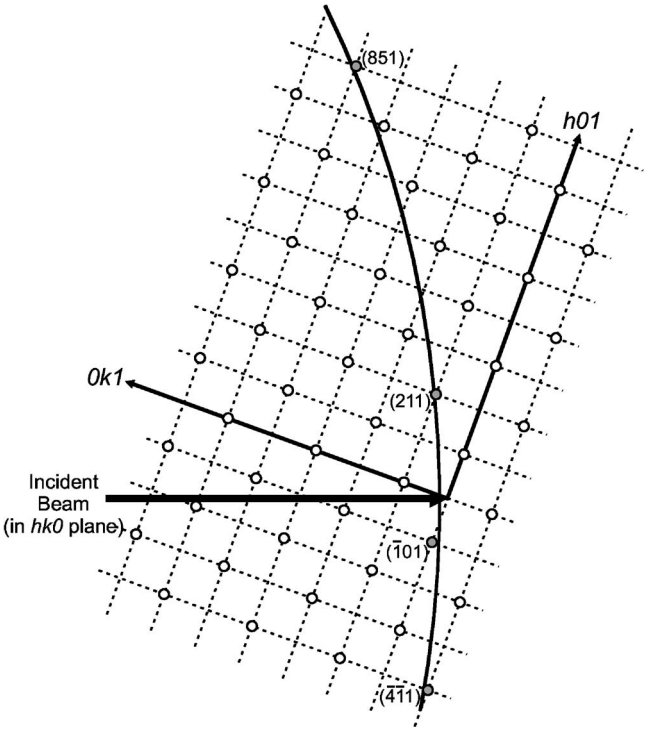

FIG. 2. The ($hk1$) reciprocal-lattice layer of the Rb-IV guest structure at 19.7 GPa, as viewed down the [00l] reciprocal axis (the *c* axis), perpendicular to the incident beam, showing the orientation necessary to give the diffraction image shown in Fig. 1. The curved line passing through the lattice marks the interception of the Ewald sphere with the ($hk1$) reciprocal-lattice layer necessary in order that the (851), (211), ($\bar{1}$01), and ($\bar{4}\bar{1}$1) Bragg reflections diffract simultaneously. The diffuse scattering observed between these Bragg reflections in Fig. 1 arises from those points within the reciprocal-lattice layer that lie on the curved intercept line.

The lines of diffuse scattering in Fig. 1 are the projection onto the detector of the interception of the sheets of diffuse scattering with the Ewald sphere. From an analysis of which ($hk1$) guest Bragg reflections are visible in Fig. 1 it is possible to determine the orientation of the reciprocal lattice with respect to the incident beam, as shown for S2 at 19.7 GPa in Fig. 2. The diffuse scattering between the four labelled Bragg peaks in Fig. 1 then arises from those parts of the diffuse sheet lying between the Bragg peaks and located on the intercept curve. Except in the immediate vicinity of the guest Bragg peaks, the intensity along each diffuse line in Fig. 1 is constant and, as this scattering probes a wide range of reciprocal space (see Fig. 2), this suggests that the sheets of diffuse scattering are uniform in intensity. This was confirmed by collecting a series of images from sample S2 as the sample was rotated about the *c* axis. The intensity of the diffuse scattering was constant in all images.

In order to quantify the diffuse scattering, only a small rectangular "slice" of each image was integrated using the

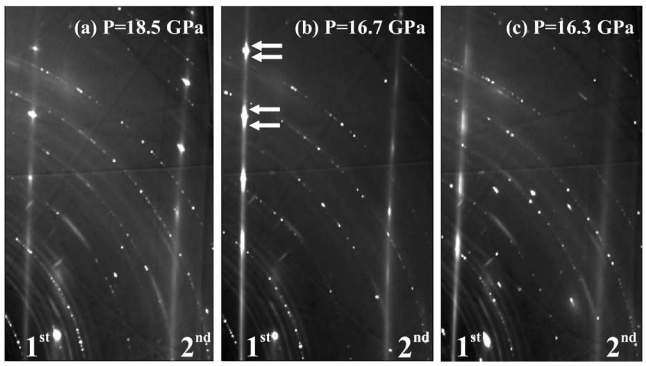

FIG. 3. Enlarged views of the first- and second-order diffuse lines from S1 of Rb-IV at (a) 18.5 GPa, (b) 16.7 GPa, and (c) 16.3 GPa. The contrast of the individual images has been enhanced so as to make both the saturated Bragg peaks and the diffuse lines visible. At 18.5 GPa, image (a), sharp Bragg peaks from the guest phase are superimposed on both the first- and second-order diffuse lines. At 16.7 GPa, image (b), these sharp Bragg peaks are still visible, although they are very much weaker on the second-order diffuse line. The Bragg peaks also have weak additional scattering centered on them, as indicated by arrows. At 16.3 GPa, image (c), the Bragg peaks from the guest are highly elongated, and are visible only on the first-order diffuse line.

program Fit2D,[28] as shown by the white integration box in Fig. 1. The extent of this box along the diffuse lines had to be chosen carefully, as if too great, the azimuthal (constant-2θ) integration procedure used by Fit2D would have resulted in an artificial asymmetry in the integrated peak from the lowest-angle diffuse sheet. The box size chosen introduced no detectable asymmetry. Considerable care was also taken to mask out any scattering in the 2D images that lay on the diffuse lines but which resulted from the crystalline guest structure, or from the background scatter from the pressure cell components. Despite this care, the extreme weakness of the diffuse scattering meant that the signal:background ratio of the strongest diffuse line was only approximately 1:6.

III. PRESSURE DEPENDENCE OF THE BRAGG PEAKS

On decreasing the sample pressure in S1 from 18.7 GPa, the ($hk2$) and ($hk3$) guest Bragg reflections from the guest chains which had been clearly visible within the second- and third-order diffuse lines [as illustrated for the ($hk2$) layer in Fig. 3(a)] decreased markedly in intensity, such that at the onset of chain melting at 16.7 GPa, only the ($hk1$) and extremely faint ($hk2$) guest Bragg peaks were observed [Fig. 3(b)]. We observed this decrease in intensity of those guest peaks with $l>1$ in our previous powder study of Rb-IV,[20] and suggested that it arose from the increase in thermal motion of the guest atoms along c as the onset of chain melting is approached. Figure 3(b) also illustrates the weak additional scattering that appears near 16.7 GPa and which is centered on the guest Bragg peaks. This scattering is elongated along the diffuse sheet and has an intensity that is estimated to be 1%–2% of the Bragg reflection. The identity of this additional scattering is currently unknown, although it may arise from thermal diffuse scattering.

At pressures below 16.7 GPa, the Bragg reflections from the guest chains of Rb-IV begin to broaden significantly perpendicular to the c axis, due to the reduced interchain correlation length in this direction.[7,20] Only the guest reflections are observed to broaden: no changes are observed in the Bragg reflections from the host component of the structure on passing through 16.7 GPa. At 16.3 GPa, the estimated interchain correlation length is less than 40 Å.[20] The guest Bragg reflections are highly elongated along the diffuse sheet, as shown in Fig. 3(c), and only the broadened ($hk1$) guest reflections are observed. Although the pressure dependence of the interchain correlation length might be obtained from the half-width of the broadened guest peaks,[20] the four minutes exposures required to obtain the necessary statistics on the diffuse sheets meant that the Bragg peaks were saturated, and it was not therefore possible to determine their widths. Despite this, the broadened Bragg peaks were observed at all pressures down to the transition to Rb-III at 16.2 GPa, confirming the existence of interchain interactions between the guest chains over the complete stability range of Rb-IV at 300 K.

IV. DATA ANALYSIS AND MODELING OF THE DIFFUSE SCATTERING

Below, we first describe a semiquantitative study of the diffuse scattering, and then model it using two different methods. The first of these describes the diffuse scattering as coming from a 1D perturbed lattice,[23–25,30] while the second model, used for the data collected below 16.7 GPa, describes the diffuse scattering profile as coming from a 1D harmonic liquid.[21,22,26]

A. Qualitative analysis of the data

While the study of diffuse scattering at ambient pressure is itself challenging,[23] considerable further challenges are introduced for studies at high pressure, in particular by the small size of the sample, by the considerable background scatter from the pressure cell, and by the pressure cell's limited diffraction aperture which restricts the q-range of the data collectable. The diffuse scattering from Rb-IV is also orders of magnitude weaker than that observed in systems such as $DIPS(C_6H_5)_4(I_3)_{0.76}$, where the intensity of the diffuse scattering is comparable with that of the main Bragg reflections.[31] As described previously, the 2D diffraction images from Rb-IV were integrated only across the narrow strip shown in Fig. 1, where it was possible to avoid the saturated Bragg peaks from the guest structure, and considerable care was taken to mask out other diffraction features, although some small unavoidable residual artifacts remained in the integrated profiles. After integration, the background determined from the empty pressure cell was subtracted from the profiles, which were then normalized by the squared atomic form factor[32,33] $f(q)^2$. The third-order sheet of diffuse scattering was both broad and extremely weak and, although just visible in the raw 2D images after optimizing their contrast

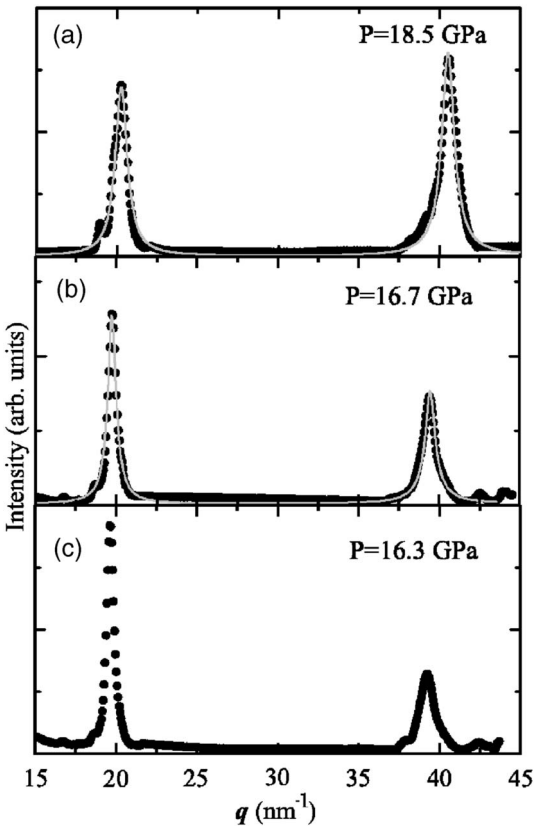

FIG. 4. Integrated diffraction profiles of the diffuse scattering from Rb-IV at (a) 18.5 GPa, (b) 16.7 GPa, and (c) 16.3 GPa. The integration limits used to obtain the profiles were as shown in Fig. 1. The grey lines superimposed on the data at 18.5 and 16.7 GPa are the fits obtained with the 1D perturbed lattice model, as discussed in the text. The additional small peaks on the high-q side of the second-order peak in profiles (b) and (c) arise from the structured background in the diffraction images.

(see Fig. 1), it was weaker than the residual artifacts remaining in the profiles. It was therefore not included in the fitting procedure and quantitative analysis, except that fits were checked for consistency with the observed weakness and breadth of this sheet. No evidence of the fourth-order diffuse sheets was observed even in longer exposures. The integrated diffraction profiles of the diffuse scattering obtained at 18.5, 16.7 and 16.3 GPa are shown in Fig. 4.

Semiquantitative analysis of the diffuse scattering can be obtained by fitting the diffuse peaks after deconvoluting the intrinsic linewidth of the experimental apparatus, as obtained from the diffraction pattern of a silicon calibrant collected at the same sample to image-plate distances. The deconvoluted full peak width at half-maximum (FWHM) and the ratio between the integrated intensities of the first- and second-order diffuse peaks, I_1/I_2, as a function of pressure are shown in Figs. 5(a) and 5(b), respectively.

At 18.7, the FWHM of the first- and second-order diffuse peaks differs by only 20%. On pressure decrease the width of the second-order peak decreases only slightly, while that of the first-order peak decreases considerably, especially below 17.5 GPa, such that at 16.7 GPa the width of the first-order peak is approximately one-half that of the second [Fig. 5(a)].

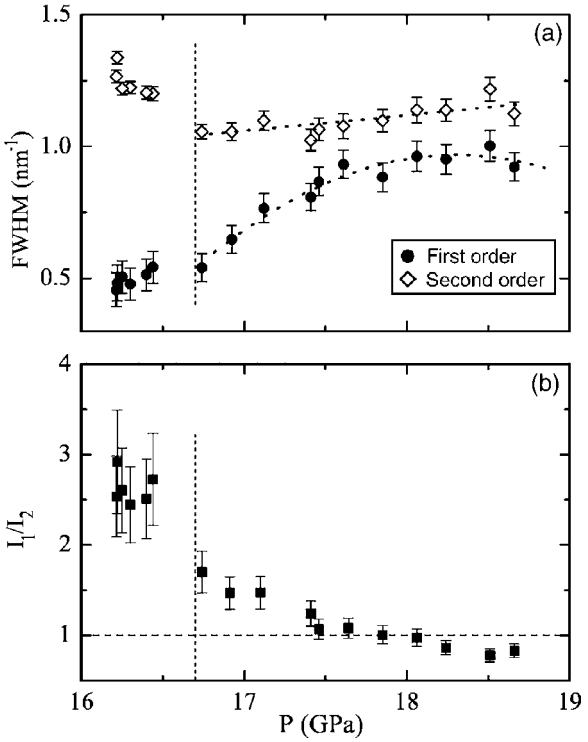

FIG. 5. (a) The deconvoluted FWHM peak width, and (b) the ratio of integrated intensities of the first- and the second-order sheets of diffuse scattering as a function of pressure. The vertical dashed line in both figures marks the location of the onset of chain melting at 16.7 GPa. The dotted lines in (a) are guides to the eye.

These changes in peak width are accompanied by changes in the relative integrated intensity of the two diffuse peaks, I_1/I_2. At 18.7 GPa, the second-order peak is slightly more intense than the first. On pressure decrease the relative intensity of the two peaks increases monotonically: they become equi-intense at 17.5 GPa and by 16.7 GPa the first-order peak is some 70% more intense than the second [Fig. 5(b)]. At 16.7 GPa there is a clear discontinuity in the width of the second-order peak [Fig. 5(a)], and perhaps also a smaller discontinuity in the width of the first. Below this pressure the second-order peak becomes broader still, while the first-order peak continues to sharpen, such that at 16.3 GPa, the second-order peak is some 2.8 times broader than the first [Fig. 5(a)]. Below 16.7 GPa, the intensity of the first diffuse peak becomes approximately 2.5 times that of the second peak, but any discontinuity in the relative intensity of the peaks at 16.7 GPa is masked by the large uncertainties in the ratio below this pressure [Fig. 5(b)].

B. Models for solid and liquid 1D chains

As stated earlier, the interchain correlation length in Rb-IV decreases rapidly below 16.7 GPa, but a fully melted chain state of Rb-IV is not observed at room temperature—interchain correlations remain to the lowest pressures.[20] The diffuse scattering expected from a 1D liquid has attracted considerable attention, particularly with regards to $Hg_{3-\delta}AsF_6$, where, at 300 K, the perpendicular Hg chains act

as a true 1D liquid.[21,22] In the 1D harmonic liquid model (see below) the widths of the diffuse sheets are proportional to the square of the order of the sheet, and thus if the guest chains in Rb-IV were truly a 1D liquid, then the width of the second-order diffuse peak should be four times that of the first. This is certainly not the case above 16.7 GPa, and the relative widths are still significantly discrepant from this value down to the lowest pressures accessible [Fig. 5(a)]. Of course, this lack of fully liquid-like behavior is to be expected in the presence of interchain correlations. However, there is evidence of a trend towards a liquid state in the increasing width ratio seen in Fig. 5(a) and in the increasing thermal amplitudes of the guest atoms along the c axis, as evident from the disappearance of the $hk2$ and $hk3$ guest Bragg reflection (Fig. 3).

In order to model the observed diffuse scattering, we thus require a nonliquid model that will incorporate the effects of the increased thermal amplitude on pressure decrease, while it is of interest to see quantitatively how well a 1D liquid model fits below 16.7 GPa after the onset of chain melting. For the nonliquid model we have used the 1D model for a perturbed lattice developed by Welberry and co-workers,[23–25,30] while for data collected below 16.7 GPa we have also used the 1D harmonic liquid model employed successfully to study the diffuse scattering from the 1D liquid-Hg chains in $Hg_{3-\delta}AsF_6$ (Ref. 21) and the 1D iodine chains in $DIPS(C_6H_5)_4(I_3)_{0.76}$.[24,26]

1. The 1D perturbed lattice model

The expression used to calculate the intensity distribution from a perturbed 1D regular lattice comprises two terms: that arising from the Bragg peaks and that from the diffuse scattering. In our analysis we were not able to include the Bragg peak intensities as they were all saturated, and we have therefore fitted only the diffuse scattering.

The expression for the diffuse scattering distribution is given by[30]

$$I(q)_{\mathrm{Diff}} = |f(q)|^2 e^{-q^2\sigma_L^2} \sum_{P=1}^{\infty} \frac{(\sigma_L^2 q^2)^P}{P!} \frac{(1-r^{2P})}{[1+r^{2P}-2r^P\cos(qd_g)]}, \tag{1}$$

where σ_L is the standard deviation of the displacements from the underlying regular lattice points [which in Rb-IV is closely related to the U_{33} atomic displacement parameter of the guest atoms], d_g is the average spacing of the guest atoms within the 1D chains, and r is the intrachain correlation coefficient.[24,30] r is usually <1 and is related to the correlation length via the equation $r=\langle x_{i-1}x_i\rangle/\sigma_L^2$, where x_i and x_{i-1} are the positions of the neighboring ith and $(i-1)$th atoms in a chain, and σ_L is as defined above. This model has been found to qualitatively reproduce the relative widths and intensities of the sheets of diffuse scattering arising from the chains of dibromodecane molecules within dibromodecane-urea composite structures.[30]

The diffraction profiles collected between 16.3 and 18.7 GPa have been fitted with Eq. (1) using $P=1,2,3,4$ terms and allowing d_g, r, and σ_L to refine freely at each pressure. As starting parameters we used the values of d_g obtained from our previous powder-diffraction study of Rb-IV,[7] while the initial value of σ_L was taken to be 0.246 Å, the value of U_{33} for the guest atoms obtained from a single-crystal structure refinement of Rb-IV at 19.2 GPa.

2. The 1D harmonic liquid model

For diffuse data collected below 16.7 GPa, we have also used the 1D harmonic liquid model reported by Spal *et al.*[22] and Albouy *et al.*,[26] to fit the data. This is obtained by solving the Hamiltonian for a 1D harmonic lattice of N atoms with mass M interacting through first neighbors.[21] In this model, the chain atoms have no long range order, and would therefore give no Bragg peaks.[35,36] The expression for the intensity distribution $I(q)$ of the diffuse sheets for such a 1D system is

$$I(q) = |f(q)|^2 \frac{\sinh\frac{1}{2}\sigma^2 q^2}{\cosh\frac{1}{2}\sigma^2 q^2 - \cos qd_g}, \tag{2}$$

where σ is the mean-squared fluctuation of the distance between first neighbors within the guest chains, and d_g is the average distance between adjacent guest atoms. As stated earlier, this model predicts that the width of the diffuse sheets varies as the square of their order.[34] Also, since $\left(\frac{\sigma}{d_g}\right)^2 = k_BT/Mc_s^2$, and $\Theta_D = 2\hbar c_s/k_B d_g$,[21] where M is the mass of the guest chain atoms, it is possible to extract estimates of both the sound velocity along the guest chains (c_s), and the effective Debye temperature of the chains (Θ_D) from the refined values of σ and d_g.

For both the perturbed lattice and 1D liquid models, the best fit to the data at each pressure was obtained by minimizing χ^2 and checking the residuals between the data and the fit. To ensure that the nonsmooth background between the diffuse peaks and any additional residual artifacts from the structured background did not affect the refinement, χ^2 was calculated using only data in the immediate vicinity of the diffuse peaks.

V. RESULTS

The perturbed 1D lattice model gave very good fits to the diffraction profiles collected above 16.7 GPa, correctly accounting for both the relative widths and the intensities of the first- and second-order diffuse peaks. Simulations of the intensity and width of the third diffuse peak were consistent with the broad, very weak peak observed (Fig. 1). The fits of the perturbed lattice model to the diffuse data collected at 18.5 GPa and 16.7 GPa are shown in Fig. 4. Below 16.7 GPa, the quality of fit to the perturbed lattice model decreased, indicating that the small discontinuities and changes in the widths and relative peak intensities observed at this pressure (see Fig. 5) mark a transition to a state where the perturbed 1D lattice model is no longer able to model the diffuse scattering completely. The fit obtained with this model to the diffuse data collected at 16.3 GPa is shown in

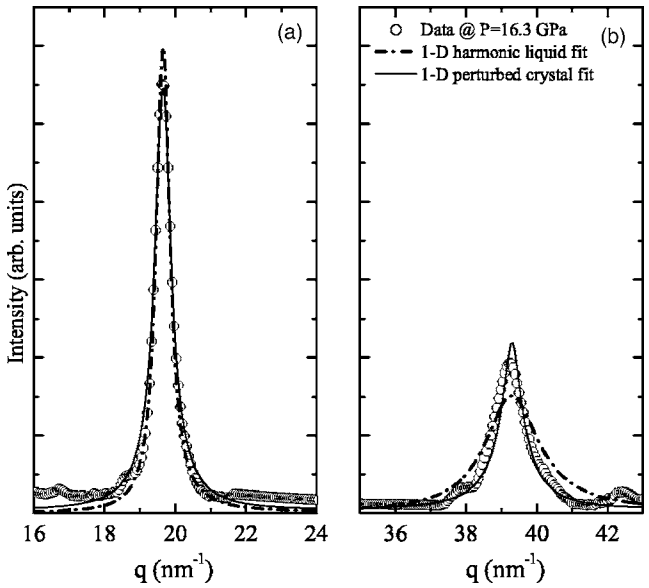

FIG. 6. Enlarged views, on the same scale, of the first- and second-order diffuse peaks observed at 16.3 GPa, showing the best fit obtained with the 1D perturbed lattice model and the 1D liquid model.

Fig. 6, where it can be seen that it slightly overestimates the width of the first-order peak, and slightly underestimates the width of the second.

Figure 6 also shows the fit of the 1D harmonic liquid model to the same diffuse data obtained at 16.3 GPa. Although this model gives a good fit to the width of the first-order peak, it overestimates the width of the second. This was to be expected, however, as the observed width of the second-order diffuse peak is not four times that of the first, as predicted by this model. As the pressure is decreased, and the interchain correlation length reduces,[20] one might expect the 1D liquid model to give an increasingly better fit to the diffuse data. Indeed, the pressure dependence of the FWHM of the diffuse peaks [Fig. 5(a)] results in an increase in the ratio of their widths, which reaches a value of $\sim$2.9 just before the transition to Rb-III.

Although the fit of the perturbed lattice model to the diffuse data below 16.7 GPa was slightly poorer than that obtained above this pressure, the fit was believed to be sufficiently good to enable the pressure dependence of the average interchain distance, d_g, the root-mean-square (RMS) displacement about the unperturbed lattice sites, σ_L, and the correlation coefficient r, to be estimated meaningfully over the full stability field of Rb-IV. The pressure dependence of d_g, and of σ_L and r, is shown in Figs. 7 and 8, respectively. For comparison, Fig. 7 also shows the pressure dependence of d_g above 16.7 GPa as obtained in our previous powder study of Rb-IV,[7] and the agreement with the present results can be seen to be excellent. Also shown in Fig. 8(a) for comparison is the U_{33} atomic displacement parameter of the guest atoms as obtained from a single-crystal structure refinement of Rb-IV at 19.2 GPa. The agreement with present results is good.

On pressure decrease little change is observed in σ_L above 18 GPa, but at pressures below this it increases steadily as the onset of chain melting is approached. We observed evidence of this behavior in our previous powder diffraction study of Rb-IV, which suggested that the along-chain RMS thermal amplitude at 16.9 GPa was $\sim$0.3 Å larger than that at 19.8 GPa.[20] The present analysis suggests the additional

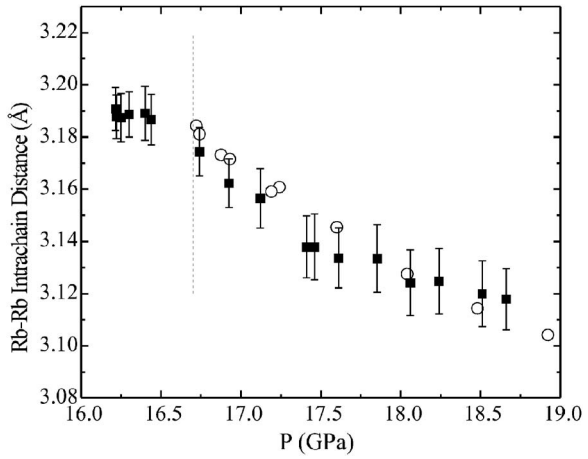

FIG. 7. Average intrachain distance, d_g, as a function of pressure in Rb-IV. The vertical dashed line marks the location of the onset of chain melting at 16.7 GPa. Values obtained from the fitting of the perturbed lattice model are shown using filled squares, while values obtained from the powder data of Ref. 7 are shown using open circles. The values obtained from fitting the diffuse data below 16.7 GPa with the 1D liquid model are the same, within error, as those obtained with the perturbed lattice model, and have been omitted for clarity.

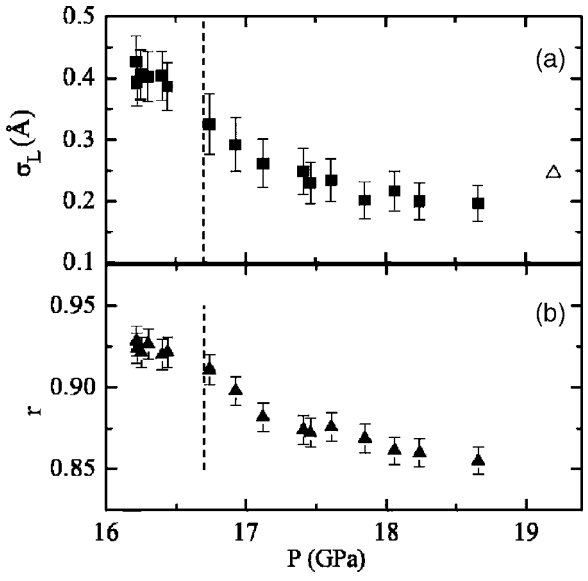

FIG. 8. Panel (a): The RMS displacement of the guest atoms from their unperturbed sites, σ_L, as function of pressure. The open triangle is the U_{33} atomic displacement parameter of the guest atoms obtained from a single-crystal structure refinement of Rb-IV at 19.2 GPa. The uncertainty in this value is smaller than the symbol used to plot the point. Panel (b): The correlation coefficient, r, as function of pressure for the guest chains. The vertical dashed line in both panels marks the location of the onset of chain melting at 16.7 GPa.

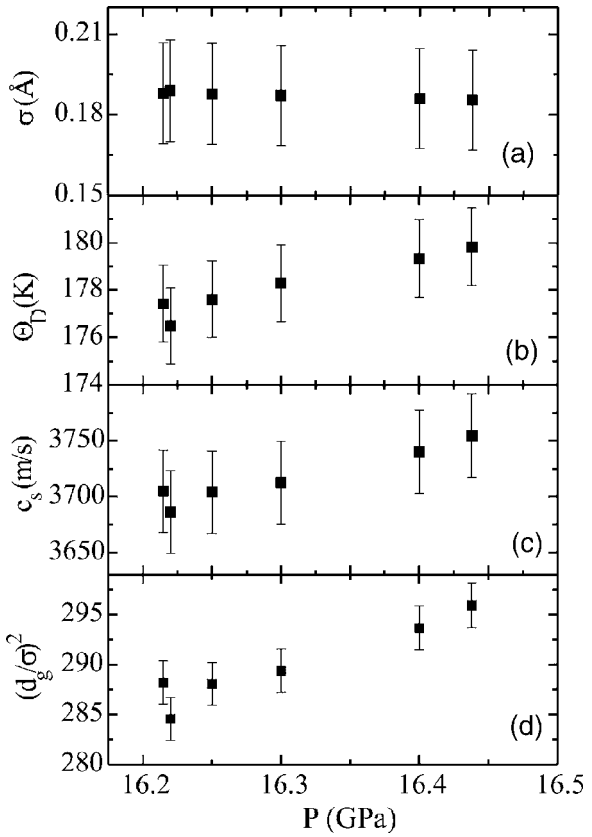

FIG. 9. The pressure dependence of (a) the RMS fluctuation, σ, in the nearest-neighbor intrachain distance, (b) the effective Debye temperature of guest chains, (c) the sound velocity along the guest chains, and (d) the correlation length $\left(\frac{d_g}{\sigma}\right)^2$ of the guest chains, all as estimated from the 1D harmonic liquid model.

RMS amplitude over this pressure range is closer to ~0.1 Å. The nearest-neighbor correlation r also increases as the pressure is decreased, suggesting that the along-chain motion of neighboring guest atoms becomes more correlated as the onset of chain melting is approached. Neither d_g, σ_L, nor r shows any discontinuities at 16.7 GPa: both σ_L and r continue to increase, reaching maximum values of 0.42 Å, and ~0.93, respectively, at 16.2 GPa, while below 16.7 GPa d_g has an almost constant value of 3.19 Å.

Although interchain correlations still exist in Rb-IV at 16.2 GPa—as evident from both the observation of (broad) Bragg reflections and the nonliquidlike ratio of the widths of the first two diffuse layers—fitting the diffuse data obtained below 16.7 GPa with the 1D liquid model enables estimates to be made of the physical properties of the chains in the liquid state. The values of d_g obtained using this model below 16.7 GPa were the same within error as those obtained with the perturbed lattice model. Figure 9 shows the pressure dependence of (a) the RMS fluctuation, σ, in the nearest-neighbor distance d_g within the chains, (b) the effective Debye temperature of the 1D liquid, (c) the longitudinal sound velocity along the guest chains, and (d) the correlation length within the guest chains, $\left(\frac{d_g}{\sigma}\right)^2$, as estimated using the methods employed by Emery and Axe[21] and Spal *et al.*[22] in their analysis of the 1D liquid chains in $Hg_{3-\delta}AsF_6$.

The RMS fluctuation, σ, in d_g has an almost pressure independent value of 0.18(1) Å, intermediate between the values of 0.08 Å and 0.3 Å found in $Hg_{3-\delta}AsF_6$ and $DIPS(C_6H_5)_4(I_3)_{0.76}$, respectively.[22,26] The estimated sound velocity along the guest chains of 3.7×10^3 ms^{-1}, and their effective Debye temperature of ~178 K, are to be compared to sound velocity values of 3.6×10^3 ms^{-1} (Ref. 34) and 4.4×10^3 ms^{-1} (Ref. 35), and a Debye temperature of 215 K,[22] obtained for $Hg_{3-\delta}AsF_6$ at room temperature and ambient pressure. The speed of sound in Rb-IV is as yet unknown, but the sound velocity in liquid-Rb at ambient pressure and 329 K is 1253 ms^{-1} (Ref. 36), and the volume compression, V/V_0, of Rb-IV at 18 GPa is 0.300.[37] Assuming that the sound velocity varies linearly with density,[38] we would then estimate the sound velocity in Rb-IV at 18 GPa to be 4.2×10^3 ms^{-1}, within ~13% of the value obtained from modeling the diffuse scattering. However, it should be noted that the inelastic scattering studies of Hastings *et al.*[35] showed that the sound velocity along the 1D liquid-Hg chains of $Hg_{3-\delta}AsF_6$ was a factor of 2 larger than that along the same direction in the 3D lattice, and a similar difference might also be present in Rb-IV. A definitive measurement of the sound velocity in both the three-dimensional (3D) lattice and 1D chains of Rb-IV might be obtained from an inelastic x-ray scattering study.

Finally, Fig. 9(d) shows the correlation length within the guest chains, $\left(\frac{d_g}{\sigma}\right)^2$, as a function of pressure. The range of values of 285(5) to 295(5), imply a correlation length—the distance over which the fluctuations of the guest atoms are correlated within the chains—of almost 300 lattice constants, a factor of 3 smaller than the correlation lengths of 1000 and 800 lattice constants found in $Hg_{3-\delta}AsF_6$ and $DIPS(C_6H_5)_4(I_3)_{0.76}$, respectively, at ambient conditions.[22,26] The greater correlation length in these other systems is consistent with the observation of higher-order sheets of diffuse scattering from these materials: Spal *et al.* observed the eighth-order diffuse sheet in $Hg_{3-\delta}AsF_6$,[22] and 13 sheets of diffuse scattering were observed in $DIPS(C_6H_5)_4(I_3)_{0.76}$.[26]

VI. DISCUSSION

The excellent fit obtained to the diffuse data collected from Rb-IV above 16.7 GPa suggests that the perturbed lattice model provides a good description of the disordering of the guest atom chains in Rb-IV at higher pressures. The motion of the atoms along the chains is highly correlated, and the ~0.2 Å RMS displacements about their equilibrium positions at 19.2 GPa is almost twice as large as the displacement of the host atoms in the same direction at the same pressure, as determined from a refinement of single-crystal diffraction data. Despite the larger displacements along the chain direction, reflections from the guest are clearly visible within the second and third diffuse sheets, as illustrated for the second sheet at 18.5 GPa in Fig. 3(a).

As the onset of melting at 16.7 GPa is approached, the RMS displacements, σ_L, of the guest atoms along the chains increases to more than 0.3 Å [Fig. 8(a)], with the result that the intensity of the ($hk2$) and ($hk3$) guest Bragg peaks decreases markedly as the localization of the chain atoms on

their unperturbed lattice sites is progressively lost. The motion of neighboring guest atoms also becomes more correlated as the pressure is decreased [Fig. 8(b)]. At 16.7 GPa, a small but clear discontinuity is observed in the width of the second-order diffuse peak [see Fig. 5(a)], and perhaps in the first-order one too, and these result in a slightly poorer fit of the perturbed lattice model to the diffuse data collected below that pressure. Despite this, the fit to the model is still good enough to enable the spacing of the guest atoms in the chains, their RMS displacements, and the correlation of neighboring atoms to be determined meaningfully down to 16.2 GPa, where the sample transformed to Rb-III. The increase in σ_L to more than 0.4 Å [Fig. 5(a)] results in the complete disappearance of all but the broadened ($hk1$) guest Bragg reflections, which are observed down to the onset of the transition to Rb-III.

The observation of these reflections confirms the existence of interchain correlations at all pressures. However, the discontinuities in the widths of the diffuse peaks at 16.7 GPa and, below that pressure, the approach of the width ratio towards the value of four expected for a liquid, suggests that the guest chains are indeed becoming more liquid-like, rather than simply more disordered, on pressure decrease. This change to liquid-like behavior is supported by the poorer fit of the perturbed lattice model below 16.7 GPa, and by the similarities in the behavior of Rb-IV with those systems, most notably $Hg_{3-\delta}AsF_6$, where true 1D liquid chains are observed. Although the guest chains in Rb-IV never become a true liquid at 300 K, the use of the 1D harmonic liquid model to fit the diffuse scattering data obtained below 16.7 GPa also yields plausible estimates of the sound velocity along the guest chains, and of the RMS fluctuations in the guest-guest distance within the chains. It still remains to be seen whether truly liquidlike chains can be observed in Rb-IV, perhaps at high or low temperatures. Further experiments are required.

VII. CONCLUSIONS

In conclusion, we have measured the diffuse scattering from single-crystals of incommensurate Rb-IV through the onset of chain melting at 16.7 GPa. Sheets of diffuse scattering are observed at all pressures, and discontinuities are observed in the widths of these sheets on passing through 16.7 GPa. We have found that a 1D perturbed lattice model fits the diffuse scattering very well, especially above 16.7 GPa, while the use of a 1D harmonic liquid model below 16.7 GPa enabled estimates to be made of the physical properties of the chains.

ACKNOWLEDGMENTS

The x-ray diffraction experiments were undertaken during beamtime allocated to proposal HS2502 at the European Synchrotron Radiation Facility. The authors would like to thank T.R. Welberry of Australian National University and R.A. Cowley of Oxford University for helpful discussions. This work was supported by grants from EPSRC, funding from CCLRC, and facilities provided by the European Synchrotron Radiation Facility and Daresbury Laboratory.

[1] R. J. Nelmes, D. R. Allan, M. I. McMahon, and S. A. Belmonte, Phys. Rev. Lett. **83**, 4081 (1999).
[2] M. I. McMahon, T. Bovornratanaraks, D. R. Allan, S. A. Belmonte, and R. J. Nelmes, Phys. Rev. B **61**, 3135 (2000).
[3] M. I. McMahon, O. Degtyareva, and R. J. Nelmes, Phys. Rev. Lett. **85**, 4896 (2000).
[4] O. Degtyareva, M. I. McMahon, and R. J. Nelmes, Phys. Rev. B **70**, 184119 (2004).
[5] O. Degtyareva, M. I. McMahon, and R. J. Nelmes, High Press. Res. **24**, 319 (2004).
[6] U. Schwarz, A. Grzechnik, K. Syassen, I. Loa, and M. Hanfland, Phys. Rev. Lett. **83**, 4085 (1999).
[7] M. I. McMahon, S. Rekhi, and R. J. Nelmes, Phys. Rev. Lett. **87**, 055501 (2001).
[8] M. I. McMahon, L. F. Lundegaard, C. Hejny, S. Falconi, and R. J. Nelmes, Phys. Rev. B **73**, 134102 (2006).
[9] C. Hejny and M. I. McMahon, Phys. Rev. Lett. **91**, 215502 (2003).
[10] M. I. McMahon, C. Hejny, J. S. Loveday, L. F. Lundegaard, and M. Hanfland, Phys. Rev. B **70**, 054101 (2004).
[11] C. Hejny, L. F. Lundegaard, S. Falconi, M. I. McMahon, and M. Hanfland, Phys. Rev. B **71**, 020101(R) (2005).
[12] T. Kenichi, S. Kyoko, F. Hiroshi, and O. Mitsuko, Nature (London) **423**, 971 (2003).
[13] R. J. Nelmes, M. I. McMahon, J. S. Loveday, and S. Rekhi, Phys. Rev. Lett. **88**, 155503 (2002).
[14] M. I. McMahon, R. J. Nelmes, and S. Rekhi, Phys. Rev. Lett. **87**, 255502 (2001).
[15] O. Degtyareva, M. I. McMahon, D. R. Allan, and R. J. Nelmes, Phys. Rev. Lett. **93**, 205502 (2004).
[16] C. Hejny and M. I. McMahon, Phys. Rev. B **70**, 184109 (2004).
[17] M. Hanfland, K. Syassen, N. E. Christensen, and D. L. Novikov, Nature (London) **408**, 174 (2000).
[18] D. A. Young, *Phase Diagrams of the Elements* (University of California Press, Berkley, CA, 1991).
[19] C. Buzea and K. Robbie, Supercond. Sci. Technol. **18**, R1 (2005).
[20] M. I. McMahon and R. J. Nelmes, Phys. Rev. Lett. **93**, 055501 (2004) and references therein.
[21] V. J. Emery and J. D. Axe, Phys. Rev. Lett. **40**, 1507 (1978).
[22] R. Spal, C.-E. Chen, T. Egami, P. J. Nigrey, and A. J. Heeger, Phys. Rev. B **21**, 3110 (1990).
[23] T. R. Welberry (private communication).
[24] T. R. Welberry, G. H. Miller, and C. E. Carrol, Acta Crystallogr., Sect. A: Cryst. Phys., Diffr., Theor. Gen. Crystallogr. **36**, 921 (1980); T. R. Welberry and B. D. Butler, Chem. Rev. (Washington, D.C.) **95**, 2369 (1995); T. R. Welberry, Rep. Prog. Phys. **48**, 1543 (1985).
[25] T. R. Welberry and B. D. Butler, J. Appl. Crystallogr. **27**, 205 (1994).
[26] P. A. Albouy, J. P. Pouget, and H. Strzelecka, Phys. Rev. B **35**,

173 (1987)
[27] F. Datchi, R. LeToullec, and P. Loubeyre, J. Appl. Phys. **81**, 3333 (1997).
[28] A. P. Hammerseley, S. O. Svensson, A. Thompson, H. Graafsma, A. Kvick, and J. P. Moy, Rev. Sci. Instrum. **66**, 2729 (1995).
[29] Sample 2 was required for a further experiment on Rb-IV and we did not want to degrade the quality of this single crystal by altering the pressure.
[30] T. R. Welberry, *Diffuse X-Ray Scattering and Models of Disorder*, International Union of Crystallography: Monographs on Crystallography (Oxford University Press, Oxford, 2004).
[31] S. Ravy, P. A. Albouy, S. Megtert, R. Moret, J. P. Pouget, and R. Comes, Phase Transitions **16/17**, 193 (1989).
[32] A. J. C. Wilson, and E. Price, *International Tables for Crystallography* (Kluwer Academic, International Union of Crystallography, Dordrecht, The Netherlands, 1999), Vol. C.
[33] A. Guinier, *X-ray Diffraction in Crystals, Imperfect Crystals and Amorphous Bodies* (Dover, New York, 1963).
[34] I. U. Heilmann, J. D. Axe, J. M. Hastings, G. Shirane, A. J. Heeger, and A. G. MacDiarmid, Phys. Rev. B **20**, 751 (1979).
[35] J. M. Hastings, J. P Pouget, G. Shirane, A. J. Heeger, N. D. Miro, and A. G. MacDiarmid, Phys. Rev. Lett. **39**, 1484 (1977).
[36] J. Jarzynski, J. R. Smirnow, and C. M. Davis, Jr., Phys. Rev. **178**, 288 (1969).
[37] M. I. McMahon and R. J. Nelmes (unpublished).
[38] F. Birch, *Solids Under Pressure*, edited by W. Paul and D. M. Warschauer (McGraw-Hill, New York, 1963), pp. 137–162.

Different incommensurate composite crystal structure for Sc-II

M. I. McMahon, L. F. Lundegaard, C. Hejny, S. Falconi, and R. J. Nelmes
SUPA, School of Physics and Centre for Science at Extreme Conditions, The University of Edinburgh, Mayfield Road, Edinburgh EH9 3JZ, United Kingdom
(Received 28 November 2005; published 5 April 2006)

The long uncertain crystal structure of the high-pressure phase of scandium, Sc-II, is found to have an incommensurate composite structure comprising a body-centered host structure and a *C*-face-centered guest structure. At 23 GPa, the shortest distance between guest atoms is ~2.7 Å, comparable to the average host-host distance of 2.8 Å. This differs from the structure proposed recently [H. Fujihisa *et al.*, Phys. Rev. B **72**, 132103 (2005)] which has a body-centered guest structure, with anomalously short guest-guest distances.

DOI: 10.1103/PhysRevB.73.134102 PACS number(s): 62.50.+p, 61.50.Ks

The development of advanced angle-dispersive powder and single-crystal diffraction techniques has led to the discovery of a number of complex incommensurate crystal structures in the elements at high pressures.[1] The group II and V elements, Ba and Sr,[2,3] and As, Sb, and Bi,[4–6] have high-pressure phases comprising an 8-atom body-centered host structure and linear chains of guest atoms lying in channels, along the *c* axis, through the host framework [Fig. 1(a)]. And these guest chains form a simple body-centered [Fig. 1(a)] or *C*-face-centered structure which is *incommensurate* with the host along their common *c* axis. The group I elements K and Rb (Refs. 1, 7, and 8) also have a composite host-guest structure at high pressure, but with a 16-atom host structure [Fig. 1(b)].

Recently, Fujihisa *et al.*[9] have reported that scandium, the first of the 3*d* transition metals, also possesses an incommensurate composite structure above 22 GPa (Sc-II), with the same body-centered host and guest structures as Bi-III and Sb-II [as in Fig. 1(a)]. This is an important result in revealing the stability of host-guest composite structures in another group of elements with a quite different electronic configuration, and it suggests that still more such phases may be found. However, this solution has an anomalously short guest-guest distance along the chains, as Fujihisa *et al.* acknowledge,[9] although the fit to the powder diffraction profiles is good. At 23 GPa, the guest-guest distance (d_4 in Ref. 9) is only 2.285 Å, some 18% shorter than the average host-host contact distance of 2.79 Å (d_1 and d_2 in Ref. 9). And this difference increases to 21% at 101 GPa, where the guest-guest spacing is only 1.957 Å. This is quite unlike all the other composite structures found to date (Ba-IV, Sr-V, K-III, Rb-IV, As-III, Sb-II, Sb-IV, and Bi-III), in which the spacing of the guest atoms differs from the host-host contact distances by no more than 2%. Fujihisa *et al.* suggest that the short spacing might arise from a difference in the electronic structure of the host and guest atoms. But the magnitude of the effect seems improbably large, noting that the spacing of 1.957 Å at 101 GPa is even smaller than the closest contact distance of 2.052(2) Å in Sc-V at the very much higher pressure of 242 GPa.[10]

In this paper we propose a different incommensurate composite solution. It has the same host structure but a guest component that has a larger spacing along the *c* axis and is *C*-face-centered rather than body-centered, isostructural with Sr-V rather than Bi- III.[1] This structure both gives a significantly better fit to our diffraction data at 23 GPa, and also results in a guest-guest spacing of 2.686(1) Å, much closer to the average host-host contact distance of 2.799(1) Å.

Powder diffraction data were collected on station 9.1 at the Synchrotron Radiation Source, Daresbury Laboratory, using an imaging plate area detector and an incident wavelength of 0.4654 Å.[11] A small number of diffraction profiles was also collected from the same sample on beamline ID09 at the European Synchrotron Radiation Facility (ESRF). The Sc samples were small (~70 μm × 70 μm × 20 μm) pieces cut under light mineral oil from the starting material of 99.9% purity, purchased from Alfa Aesar. These pieces were loaded into diamond-anvil pressure cells with the mineral oil as a pressure transmitting medium. The pressure was measured using the ruby fluorescence scale in Ref. 12, and the two-dimensional (2D) diffraction patterns were integrated azimuthally to give standard powder diffraction profiles.[11,13]

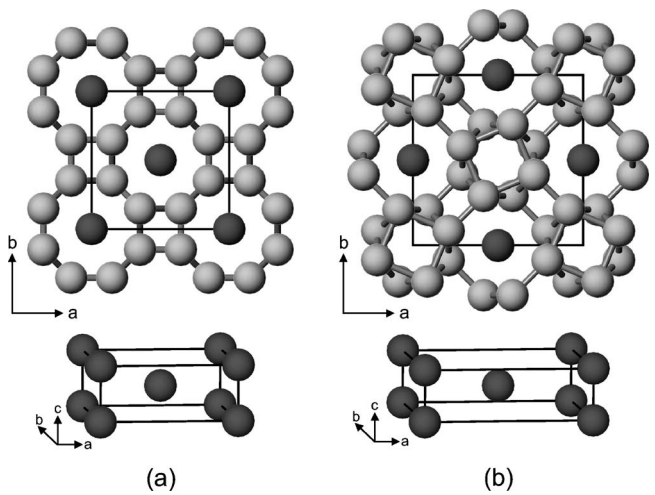

FIG. 1. Composite incommensurate structures with a host framework (shown gray) and guest chains (shown black), viewed along the *c* axis, for (a) an 8-atom host and (b) a 16-atom host. Perspective drawings show body-centered guest structures such as found in Bi-III (with the 8-atom host) and Rb-IV (with the 16-atom host). Other systems have *C*-face-centered guest structures with the same host structures. Crystallographic axes are labeled.

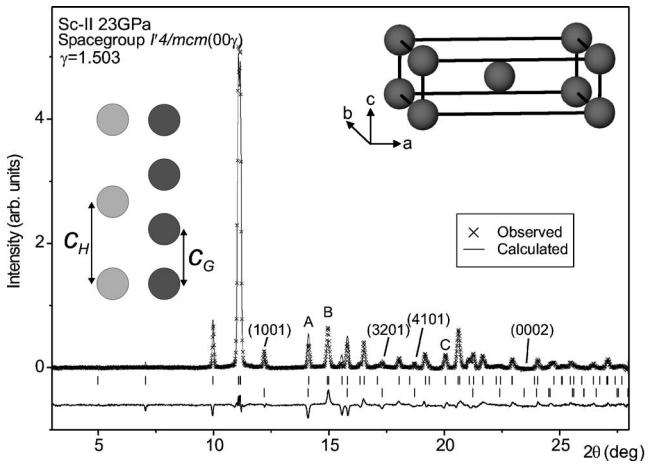

FIG. 2. Rietveld refinement of Sc-II at 23 GPa in the $I'4/mcm(00\gamma)$ superspace group proposed by Fujihisa *et al.* (Ref. 9) (body-centered guest). Upper tick marks show calculated peak positions for $hkl0$ host reflections and $hk00$ host/guest reflections, and lower ones mark $hk0m$ guest-only reflections. Differences between observed and calculated profiles are shown below the tick marks. The four guest-only reflections not overlapped by $hkl0$ or $hk00$ reflections are indexed and peaks marked "*A*," "*B*," and "*C*" are explained in the text. Right inset: perspective view of the body-centered guest structure, with axes as labeled. Left inset: incommensurate relationship of the host (c_H) and guest (c_G) *c* axes.

Structural refinements in 4D superspace were performed using JANA2000.[14]

At ambient pressure Sc-I has the hexagonal-close packed (hcp) structure. On compression, the transition to the Sc-II phase was observed to start at 20.5 GPa and single-phase profiles of Sc-II were observed above 23 GPa. In contrast to the smooth Debye-Scherrer (DS) rings observed in the diffraction patterns from Sc-I, the DS rings from Sc-II were spotty, showing that the Sc-I→Sc-II transition is accompanied by some recrystallization of the sample. To minimize the effects of this behavior on the relative intensities of the diffraction peaks, the sample pressure was decreased to take the sample back into the hcp phase, and then increased again into Sc-II. The resulting DS powder rings were considerably smoother, sufficient to give accurate relative intensities on past experience. The diffraction peaks in the integrated profiles were also sharper, similar to the data of Fujihisa *et al.*[9] In particular, they reported resolving the strongest diffraction peak in the Sc-II pattern as a doublet, and we observed the same. However, in contrast to the data of Fujihisa *et al.*, the most intense guest-only reflection [indexed as (1001) in Fig. 2] had the same width as the other reflections, and we therefore see no evidence of the chain melting[15] previously suggested.[9] The weakness and apparent broadening of the guest-only reflections reported by Fujihisa *et al.* may indicate texture or preferred orientation effects.

Figure 2 shows the Rietveld fit to the Sc-II profile obtained at 23 GPa, using the $I'4/mcm(00\gamma)$ composite structure proposed by Fujihisa *et al.*, where $I'4/mcm(00\gamma)$ is the superspace group symmetry of the composite structure with a body-centered guest, and I' denotes the centering $(\frac{1}{2},\frac{1}{2},\frac{1}{2},\frac{1}{2})$ in superspace. (Hereafter, we refer to the superspace group in relation to structure refinements, but to the separate host and guest components of the composite structure in other contexts.) The best-fitting parameters at 23 GPa are $a=7.5679(1)$ Å, $c=3.4390(2)$ Å, and $\gamma=1.5028(3)$, with the host and guest atoms at (0.1476(2),0.6476(2),0) and (0,0,0), respectively. *c* is equal to the *c*-axis repeat of the host component, c_H; the repeat of the guest component, c_G, is c/γ. The *R* factor of the fit was $R_{wp}=1.4\%$, compared with 3.2% obtained by Fujihisa *et al.* with their data.[9] The number of atoms in the host unit cell is $8+(2\times\gamma)=11.01$, and the spacing of the guest atoms within the linear chains in this structure is $c/\gamma=2.288(1)$ Å, some 18% shorter than the average host-host distance of 2.802 Å, and in close agreement with the distances reported by Fujihisa *et al.*

Given the apparent problem with the shortness of this guest-guest distance, we made a systematic search for other possible solutions to the structure. On the basis that the spacing of the guest atoms within the chains can be no shorter than that reported by Fujihisa *et al.*, γ must be $\leqslant 1.50$. The other physical limit is that the density cannot decrease at the Sc-I→Sc-II transition. Refinement of a mixed-phase pattern at 22 GPa gave an atomic volume of 19.16 Å^3 for the Sc-I component, and the measurements of Akahama *et al.*[10] show a pressure dependence of ~0.20 Å^3/GPa. Hence the maximum atomic volume for Sc-II at 23 GPa is 18.96 Å^3, and then the number of atoms in the host unit cell must be at least 10.38, which means that γ has to be $\geqslant 1.19$. These limits allow the guest-only reflection at 12.2° to be indexed as (1001), (1101), (2001), or (2101), corresponding to γ values of 1.503, 1.432, 1.280, and 1.198, respectively. And there are no other possibilities. These γ values correspond in turn to atom spacings along the guest chains of 2.288, 2.402, 2.687, and 2.871 Å, respectively. The only variable in the guest structure is the position along *c* of the chain at $x=y=\frac{1}{2}$ relative to those at $x=y=0$ (see Fig. 1), and so the possible arrangements are body centered, *C*-face centered, and primitive. The primitive option can be ruled out in all cases because it would predict several nonoverlapped guest-only reflections none of which is observed. Since (1001) and (2101) are not allowed for *C*-face centering, and (1101) and (2001) are not allowed for body centering, the only possible guest structures thus emerge as body-centered with γ values of 1.503 and 1.198, and *C*-face-centered with γ values of 1.432 and 1.280.

Of these four, the *C*-face-centered structure with γ of 1.432 can be discarded since, despite having a good overall fit ($R_{wp}=1.3\%$), it cannot account for the clearly observed guest reflection at 17.3° [indexed as the (3201) in Fig. 2]. And trial refinements of the body-centered structure with $\gamma=1.198$ showed that, in addition to giving a considerably poorer overall fit ($R_{wp}=1.8\%$) to the diffraction data than the $\gamma=1.503$ solution of Fujihisa *et al.*, the structure cannot simultaneously fit the guest peak at 10.0° and the peak at 12.2°. This is illustrated in Fig. 3, which shows a Rietveld refinement of this structure to the same 23 GPa data as in Fig. 2. The value of γ necessary to fit the position of the guest-only peak indexed as (2101) at 12.2° is 1.198 [inset (a)]. The calculated position of the lower-angle (1001) guest-only reflection is then 9.94°, and this overlaps the

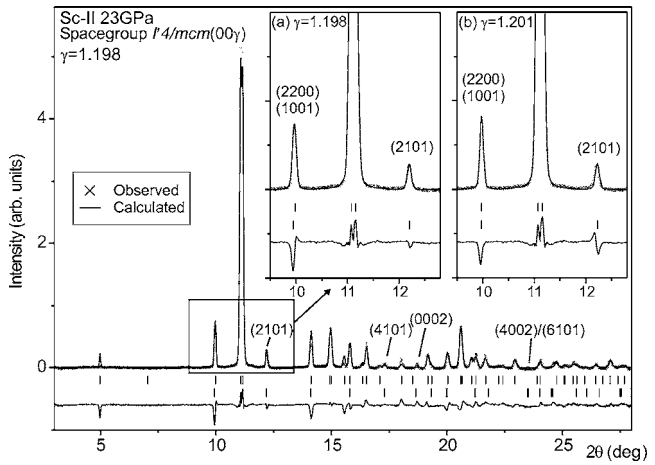

FIG. 3. Rietveld refinement of Sc-II at 23 GPa in superspace group $I'4/mcm(00\gamma)$ with $\gamma=1.198$ (body-centered guest). The tick marks, difference profile, and indexing (in the main profile) are as explained in Fig. 2. Inset (a): enlarged view of the low-angle part of the main profile, showing the fit to the peaks as indexed at 10.0° and 12.2°. Inset (b): fit to the same part of the profile with $\gamma=1.201$.

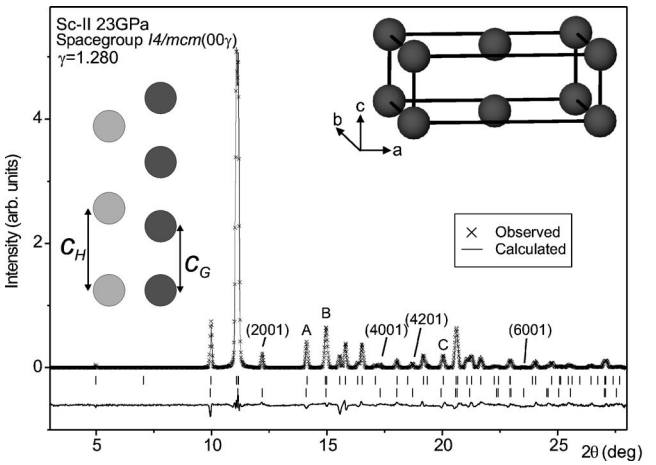

FIG. 4. Rietveld refinement of Sc-II at 23 GPa in superspace group $I4/mcm(00\gamma)$ (C-face-centered guest). The tick marks, difference profile, indexing, and peak labeling are as explained in Fig. 2. Right inset: perspective view of the C-face-centered guest structure, with axes as labeled. Left inset: incommensurate relationship of the host (c_H) and guest (c_G) c axes.

γ-independent (2200) host/guest reflection at 9.98° to produce a combined calculated peak that is displaced, as shown in inset (a). This misfit is much larger than is seen for any of the host-only peaks, and is certainly more than expected for data of this quality. If, instead, the value of γ is increased slightly, to 1.201, so as to fit the position of this peak at 10°, then the fit to the position of the (2101) peak becomes unsatisfactory [inset (b) to Fig. 3]. This possible solution can thus be discarded as well, considering also the poorer overall fit it provides, and there then remain only the original solution of Fujihisa *et al.* and the C-face-centered structure with γ of 1.280.

Figure 4 shows a Rietveld fit to the Sc-II profile obtained at 23 GPa using this C-face-centered solution for the guest. This has superspace group $I4/mcm(00\gamma)$, and the best-fitting parameters are $a=7.5672(1)$ Å, $c=3.4398(1)$ Å, and $\gamma=1.2804(3)$, with the host and guest atoms at (0.1490(2),0.6490(2),0) and (0,0,0), respectively. The fit gave $R_{wp}=1.1\%$, significantly lower than the value of 1.4% obtained with the same data for the body-centered guest structure, and the lowest for all the structures tested. The spacing of the guest atoms is $c/\gamma=2.686(1)$ Å, 0.40 Å longer than that obtained with the body-centered guest structure, and considerably closer to the average host-host distance of 2.799(1) Å.

Although the C-face-centered solution is the more physically plausible and gives a better fit to our data, it remains to be shown that this is decisively the correct solution. This is difficult because of the degree of overlap of host and guest reflections, such that there are only the four detectable non-overlapped guest-only peaks in the whole pattern. However, a detailed analysis yields two distinguishing features. The first concerns the observed peak at 20.0°, labeled "C" in Figs. 2 and 4. It can be seen in Fig. 2 that the body-centered guest structure fits this as a singlet [which indexes as the (4400) host/guest reflection], whereas the C-centered structure (Fig. 4) fits it as an unresolved doublet of (4400) and the (0002) guest-only reflection. [Note that (0002) is placed at a much higher angle for the body-centered guest structure, as indexed in Fig. 2.] Although the doublet is not resolved, these two reflections are at different 2θ angles, as shown by the tick marks in Fig. 4. Figure 5 shows a diffraction profile obtained on beamline ID09 at the ESRF, from the same sample as was used to obtain the data in Figs. 2–4, with the

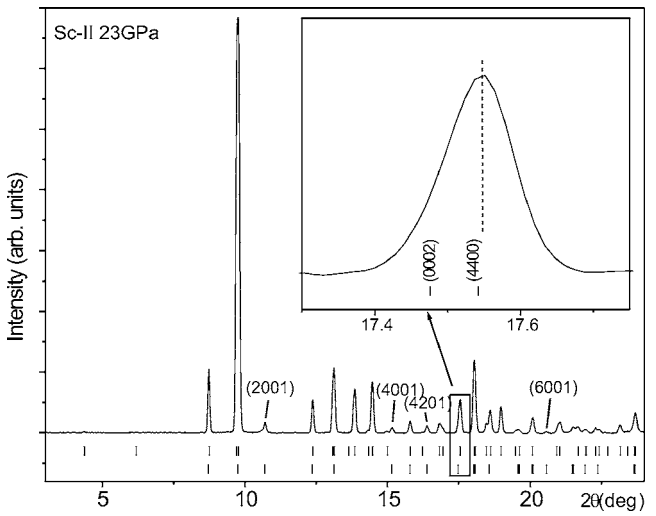

FIG. 5. Diffraction profile obtained at the ESRF from the same sample as that used to obtain the data in Figs. 2–4. Small differences in relative peak intensities compared to those data can be attributed to powder averaging over a smaller sample volume because a much smaller x-ray beam was used (10 μm × 10 μm). Differences in diffraction angles from Figs. 2–4 result from the use of a shorter x-ray wavelength (0.410 08 Å). Tick marks are as explained in Fig. 2, here for the best-fitting $I4/mcm(00\gamma)$ structure (with $\gamma=1.280$ Å as in Fig. 4). Inset: enlarged view of the (4400)/(0002) doublet, showing asymmetry of the peak. The vertical dashed line is a guide to the eye.

calculated peak positions for the best-fitting $I4/mcm(00\gamma)$ structure (*C*-face-centered guest). The inset shows an enlarged view of the observed peak *C* and the calculated positions of the (4400) and (0002) reflections. The diffraction peak is clearly asymmetric, and its shape is well accounted for by the (4400)/(0002) doublet. By contrast, this asymmetry cannot be explained by the $I'4/mcm(00\gamma)$ structure (body-centered guest), where the reflection is a singlet. The other evidence comes from the peaks marked "*A*" and "*B*" in Figs 2 and 4. As shown by the difference profiles, they have the largest misfits to the structure with the body-centered guest (Fig. 2), but fit well with the *C*-face-centered guest (Fig. 4). In both cases, the host and *hk*00 host/guest reflections are (4000) at *A* and (3300)/(3210) at *B*. For the body-centered guest (Fig. 2), peak *A* includes the (2101) guest-only reflection (shown by the lower tick mark), and there is no guest-only reflection at *B*. For the *C*-centered case (Fig. 4), there are guest-only reflections (2201) at *A* and (3101) at *B*. The (2201) reflection has a multiplicity of 8 compared with 16 for (2101) in Fig. 2 and can thus remove the overestimation of the intensity shown at *A* in Fig. 2; and the addition of the (3101) reflection removes the underestimation at *B* in Fig. 2. These features, taken together with the improved overall fit, provide strong support for the $I4/mcm(00\gamma)$ structure, which also resolves the issue of the guest-guest distances.

The number of atoms in a unit cell of the $I4/mcm(00\gamma)$ structure is $8+(2\times\gamma)=10.56$ at 23 GPa, somewhat smaller than the value of 11.01 obtained from the refinement using the $I'4/mcm(00\gamma)$ structure. As a result, the density of Sc-II is 4% less than that calculated by Fujihisa *et al.*[9] They quote a volume change of 9% at the transition, which is equivalent to ~7% as $\Delta V/V_0$, and this is reduced to 3.2% by the 4% smaller density for the $I4/mcm(00\gamma)$ structure. But fits to our mixed-phase angle-dispersive data, showing Sc-I and Sc-II coexisting at 22 GPa, give a volume (or density) difference between them of only 1.3(1)% for the $I4/mcm(00\gamma)$ structure. Since we agree with Fujihisa *et al.* concerning the density of Sc-II within 0.5%, we conclude that the atomic volume of Sc-I at the transition is about 2.5% smaller than found in previous measurements,[9,10] at 19.16 Å^3 as quoted above.

In conclusion, we show that an incommensurate composite host-guest structure with a *C*-face-centered guest in superspace group $I4/mcm(00\gamma)$ gives a better fit to the diffraction data for Sc-II at 23 GPa than the $I'4/mcm(00\gamma)$ solution recently proposed by Fujihisa *et al.*, and that details in the fitting strongly suggest this to be the unique correct solution. This structure also removes the improbably small separation of atoms in the guest chains required for the $I'4/mcm(00\gamma)$ solution. [Host-guest distances are unaltered, and are distributed from 2.885(1) Å to 3.011(1) Å at 23 GPa as for d_3 in Ref. 9.] When the pressure dependence of γ in Fig. 3b of Ref. 9 is adjusted to the $I4/mcm(00\gamma)$ solution, γ increases from 1.28 at 23 GPa to 1.36 at 101 GPa, passing through the commensurate value of $\frac{4}{3}$ at 72 GPa, and the spacing of the guest atoms at 101 GPa increases from 1.957 to 2.27 Å.

Although Sc-II is thus found to be isostructural with Sr-V, it is intriguing that its structural dimensions are more similar to those found in Bi-III and Sb-II. In particular, the Sc-II incommensurate wave vector of 1.2804(1) is considerably closer to the values of 1.309(1) and 1.310(1) found in Bi-III and Sb-II, respectively, than the value of 1.404(1) found in Sr-V.[1] And, similarly, the c/a ratio of the Sc-II host unit cell of 0.454(1) is closer to the values of 0.489(1) and 0.484(1) found in Bi-III and Sb-II, respectively, than the value of 0.570(1) found in Sr-V.[1] We note that the fact that Sc passes through a simple $\frac{4}{3}$ commensurate form at 72 GPa opens up the first opportunity for exact calculations of any of these systems.

We thank M. Roberts of Daresbury Laboratory for setting up the 9.1 beamline, and M. Hanfland of the ESRF for setting up the ID09 beamline. This work was supported by grants from EPSRC, funding from CCLRC, and facilities provided by Daresbury Laboratory.

[1] M. I. McMahon and R. J. Nelmes, Z. Kristallogr. **219**, 742 (2004).
[2] R. J. Nelmes, D. R. Allan, M. I. McMahon, and S. A. Belmonte, Phys. Rev. Lett. **83**, 4081 (1999).
[3] M. I. McMahon, T. Bovornratanaraks, D. R. Allan, S. A. Belmonte, and R. J. Nelmes, Phys. Rev. B **61**, 3135 (2000).
[4] O. Degtyareva, M. I. McMahon, and R. J. Nelmes, Phys. Rev. B **70**, 184119 (2004).
[5] U. Schwarz, L. Akselrud, H. Rosner, A. Ormeci, Y. Grin, and M. Hanfland, Phys. Rev. B **67**, 214101 (2003).
[6] M. I. McMahon, O. Degtyareva, and R. J. Nelmes, Phys. Rev. Lett. **85**, 4896 (2000).
[7] M. I. McMahon, R. J. Nelmes, U. Schwarz, and K. Syassen (unpublished).
[8] M. I. McMahon, S. Rekhi, and R. J. Nelmes, Phys. Rev. Lett. **87**, 055501 (2001).
[9] H. Fujihisa, Y. Akahama, H. Kawamura, Y. Gotoh, H. Yamawaki, M. Sakashita, S. Takeya, and K. Honda, Phys. Rev. B **72**, 132103 (2005).
[10] Y. Akahama, H. Fujihisa, and H. Kawamura, Phys. Rev. Lett. **94**, 195503 (2005).
[11] R. J. Nelmes and M. I. McMahon, J. Synchrotron Radiat. **1**, 69 (1994).
[12] H. K. Mao, J. Xu, and P. M. Bell, J. Geophys. Res. **91**, 4673 (1986).
[13] A. P. Hammersley, S. O. Svensson, M. Hanfland, A. N. Fitch, and D. Haüsermann, High Press. Res. **14**, 235 (1996).
[14] V. Petricek, M. Dusek, and L. Palatinus, *The Crystallographic Computing System JANA2000* (Institute of Physics, Praha, Czech Republic, 2000).
[15] M. I. McMahon and R. J. Nelmes, Phys. Rev. Lett. **93**, 055501 (2004).

X-ray Diffraction Study of Liquid Cs up to 9.8 GPa

S. Falconi, L. F. Lundegaard, C. Hejny, and M. I. McMahon
School of Physics and Centre for Science at Extreme Conditions, The University of Edinburgh, Mayfield Road, Edinburgh, EH9 3JZ, United Kingdom
(Received 30 November 2004; published 1 April 2005)

We describe an x-ray diffraction study of liquid Cs at high pressure and temperature conducted in order to characterize the structural changes associated with the complex melting curve and phase transitions observed in the solid phases. At 3.9 GPa we observe a discontinuity in the density of the liquid accompanied by a decrease in the coordination number from about 12 to 8, which marks a change to a nonsimple liquid. The specific volume of liquid Cs, combined with structural analysis of the diffraction data, strongly suggest the existence of dsp^3 electronic hybridization above 3.9 GPa, similar to that reported on compression in the crystalline phase.

DOI: 10.1103/PhysRevLett.94.125507 PACS numbers: 61.10.Nz, 61.20.–p, 61.25.Mv

Cs has one of the most interesting pressure-temperature (P-T) phase diagrams of all the elements. It exhibits numerous solid phases with very different bulk modulii, and a melting curve whose gradient varies dramatically with pressure (see Fig. 1) [1,2]. At ambient conditions Cs-I has the eightfold coordinated bcc structure and this transforms to 12-coordinated fcc Cs-II at 2.4 GPa. At 4.2 GPa, the close-packed Cs-II transforms to Cs-III, which was long thought to also have an fcc structure, but which has a complex orthorhombic structure with 84 atoms in a C-centered unit cell [3]. Cs-III is ninefold or tenfold coordinated and exists over only a very narrow pressure range, and at 4.4 GPa transforms to eightfold coordinated tetragonal Cs-IV. The Cs-II $\rightarrow$ Cs-III $\rightarrow$ Cs-IV transition sequence is accompanied by abrupt changes in resistivity [1] and this phenomenon has been attributed to the collapse of the 6s electronic orbital onto the 5d orbitals (so called s-to-d electron transfer) [4]. The Cs melting curve exhibits abrupt changes in slope with pressure; initially it shows a positive slope and there are two maxima at 2.25 GPa and $T_m = 197\,^{\circ}\mathrm{C}$ and 3.05 GPa and $T_m = 198\,^{\circ}\mathrm{C}$ [1]. On further pressure increase, the gradient of the melting curve becomes strongly negative until the Cs-II–Cs-III–liquid triple point, where it becomes almost constant at $T_m = 88\,^{\circ}\mathrm{C}$ before again becoming strongly positive at pressures above the Cs-III–Cs-IV–liquid triple point up to 9.8 GPa, the highest pressure at which it has been determined [1,5]. As with the solid phases, the changes in the melting curve are accompanied by changes in resistivity of the liquid [1]. But these changes are more continuous than those observed in the solid and this led early studies of l-Cs to conclude that if s-to-d transfer occurs in the liquid, then the mechanism is different from that found in the solid [1]. Further studies by Tsuji *et al.* [6] have suggested that the structural changes in the liquid are similar to those in the solid [1], with a change from a bcc-like structure to an fcc-like structure at 2.0 GPa, and a decrease in the coordination number between 2.9 and 4.3 GPa. However, the data in this study were collected at only four P-T points, and the maximum pressure achieved, 4.3 GPa, was not high enough to investigate the liquid above the Cs-IV phase.

In order to investigate the structure of l-Cs across the strong discontinuity in the melting curve at 4.4 GPa, and to further explore the structural changes in the liquid that accompany the known complex changes in the crystalline structure, we have conducted detailed x-ray diffraction studies up to 9.8 GPa at 220 °C and 350 °C, a factor of more than two higher in pressure than the earlier studies [6]. We observe significant densification of the liquid over this pressure range accompanied by a discontinuity in the density, and a change in coordination from 11–12 to 7–8, behavior that closely follows that observed in the solid phases. The P-T points at which we have collected x-ray diffraction data from the liquid phase are shown in Fig. 1. The data were collected on beamline 9.1 at the Synchrotron

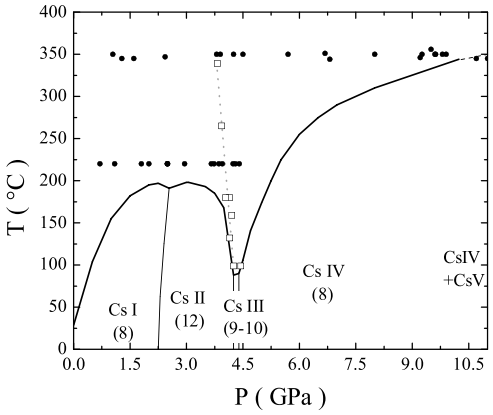

FIG. 1. The phase diagram of Cs up to 11 GPa [1,5]. The filled symbols show data collected on pressure increase and decrease at the fixed temperatures of $T = 220\,^{\circ}\mathrm{C}$ and $T = 350\,^{\circ}\mathrm{C}$. The open symbols show the thermodynamic path followed on heating a sample of Cs-III up to $T = 340\,^{\circ}\mathrm{C}$ at ~4.1 GPa. The dashed line through these points is a guide for the eye. The coordination numbers of the solid phases are given in parentheses below the name of the solid phase.

Radiation Source, Daresbury Laboratory, using a wavelength of 0.4654 Å [7]. The sample was contained in a diamond anvil cell equipped with W or Re gaskets [8], and the high temperatures were generated using a resistive heater. The pressure was determined using Mo as an internal calibrant [9]. The maximum diffraction angle of $2\theta \sim 36°$ corresponded to a maximum Q value of ~ 8.3 Å^{-1}.

The analysis procedure required to obtain the atom-atom structure factors from angle-dispersive x-ray diffraction data from liquids under extreme P-T conditions have been fully described by Eggert *et al.* and Kaplow *et al.* [10]. Spurious diffraction features, such as those from the Mo pressure calibrant, and the background scatter from the pressure cell were removed. The Bragg peaks from the Mo were easily identified and subtracted, and the background contribution was determined by measuring the diffraction pattern from the empty cell. The data were then normalized by the atomic form factor, taking into account the Compton scattering, the sample transmission coefficient, and a scale factor for the atomic form factor determined from the assumption that for sufficiently high Q, $S(Q) \sim 1$ [10]. Finally, for a homogeneous and isotropic medium such as a liquid or an amorphous solid, the structure factor can be written in terms of the atom-atom radial distribution function, $g(r)$, as

$$S(Q) - 1 = 4\pi\rho \int r^2[g(r) - 1]\frac{\sin Qr}{Qr}dr. \qquad (1)$$

This equation can be inverted to obtain $g(r)$, provided that the number density ρ is known [10,11].

Examples of the resulting $S(Q)$ data measured as a function of pressure at 220 °C and 350 °C near the melting curve are shown in Fig. 2. On increasing pressure at 220 °C, the profiles show a continuous change in shape. At low pressures the $S(Q)$ profiles are typical for a simple liquid which we have modeled as a system of hard spheres (HS) using the Percus-Yevick equation [11–13]. In such a liquid, it is known empirically that the height of the first peak in $S(Q)$ is between 2.5 and 3.0; that there are no shoulders on the high-Q side of this first peak; and that the ratio between the positions of the first and second peaks (Q_2/Q_1) is ~ 1.8 [14]. Our l-Cs profiles satisfy all three of these criteria up to 3.9 GPa and are in excellent agreement with the $S(Q)$ data of Tsuji *et al.* [6]. However, at pressures above 3.9 GPa, an asymmetry begins to appear on the high-Q side of the first peak; the intensity of the first peak decreases abruptly by ~ 0.2 at 3.9 GPa and approaches a value of ~ 1.8 at 9.8 GPa; and the ratio Q_2/Q_1 becomes almost pressure independent above 3.9 GPa, with a value of ~ 2.0. These changes all suggest that Cs is no longer a simple liquid above 3.9 GPa.

Further evidence of this change of character is observed in the density of the liquid. Below 3.9 GPa, this can be estimated using two different procedures. The position of the first peak of the $S(Q)$ of a liquid is very sensitive to pressure, as observed previously in l-Cs [6]. The shift with pressure of this peak can be related empirically to the change in the sample volume (and hence density) through the relationship $\frac{V_0}{V_P} = (\frac{Q_0}{Q_P})^{-3}$, where V_0,V_P, Q_0, and Q_P are the volumes and positions of the first peak at ambient pressure, and at a pressure P [6,12,13]. This empirical law has been used extensively at high pressure [6,13,14] and is applicable while the structure factor profile is that of a simple liquid. As a cross check, the specific volume was also obtained from the measured structure factors by fitting them using the HS model developed for liquid alkali metals [12]. In this model, the packing fraction η just above the melting curve is assumed to be constant and equal to 0.45 [12]. The specific volume and the hard sphere diameter (σ) were then obtained by a least-squares fit to the structure factors. η is related directly to the diameter of HS's and to the density via the relationship $\eta = \frac{\pi}{6}\rho\sigma^3$. The specific

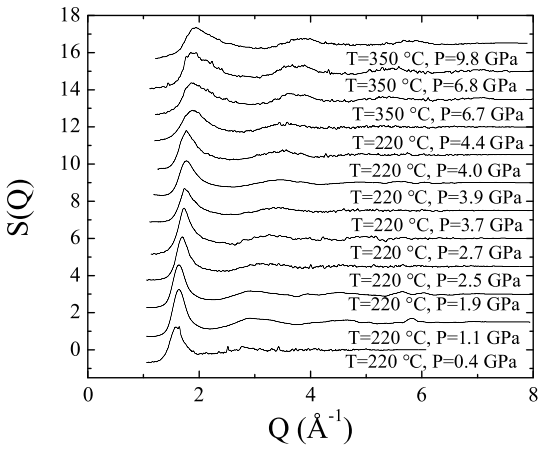

FIG. 2. Structure factors of l-Cs collected close to the melting curve in the range of pressure between 0.4 and 9.8 GPa. A constant offset of 1 has been used to separate the profiles.

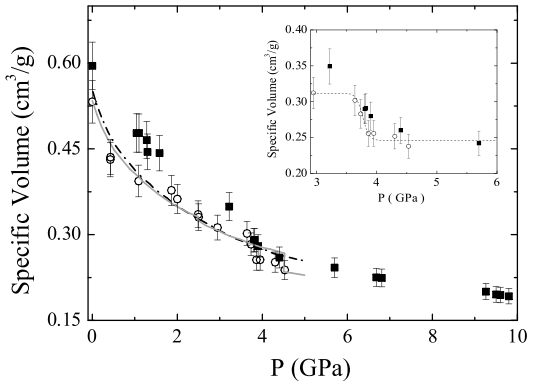

FIG. 3. The specific volume of l-Cs at $T = 220$ °C (open circles) and $T = 350$ °C (filled squares) as a function of pressure. The solid and dot-dashed lines are the specific volume data of the solid at 20 °C and liquid at 198 °C, respectively, from Ref. [1]. The inset shows an enlarged view of the data in the region 2.9 and 6 GPa. The dashed line is a guide for the eye.

volume of Cs below 3.9 GPa obtained using these two different methods agreed with each other to within 7%, and their average was used at each pressure.

However, neither of these methods can be used to determine the density above 3.9 GPa in the nonsimple regime. Up to 5.7 GPa the density of the liquid was estimated from the change in volume on melting reported in Ref. [1,5] and the density of the corresponding solid phases. From 5.7 to 9.8 GPa, the volume change on melting is not available in the literature. At the highest pressure of 9.8 GPa, the density of the solid was determined from the structure of crystalline Cs-IV at 9.8 GPa and 300 °C and the known slope of the melting curve at this pressure. It was also assumed that the change in entropy on melting at 9.8 GPa is the same as that at 5 GPa, the highest pressure at which it has been measured [1]. The resulting estimation of the specific volumes at 220 °C and 350 °C is shown in Fig. 3 and can be seen to be in very good agreement with those measured previously at 198 °C by Kennedy *et al.* [1]. At 220 °C, the specific volume of *l*-Cs decreases monotonically up to 3.7 GPa at which point it shows evidence of a sharp densification of 17(4)%. We note that this densification occurs at a lower pressure than the volume discontinuity of 12.5(2)% observed in the solid at the combined Cs-II → Cs-III → Cs-IV transitions [3] (which occur at 4.2 and 4.4 GPa at 20 °C). Unfortunately, we could measure the compressibility of the denser state up to only 4.4 GPa at 220 °C, only slightly higher than the pressure reached by Tsuji *et al.*. However, by raising the temperature to 350 °C (see Fig. 1), it was possible to extend the compressibility measurements of the liquid to ~10 GPa, as shown in Fig. 3. Below ~3 GPa, the specific volume of *l*-Cs at 350 °C is greater than that at 220 °C, as expected from thermal expansion. However, at higher pressures, the volumes at 220 °C and 350 °C are much more similar, suggesting that temperature has little effect on the specific volume at these pressures. To confirm this, we have measured the temperature evolution of $S(Q)$ at an (almost) constant pressure of 4.2 GPa, the pressure at which the melting temperature is lowest (Fig. 1).

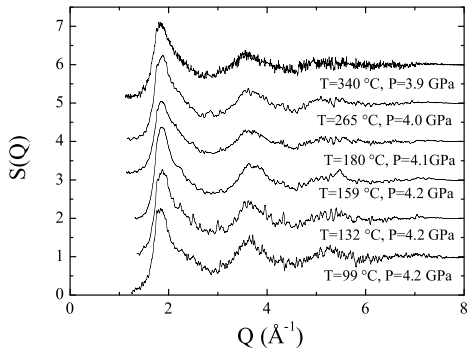

FIG. 4. Structure factors of *l*-Cs collected in the pressure range between 4.1 and 3.8 GPa and the temperature range between $T = 99$ °C and $T = 340$ °C.

The $S(Q)$ profiles obtained on heating from 99 °C up to 340 °C are shown in Fig. 4. The 99 °C profile exhibits a shoulder on the high-Q side of the first peak, and, although the shoulder becomes less pronounced at higher temperatures, the liquid remains nonsimple to the highest temperature. The position of the first peak of $S(Q)$ shows very little change with temperature, and the change in the specific volume heating from 99 °C to 340 °C at 4.2 GPa is only 0.003(1) cm^3/g. This thermal expansion is considerably smaller than that obtained on heating *l*-Cs from 220 °C to 340 °C below 2 GPa, where the specific volume changes by ~0.06(1) cm^3/g (see Fig. 3), and is consistent with the similar specific volumes observed at 220 °C up to 340 °C above 4 GPa.

As said previously, the $S(Q)$ data can be inverted to obtain the radial distribution function $g(r)$, and hence obtain both coordination numbers (C_{NN}) and the average nearest-neighbor distances (d), as illustrated in Fig. 5. The distance between nearest neighbors (d) was taken as the position of the first peak of $g(r)$, and C_{NN} was determined by integrating $g(r)$ up to the first minimum. The coordination number of *l*-Cs just above atmospheric pressure is ~12, in good agreement with the previous determination of Tsuji *et al.* [6], and slightly higher than the value of 11 expected for a system of hard spheres (as shown by the dotted horizontal line in Fig. 5). On initial compression at 220 °C, C_{NN} increases slightly with pressure while d compresses uniformly, both as expected for a simple liquid and

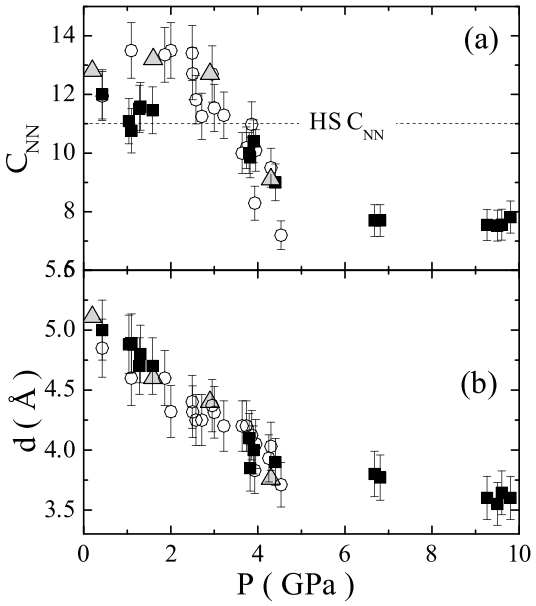

FIG. 5. (a) Coordination number C_{NN} of liquid Cs as a function of pressure. The horizontal dashed line is the coordination number (11) for a system of hard spheres. (b) The nearest-neighbor distance as a function of pressure. In both panels, the data collected at 220 °C and 350 °C are shown using open circles and filled squares, respectively, while the filled triangles are the data from the work of Tsuji *et al.* [6].

in agreement with Tsuji *et al.* [6] [Fig. 5(a)]. However, above ~2.5 GPa, C_{NN} begins to decrease, and becomes less than 11 at ~3.9 GPa, the pressure at which the $S(Q)$ profiles cease to be those of a simple liquid. C_{NN} decreases still further above 3.9 GPa, and, by 4.5 GPa, the coordination number is only 7 or 8 and this is maintained up to 9.8 GPa. The changes in coordination reported previously by Tsuji *et al.* [6] up to 4.3 GPa are in excellent agreement with the present results. The pressure dependence of the nearest-neighbor distance d is shown in Fig. 5(b). Up to 4.5 GPa it decreases almost uniformly with pressure, before becoming much less compressible once the low-coordination form is obtained above this pressure. The values of d from Tsuji *et al.* [6] up to 4.3 GPa are again in excellent agreement. The changes in the coordination and nearest-neighbor distance in the liquid can be compared to those that occur in the solid phases over the same pressure range. The two solid phases stable up to 3.6 GPa, Cs-I (bcc) and Cs-II (fcc), have coordination numbers of 8 and 12, respectively, compared to the coordination number of the simple liquid of 11–12 over this pressure range (0 to 3.6 GPa). The transitions from Cs-II to Cs-III and Cs-IV at 4.2 and 4.4 GPa, are accompanied by a 12.5(2)% increase in density, and a decrease in coordination number from 12 (Cs-II) to 9 or 10 (Cs-III) to 8 (Cs-IV) [3]. These changes in structure and coordination of the solid have long been attributed to an s-to-d electronic transition, and, at higher pressures, to dsp^3 hybridization of the electronic orbitals [2,4,15,16]. In particular, the relatively low eightfold coordination of Cs-IV has been attributed to the existence of directional bonding as a result of the occupation of d-orbitals. The structural changes in l-Cs over the pressure range 3.6–4.5 GPa are very similar, with a density increase of 17(4)% and a decrease in coordination number from ~11 to ~8. This close similarity in the behavior of the solid and liquid strongly suggests that the electronic phenomenon responsible for the changes in the solid is also occurring in the liquid. In particular, the reduced coordination number in the liquid suggests that there must be some form of preferential orientation within the liquid in order to reduce C_{NN} below the typical simple-liquid value of 11. Such a preferential orientation would arise from the existence of the hybridization of s, d, and p orbitals, and the resulting anisotropy in the local structure would then be in agreement with the asymmetry in the shape of the first peak of $S(Q)$ (see Fig. 3 and 4). The local structure would account for the asymmetry which occurs continuously over the pressure range 3.6–4.1 GPa where the liquid is denser than the solid.

The exact nature of this structural anisotropy, and hence an identification of the atomic orbitals involved, might be obtainable from *ab initio* simulations of the liquid phase, as has been done previously for liquid Rb [17,18]. We are currently conducting such simulations using a cluster of 264 atoms, the full results of which will be published separately.

In conclusion, liquid Cs undergoes a discontinuous change to a high-density low-coordination form at pressure above 3.9 GPa at 220 °C which cannot be modeled as a simple liquid. The similarities in the density and coordination change to those observed in the solid phases suggests that the cause of this densification is the same electron transfer and hybridization observed over the same pressure range in the solid phase.

We thank Professor R. J. Nelmes and Dr. J. S. Loveday for useful discussions and revisions. We thank also Dr. M. Roberts of Daresbury Laboratory for his assistance in setting up the 9.1 beam line at SRS. This work was supported by grants from EPSRC, funding from CCLRC, and beam time and other resources provided by SRS.

[1] G. C. Kennedy, A. Jayaraman, and R. C. Newton, Phys. Rev. **126**, 1363 (1962); A. Jayaraman, R. C. Newton, and J. M. McDonough, Phys. Rev. **159**, 527 (1967).
[2] K. Takemura, S. Minomura, O. Shimomura, Phys. Rev. Lett. **49**, 1772 (1982); K. Takemura and K. Syassen, Phys. Rev. B **32**, 2213 (1985).
[3] M. I. McMahon, R. J. Nelmes, and S. Rekhi, Phys. Rev. Lett. **87**, 255502 (2001).
[4] A. K. McMahan, Phys. Rev. B **29**, R5982 (1984).
[5] R. Boehler *et al.*, Physica B&C (Amsterdam) **140**, 233 (1986).
[6] K. Tsuji *et al.*, J. Non-Cryst. Solids **117-118**, 72 (1990); Y. Katayama and K. Tsuji, J. Phys. Condens. Matter **15**, 6085 (2003).
[7] R. J. Nelmes and M. I. McMahon, J. Synchrotron Radiat. **1**, 69 (1994).
[8] No reaction was observed between the Cs sample and the gasket materials. On returning the liquid samples to room temperature after heating, only diffraction peaks from crystalline Cs and the Mo pressure calibrant were observed.
[9] Y. Zhao *et al.*, Phys. Rev. B **62**, 8766 (2000).
[10] J. H. Eggert *et al.*, Phys. Rev. B **65**, 174105 (2002); R. Kaplow, S. L. Strong, and B. L. Averbach, Phys. Rev. **138**, A1336 (1965).
[11] J. P. Hansen and I. R. McDonald, in *Theory of Simple Liquids* (Academic Press, London, 1990).
[12] N. W. Ashcroft and J. Lekner, Phys. Rev. **145**, 83 (1966).
[13] G. Shen *et al.*, Phys. Rev. Lett., **92**, 185701 (2004).
[14] T. Hattori *et al.*, Phys. Rev. B **68**, 224106 (2003), and references therein; K. Tsuji *et al.*, J. Phys. Condens. Matter **16**, S989 (2004).
[15] M. M. Abd-Elmeguid, H. Pattyn, and S. Bukshpan, Phys. Rev. Lett., **72**, 502 (1994).
[16] I. Loa *et al.*, High Press. Res. **23**, 1 (2003).
[17] F. Shimojo *et al.*, Phys. Rev. B **55**, 5708 (1997).
[18] J. Chihara and G. Kahl, Phys. Rev. B **58**, 5314 (1998).

PHYSICAL REVIEW B **71**, 020101(R) (2005)

Incommensurate sulfur above 100 GPa

C. Hejny, L. F. Lundegaard, S. Falconi, and M. I. McMahon
School of Physics and Centre for Science at Extreme Conditions, The University of Edinburgh, Mayfield Road, Edinburgh, EH9 3JZ, United Kingdom

M. Hanfland
ESRF, BP220, 38043 Grenoble, France
(Received 19 October 2004; published 21 January 2005)

S-III, the high-pressure phase of sulfur stable above 80 GPa, is found to have the same incommensurately modulated monoclinic crystal structure as Te-III and Se-IV and is the first element observed to have a modulated structure above 100 GPa. A previously unreported phase is found between S-II and S-III on pressure decrease, and there is also evidence that the same phase exists on pressure increase. This phase has the same triclinic structure as Te-II and Se-III.

DOI: 10.1103/PhysRevB.71.020101 PACS number(s): 61.50.Ks, 62.50.+p

Sulfur is a member of the group VIa elements and exists in a large number of complex allotropic forms at ambient conditions.[1,2] Numerous high-pressure forms have also been reported, and it is only recently that this extremely complex behavior has begun to be simplified.[3] The stable crystal structure at ambient conditions comprises covalently-bonded S_8 rings arranged in an orthorhombic structure.[1,4] On compression at room temperature, this orthorhombic form is reported to undergo a gradual transition to an amorphous form, such that above 26.5 GPa no diffraction peaks are observed.[5–7] Further compression results in recrystallisation, with diffraction peaks first reappearing at 37 GPa,[6] and complete recrystallization occurring at 54.5 GPa (Ref. 7) or 75 GPa.[6] The structure of this recrystallized form, named S-II, has long been uncertain, but recently it has been shown to have a body-centered tetragonal structure comprising parallel chains of atoms with 4_1 and 4_3 symmetry running along the *c* axis.[8,9] A further phase transition, to S-III, occurs on further compression to 83–86 GPa,[6,7,9] although peaks from S-II are observed at pressures up to ~100 GPa.[6] S-III is reported to have the same base-centered orthorhombic (bco) structure as Te-III and Se-IV (Refs. 6, 7, and 10) and is both a metal[11] and a superconductor,[12–14] with a superconducting temperature that increases from $T_c = 10$ to 14 K over the pressure range 90–160 GPa. On further pressure increase Luo *et al.* observed a transition to the rhombohedral β-Po structure at 162 GPa, and this phase is stable to at least 212 GPa.[6] The β-Po phase is also a superconductor, with a maximum T_c of 17.3(5) K at 200 GPa.[14]

Recently, we have shown that the phases of Te and Se previously reported as having the bco structure, Te-III and Se-IV, are in fact monoclinic, with incommensurately modulated atomic coordinates.[15,16] In McMahon *et al.*[16] we commented that the bco structure of S-III might have the same incommensurate structure, but that the earlier S-III diffraction data of Akahama *et al.*[7] and Luo *et al.*[6] were of insufficient quality to observe any of the satellite diffraction peaks arising from the modulation. A recent reinvestigation of S-III has reported that the structure is indeed incommensurately modulated.[17] To investigate the structure of S-III further, we have performed diffraction studies of sulfur to 100.5 GPa. We show that it does indeed have the same incommensurately modulated structure as Te-III and Se-IV, with an incommensurate *q* vector and modulation amplitudes similar to those seen in these other group VIa elements. We also find a previously unreported high-pressure phase of sulfur between S-II and S-III, the triclinic structure of which is the same as that of Te-II and Se-III.[18]

Powder diffraction data were collected on station ID09a at the European Synchrotron Radiation Facility (ESRF), Grenoble, using an incident x-ray wavelength of 0.41756 Å and a beamsize of 10 μm × 10 μm. The powdered sample of orthorhombic S_8 was provided by Mezouar (ESRF)[19] and was loaded into a diamond-anvil cell with He as a pressure transmitting medium. The pressure was measured using both the fluorescence from a small grain of $SrB_4O_7:Sm^{2+}$ placed within the gasket hole,[20] and from the lattice parameters of the helium within the irradiated part of the sample via its equation of state (EOS).[21] At pressures above ~35 GPa, the principal fluorescence peak from the $SrB_4O_7:Sm^{2+}$ was observed to broaden, and the pressure determined from the $SrB_4O_7:Sm^{2+}$ and the He-EOS differed, suggesting a pressure gradient across the gasket hole. The maximum pressure gradient of 6 GPa was observed at a pressure of 70 GPa, and at pressures above this the pressure gradient decreased. At all pressures above 35 GPa, therefore, the sample pressure was determined from the EOS of the helium as this gave a better estimate of the true sample pressure. At the highest pressure reached in this study, 100.5 GPa, the pressures determined by the $SrB_4O_7:Sm^{2+}$ (102 GPa) and He-EOS (100.5 GPa) differed by only 1.5 GPa. The diffraction data were collected on an image-plate detector placed approximately 365 mm from the sample. To improve powder averaging, the sample was oscillated by ±3° during the 40 s exposures. The resulting two-dimensional diffraction images were integrated using FIT2D (Ref. 22) to give standard diffraction profiles. Rietveld refinement of these profiles was performed using the JANA2000 software package.[23]

On pressure increase, we observe S-I to transform directly to tetragonal S-II at 37.5(1.5) GPa, with no evidence of any intermediate amorphous form. We suggest that the previous reports of such a phase arose because of the absence of any hydrostatic medium in those studies.[6,7] The transition from S-II to S-III was observed to start at 75 GPa, and two phase

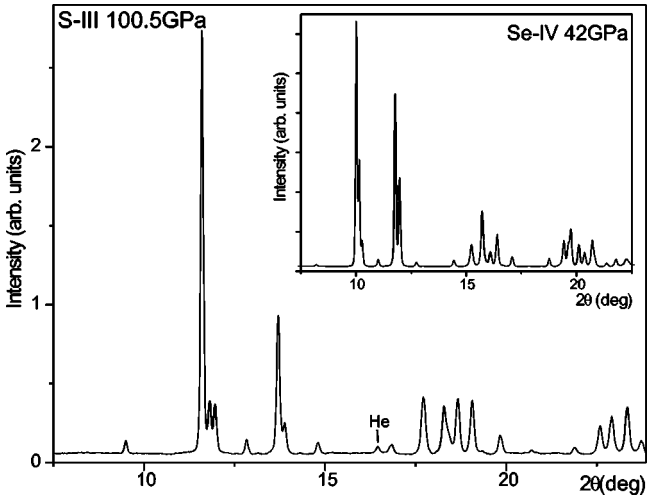

FIG. 1. Powder diffraction profile of S-III at 100.5 GPa. The strongest peak from the He pressure medium is identified. For comparison with the S-III profile, the inset shows a diffraction profile from incommensurate Se-IV at 42 GPa.

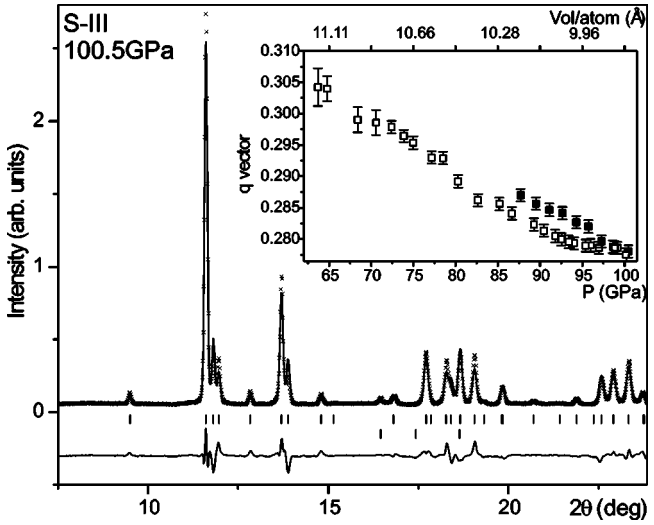

FIG. 2. Rietveld refinement of incommensurate S-III at 100.5 GPa. The upper tick marks below the profile show the calculated peak positions from the main and modulation peaks, while the lower tick marks show the calculated peak positions from the He pressure transmitting medium. The difference between the observed and calculated profiles is shown below the tick marks. The inset shows the pressure dependence of the incommensurate wave vector q both as a function of pressure and volume per atom. Filled (unfilled) symbols denote data collected on pressure increase (decrease).

S-II/S-III mixtures were observed up to 95 GPa. The single-phase diffraction profile of S-III observed at 100.5 GPa, the highest pressure reached in this study, is shown in Fig. 1 and is clearly similar to those from Se-IV,[16] a diffraction profile from which is shown in the inset to Fig. 1 for comparison. All the diffraction peaks from S-III can be indexed on the same $I'2/m(0q0)s0$ super spacegroup as Se-IV,[16] with $a=2.805(2)$ Å, $b=3.457(2)$ Å, $c=2.210(2)$ Å, $\beta=113.1(2)°$, and $q=0.279(3)$ at 100.5 GPa.[24]

Although all the peak positions in S-III can be accounted for by an incommensurate Se-IV-like structure, the relative peak intensities in S-III and Se-IV are different (see Fig. 1) as a result of preferred orientation (PO) in the S-III sample. The best Rietveld fit to the S-III diffraction profile at 100.5 GPa, which included the refinement of a correction for preferred orientation and the refinement of the amplitudes of the atomic modulations B_{1x} and B_{1z},[25] is shown in Fig. 2. The refined structural parameters are $a=2.802(1)$ Å, $b=3.455(1)$ Å, $c=2.208(1)$ Å, $\beta=113.15(1)°$, and $q=0.281(1)$, with $B_{1x}=0.028(1)$, $B_{1z}=0.118(1)$, and a single atom at (0, 0, 0). Tests to determine the effect of different PO corrections on the modulation amplitudes at 100.5 GPa revealed that the refined value of B_{1z} was almost independent of the choice of PO model, but that the value of B_{1x} varied in the range 0.002–0.028. However, the overall fit to the S-III profiles was very poor for many of these PO models, and the values for B_{1x} and B_{1z} given above are those from the best-fitting model.

The modulation amplitudes in S-III at 100.5 GPa are similar to those observed in Te-III at 8.5 GPa, where $B_{1x}=0.0215(9)$ and $B_{1z}=0.0925(7)$,[15] and in Se-IV at 42 GPa, where $B_{1x}=0.0236(11)$ and $B_{1z}=0.0900(8)$.[16] In the unmodulated S-III structure, which has spacegroup $I2/m$, each sulfur atom is six-fold coordinated with two nearest neighbors at a distance of 2.208(1) Å and four further atoms at a distance of 2.225(2) Å. The nearest-neighbor distance is equal to the c-axis lattice parameter and is thus unaffected by the modulation. However, the next-nearest-neighbor contact distance varies from 2.082(2) Å to 2.441(2) Å as a result of the modulation, with an average distance of 2.243(1) Å.[26] The closest approach distance at 100.5 GPa is similar to the average S—S bondlength of 2.060(3) Å found within the S_8 molecules at ambient conditions,[1] and with the S—S bondlengths of 2.070(4) Å and 2.096(7) Å found within the chains of the polymeric form of sulfur recently reported to exist at 3 GPa and 400 °C,[3] but is slightly longer than the S—S intrachain distance of 1.96(1) Å we find in S-II at 85.4 GPa—the highest pressure at which we could refine the detailed structure of S-II.

On pressure decrease, the sample was found to remain single-phase S-III down to 90 GPa. Although additional diffraction peaks appeared at this pressure, and they increased in intensity on further pressure decrease, as illustrated in Fig. 3, diffraction peaks from S-III were visible at all pressures down to 63.7 GPa. The pressure dependence of the incommensurate q vector was obtained by least-squares fitting to the positions of the S-III diffraction peaks and is shown in the insert to Fig. 2. As in Te-III and Se-IV,[15,16] q varies strongly with volume, and, over the pressure range 64–100 GPa, decreases approximately linearly with volume at the rate $2.11(5)\times10^{-2}$ Å^{-3}. This is only ~20% less than the linear pressure dependence of $2.7(1)\times10^{-2}$ Å^{-3} observed in Se-IV between 34 and 42 GPa (Ref. 16) and is considerably larger than the pressure dependence of $1.35(6)\times10^{-2}$ Å^{-3} observed in Te-III between 5.0 and 8.5 GPa.[15] Although the pressure dependence of q is initially linear in both Te-III and Se-IV, at higher pressures the pressure dependence becomes strongly nonlinear.[15,16] Further data over an

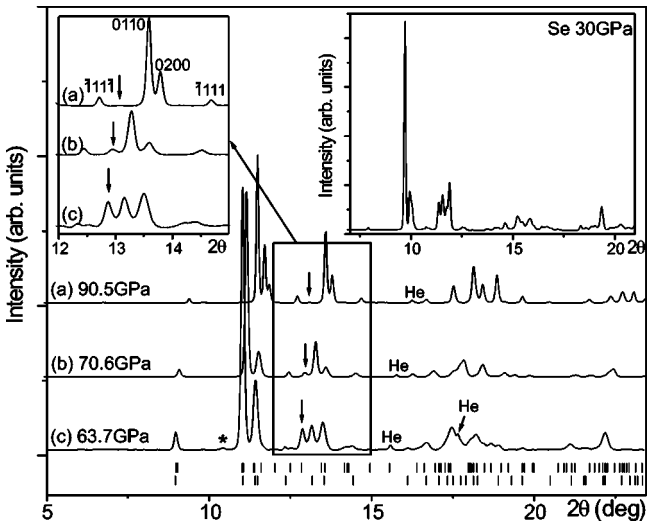

FIG. 3. Diffraction profiles collected from sulfur on pressure decrease. Diffraction peaks from the He pressure medium are labeled. The most intense sulfur-V peak first appears at 90 GPa, as identified by the arrow in profile (a), and it increases in intensity as the pressure is decreased, as identified in profiles (b) and (c), and enlarged in the left-hand inset. The mixed-phase profile at 63.7 GPa is very similar in appearance to the diffraction profile from a mixture of Se-III/Se-IV at 30 GPa, as shown in the right-hand inset for comparison. The upper (lower) tickmarks beneath the 63.7 GPa profile show the calculated peak positions from S-V (S-III). The single peak in the 63.7 GPa profile not accounted for by either S-III or S-V is identified with an asterisk.

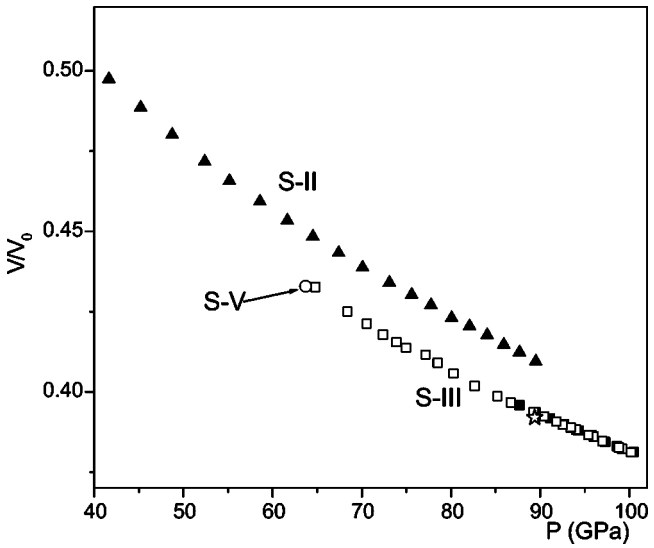

FIG. 4. The compressibility of sulfur from 40 to 101 GPa. Filled (unfilled) symbols denote data collected on pressure increase (decrease). The data point plotted as a star at 89.4 GPa, is from Ref. 7. The unfilled circle at 63.7 GPa is from triclinic sulfur-V.

extended pressure range are necessary to determine whether similar behavior is observed in S-III.

The weak additional peaks that first appear in the S-III profiles at 90 GPa—see profile (a) of Fig. 3—are not from the tetragonal S-II phase. Rather, their positions relative to the S-III peaks are reminiscent of the positions of peaks from Te-II and Se-III relative to those from Te-III and Se-IV, respectively,[18] as illustrated for Se in the inset to Fig. 3. Close examination of the mixed S-II/S-III patterns obtained between 75 and 95 GPa on pressure increase clearly shows that the most intense of these additional peaks (that indicated by the arrow in Fig. 3) is also visible in a profile collected at 91 GPa on compression. We call this new high-pressure phase of sulfur S-V. As with Te-II and Te-III,[18] S-III and S-V form mixed-phase profiles, but attempts to obtain a single-phase profile of S-V at lower pressures were unsuccessful as both the gasket hole and diamonds failed on attempting to decrease the pressure below 63.7 GPa. Although the 63.7 GPa profile shown in Fig. 3 still contains many reflections from S-III, it is possible to index all but one of the remaining peaks on a triclinic body-centered Te-II-like structure[18] with $a=2.966(8)$ Å, $b=10.666(3)$ Å, $c=2.284(2)$ Å, $\alpha=86.67(2)°$, $\beta=111.89(1)°$, and $\gamma=91.30(1)°$ at 63.7 GPa. Although this cell is nonprimitive[27] and thus nonstandard, we chose it previously to describe Te-II and Se-III because it highlights the close relationship to the (commensurate) structures of Te-III and Se-IV when their q vectors are $(0,\frac{1}{3},0)$, and thus when their b axes are tripled in length.[18] We have chosen to use the nonstandard space-group here as the same close structural relationship exists between S-III and S-V. The compressibility of sulfur from 40 to 101 GPa is shown in Fig. 4. The volume change $(\Delta V/V_0)$ at the S-II→S-III transition is 1.6(1)%, while no volume change, within error, is observed at the S-III→S-V transition. The density of the bco structure of S-III reported by Akahama *et al.*,[7] reinterpreted using a Te-III-like monoclinic unit cell,[28] is in excellent agreement with our results.

Sulfur thus joins its group VIa neighbors Se and Te in having a phase with an incommensurately modulated crystal structure at high pressure, and is the first element observed to have such a structure above 100 GPa. The reasons why these elements should adopt such complex structures is still not completely clear. However, *ab initio* calculations of the Se-IV structure using commensurate approximants with $q=\frac{1}{4}$ and $q=\frac{2}{7}$ have indicated that the incommensurate modulation might arise via a Kohn anomaly that reduces the energy of a phonon mode at $q=2k_F$ to below zero. The resulting pseudogap at the Fermi energy reduces the overall energy of the structure.[29]

In conclusion, we have shown that S-III is isostructural with Te-III and Se-IV, and has an incommensurately modulated crystal structure. Although the current study was limited to 100.5 GPa, the previous study of Luo *et al.* suggests that S-III is stable to 162 GPa,[6] although the more recent study of Degtyareva *et al.* reports a transition pressure of 153 GPa.[17] Triclinic S-V has not been observed in previous studies of sulfur, but the observation of this Te-II-like structure, the isostructural nature of S-III, Se-IV, and Te-III, and the recent observation of a S-II-like structure in selenium,[8,9,17] reveals that the high-pressure behavior of S, Se, and Te is much more similar than previously believed.

This work was supported by grants from EPSRC and facilities provided by the European Synchrotron Radiation Fa-

cility. We acknowledge helpful discussion with our colleague Professor R.J. Nelmes, and thank Dr. M. Mezouar and Dr. H. Muller of the ESRF for providing the purified sample of S_8.

[1] J. Donohue, *The Structure of the Elements* (Wiley, New York, 1974).
[2] D. A. Young, *Phase Diagrams of the Elements* (University of California Press, Berkely, CA, 1991).
[3] W. A. Crichton, G. B. M. Vaughan, and M. Mezouar, Z. Kristallogr. **216**, 417 (2001).
[4] S. J. Rettig and J. Trotter, Acta Crystallogr., Sect. C: Cryst. Struct. Commun. **43**, 2260 (1987).
[5] H. Luo and A. L. Ruoff, Phys. Rev. B **48**, 569 (1993).
[6] H. Luo, R. G. Greene, and A. L. Ruoff, Phys. Rev. Lett. **71**, 2943 (1993).
[7] Y. Akahama, M. Kobayashi, and H. Kawamura, Phys. Rev. B **48**, 6862 (1993).
[8] H. Fujihisa, Y. Akahama, H. Kawamura, H. Yamawaki, M. Sakashita, T. Yamada, K. Honda, and T. Le Bihan, Phys. Rev. B **70**, 134106 (2004).
[9] O. Degtyareva, E. Gregoryanz, M. Somayazulu, P. Dera, H. K. Mao, and R. J. Hemley (unpublished).
[10] K. Aoki, O. Shimomura, and S. Minomura, J. Phys. Soc. Jpn. **48**, 551 (1980).
[11] H. Luo, S. Desgreniers, Y. K. Vohra, and A. L. Ruoff, Phys. Rev. Lett. **67**, 2998 (1991).
[12] S. Kometani, M. Eremets, K. Shimizu, M. Kobayashi, and K. Amaya, J. Phys. Soc. Jpn. **66**, 2564 (1997).
[13] V. V. Struzhkin, R. J. Hemley, H. K. Mao, and Yu. A. Timofeev, Nature (London) **390**, 382 (1997).
[14] E. Gregoryanz, V. V. Struzhkin, R. J. Hemley, M. I. Eremets, H. K. Mao, and Y. A. Timofeev, Phys. Rev. B **65**, 064504 (2002).
[15] C. Hejny and M. I. McMahon, Phys. Rev. Lett. **91**, 215502 (2003).
[16] M. I. McMahon, C. Hejny, J. S. Loveday, L. F. Lundegaard, and M. Hanfland, Phys. Rev. B **70**, 054101 (2004).
[17] O. Degtyareva, E. Gregoryanz, M. Somayazulu, H.K. Mao, and R. J.Hemley (unpublished).
[18] C. Hejny and M. I. McMahon, Phys. Rev. B **70**, 184109 (2004).
[19] The sample was prepared by Dr. H. Muller (ESRF) by first dissolving high purity sulfur in toluene or dichloromethane and then letting the solution cool slowly to 238 K. The pale yellow precipitate that formed was collected by filtration and dried in a vacuum.
[20] F. Datchi, R. LeToullec, and P. Loubeyre, J. Appl. Phys. **81**, 3333 (1997).
[21] P. Loubeyre, R. LeToullec, J. P. Pinceaux, H. K. Mao, J. Hu, and R. J. Hemley, Phys. Rev. Lett. **71**, 2272 (1993).
[22] A. P. Hammersley, S. O. Svensson, M. Hanfland, A. N. Fitch, and D. Hausermann, High Press. Res. **14**, 235 (1996).
[23] V. Petricek and M. Dusek, *The crystallographic computing system JANA2000*, Institute of Physics, Praha, Czech Republic, 2000.
[24] Super spacegroup $I'2/m(0q0)s0$ is a nonstandard setting of spacegroup $C2/m(0q0)s0$. We have chosen to use the nonstandard setting for consistency with our previous descriptions of Te-III (Ref. 15) and Se-IV (Ref. 16). In the $C2/m(0q0)s0$ setting the structural parameters of S-III at 100.5 GPa are $a=2.808$ Å, $b=3.457$ Å, $c=2.210$ Å, $\beta=113.27°$, with $q=0.721$.
[25] The modulation is modeled as a sum of Fourier amplitudes, as described in Ref. 15. For the refinement of only first-order Fourier components, the superspace symmetry of S-III reduces the number of refineable modulation parameters to 2, B_{1x} and B_{1z}.
[26] Different models of preferred orientation have little effect on the variation in next-nearest-neighbor distance—all the models investigated resulted in a variation in the range 2.11(2)–2.42(3) Å at 100.5 GPa.
[27] The equivalent primitive unit cell for S-IV at 63.7 GPa is $a=2.284$ Å, $b=2.966$ Å, $c=5.508$ Å, $\alpha=102.35°$, $\beta=92.91°$, and $\gamma=111.89°$.
[28] The relationship between the bco cell of Akahama *et al.* (Ref. 7) (A) and the present monoclinic cell (I), is $\vec{a}_A=-\vec{b}_I$, $\vec{b}_A=2\vec{a}_I+\vec{c}_I$ and $\vec{c}_A=\vec{c}_I$.
[29] G. J. Ackland and H. Fox (unpublished).

Confirmation of the incommensurate nature of Se-IV at pressures below 70 GPa

M. I. McMahon, C. Hejny, J. S. Loveday, and L. F. Lundegaard
School of Physics and Centre for Science at Extreme Conditions, The University of Edinburgh, Mayfield Road, Edinburgh EH9 3JZ, United Kingdom

M. Hanfland
ESRF, BP220, 38043 Grenoble, France
(Received 28 March 2004; published 5 August 2004)

Se-IV, the high-pressure phase of selenium stable above 28 GPa, is shown to have an incommensurately modulated structure to a least 70 GPa, the highest pressure reached in this study. Although the previously reported phase transition at 40–60 GPa to primitive rhombohedral Se-V is not observed, extrapolation of the Se-IV structural parameters suggests a continuous transition to Se-V would occur at 82 GPa. The incommensurate wave vector of Se-IV is significantly pressure dependent, varying from 0.314(1) at 28.9 GPa to 0.277(1) at 56 GPa.

DOI: 10.1103/PhysRevB.70.054101 PACS number(s): 61.50.Ks, 62.50.+p

The high-pressure behavior of Se has long been the subject of interest.[1,2] At ambient conditions Se is a semiconductor with a trigonal structure comprising infinite helical chains.[3] While the radius of the helical chains decreases only very slightly with increasing pressure, the interchain distance decreases strongly,[4] and, at 14 GPa, Se-I transforms to Se-II[5–8] which is a semiconductor[9,10] with a C-centered monoclinic structure.[11] Se-II is stable to 23 GPa where it undergoes a semiconductor-metal transition to superconducting Se-III,[9,10] which in turn transforms to Se-IV at 28 GPa.[6–8,11] Se-III and Se-IV are reported to be primitive monoclinic [7,11] and orthorhombic,[7] respectively, and isostructural with Te-II and Te-III.[12] Se-IV transforms to primitive rhombohedral Se-V at 40–60 GPa[7,8,13] and to a body-centered-cubic phase at 140 GPa,[14] and these structures are isostructural with Te-IV and Te-V, respectively. This extended sequence of low-symmetry structures has also stimulated a number of computational studies of high-pressure Se[11,15–20] which have, in general, confirmed the structures proposed by the diffraction work, although the stability of the orthorhombic Se-IV structure has been questioned.[20]

Recently, however, we have reported that Te-III is not orthorhombic but has an incommensurately modulated monoclinic structure that is stable to 27 GPa, and that rhombohedral Te-IV was not observed.[21] Preliminary data showed that at 35.4 GPa, a diffraction profile of Se-IV could also be fitted by the same modulated structure.[21] In light of the similarities in the high-pressure behavior of Se and Te detailed above, and the new structural data on Te, we have made a detailed diffraction study of Se-IV from 28 to 70 GPa. We find that Se-IV is indeed incommensurate and isostructural with Te-III, and, moreover, that Se-IV is stable to at least 70 GPa, the highest pressure reached in this study. The reported transition to primitive rhombohedral Se-V at 40–60 GPa is not observed. We believe that the previous identification of this transition probably arose because the limited resolution of earlier diffraction studies was unable to distinguish the diffraction pattern of Se-IV from rhombohedral Se-V above 40 GPa. The pressure dependence of the incommensurate wave vector of Se-IV has been determined to 66 GPa, and, as in Te-III, it is found to be strongly pressure dependent.

The sample was prepared from starting material of 99.9999% purity obtained from the Aldrich Chemical Company. To ensure that the sample did not contain any amorphous component, we prepared crystalline starting material using the method reported previously[7,14] by heating a finely ground powder in a vacuum oven at 200 °C for 2 h. The resulting material contained a mass of small, beautifully formed crystals, which were then lightly reground to make a crystalline powder. Diffraction profiles collected at ambient pressure revealed only peaks from the known trigonal phase. The sample was loaded into a diamond-anvil cell with a methanol:ethanol:water pressure transmitting medium in a 16:3:1 ratio. The sample pressure was measured using the ruby fluorescence technique.[22] Diffraction data were collected in beamline ID09 at the European Synchrotron Radiation Facility, Grenoble, using an incident x-ray wavelength of 0.4176 Å and a beamsize of 20 μm $\times$ 20 μm. The diffraction data were collected on an image-plate detector placed approximately 360 mm from the sample, and the two-dimensional diffraction images were integrated using FIT2D [23] to give standard diffraction profiles. Rietveld refinement of these profiles was performed using the JANA2000 software package.[24] The exposure time for each image was typically 20 s and diffraction data were collected from two different samples with identical results.

The transitions from Se-I to Se-II and Se-II to Se-III were observed at 15.6(5) and 21.8(3)GPa, respectively. Diffraction peaks from Se-IV were first observed at 29.3(6)GPa, but faint traces of Se-III were still visible at pressures up to 41 GPa. A typical diffraction profile from Se-IV collected at 42 GPa is shown in Fig. 1. Comparison of the Se-IV profile with those obtained from Te-III[21] (Fig. 1 inset) shows them to be extremely similar, and, using the Te-III profiles to aid indexing, we find that all the diffraction peaks in Se-IV can be accounted for by the incommensurate body-centered monoclinic Te-III structure with super spacegroup $I'2/m(0q0)s0$, and with $a=3.2511(1)$, $b=4.0026(1)$,

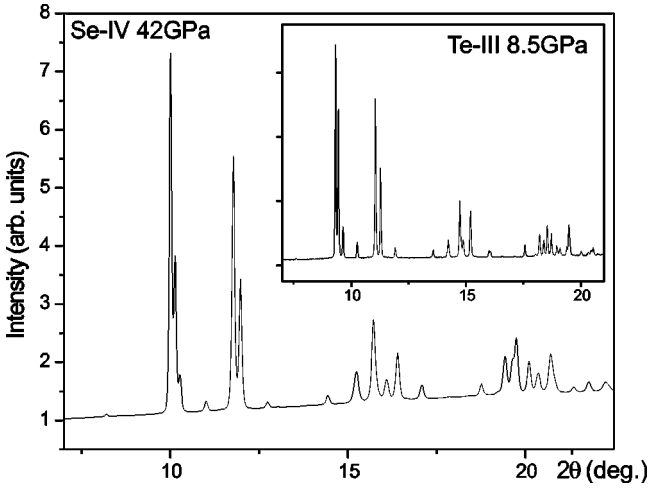

FIG. 1. Powder diffraction profile from Se-IV at 42 GPa. The inset shows a diffraction profile from Te-III at 8.5 GPa for comparison.

$c=2.5735(1)$ Å, $\beta=113.277(3)°$ at 42 GPa. The incommensurate wave vector at the same pressure is $(0,0.2866(5),0)$. As in Te-III, only first order modulation reflections were observed, and the modulation of the atomic positional parameters in Se-IV can be modeled as a sum of Fourier components,[24,25] of which only the two first-order terms are nonzero.[21] The full Rietveld refinement of Se-IV at 42 GPa is shown on Fig. 2, and the refined modulation parameters at this pressure are $B_{1x}=0.0236(11)$ and $B_{1z}=0.0900(8)$. These are similar to the values of 0.0215(9) and 0.0925(7), respectively, found in Te-III at 8.5 GPa.[21]

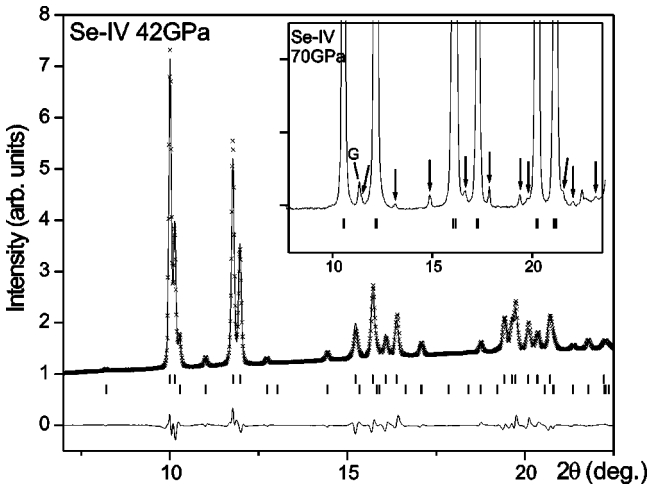

FIG. 2. Rietveld fit to Se-IV at 42 GPa. The upper and lower tick marks below the profile show the positions of the main and first-order satellite reflections, respectively. The inset shows an enlarged view of the profile from Se-IV at 70 GPa. The arrows mark the positions of the ten satellite reflections that are still clearly visible at this pressure and the tick marks beneath the profile show the positions of the main reflections. Only the two main reflections at ~16° are separated enough to allow their individual positions to be determined accurately. The peak marked with a "*G*" is from the tungsten gasket.

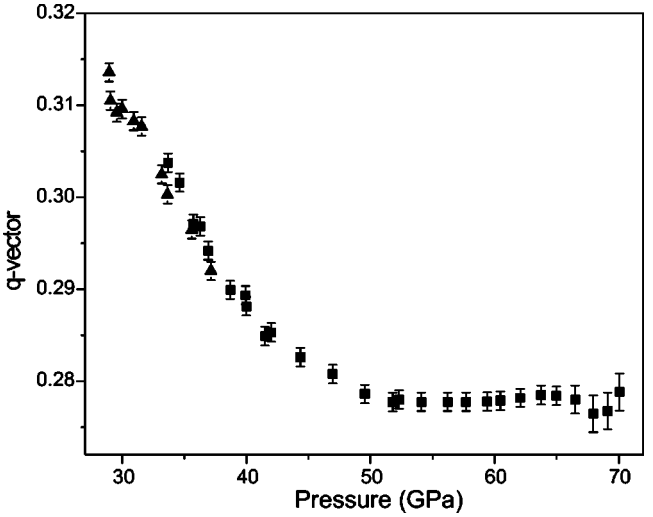

FIG. 3. The pressure dependence of the incommensurate wave vector $(0q0)$ in Se-IV to 70 GPa. Data from two different samples are identified with different symbols.

As in Te-III, increasing the pressure on Se-IV has two principal effects on the diffraction profiles—the coalescing of the main diffraction peaks into singlets and a reduction in the intensity of the satellite peaks. Above 56 GPa, the main diffraction peaks overlap to such an extent that it is no longer possible to resolve and measure their individual positions well enough to obtain accurate lattice parameters (see inset to Fig. 2). However, many of the satellite reflections remain nonoverlapped, and, although extremely weak, the very high intensity available on ID09 meant that these reflections were easily observable at all pressures (Fig. 2 inset). Above 56 GPa, therefore, the lattice parameters and incommensurate wave vector could still be obtained to high precision from a least-squares fit to the measured positions of two main reflections and ten satellite reflections.

The pressure dependence of the incommensurate wave vector of Se-IV, $(0q0)$, is shown in Fig. 3. As in Te-III,[21] q is strongly pressure dependent, decreasing from 0.314(1) at 28.9 GPa, the lowest pressure at which it could be measured, to 0.277(1) at 56 GPa. Above 56 GPa, $(0q0)$ is almost independent of pressure, and may even increase slightly, reaching a value of 0.279(2) at 70 GPa. However, the increase in q is, as yet, tentative, as the extreme weakness of the satellite peaks above 64 GPa means that the uncertainties in the value of q are larger than at lower pressures. We emphasize, however, that incommensurate satellite peaks were visible at all pressures up to 70 GPa (see inset to Fig. 2), the highest pressure reached in this study, and significantly above the reported transition pressure of 40–60 GPa to Se-V.[6–8] While the diffraction profiles collected above 60 GPa do indeed resemble those that would be expected from a primitive rhombohedral phase, the high resolution afforded by image-plate techniques reveals that the main Bragg peaks are still not fully combined into the singlets of the rhombohedral phase (Fig. 2 inset). And, as said, the satellite peaks are still clearly visible at 70 GPa. This suggests that, as in the case of the Te-III→Te-V transition, the misinterpretation of a transition to a rhombohedral phase almost

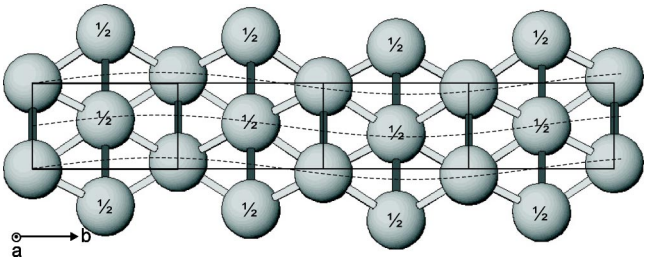

FIG. 4. Four unit cells of the modulated structure of Se-IV at 42 GPa as viewed down the *a* axis. The nearest-neighbor contact distances for each atom are shown, and those atoms at the body center are labeled with "$\frac{1}{2}$". Contact distances indicated with light bonds are affected by the modulation, while those distances denoted with darker bonds are not. The modulation wave is indicated with dotted lines.

certainly arose through a lack of resolution and sensitivity in the previous energy dispersive[8,13] and laboratory based[6–8,26] diffraction studies.

Four unit cells of the modulated structure of Se-IV are shown in Fig. 4. The unmodulated structure is six-fold coordinated, with two nearest-neighbor atoms at a distance of 2.5735(1)Å (identified using the darker shaded bonds in Fig. 4) at 42 GPa and four next-nearest neighbors at 2.5788(9)Å (identified with lighter shaded bonds in Fig. 4). The nearest-neighbor distance is equal to the *c*-axis lattice parameter and is thus unaffected by the modulation. The contact distances to the four next-nearest (*n*-*n*) neighbors *are* affected by the modulation, and in Te-III the atomic modulations were such as to make the closest Te-Te approach distance of these atoms almost independent of pressure over the range 5–27 GPa.[21] Figure 5 shows the closest and furthest approach of the next-nearest neighbors as a function of pressure, as determined from the refined *q* vector and modulation parameters.[25] The unmodulated distance is also shown for comparison. Refinements of the modulation parameters were only possible over the range 34.5–57.7 GPa: below 34 GPa

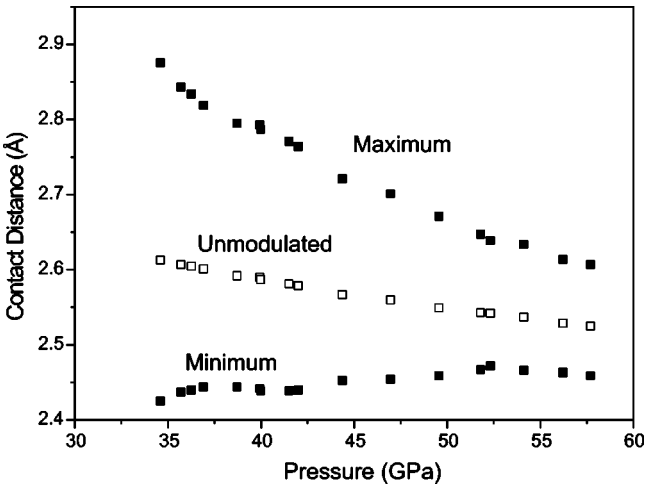

FIG. 5. The pressure dependence of the maximum and minimum contact distance of the next-nearest-neighbor atoms in Se-IV. The pressure dependence of the same contact distance in the unmodulated structure is shown for comparison.

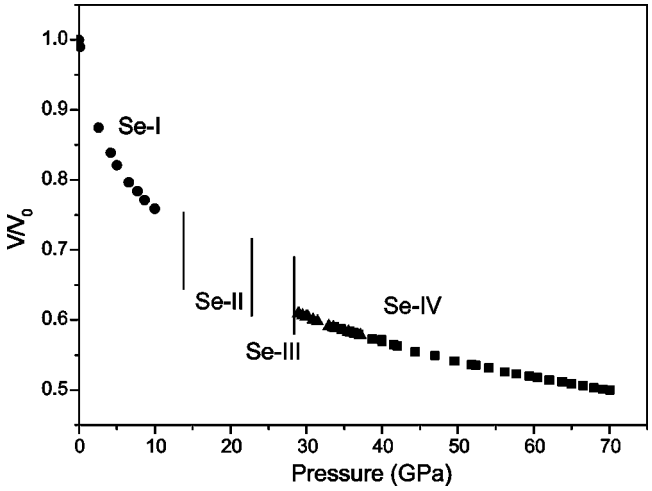

FIG. 6. The equation of state of Se-IV to 70 GPa. Data from two different samples are identified with different symbols. The data from Se-I are taken from Ref. 4.

the profiles contained overlapping peaks from Se-III, while above 58 GPa the extreme weakness of the satellite peaks meant that the modulation amplitudes could not be determined with confidence. In contrast to Te-III, the closest contact distance actually *increases* slightly by +0.034(6)Å from 2.425(4)Å at 34.5 GPa to 2.459(5)Å at 37.7 GPa. In the unmodulated structure, the same contact distance would have *decreased* by −0.088(3) from 2.617(2) to 2.525(2)Å over the same pressure range.

The compressibility of Se-IV to 70 GPa is shown in Fig. 6. In contrast to those studies which reported discontinuities in the compressibility and peak positions at the transition to rhombohedral Se-V at 40–60 GPa,[7,8] we observe no such changes. The lack of any structural transition is also compatible with the smooth variation seen in the superconducting

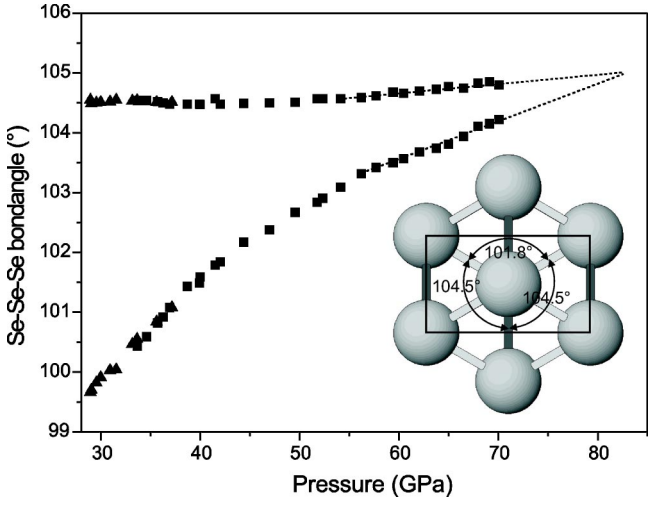

FIG. 7. Pressure dependence of the Se-Se-Se interatomic angles in Se-IV. Extrapolation of the data to higher pressures (dotted lines) indicates that the bond angles will become equal, and the structure will become rhombohedral, at 82 GPa. The inset shows an (unmodulated) unit cell of Se-IV at 42 GPa, identifying the interatomic angles that are plotted in the main profile.

temperature T_c over the same pressure range.[27]

While no transition to Se-V was observed up to 70 GPa, it is possible to estimate the transition pressure to Se-V from the pressure dependence of Se-IV. Se-V has the β-Po primitive rhombohedral structure which is a distortion of the simple cubic structure: in simple cubic each atom is eight-fold coordinated and the rhombohedral angle is 90°, while in the β-Po structure each atom is six-fold coordinated and the rhombohedral angle is ~104°. The inset to Fig. 7 shows a single unit cell of the (unmodulated) Se-IV structure at 42 GPa as viewed down the *a* axis. Even at 42 GPa the Se-IV structure is very β-Po-like, with each atom being six-fold coordinated. However, the 6 Se-Se-Se interatomic angles that are all equal to the ~104° rhombohedral angle in Se-V are ~101° and ~104° in Se-IV. The pressure dependence of these two interatomic angles is shown in Fig. 7. Assuming a continuous transition, extrapolation to higher pressures suggests that the angles will become equal, and the structure will transform to Se-V, at a pressure of 82 GPa.

The reinterpretation of both Te-III and Se-IV as having an incommensurate monoclinic structure raises the question as to whether this structure exists in other systems. We note that sulphur is reported to be metallic and isostructural with Te-III and Se-IV at pressures between 83 and 162 GPa.[28,29] From the published diffraction profiles, it is not possible to identify any of the strongest incommensurate satellite reflections because of overlaps with peaks from the gasket or gold pressure marker.[28,29] Further data are thus required, both to identify the true nature of the structure of sulphur above 80 GPa, and to investigate the nature of the reported transition to a β-Po phase at 162 GPa. The latter is particularly important in light of the pressure dependence of the superconductivity temperature in S, which is very different to that found in Se and Te.[27]

In summary, we have shown that Se-IV has the same incommensurate structure as Te-III, and, furthermore, that this structure is stable to at least 70 GPa, the highest pressure reached in this study. The previously reported transition to Se-V at 40–60 GPa is not observed, but extrapolation of the structural parameters of Se-IV suggests that a transition to Se-V will take place at 82 GPa. The incommensurate wave vector of Se-IV is significantly pressure dependent at pressures up to 56 GPa, after which it is almost pressure independent.

The authors acknowledge helpful discussion with Professor R. J. Nelmes. This work was supported by grants from EPSRC and facilities provided by the ESRF. M.I.M. acknowledges support from the Royal Society.

[1] P. W. Bridgman, Phys. Rev. **60**, 351 (1941).
[2] P. W. Bridgman, Proc. Am. Acad. Arts Sci. **74**, 425 (1942).
[3] J. Donahue, *The Structure of the Elements* (Wiley, New York, 1974).
[4] R. Keller, W. B. Holzapfel, and H. Schulz, Phys. Rev. B **16**, 4404 (1977).
[5] D. R. McCann and L. Cartz, J. Chem. Phys. **56**, 2552 (1972).
[6] H. K. Mao, G. Zhou, and P. M. Bell, Year Book - Carnegie Inst. Washington **80**, 283 (1980).
[7] Y. Akahama, M. Kobayashi, and H. Kawamura, Solid State Commun. **83**, 269 (1992).
[8] G. Parthasarathy and W. B. Holzapfel, Phys. Rev. B **38**, 10105 (1988).
[9] F. P. Bundy and K. J. Dunn, Phys. Rev. B **22**, 3157 (1980).
[10] Y. Akahama, M. Kobayashi, and H. Kawamura, Solid State Commun. **84**, 803 (1992).
[11] Y. Ohmasa, I. Yamamoto, M. Yao, and H. Endo, J. Phys. Soc. Jpn. **64**, 4766 (1995).
[12] K. Aoki, O. Shimomura, and S. Minomura, J. Phys. Soc. Jpn. **48**, 551 (1980).
[13] T. Kruger and W. B. Holzapfel, Phys. Rev. Lett. **69**, 305 (1992).
[14] Y. Akahama, M. Kobayashi, and H. Kawamura, Phys. Rev. B **47**, 20 (1993).
[15] H. C. Hsueh, C. C. Lee, C. W. Wang, and J. Crain, Phys. Rev. B **61**, 3851 (2000).
[16] M. Geshi, T. Oda, and Y. Hiwatari, J. Phys. Soc. Jpn. **67**, 3141 (1998).
[17] M. Geshi, T. Oda, and Y. Hiwatari, J. Phys. Soc. Jpn. **68**, 3341 (1999).
[18] M. Geshi, T. Oda, and Y. Hiwatari, J. Phys.: Condens. Matter **13**, 9401 (2001).
[19] M. Geshi, T. Oda, and Y. Hiwatari, J. Phys.: Condens. Matter **14**, 10885 (2002).
[20] S. P. Rudin, A. Y. Liu, J. K. Freericks, and A. Quandt, Phys. Rev. B **63**, 224107 (2001).
[21] C. Hejny and M. I. McMahon, Phys. Rev. Lett. **91**, 215502 (2003).
[22] H. K. Mao, J. Xu, and P. M. Bell, J. Geophys. Res., [Solid Earth Planets] **91**, 4673 (1986).
[23] A. P. Hammersley, S. O. Svensson, M. Hanfland, A. N. Fitch, and D. Hausermann, High Press. Res. **14**, 235 (1996).
[24] V. Petricek and M. Dusek, *The Crystallographic Computing System JANA2000* (Institute of Physics, Praha, Czech Republic, 2000).
[25] S. van Smaalen, Crystallogr. Rev. **4**, 79 (1995).
[26] Y. Akahama, M. Kobayashi, and H. Kawamura, Solid State Commun. **83**, 273 (1992).
[27] E. Gregoryanz, V. V. Struzhkin, R. J. Hemley, M. I. Eremets, H. K. Mao, and Y. A. Timofeev, Phys. Rev. B **65**, 064504 (1992).
[28] Y. Akahama, M. Kobayashi, and H. Kawamura, Phys. Rev. B **48**, 6862 (1993).
[29] H. Luo, R. G. Greene, and A. L. Ruoff, Phys. Rev. Lett. **71**, 2943 (1993).